In vivo imaging of the lamina cribrosa

A thesis submitted for the degree of Doctor of Philosophy at the
University of London, U.K.

Aachal Kotecha BSc (Hons) MCOptom

Laboratory of Physiological Optics, Department of Visual Science
and
Wound Healing Research Group, Department of Pathology
Institute of Ophthalmology
London

Glaucoma Research Unit
Moorfields Eye Hospital
London

January 2003

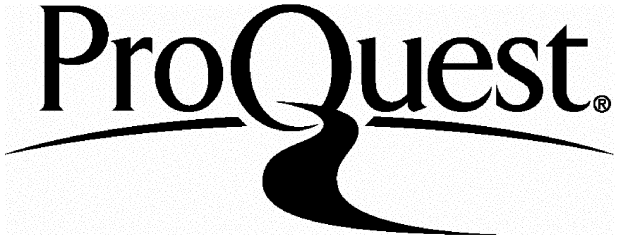

Abstract

This thesis describes the development of techniques to image the lamina cribrosa within the optic nerve head of the living human eye using a confocal scanning laser ophthalmoscope.

The axons from the retinal ganglion cells pass through the pores of the lamina cribrosa to synapse in the higher levels of the brain. The lamina cribrosa has been implicated as one of the main sites of damage to the ganglion cell axons in one of the leading causes of blindness, glaucoma, where it is thought that the raised intraocular pressure results in a backward bowing of the lamina, with consequent deformation of the ganglion cell axons. Most of our understanding of this process to date has come from investigations in post-mortem tissue, since the structure is difficult to visualise due to the optical scattering properties of the overlying neural tissue.

The development of new imaging technologies has enabled the investigation of the optic nerve *in vivo* to quantify its structure in the living human eye. These make use of the optical sectioning effects and improved depth resolution of confocal laser scanning ophthalmoscopy. The purpose of this study was to use these advances to image the lamina cribrosa in vivo, and determine whether using these techniques its structure could be reasonable quantified.

Two confocal scanning laser ophthalmoscope systems were used to obtain images of the lamina cribrosa area. These instruments used different lasers, and had different depth and spatial resolution, and were compared for image quality. A comparison was made between imaging with a near infrared laser and the helium neon laser, and it was predicted that the former might give better pore visibility due to greater tissue penetration. However, it was found that using the near infrared laser gave no benefit to lamina pore visibility. It was also found that

lamina cribrosa images were best obtained with one of the two instruments- the Zeiss cSLO.

Images obtained by these two instruments were digitised, and these digitised *in vivo* images of the lamina cribrosa underwent a series of image processing techniques to maximise the visibility of the pore-like structure. A method was developed which incorporated the use of Fourier analysis to select the optimum spatial frequency components to reduce the effects of image degradation. The result was a method that, for the first time, provided adequate image quality that allowed quantification of the morphology of the pores of the lamina cribrosa and without operator intervention. This has the advantage of removing possible sources of error due to the operator. In addition, unlike earlier studies, an unselected series of eyes were imaged without pre-selection for pore visibility.

A further study was performed to determine the relationship between the lamina pore characteristics and the optic nerve head topography using three dimensional reconstruction, to determine whether any differences existed between pore characteristics of normal and glaucomatous eyes. It was found that with increasing acquired neuroretinal rim loss, the average pore area and pore number increased. This agreed with post-mortem studies.

Histological studies were performed on hydrated post-mortem tissue in a range of aged eyes. The purpose of this was to establish the longitudinal thickness of the lamina cribrosa in order to evaluate the imaging depth of the cSLO. This study found that the longitudinal thickness of the lamina cribrosa was approximately two thirds larger than that previously found. This was attributed to the fact that most previous studies used dehydration and digestion techniques during tissue preparation.

This work has shown that it is possible to image the lamina cribrosa *in vivo* and obtain quantitative information about the pore structure without operator

intervention in unselected eyes. An image processing routine was developed to highlight the lamina pore structure using a technique based on Fourier analysis.

Publications and Presentations

Here follows a list of presentations and publications that have resulted either directly or indirectly from the work undertaken for this thesis.

Paper Presentations

- In vivo Imaging of the Lamina Cribrosa and its Relationship to Optic Nerve Head Topography, Kotecha A, Khaw PT, Hitchings RA, Fitzke FW; Association for Research and Vision in Ophthalmology (ARVO) meeting, May 2000.
- Segmental Optic Disc and Visual Field Changes following Trabeculectomy, Kotecha A, Siriwardena D, Garway-Heath DF, Khaw PT, Hitchings RA, Fitzke FW; ARVO May 1999.
- Optic Disc Changes Following Glaucoma Filtration Surgery, Kotecha A, Lowe T, Wilkins M, Fitzke FW, Khaw PT. Oxford Ophthalmological Congress 1997.

Poster Presentations

- In vivo Imaging of the Lamina Cribrosa and its Relationship to Optic Nerve Head Topography; Kotecha A, Khaw PT, Hitchings RA, Fitzke FW; European Glaucoma Society meeting June 2000, London, U.K.
- Image Size Variations using the Scanning Laser Ophthalmoscope, Kotecha A, Garway-Heath DF, Lowe T, Khaw PT, Hitchings RA, Fitzke FW. Invest Ophthalmol & Vis Sci 1997; 38: S3863.

Publications

- Optic disc changes following trabeculectomy: longitudinal and localisation of change, Kotecha A, Siriwardena D, Fitzke FW, Hitchings RA, Khaw PT, Br J Ophthalmol. 2001 Aug;85(8):956-61.
- Anterior chamber flare after trabeculectomy and after phacoemulsification, Siriwardena D, Kotecha A, Minassian D, Dart JK, Khaw PT, Br J Ophthalmol. 2000 Sep;84(9):1056-7.
- Sponge delivery variables and tissue levels of 5-fluorouracil, Wilkins MR, Occleston NL, Kotecha A, Waters L, Khaw PT, Br J Ophthalmol. 2000 Jan;84(1):92-7.

Declaration

I declare that the work presented in this thesis has been undertaken by myself, with prior discussion with my two supervisors. The data presented herein is my own original work, unless otherwise stated.

Aachal Kotecha, BSc(Hons) MCOptom

Acknowledgements

This work could not have been done without the help of many people from the Institute of Ophthalmology and Moorfields Eye Hospital.

Firstly, I'd like to thank my 2 supervisors, Professor Fred W. Fitzke and Professor Peng T. Khaw for their support and advice over the last 5 years. Fred's positive and calming attitude has helped me get over most of the obstacles that have presented themselves along this journey. He gave me faith both in myself and in my work, which is crucial to any success story, as faith does has a habit of slipping away when one is in the midst of things! Peng had total conviction in me right from the beginning, and had it not been for his encouragement, endless wisdom and contagious enthusiasm, I'd have never started this project. So thank you very much, both of you.

I'd also like to thank Professor Roger Hitchings for lending me some of his precious time to give me general guidance and encouragement along the research road, and for all his help with the ARVO presentations!
Thanks too to Ted Garway-Heath, whose advice on all things optic disc related (and unrelated) has been invaluable. I'd like to thank Mark Wilkins and Dilani Siriwardena, Rachel Michel and Melissa Harden from the 5-FU trial, for their encouragement and help during my time on the trial. I must also thank all the 5FU trial patients and their families for being such willing volunteers.

I am most grateful for the help of Natascha Bastiaan and Vy Luong from the Institute's Visual Science department with all things administrative and technical, and I thank Dr. Glen Jeffrey for the use of his lab and his 'eyes' for the anatomical studies in this thesis. I'd also like to thank Paul J, Ian and Paul II from the Institute workshop, for whom any task was never any trouble, and who always greeted me and my model eye with a smile! I'd also like to mention Roger

Chan, whom I met at the Institute. His musical talent ('name that tune') and dry wit made working at the Institute heaps of fun. The place was never the same once he left, and although his bombardment of 'done it yet?' emails were not always that helpful (he often received rather impolite replies), they brought a smile my occasionally (!) sullen face.

Finally, and most importantly, I'd like to thank my mum and dad, my sister Chhaya and my brother Serju for being my family, and my Baba for reminding me that this drama of life is just a game.

Table of Contents

IN VIVO IMAGING OF THE LAMINA CRIBROSA 1

ABSTRACT 2

PUBLICATIONS AND PRESENTATIONS 5

DECLARATION 6

ACKNOWLEDGEMENTS 7

TABLE OF CONTENTS 9

LIST OF FIGURES 15

LIST OF TABLES 17

LIST OF ABBREVIATIONS 19

CHAPTER 1: INTRODUCTION 20

1.1 THE LAMINA CRIBROSA 21

1.2 IMAGING THE EYE 22

1.2.1 Introduction 22

1.2.2 Confocal Scanning Laser Ophthalmoscopy 23

1.2.2.1 Confocal Optics 26

1.2.3 Imaging the fundus 27

1.2.3.1 The Ocular Media 27
1.2.3.2 The Fundus 31

1.3 ANATOMY OF THE OPTIC NERVE HEAD 33

1.3.1 The structure of the eye 33

1.3.2 The optic nerve 33
1.3.2.1 Intraocular Portion 33
1.3.2.2 Retrobulbar Portion 35
1.3.2.3 Intracanalicular Portion 35
1.3.2.4 Intracranial Portion 36

1.3.3 Normal Lamina Cribrosa 36
1.3.3.1 Extracellular Matrix 36
1.3.3.2 Changes with Age 36
1.3.3.3 Structural Architecture 37

1.4 GLAUCOMA 38

1.4.1 Definition 38

1.4.2 Normal Aqueous Dynamics 38
1.4.2.1 Aqueous Production 38
1.4.2.2 Aqueous Outflow 38
1.4.2.3 The Effect of Increasing Age 39

1.4.3 Intraocular Pressure 41

1.4.4 Glaucoma and the optic disc 41

1.5 EVALUATION OF CURRENT METHODS FOR OPTIC NERVE HEAD ASSESSMENT 42

1.5.1 Qualitative Assessment of the ONH 42

1.5.1.1 Direct and indirect ophthalmoscopy 42
1.5.1.2 Stereophotography 43

1.5.2 Quantitative Assessment of the ONH 43
1.5.2.1 Planimetry 43
1.5.2.2 Videographic Image Analysis 43
1.5.2.3 Scanning Laser Ophthalmoscopy 44
1.5.2.4 Optical Coherence Tomography 44

1.6 IMAGING THE LAMINA CRIBROSA 46

1.6.1 Aims 47

CHAPTER 2: MATERIALS AND METHODS 49

2.1 IMAGE ACQUISITION AND PROCESSING 50

2. 1.1 Hardware 50
2.1.1.1 Heidelberg Retina Tomograph 50
2.1.1.2 Zeiss Jena cSLO 51

2.1.2 Calibration of cSLO 52
2.1.2.1 Resolution of Images 52
2.1.2.2 Image Distortions with the Zeiss and HRT cSLO 58

2.1.3 Real Size of Fundus Features 62
2.1.3.1 Calculating the real size of fundus features 62
2.1.3.2 Ocular Factor 65

2.1.4 Image Processing 66
2.1.4.1 Introduction to Image Processing 66
2.1.4.2 Image Enhancement I- Processing in the Spatial Domain 66
2.1.4.3 Image Enhancement II- Processing in the Frequency Domain 78
2.1.4.4 Image restoration- Deconvolution 97

2.1.4.5 Mean luminance of images 108
2.1.4.6 Final Image Processing Steps 112

2.1.5 Scanning Laser Ophthalmoscopes II- Laser sources and penetration 115

2.1.5.1 Imaging the Lamina Cribrosa- Considerations 115
2.1.5.2 Wavelength of laser light and imaging the lamina cribrosa 115

CHAPTER 3: IN VIVO IMAGING OF THE LAMINA CRIBROSA 126

3.1 IMAGE ACQUISITION WITH THE HRT AND THE ZEISS 127

3.1.1 Introduction 127

3.1.2 Materials and Methods 127
3.1.2.1 Image Acquisition 127
3.1.2.2 Image Processing – HRT images 128
3.1.2.3 Image Processing – Zeiss cSLO 128
3.1.2.4 Image Quality Measurement: Variance 129
3.1.2.5 Lamina Pore Quantification 131
3.1.2.6 Initial Study -Subjects 131

3.1.3 Results 131

3.1.4 Discussion 134

CHAPTER 4: IN VIVO IMAGING II- PORE QUANTIFICATION TECHNIQUES 137

4.1 AUTOMATED VERSUS MANUAL THRESHOLDING 138

4.1.1 Introduction 138

4.1.2 Materials and Methods **138**

4.1.3 Results **139**

4.1.3.1 Automated thresholding versus manual-draw methods for quantifying pores 139

4.1.3.2 Manual Zeiss vs. Manual HRT 152

4.1.3.3 Total Pore Area 154

4.1.4 Discussion **156**

4.1.4.1 Automated vs. Manual 156

4.1.4.2 HRT vs. Zeiss 158

CHAPTER 5: IN VIVO IMAGING III 159

5.1 LAMINA PORE MORPHOLOGY AND OPTIC DISC TOPOGRAPHY **160**

5.1.1 Introduction **160**

5.1.2 Materials and Methods **160**

5.1.2.1 Image Acquisition 160

5.1.2.2 Initial Study -Subjects 160

5.1.2.3 Lamina pore characteristics 163

5.1.3 Results **164**

5.1.4 Discussion **177**

5.1.4.1 Pore morphology 177

5.1.4.2 Relationship to optic nerve head topography 178

CHAPTER 6: ANATOMICAL STUDIES 181

6.1 ARCHITECTURE OF LAMINA CRIBROSA **182**

6.1.1 Introduction **182**

6.1.2 Materials and Methods 183
6.1.2.1 Tissue Preparation 183
6.1.2.2 Measurement I: Thickness of Lamina 184
6.1.2.3 Measurement II: Thickness of Laminar Plates 184

6.1.3 Results 189

6.1.4 Discussion 194

CHAPTER 7: CONCLUSIONS 200

7.1 CONCLUSIONS 201

APPENDICES 203

Appendix I: The Heidelberg Retina Tomograph 204

Appendix II: Principals of adaptive optics 214

Appendix III: Matlab Script for variance measure 219

REFERENCES 220

List of Figures

FIGURE 1.1: SCHEMATIC DIAGRAM OF CONFOCAL SCANNING LASER OPHTHALMOSCOPE 25
FIGURE 1.2: PERCENTAGE TRANSMISSION OF NORMAL CRYSTALLINE LENSES. 30
FIGURE 1.3: PERCENTAGE TRANSMISSION IN CATARACTOUS LENSES. 30
FIGURE 1.4: DIAGRAM OF STRUCTURE OF THE EYE 34
FIGURE 1.5: SCHEMATIC DIAGRAM SHOWING AQUEOUS DYNAMICS 40
FIGURE 2.1B: AXIAL RESOLUTION OF THE ZEISS CSLO 56
FIGURE 2.2: THE MODEL EYE 59
FIGURE 2.3: ELONGATION FACTOR - ZEISS, HRT AND NIKON CAMERA 61
FIGURE 2.4: P VALUE FOR HRT AND ZEISS 64
FIGURE 2.5: RANK LEVELLING OPERATIONS 68
FIGURE 2.6: UNSHARP MASKING 71
FIGURE 2.7: CONTRAST STRETCHING I: WHY CONTRAST STRETCH? 73
FIGURE 2.8: CONTRAST STRETCHING II: EXTENDING THE RANGE OF PIXEL VALUES 74
FIGURE 2.9: IMAGE PROCESSING IN THE SPATIAL DOMAIN: SUMMARY 75
FIGURE 2.10: THRESHOLDING 77
FIGURE 2.11: IMAGE PROCESSING IN THE FREQUENCY DOMAIN 80
FIGURE 2.12: PROCESSING IN THE FREQUENCY DOMAIN- ANNULAR FILTERS 81
FIGURE 2.13: THRESHOLDING 82
FIGURE 2.14:THE INFLUENCE OF PERIODIC NOISE- BLANK SCREEN 84
FIGURE 2.15: PERIODIC NOISE IN OPTIC DISC IMAGES 88
FIGURE 2.16: SCHEMATIC DIAGRAM ILLUSTRATING THE EFFECT OF SACCADIC EYE MOVEMENTS ON PERIODIC NOISE 90
FIGURE 2.17: THE INFLUENCE OF PERIODIC NOISE- OPTIC DISC IMAGES 91
FIGURE 2.18: IMAGE ARTEFACTS 95
FIGURE 2.19: IMAGE RESTORATION I- BLIND DECONVOLUTION OF HRT IMAGES. 100
FIGURE 2.20: IMAGE RESTORATION II- PROCESSING THE HRT IMAGES. 101
FIGURE 2.21: IMAGE RESTORATION III- THRESHOLDING THE HRT IMAGES. 102
FIGURE 2.22: IMAGE RESTORATION IV- BLIND DECONVOLUTION OF ZEISS IMAGES. 103

FIGURE 2.23: IMAGE RESTORATION V- PROCESSING THE ZEISS IMAGES. 104
FIGURE 2.24: IMAGE RESTORATION VI- THRESHOLDING THE ZEISS IMAGES. 105
FIGURE 2.25: IMAGE RESTORATION VII- ARTEFACTS WITH DECONVOLUTION. 106
FIGURE 2.26: IMAGE RESTORATION VIII- ARTEFACTS WITH DECONVOLUTION. 107
FIGURE 2.27: THE EFFECT OF MEAN LUMINANCE ON THRESHOLDING I 109
FIGURE 2.28: THE EFFECT OF MEAN LUMINANCE ON THRESHOLDING II 110
FIGURE 2.29: THE EFFECT OF MEAN LUMINANCE ON THRESHOLDING III 111
FIGURE 2.30: IMAGING WITH DIFFERENT WAVELENGTHS I 118
FIGURE 2.31: IMAGING WITH DIFFERENT WAVELENGTHS II 119
FIGURE 2.32: IMAGING WITH DIFFERENT WAVELENGTHS III 120
FIGURE 2.33: IMAGING WITH DIFFERENT WAVELENGTHS IV 121
FIGURE 2.34: IMAGING WITH DIFFERENT WAVELENGTHS V 122
FIGURE 2.35: IMAGING WITH DIFFERENT WAVELENGTHS VI 123
FIGURE 3.1: OPTIC DISC AREA WITHIN ZEISS AND HRT IMAGES. 130
FIGURE 3.2: SOURCES OF ERROR WITH AUTOMATED THRESHOLDING 136
FIGURE 4.1: BLAND- ALTMAN PLOT FOR PORE NUMBER MEASUREMENTS 143
FIGURE 4.2: BLAND- ALTMAN PLOT FOR PORE AREA MEASUREMENTS 144
FIGURE 4.3: BLAND- ALTMAN PLOT FOR PORE ELONGATION MEASUREMENTS 145
FIGURE 4.4: GRAPH SHOWING DIFFERENCE IN PORE NUMBER (AT/MD) VS. CUP AREA 148
FIGURE 4.5 GRAPH SHOWING DIFFERENCE IN PORE NUMBER FOUND WITH AT/MD TECHNIQUES AND CD RATIO 149
FIGURE 4.6 GRAPH SHOWING DIFFERENCE IN PORE AREA FOUND WITH AT/MD TECHNIQUES AND CUP AREA 150
FIGURE 4.7 GRAPH SHOWING DIFFERENCE IN PORE AREA FOUND WITH AT/MD TECHNIQUES AND CD RATIO 151
FIGURE 5.1: RELATIONSHIP BETWEEN PORE MORPHOLOGY AND DISC AREA 170
FIGURE 5.2: RELATIONSHIP BETWEEN PORE MORPHOLOGY AND CUP PARAMETERS 171
FIGURE 5.3: RELATIONSHIP BETWEEN PORE MORPHOLOGY 3RD MOMENT 173
FIGURE 5.4: RELATIONSHIP BETWEEN PORE MORPHOLOGY AND RIM INDEX. 175

FIGURE 6.1: SCHEMATIC DIAGRAM ILLUSTRATING METHOD OF SECTIONING OPTIC NERVE HEAD 186
FIGURE 6.2: SECTION OF LAMINA CRIBROSA TO ILLUSTRATE AREAS OF CRIBROSAL PLATE THICKNESS MEASUREMENTS 187
FIGURE 6.3: MEASUREMENT OF CRIBROSAL PLATE WIDTH 188
FIGURE 6.4: CHANGE IN LAMINA CRIBROSA THICKNESS WITH AGE 190
FIGURE 6.5: THICKNESS OF CRIBROSAL PLATES THROUGH LAMINA CRIBROSA 191
FIGURE 6.6: CHANGE IN CRIBROSAL PLATE THICKNESS WITH AGE 192
FIGURE 6.7: OCT IMAGE OF OPTIC DISC OBTAINED USING THE STANDARD OCT 198
FIGURE 6.8: *EN FACE* IMAGE OF OPTIC NERVE HEAD TAKEN WITH A MODIFIED OCT 199
FIGURE A1A: OPTICAL SECTIONS: 207
FIGURE A1B: Z-PROFILE OF PIXEL (X,Y) IN IMAGE SERIES: 207
FIGURE A2: TOPOGRAPHY AND REFLECTIVITY IMAGE 208
FIGURE A3: STEREOMETRIC PARAMETERS – HRT I 209
FIGURE A4: DISC ANALYSIS WITH HRTII- MOORFIELDS ANALYSIS FEATURE 210
FIGURE A5: MOORFIELDS ANALYSIS FEATURE- DETAILS 211
FIGURE A6: DISC ANALYSIS- GLAUCOMATOUS DISC 212
FIGURE A7: MOORFIELDS ANALYSIS FEATURE- DETAILS 213
FIGURE A8: PRINCIPLE OF DEFORMABLE MIRROR 214
FIGURE A9: PRINCIPLE OF AN ADAPTIVE OPTICS SYSTEM. 217
FIGURE A10: SCHEMATIC DIAGRAM OF WAVEFRONT DETECTOR. 218

List of Tables

TABLE 2.1: MICROMETER DISPLACEMENT AND AVERAGE INTENSITY OF REFLECTOR FOR DIFFERENT STOP SIZES. 57
TABLE 2.2: COMPARISON OF IMAGE PROCESSING METHODS FOR HRT AND ZEISS CSLO IMAGES. 114
TABLE 2.3: VARIANCE MEASURES OF PROCESSED OPTIC DISC IMAGES FOR THE DIFFERENT WAVELENGTHS OF LASERS USED. 124
TABLE 3.1: COMPARISON OF PORE DETAILS FOUND WITH HRT AND ZEISS CSLO'S. 133

TABLE 4.1: COMPARISON OF PORE DETAILS FOUND BY AUTOMATED THRESHOLDING (AT) METHOD AND BY MANUAL DRAWING (MD) FOR HRT CSLO. 141
TABLE 4.2: COMPARISON OF PORE DETAILS FOUND BY AUTOMATED THRESHOLDING (AT) METHOD AND BY MANUAL DRAWING (MD) FOR ZEISS CSLO 142
TABLE 4.3: COMPARISON OF PORE DETAILS FOUND BY MANUAL DRAWING TECHNIQUE FOR ZEISS AND HRT CSLO'S. 153
TABLE 4.4: TOTAL PORE AREA FOR EACH SUBJECT WITH BOTH IMAGING TECHNIQUES AND LAMINA PORE QUANTIFICATION METHODS. 155
TABLE 4.5 DISC DATA AND DIFFERENCE BETWEEN AT AND MD METHODS OF PORE QUANTIFICATION FOR HRT AND ZEISS CSLO'S. 147
TABLE 5.1: LAMINA PORE MORPHOLOGY AND OPTIC DISC TOPOGRAPHY- GLAUCOMAS 166
TABLE 5.2 : LAMINA PORE MORPHOLOGY AND OPTIC DISC TOPOGRAPHY- NORMALS 167
TABLE 5.3: RANGE OF PORE AREAS FOUND FOR EACH SUBJECT GROUP 168
TABLE 5.4: RELATIONSHIP BETWEEN PORE CHARACTERISTICS AND OPTIC NERVE HEAD TOPOGRAPHY. 169
TABLE 6.1: CRIBROSAL PLATE THICKNESS CHANGE WITH AGE. 193

List of Abbreviations

AO	Adaptive optics
Ar	Argon
AT	Automated thresholding
CDR	Cup:disc ratio
CSLO	Confocal scanning laser ophthalmoscope
FFT	Fast Fourier transform
HeNe	Helium Neon
HRT	Heidelberg retina tomograph
IOP	Intraocular pressure
MD	Manual draw
ONH	Optic nerve head
OCT	Optical coherence tomography
mmHg	Millimetres of mercury (pressure)
NIR	Near infra-red
nm	Nanometers
POAG	Primary open angle glaucoma
RNFL	Retinal nerve fibre layer
SD	Standard deviation
TPA	Total pore area
μ	microns

Chapter 1: Introduction

1.1 The lamina cribrosa

The lamina cribrosa is the structure within the optic nerve head that is the point of exit and entrance of the retinal nerve fibres and the central retinal vessels respectively. It is implicated in some conditions that affect the optic nerve, particularly in high-tension glaucoma, where it is thought to be the area of primary insult of the nerve fibres. Detailed knowledge of the areas elaborate architecture is required in order to produce accurate models to determine its role in optic nerve head pathologies. Recent emphasis has been put on recreating virtual models of the area in order to understand how raised intraocular pressure distorts the shape of the cribrosal plates in order to further our understanding of the mode of nerve fibre damage in glaucoma. (Bellezza, Hart et al. 2000)

One of the first studies detailing the anatomy of the lamina cribrosa was performed by Wilczek in 1947(Wilczek 1947). A model of the structure was made using a mixture of paraffin and beeswax after making casts of 20 micron thick microtomed sections of the area from human cadaver samples. This was one of the first times that the intricate 3 dimensional lamina structure was reconstructed and described. Since then, the area has been investigated in great detail, using scanning electron microscopic techniques in order to obtain high resolution images of the area. Studies have been performed detailing its regional variation, pore sizes, variation between normals and glaucomas (Anderson 1969; Emery, Landis et al. 1974; Radius and Anderson 1979; Quigley and Addicks 1981; Radius and Gonzales 1981; Ogden, Duggan et al. 1988) but all of these studies have used post mortem tissue in their investigations. In the analysis of post mortem tissue, the sample undergoes a series of procedures that digest, dehydrate and slice the tissue, which are known to cause artefacts(Birch, Brotchie et al. 1997).

The purpose of this project was develop a technique that adequately imaged the lamina cribrosa area in vivo, with a view to using it in the assessment of glaucomatous and non-glaucomatous eyes to highlight differences in lamina structure that may help in the evaluation and understanding of the disease process.

1.2 Imaging the Eye

1.2.1 Introduction

The introduction of the ophthalmoscope in 1850 by Helmholtz enabled *in vivo* visualization of the human fundus, and had a major impact in understanding many eye diseases. Von Jaeger published the first atlas of fundus drawings in 1869 (von Jaeger 1869), describing changes in many eye diseases, in particular glaucoma. However, making sketches of the fundus was a rather arduous task, and attempts were made to produce permanent records of fundal appearance using photography in 1863 by Liebrecht in Berlin and Noyes in New York. In 1910, Swedish ophthalmologist Allvar Gullstrand produced the 'large ophthalmoscope' that enabled binocular examination of the eye. The first commercially available fundus camera was introduced by Nordeson in 1925(1990; Varma and Spaeth 1993).

In ophthalmology, a team at St. Thomas' hospital attempted a production of televised ophthalmoscopy in 1949 (Ridley 1950). The system was developed with the help of Marconi, and was based on the indirect ophthalmoscope. It utilized a number of condensing lenses and prisms placed in front of the eye so that the fundus could be viewed free of the corneal reflex. The system could use monochromatic or colour television, but the latter required 8 times more light for viewing. The system was successful, but very bulky and impractical to use routinely.

Developments in quantitative imaging based on digital technologies have developed rapidly. Digital imaging was first used by government agencies in earth orbiting satellite programs in the early 1950's (pers. comm. R.D Launius, NASA chief historian). Since then, digital image capturing systems have become more sophisticated and their use in medical imaging as diagnostic tools and follow up of medical conditions has opened up new opportunities.

In general medicine, radiologists have used digital image processing in the enhancement of images obtained using x-rays, computerized tomography and magnetic resonance imaging, in order to aid visualisation and diagnosis of

diseases (Lingren 1968). These have made visible, for the first time, structures that could not previously be seen in the living human.

In ophthalmology, the advent of digital imaging technologies has provided a method of objectively quantifying the grade of ocular disease. Digital image processing techniques can provide an objective and repeatable method of quantifying points of interest within the image. Techniques have been used in grading the degree of diabetic retinopathy (Spencer, Phillips et al. 1992; Spencer, Olson et al. 1996; George, Lusty et al. 1999), as well as in the assessment and management of glaucomatous patients (Caprioli, Klingbeil et al. 1986; Weinreb, Dreher et al. 1989; Assad and Caprioli 1992; Cioffi, Robin et al. 1993; Wollstein, Garway-Heath et al. 1998; Kamal, Viswanathan et al. 1999). Some of these techniques have used either digital fundus cameras or the digitisation of fundus photographs, and some have utilised the confocal scanning laser ophthalmoscope.

1.2.2 Confocal Scanning Laser Ophthalmoscopy

In 1980, a group from Boston, USA, created a device that used a laser light source to illuminate the fundus and produce an image of it on a television monitor. They described this device as the ' Flying Spot T.V Ophthalmoscope' (Webb, Hughes et al. 1980). The scanning laser ophthalmoscope (SLO), as it was later termed, provides a high quality image of the fundus using less than 1/1000 of the light necessary to illuminate the fundus with conventional light ophthalmoscopy (Webb and Hughes 1981; Mainster, Timberlake et al. 1982). Only one point on the fundus is illuminated at any one time, and the laser sweeps across the fundus in a raster-like fashion so that a piece-by-piece image of the fundus is built up on the television screen (Figure 1.1). In addition, because the SLO only illuminates a small area of the fundus at any one time, only a small amount of the patients' pupil –normally about 0.9mm- is used for illumination, allowing the rest of it to be available for light collection. This is quite different from conventional indirect ophthalmoscopy, where almost the whole pupil is used for the illumination of the fundus, and only about $1/10^{th}$ of the pupil is used to view it.

However, it must be mentioned that in reflex-free indirect ophthalmoscopes, a circumferential ring of light is used to illuminate the fundus, leaving the central pupillary area free for viewing- this helps to eliminate obstructive reflections caused by the corneal reflex. This set-up still uses more of the pupil than the SLO, and for optimum fundus viewing, the pupil must be dilated. Light levels in the SLO are less than 70 $\mu W/cm^2$ compared with 100,000$\mu W/cm^2$ for indirect ophthalmoscopy (Webb, Hughes et al. 1980; Webb and Hughes 1981).

Figure 1.1: Schematic diagram of confocal scanning laser ophthalmoscope

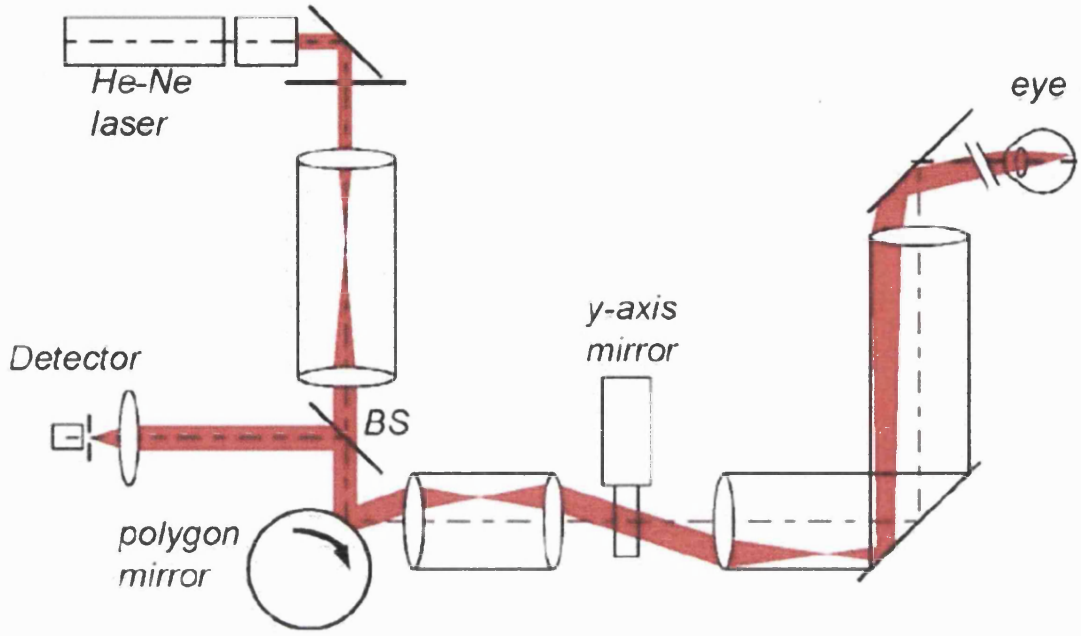

The red shows the path of the scanning laser beam. The laser light source (denoted by the HeNe) enters a lens system that controls the focus. Raster scanning is facilitated by the combination of a rotating polygon (horizontal) and a galvanometer scanning mirror (vertical). BS denotes the beam splitter, to enable light reflected back through the eye to be relayed to the detector, which in turn is connected to the television monitor.

1.2.2.1 Confocal Optics

A unique property of the SLO is that it can use confocal optics. Confocality of the system is achieved by placing a pinhole in front of the detector that is conjugate to the laser focus. In the confocal mode, light that is reflected or scattered by other retinal layers is blocked by the pinhole, thus removing the masking reflections from structures at different depths and lateral locations. The size of the pinhole determines the degree of confocality, such that a small pinhole aperture will give a highly confocal image. (Dreher, Bille et al. 1989; Woon, Fitzke et al. 1990; Woon, Fitzke et al. 1992; Fitzke and Masters 1993). The image produced is a narrow optical section of the area of fundus under investigation. Unlike conventional ophthalmic imaging, where objects outside the plane of interest contribute to the image therefore degrading the quality of the image, in the confocal SLO the contrast is improved.

Confocal scanning laser ophthalmoscopes have been used to image the retinal cone mosaic (Wade 1998), as well as in optic nerve head and macula investigations to provide a three-dimensional tomography of the area. The axial and lateral resolution of the cSLO is discussed in more detail in chapter 2.

1.2.3 Imaging the fundus

In fundal imaging the incident and reflected light passes through a series of ocular structures. In general, biological tissues have variations in hydration and irregularities that change the refractive index of these tissues and give rise to reflections. Changes in the refractive index through the material will cause a scattering of light as, due to Snell's law, reflections will occur at interfaces between media of differing refractive indices and refraction will cause attenuation of light rays. This is especially so with imaging in white light since different wavelengths will be refracted differently.

The use of monochromatic light when imaging through these structures will help limit this problem. In addition, anatomical details of fundus structures are more easily seen using monochromatic light, because of the different absorption and reflectance characteristics of the stratified layers of the fundus (Delori and Gragoudas 1976; Delori, Gragoudas et al. 1977; Delori and Pflibsen 1989). The following discusses the effects of these layers and those of the ocular media on imaging.

1.2.3.1 The Ocular Media

Cornea

The cornea provides the greatest proportion of the overall refraction of the eye, accounting for two thirds of its refractive power, not taking into account the effect of the tear film. The cornea is a transparent tissue, transmitting about 90% of incident light (555nm) (Feuk 1970). Its refractive index, radius of curvature and transparency to visible light determine its optical properties. The refractive index is determined by its chemical composition and degree of hydration. The radius of curvature is determined by normal growth and development. Its transparency is determined by its avascularity, chemical composition and morphology.

The corneal stroma is composed of lamellae of parallel collagen fibrils in a mucopolysaccharide ground substance. The geometric arrangement of collagen fibrils within the corneal stroma play a significant role in corneal transparency

(Lerman 1984.) There are light scattering particles within the corneal structure, but it has been suggested that transparency is maintained because the density of these particles is uniform throughout the structure- therefore the total intensity of internal scattered light is zero (Benedek 1971).
Transmission of light through the cornea increases with increasing wavelength of light. At wavelengths between 600 – 1000 nm, transmission is 95% or greater, and there appears to be no decrease in transmission in healthy corneas with age (Beems and Van Best 1990).
The refractive index of the cornea is typically taken as 1.376 (Bennett and Rabbetts 1984).

Lens

The human crystalline lens is a unique, biconvex, transparent and avascular organ, consisting of 65 % water and 35 % matter, the majority of which are structural proteins called crystallins (Lerman 1984).
The lens fibres originate from an anterior layer of epithelial cells and grow and differentiate into long fibres packed into a regular, quasi-hexagonal array (Delaye and Tardieu 1983). The variation in the distribution of the concentration of crystallins within the lens leads to a higher refractive index towards the centre of the lens. This reduces spherical aberration. Overall, light absorption is negligible, as the lens contains few visible chromophores (lens pigments). However, with age there is an increase in photochemically generated fluorescent chromophores, due to the constant exposure of the eye to UV radiation over its lifetime. These pigments are confined to the lens nucleus. The amount of short wavelength absorption increases with age, due to the increase in these chromophores Transmission studies have shown that the transmission of wavelengths between 300 and 400 nm (ultraviolet spectrum) is only about 20% in eyes over 25 years (Lerman and Borkman 1976) (see figure 1.2).
Transmission of light between 400 and 800 nm steadily increases over the range, from approximately 25% at 400nm to between 50-60% at 800 nm. Absorption in the ocular media affects both incident and reflected light. In the cataractous eye,

the transmission of visible light varies with the type of cataract (Lerman and Borkman 1976; Nishimoto and Sasaki 1995) (figure 1.3). Light scattering arises from short-range fluctuations of the refractive index. There is a high concentration of lens proteins and few cellular organelles, so that the light scattering is determined by the spatial arrangement of the crystallin proteins.

Figure 1.2: Percentage transmission of normal crystalline lenses.

6 eyes ranging from ages 6 months to 82 years.

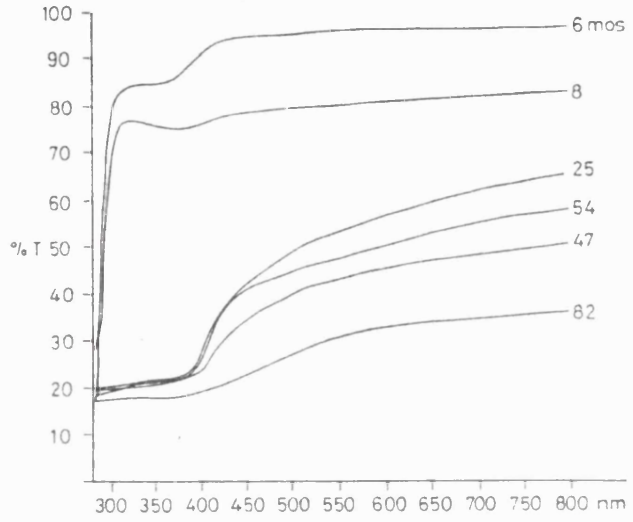

The amount of short wavelength absorption increases with age.

Figure 1.3: Percentage transmission in cataractous lenses.

68 and 80 year old cortical cataracts (suffix 'c'), 70 and 86 year old nuclear cataracts (suffix 'n') and 74 year old mixed cataract (suffix 'm')

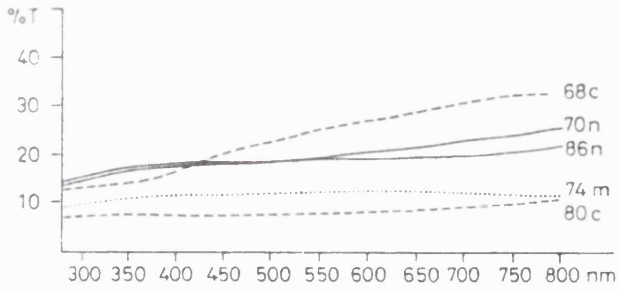

Taken from Lerman and Borkman (Lerman and Borkman 1976), with kind permission.

1.2.3.2 The Fundus

Spectral reflectance of the fundus

The colour of the fundus is characterised by the mixture of reflected wavelengths. The mixture is determined by the amount of light reflected at various reflecting surfaces in the eye. The reflectance spectrum has been modelled (Delori and Pflibsen 1989) .The model takes into account the absorbing properties of melanin and the blood in choroidal vessels and the scattering properties of the choroid and sclera. In the model (Delori and Pflibsen 1989) for nasal fundus, choroid and sclera account for about 6 – 15% of the total reflectance at 540nm and 50 – 80% at 675nm. Removal of the scleral component from the model reduces the total reflectance by only 1 – 4% in the darkest fundi at 675nm, and by 40 – 55% in the lightest. Thus, choroidal scattering causes a substantial amount of light to be reflected from the stroma.

The absorption of light by blood occurs mainly in the choriocapillaris, and the contribution made by the retinal capillaries is very small by comparison (Delori and Pflibsen 1989). However, the optic nerve head is the entry and exit point for the central retinal artery and vein. These larger vessels often obscure part of the optic cup and overlie the neuroretinal rim, and so hamper the visualization of the optic cup area. Light absorption by oxyhemoglobin varies with wavelength, being greatest at the lower wavelengths, reducing slowly and peaking again at 575 nm, before dropping off to little absorption at 700 nm. Therefore, blood vessels become highly reflective at the higher wavelengths. Retinal blood vessels are best observed at wavelengths of between 540 and 580 nm, whilst the deeper choroidal vessels are optimum at wavelengths greater 600 nm (Delori, Gragoudas et al. 1977; Delori and Pflibsen 1989).

It has been reported that fundus reflectance is lower for shorter wavelength light and increases with increasing wavelength (Delori and Pflibsen 1989; Elsner, Burns et al. 1996). In addition, the longer the wavelength, the deeper the penetration, and it has been shown that near-infrared imaging is well suited for

investigating sub-retinal structures (Manivannan, Kirkpatrick et al. 1994; Elsner, Burns et al. 1996).

Properties of the sclera

The sclera is an important reflector within the fundus. It is opaque to light, scattering almost all visible frequencies (thus appearing white). The stroma is composed of lamellae of parallel collagen fibrils, but the size and spacing of the fibrils is much less uniform than in the cornea. Reflectance in enucleated eyes has been recorded as being up to 70% at 675nm, and in vivo in eyes with colobomas as 33 % at 675nm (Delori and Pflibsen 1989). Scleral reflectance decreases slightly with increasing wavelength.

Knowledge of the absorption and reflectance characteristics of the ocular media and fundus gives information that helps to determine the best wavelength of light through which to view the lamina cribrosa. The subject of best wavelength for imaging the lamina cribrosa will be discussed further in chapter two.

1.3 Anatomy of the Optic Nerve Head

1.3.1 The structure of the eye

The structure of the human eye is illustrated on the following page.

1.3.2 The optic nerve

The optic nerve head is the point of exit of the retinal nerve fibres from the eye. For the purposes of anatomical description, the optic nerve may be divided into four areas:

a) intraocular (1 mm)
b) retrobulbar (25 mm)
c) intracanalicular (5-20mm)
d) intracranial (10mm)

(Ritch, Shields et al. 1989; Shields 1989; Bron, Tripathi et al. 1997)

1.3.2.1 Intraocular Portion

The intraocular portion comprises of the retinal ganglion cell layer, the retinal nerve fibre layer and the optic disc.

The optic disc (prelaminar zone)

The retinal ganglion cell axons converge to the optic nerve head before they exit the eye through the scleral foreamen. The optic nerve head, also known as the optic disc, is a slightly vertically oval structure and there is a large interindividual variability in its size. Average disc areas have been reported as 2.60mm^2 $\pm$ 0.72mm^2 (Dandona, Quigley et al. 1990), with an interindividual variability of 1:7. Viewing with an ophthalmoscope, the nerve head consists of two distinct areas; the neuroretinal rim, and the optic 'cup'. The neuroretinal rim is composed mainly of ganglion cell axons, but also includes small capillaries and astrocytes. The optic cup has no neural tissue, although the astrocytes do continue into this area. The optic disc is surrounded by a halo termed Elschnig's rim, which is the rim of sclera

Figure 1.4: Diagram of structure of the eye

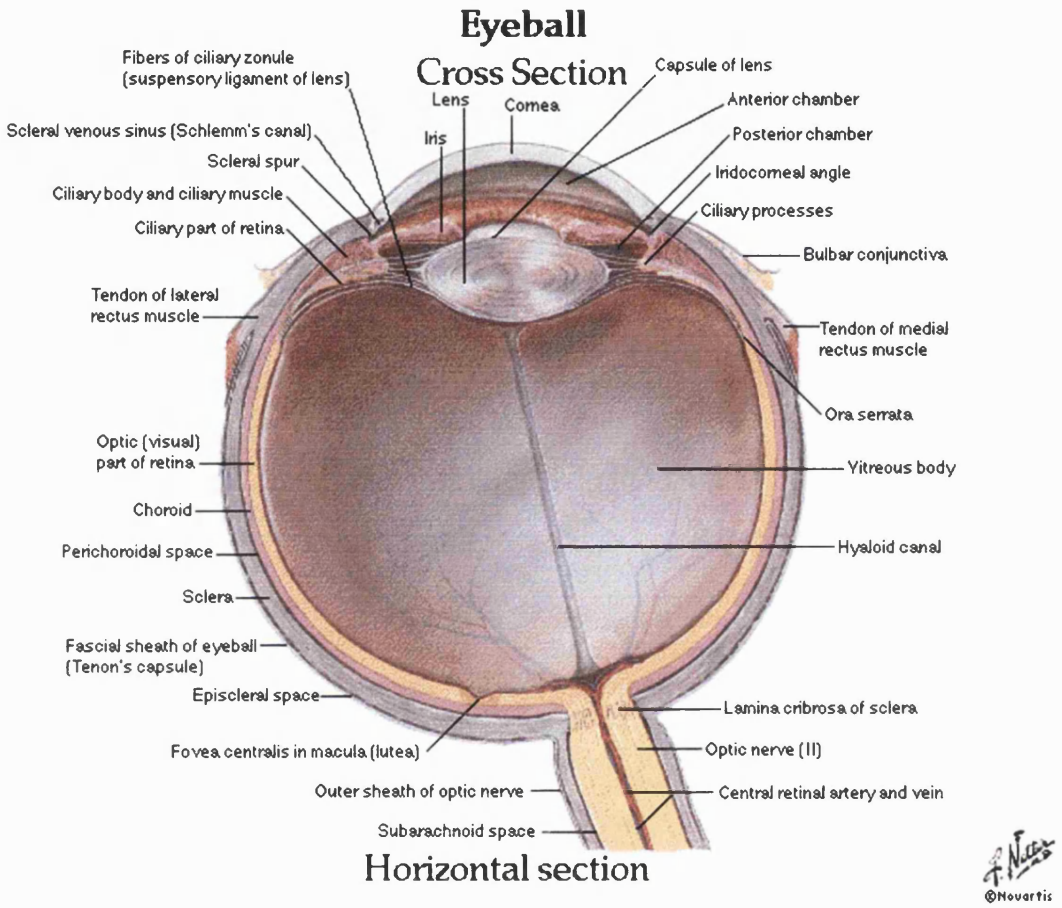

at the scleral foramen. It is composed of dense collagenous tissue, with glial and elastic fibres.
At the surface of the nerve head, axons bend acutely through about 90 deg. to exit the globe.
The central retinal vessels and their connective tissues occupy the central part of the optic nerve head.

Lamina Zone

The lamina cribrosa will be discussed in more detail in subsequent sections, but briefly, this zone consists of a mesh of interconnected connective tissue beams that are extensions from the surrounding sclera. These beams produce a pore-like structure through which the nerve fibre bundles pass through as they exit the eye.

Postlaminar Zone

This is the myelinated intraorbital portion of the optic nerve. The thickness of the optic nerve at this point is at least doubled due to the myelination of nerve fibres.

1.3.2.2 Retrobulbar Portion

This area of the nerve lies just beyond the lamina cribrosa, and is composed of optic nerve fibres, the supportive cells that form the myelin sheath and those that separate the fibres from the surrounding connective tissue septae and blood vessels, and the meningeal sheaths. The optic nerve travels for about 2-3cm from the posterior surface of the globe to the anterior portion of the optic canal. As the distance between the globe and optic canal is less than 2-3 cm, the optic nerve takes an S-shaped course as it travels to the canal. This extra length of optic nerve allows for eye movement in all directions.

1.3.2.3 Intracanalicular Portion

The optic nerve passes through the optic canal surrounded by the three meningeal sheaths. As it passes through the canal, the optic nerve is fixed and immobile.

1.3.2.4 Intracranial Portion

This part of the optic nerve extends from the posterior edge of the optic canal to the optic chiasm.

1.3.3 Normal Lamina Cribrosa

The lamina cribrosa is a series of approximately 10 plates of collagenous tissue that are stretched across the scleral canal (Anderson 1969; Emery, Landis et al. 1974; Radius and Anderson 1979; Radius and Gonzales 1981; Spileers and Goethals 1992). Each cribriform plate is perforated by several hundred openings, that are referred to as lamina pores. There is an increase in the number of pores in the deeper plates of the lamina cribrosa than in the more superficial plates and as a result, pores in consecutive plates do not lie in perfect alignment (Emery, Landis et al. 1974; Ogden, Duggan et al. 1988).

1.3.3.1 Extracellular Matrix

The cribriform plates are made up of a core of elastic fibres and collagen types I, III, IV, V and VI (Hernandez, Luo et al. 1987; Hernandez, Luo et al. 1989; Hernandez, Andrzejewska et al. 1990; Albon, Karwatowski et al. 1995) laminin and fibronectin. Collagen types I and III are the major types within the lamina cribrosa (Morrison, Jerdan et al. 1989). Type I collagen normally provides structural support, strength and rigidity. Type III collagen is a prominent constituent of several distensible tissues including the uterus, skin and blood vessels. It is associated with low tensile strength, but greater resilience. Type IV collagen is a ubiquitous component of basement membranes, and types V and VI connect the fibrillar collagens to the surrounding connective tissue structures.

1.3.3.2 Changes with Age

Studies have shown that, with age, there is an alteration in the collagen components of the extracellular matrix. In the young eye, there is an abundance of collagen type III within the laminar beams (Morrison, Jerdan et al. 1989), and with age there is an increase in collagen type I within the cribrosal plates (Hernandez, Luo et al. 1989; Morrison, Jerdan et al. 1989). Indeed, there is an

increase in the total collagen content of the lamina cribrosa with age- from 20% in the young eye to over 50% in the adult eye (Albon, Karwatowski et al. 1995). Thus, the young human lamina cribrosa is a flexible structure that is resilient to fluctuations in intraocular pressure. In contrast, the elderly lamina cribrosa is a more resilient structure, and this alteration in its mechanical properties could make it more susceptible to permanent deformation by raised intraocular pressure.

Recent experimental work using scanning laser ophthalmoscopic techniques on *ex vivo* human tissue has shown that the compliance of the lamina cribrosa does alter with age (Albon, Purslow et al. 2000), and this may be a contributory factor of the increased susceptibility of elderly to axonal damage in POAG.

1.3.3.3 Structural Architecture

The structural architecture of the lamina cribrosa has been extensively studied, using post-mortem tissue. In the normal human eye, it has been found that laminar beams that make up the cribriform plates are thicker in the nasal-temporal axis of the nerve head, and thinner in the superior-inferior axis (Quigley and Addicks 1981; Quigley, Addicks et al. 1981; Radius 1981; Radius and Gonzales 1981). The lamina pores are larger in the superior and inferior regions of the nerve head (Quigley and Addicks 1981; Quigley, Addicks et al. 1981; Dandona, Quigley et al. 1990). The structure has a saddle-like shape, such that the nasal- temporal axis is closer to the vitreous face (Quigley and Addicks 1981).

The thickness of the lamina cribrosa has been reported as being on average 0.237 ± 0.038 mm in the normal optic nerve, and 0.143 ± 0.059 mm in the glaucomatous nerve (Quigley, Hohman et al. 1983). This measurement was made using human cadaver optic nerve heads that had undergone a trypsin digestion technique that removed all the neural and glial elements of the nerve, leaving behind only the connective tissue structures. It is known that such digestion techniques can alter the tissue (Birch, Brotchie et al. 1997), and so it is

important to estimate the true dimensions by controlling post mortem shrinkage. This will be investigated and the results presented in Chapter 3.

1.4 Glaucoma

1.4.1 Definition

Glaucoma can be defined as a progressive optic neuropathy characterised by a classical pattern of optic nerve head and visual field damage. Raised intraocular pressure (IOP) is a major risk factor for development of the disease and its progression. The glaucoma's encompass a wide group of diseases that are characterised by widely diverse clinical and histopathological manifestations, and are the major cause of irreversible blindness in the developed world.

1.4.2 Normal Aqueous Dynamics

The aqueous humor is the fluid that fills the anterior cavity of the eye (figure 1.4). Its primary role is to provide oxygen and nutrients to the crystalline lens and corneal endothelium. The rate of fluid entrance and outflow- or *aqueous dynamics*-regulates the intraocular pressure (IOP). Aqueous is produced by the ciliary body epithelium (Ritch, Shields et al. 1989; Shields 1989).

1.4.2.1 Aqueous Production

The primary method of aqueous production is by active transport of fluid from the epithelial cells. A small proportion of the fluid is produced by ultrafiltration. The aqueous then enters the posterior chamber of the eye, between the iris and lens, and undergoes a metabolic change. The composition of the aqueous is altered either by reabsorption by the iris or ciliary body, or by addition of compounds from the crystalline lens. The aqueous then enters the anterior chamber of the eye through the pupil (Figure 1.5).

1.4.2.2 Aqueous Outflow

The mode of aqueous outflow from the eye is thought to be by two routes. The **direct** outflow pathway through the angle of the eye through the trabecular

meshwork into Schlemm's canal leads to aqueous drainage into intrascleral channels. This then reunites with the blood system in the episcleral veins. The **indirect** pathway involves the fluid draining through the interstitial spaces of the ciliary body and choroid, or the suprachoroidal space through the sclera. This pathway of drainage is known as the **uveoscleral flow**.

1.4.2.3 The Effect of Increasing Age

In the ageing eye, the beams of the trabecular meshwork thicken, and there is also a loss of the cellular structure. This leads to the development of extracellular material, or **plaques**. However, in the normal eye, there is no concomitant increase in IOP when this occurs, and this is probably due to the simultaneous reduction in aqueous production with increasing age.

In primary open angle glaucoma, there are many theories as to the region of the increased resistance to aqueous outflow. It is probable that it lies within a combination of all of the above methods of outflow, with the greatest resistance being at the level of the trabecular meshwork

Figure 1.5: Schematic diagram showing aqueous dynamics

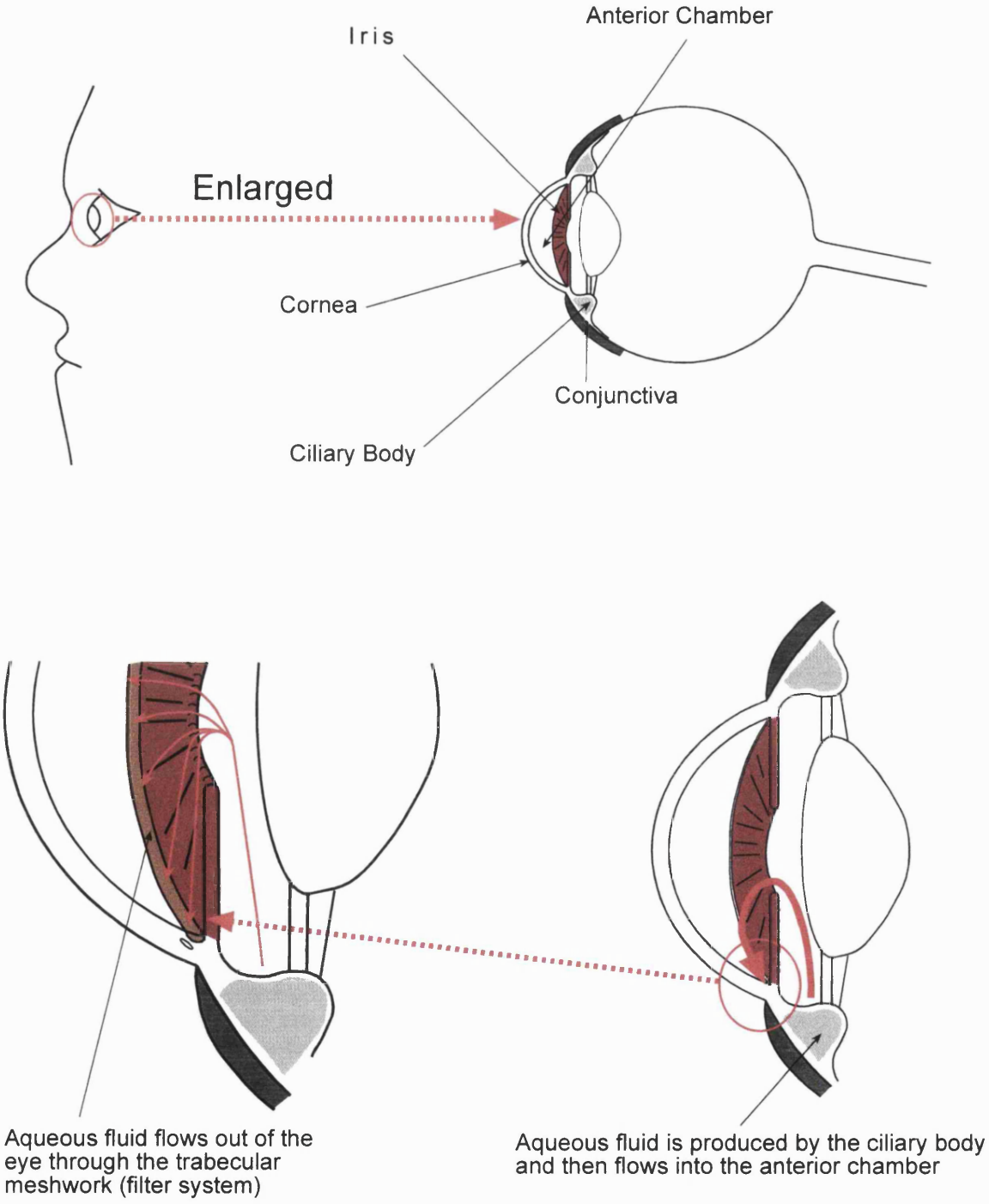

(C) M.R.Wilkins with kind permission

1.4.3 Intraocular Pressure

IOP is an expression of the degree to which the pressure within the corneo-scleral coat of the eye exceeds atmospheric pressure. It is expressed in millimetres of mercury (mmHg). The intraocular pressure is regulated by aqueous humor dynamics. The distribution of intraocular pressure within a normal Caucasian population is almost Gaussian, with a slight skew towards the higher pressures (Ritch, Shields et al. 1989; Shields 1989). The mean value is approximately 15.5 mmHg, with a 'normal' range of between 11 and 21 mmHg. However, a skewed distribution indicates that 95% of the area under the distribution curve will not lie within 2 standard deviations of the mean. Therefore, the upper limit of 'normal' will not necessarily be 21 mmHg, nor will an eye with 'normal' IOP be immune to glaucomatous damage. In addition, the range of normal IOP varies in different populations, e.g. in a Japanese population, the mean IOP has been reported as 13.3mmHg (SD 3.0mmHg) (Shiose 1984), compared with a Caucasian population in the Rhonda Valley, Wales with a mean IOP of 16.3mmHg (SD 3.0mmHg) (Hollows and Graham 1966). There is a diurnal variation in the intraocular pressure, with a mean amplitude of daily fluctuation ranging from between 3-6 mmHg. Therefore, the term 'normal IOP' is more an estimation, and other factors need to be considered when assessing normality.

1.4.4 Glaucoma and the optic disc

The pathological process in glaucoma is a loss of ganglion cell axons. As axons are lost, the amount of neural tissue occupying the optic nerve head decreases, resulting in alterations in the appearance of the optic disc rim and cup.
It is believed that the main site of glaucomatous damage is at the lamina cribrosa area, and that raised intraocular pressure causes a bowing back of the lamina, resulting in the damage to the nerve fibre bundles passing through the cribrosal plates (Emery, Landis et al. 1974; Quigley, Addicks et al. 1981). As discussed in section 1.3.3, the structural architecture of the lamina cribrosa varies in different regions, such that the superior and inferior lamina areas have larger pores and

finer connective tissue beams between them. This would make nerve fibres passing through these pores more susceptible to damage by raised IOP. The pattern of optic disc cupping enlargement in glaucoma generally tends to follow this pattern of 'weakness' in the optic nerve head, such that the inferior and superior disc regions show neural loss before the temporal and finally nasal regions (Jonas, Gusek et al. 1988; Airaksinen, Tuulonen et al. 1992)

1.5 Evaluation of Current Methods for Optic Nerve Head Assessment

1.5.1 Qualitative Assessment of the ONH

Glaucoma results in the loss of nerve axons in the optic nerve head, resulting in a widening and deepening of the optic nerve head. Progressive enlargement of the optic nerve head in a glaucomatous patient is a reliable indicator that the IOP is inadequately controlled. Accurate detection of progressive cupping, therefore, is paramount in monitoring the disease.

1.5.1.1 Direct and indirect ophthalmoscopy

Direct ophthalmoscopy is probably the most widely used technique to evaluate the optic nerve head in glaucoma. The instrument provides a virtual, upright image of the fundus with about x15 magnification (Bennett and Rabbetts 1984). Indirect ophthalmoscopic techniques of optic nerve head assessment tend to be with the slit-lamp, as the apparent magnification can be increased with the optics of the slit-lamp itself, giving excellent resolution (Shields 1989; Varma and Spaeth 1993). The image produced is real and inverted.

Although ophthalmoscopy is the most popular method for evaluating the optic nerve head, subjective estimates of nerve head dimensions vary considerably among observers (Lichter 1977). As a consequence of this variation between observers, the confidence to detect real changes in nerve head topography is low, and only large changes are likely to be detected reliably (Hitchings 2000).

1.5.1.2 Stereophotography

The advantage of using optic nerve head photography is that it gives a permanent record of the appearance of the nerve head over time. Stereophotography gives information about the contour, volume and depth of the optic nerve head and cup. Studies have shown that agreement between observers in detecting glaucomatous damage is best using stereophotographs and that it remains one of the most useful methods of patient follow-up (Odberg and Riise 1985; Takamoto and Schwartz 1985; Tielsch, Katz et al. 1988; O Connor, Zeyen et al. 1993).

1.5.2 Quantitative Assessment of the ONH

1.5.2.1 Planimetry

Planimetry is the name given to measurements from photographic images. Although analysis can be done by projecting the image using an overhead projector, and performing manual measurements, nowadays the images are digitized and analysed by computer software (THOT software). A number of programs are available to perform the analyses. An observer outlines the margin of the optic nerve head and the neuroretinal rim/ optic cup border, using a mouse, and the computer program calculates the area of the neuroretinal rim, after correcting for the ocular and camera magnification.
One of the limitations of planimetry is that it relies on the judgment of the observer as to the position of the optic nerve head and neuroretinal rim/ optic cup borders, which usually differs between observers. Agreement between observers has been shown to be dependant on the level of experience (Sturmer, Poinoosawmy et al. 1992; Bartz-Schmidt, Sundtgen et al. 1995; Garway-Heath, Poinoosawmy et al. 1999).

1.5.2.2 Videographic Image Analysis

These can give a more objective analyses of the optic nerve head. One device, the Optic Nerve Head Analyzer (Rodenstock Instruments) projects stripes of light onto the optic nerve head which are deformed according to the surface

topography. The instrument simultaneously records stereoscopic videographic images, and depth information is gained by cross-correlating the deformations of the striped pattern in the two stereo-pairs. An observer outlines the edge of the optic nerve head, and the display provides a colour coded depth map of the optic nerve head. The software computes the optic cup margin and its depth profile by identifying the neuroretinal rim margin that lies at a set depth below the optic nerve head (the reference plane). The definition of the optic cup is therefore more objective than the planimetric definition.

1.5.2.3 Scanning Laser Ophthalmoscopy

The optics of the confocal scanning laser ophthalmoscope have been described earlier in the chapter. The most widely used commercially available instrument is the Heidelberg Retina Tomograph (HRT, Heidelberg Engineering, Germany). Due to the confocal optics of the instrument, high resolution 'optical sections' of the area of fundus under investigation are obtained. In the image acquisition sequence, the instrument changes focus in an axial manner, thus generating a series of optical sections through the depth of the fundus. The HRT takes 32 sections, beginning just in front of the optic nerve head in the vitreous and ending just behind the lamina cribrosa. These images are aligned and a topography map of the area is generated. An operator has to define the edge of the optic nerve head, but once that information is received, area and volumetric information about the optic nerve head is available. The reproducibility of the HRT has been established (Dreher, Tso et al. 1991; Rohrschneider, Burk et al. 1993; Chauhan, LeBlanc et al. 1994; Rohrschneider, Burk et al. 1994). Image acquisition and analysis with the HRT is discussed in detail in Appendix I.

1.5.2.4 Optical Coherence Tomography

Optical coherence tomography (OCT) is a relatively new imaging modality. The principles of it are similar to those used in ultrasound technology. However, whereas ultrasound produces images from backscattered sound "echoes," OCT uses infrared light waves that reflect off the internal microstructure within the biological tissues. The frequencies and bandwidths of infrared light are orders of

magnitude higher than medical ultrasound signals resulting in greatly increased image resolution (Huang, Swanson et al. 1991; Fercher, Hitzenberger et al. 1993; Izatt, Hee et al. 1994; Fujimoto, Brezinski et al. 1995). Interferometric techniques are required to extract the reflected optical signals from the infrared light used in OCT. The output, measured by an interferometer, is processed to produce high-resolution, real time, cross sectional or 3-dimensional image of the tissue, which is ideal for biomedical imaging. It functions as a type of optical biopsy, but with the difference that tissue pathology is imaged in situ and in real time.

The interest in OCT in ophthalmology has grown as it offers an increased depth resolution that promises to provide information on structures not discernable with the cSLO. One of the first ophthalmic uses of OCT was in investigations of the macular area (Puliafito, Hee et al. 1995). It is used in glaucoma research with respect to studying changes in the retinal nerve fibre layer (RNFL). RNFL thickness is measured at standardized locations around the optic nerve head. A circular scan produces a cylindrical cross-section of the retina, from which the RNFL can be analyzed. In addition, radial scans through the optic nerve head are used to evaluate cupping and juxtapapillary RNFL thickness (Schuman, Hee et al. 1995).

The images produced using the commercially available OCT are longitudinal sections through the retina. Research is currently underway here and elsewhere into developing its use for *en face* retinal imaging (Podoleanu A. Gh., Rogers J.A. et al. 2000; Rogers J.A., Podoleanu A. Gh. et al. 2001).

Research using the OCT for retinal investigations has shown that although the instrument resolution obtainable is of the order of 3 microns (Drexler, Morgner et al. 2001), there is not as much of an improvement in resolution when imaging the eye. Microsaccadic eye movements cause distortions in the images produced, such that when comparing real-time OCT images with histological images, there is not the same level of detail (Chauhan and Marshall 1999). Rogers and co-workers have also found this with *en face* imaging (Rogers J.A., Podoleanu A. Gh. et al. 2001). The orientation of the eye and tilt (particularly of the optic nerve

head) has a major effect in such images. These changes in orientation manifest themselves as fragmentation and asymmetry within the image. Further work needs to be done before *en-face* OCT imaging becomes practical.

1.6 Imaging the Lamina Cribrosa

The lamina cribrosa area at the posterior pole of the eye provides the entrance and exit point of retinal blood vessels and ganglion cell axons. In glaucoma, it is thought that one of the main sites of damage to the ganglion cell axons occurs at the level of the lamina, particularly in cases of high tension glaucoma, where it is thought that the raised intraocular pressure results in a backward bowing of the lamina, resulting in the deformation of ganglion cell axons (Quigley, Addicks et al. 1981; Radius and Gonzales 1981; Maumenee 1983; Quigley, Hohman et al. 1983; Morgan, Jeffery et al. 1998).

The areas' architecture has been investigated in great detail using post mortem tissue. The largest lamina pores seem to be found in the superior and inferior poles of the optic nerve head and pores are smaller in the central part of the nerve compared with the periphery (Emery, Landis et al. 1974; Quigley and Addicks 1981; Jonas, Mardin et al. 1991). The lamina pores sub-divide as they traverse through the cribrosa, resulting in more numerous pores deeper in the lamina, and there is a degree of pore misalignment (section 1.3.3) (Emery, Landis et al. 1974; Radius and Anderson 1979; Quigley and Addicks 1981; Radius and Gonzales 1981; Ogden, Duggan et al. 1988).

Qualitative analysis of optic disc photographs have shown that a change in the appearance of the lamina pores accompanies acquired neuroretinal rim tissue loss with progression of glaucoma (Miller and Quigley 1988). The development of the scanning laser ophthalmoscope has led to imaging the nerve head *in vivo*. *In vivo* imaging offers the chance to investigate the structure in more detail, allowing us an insight into how the area appears in the normal eye as well as how it is affected by intraocular pressure changes. There have been experimental studies looking at the mechanical response of the area under different pressure loads

(Yan, Coloma et al. 1994; Yan, Flanagan et al. 1998) and its response in different aged eyes (Albon, Purslow et al. 2000) using human cadaver tissue.
The cSLO has been used to image the lamina cribrosa in recent times (Bhandari, Fontana et al. 1997; Fontana, Bhandari et al. 1998; Maeda, Nakamura et al. 1999). In the studies by Bhandari and Fontana, the patients were selected on the basis of visible lamina cribrosa on ophthalmoscopy. Pore morphometry was examined, but the authors did not give area values corrected for ocular and instrument magnification, and kept with pixel measures. In addition, the total pore area was measured, rather than an analysis of individual pores. A relationship between pore elongation and depth of visual field defect (total deviation as measured using a Humphrey Visual Field Analyser) was found. The deeper the depth of field defect, the more elongated the pores were.
The authors used the unsharp masking technique to analyse the image, which is discussed further in chapter 2.
The unsharp masking technique was used by Maeda and co-workers (Maeda, Nakamura et al. 1999), who also evaluated the pore shape in 6 subjects. Their findings agreed with Fontana's in that the pore shape became more elongated in more severe disease. However, lamina cribrosa visibility by ophthalmoscopy was an inclusion criterion for their study.

1.6.1 Aims

Since the work of Bhandari and Fontana at this institute, the cSLO used in their study has been upgraded with respect to image resolution.
The aims of this project were to

1. investigate the ability of the upgraded set-up in imaging the in vivo lamina cribrosa, and compare the images obtained with this and with the commercially available Heidelberg Retina Tomograph,
2. investigate the effect of imaging the lamina area with different wavelengths of laser light to determine the optimum for lamina pore visibility,

3. develop an image processing technique using Fourier Transform analysis to enable quantification of the lamina pore structure,
4. investigate the relationship between in vivo pore structure and optic nerve head topography,
5. establish the relationship between the in vivo lamina images and the histological appearance of the area through post mortem studies.

Chapter 2: Materials and Methods

2.1 Image Acquisition and Processing

2. 1.1 Hardware

As mentioned in Chapter 1, confocal scanning laser ophthalmoscopes allow visualization of a fine optical section of the structure under investigation. The cSLO's used in this study were the commercially available Heidelberg Retina Tomograph (HRT, Heidelberg Engineering, Germany) and a prototype Zeiss cSLO (Zeiss, Jena GmbH, Germany). Both of these instruments were evaluated in their imaging of the lamina cribrosa.

2.1.1.1 Heidelberg Retina Tomograph

Hardware description

The Heidelberg Retina Tomograph (HRT, Heidelberg Engineering GmbH) is a cSLO used to acquire and analyse three-dimensional images of the fundus. The laser source is a HeNe diode laser of wavelength 670 nm. The laser raster scans the x-y plane to obtain confocal optical sections of the retina. Once one plane has been scanned, the laser changes focus to scan a slightly deeper plane of the retina. This continues 32 times and results in a stack of optical sections that represent both an area (x-y) and depth (z) image of the retinal structure under investigation. The field of view can be set to three levels, 10 x 10 degrees, 15 x 15 degrees or 20 x 20 degrees. The depth to which the laser scans varies between 0.5 and 4mm in 0.5 mm steps. Thirty two optical sections are generated at all of these depth levels, so the spacing between sections is closer at the lower depth levels, and greater at the higher depth levels.

Image Acquisition and Software description

The HRT generates a topography and reflectivity image from which quantitative information about the retinal structure under investigation can be obtained. The HRT image acquisition and analysis features are detailed in Appendix I.

2.1.1.2 Zeiss Jena cSLO

Hardware description

The SLO used for this study was a prototype model donated by Carl Zeiss, Jena GmbH that is intended for clinical research. The SLO was divided into two units: a large, floor-mounted unit which contained the lasers, photodetector, video decoder and control circuitry and a smaller, imaging 'head' which contained the scanning system and imaging optics.

The main unit of the SLO contained two, interchangeable laser sources: a helium neon (HeNe) beam at 632.8nm and an argon (Ar) beam at 512nm which were both directed into the head of the unit through a single, shared fibre optic cable. After scanning the target and passing through the confocal pinhole, the return beam was channelled through a fibre optic cable to a photodetector in the main body of the SLO. Signal attenuation due to fibre optic insertion losses was less that 13% (Zeiss, pers. comm.). After calibration, the illuminant beam profile was nominally a Gaussian, but the stability of this could not be guaranteed due to unavoidable movement of the fibre optics during everyday use of the machine. The final beam intensities on leaving the imaging head were typically 200μW (argon), and 160μW (HeNe) although moving blocking filters into and out of the beam path could alter these. In normal, clinical use the SLO could be switched between two diagonal scan angles of 20° or 40°.

Image Acquisition

The SLO de-scanning system generated an interlaced PAL video signal of 768 pixels x 576 lines that was recorded using a Super-VHS video system. (Panasonic AG7330). Video sequences of between 32 and 64 frames in length (at 25 frames per second) were digitised from videotape in real-time using a PULSAR PCI frame grabber (Matrox Electronic Imaging Inc., Québec, Canada) in a standard desktop PC.

Image Alignment and Averaging

When imaging an object with the SLO, pixels in regions of the scene that appear uniform actually vary in value due to electronic noise within the system. This variation in pixel value is known as **noise** and the ratio of the contrast within an image that is due to actual difference within the object scene and that caused by the noise level is termed the **signal to noise ratio** (SNR). When the SNR is low, features within an object scene may appear almost invisible to the observer.
By adding together video frames of the same object scene, there is an improvement in the quality of the image that is proportional to the square root of the number of frames (Russ 1998). This technique is termed **averaging**.
For the purposes of this study, 32 frames were averaged. When averaging a number of frames, it is important that the pixels within the object scene are in the same position in each frame. The living human eye is not perfectly stable even in subjects with excellent fixation, and is prone to involuntary, saccadic eye movements. Because of this it was necessary to align individual frames to each other before the averaging process. The alignment routine compensated for small changes in both the position and orientation of the retina over the time-course of the video sequence. Digitisation, alignment and averaging of individual video frames were performed using purpose written software (Wade and Fitzke 1998; Halfyard, Wade et al. 1999).
The averaged image was stored on a P.C in tagged-image file (TIFF) format.

2.1.2 Calibration of cSLO

2.1.2.1 Resolution of Images

Introduction

In a perfect optical system, one would predict that the image of a point object would be a point. However, in reality the resultant image is a pattern that spreads over a finite area, due to the diffraction of light at the edges of the optical system (Bennett and Rabbetts 1984). The modulation transfer function (MTF) is a

measure of the optical quality of an imaging system, giving a value as to how much information in the object is being transferred to the final image. Increasing the stop size of a system can increase the resolution of a diffraction-limited optical system. In the human eye, the stop is the iris diaphragm, and so theoretically, by increasing the size of the pupil diameter, the resolution of the eye should increase. However, the human eye is not diffraction limited, and when the size of the pupil increases aberrations are introduced by the peripheral cornea and crystalline lens (Campbell and Gubisch 1966). It has been shown that the eye behaves as a diffraction limited system at around a pupil size of 2.4mm. Anything smaller, and the effects of diffraction outweigh the effects of the eyes' aberrations; anything much larger, and the aberrations increasingly degrade the image. This has implications in imaging systems, particularly when considering the depth resolution of the scanning laser ophthalmoscope.

Resolution of the cSLO

With three-dimensional images, image quality is dependant on both the lateral and axial ('depth') resolutions. It has been said before that a point object is imaged as a discrete circular pattern. The pattern resembles a Gaussian type curve. The formula of the Gaussian curve is given by:

$$I = [\mathrm{Sin}\ (u/4)] / (u/4),$$

where *I* is the intensity of light collected.

The axial resolution of the instrument can be calculated by finding the area under the curve of the Gaussian profile that the object produces, using integration. This 'integrated intensity', $I_{int}(u)$, is defined by (Dreher, Bille et al. 1989) as

$$I_{int}(u) \approx \int_0^{V_0} I(u,v)\, dv$$

The limit V_0 is given by $V_0 = (2\pi/\lambda)\, r_0\, (a/f)$,

where r_0 is the radius of the confocal pinhole, f is the focal length of the collector lens and a is the beam radius at the lens. u is related to the axial distance of the object z by:

$$u = 2\pi/\lambda\,(A)^2 z,$$

where A is the pupil size and λ is the wavelength of the laser light source used. The formulae above indicate that the factors influencing the axial resolution are confocal aperture size, pupil size, size and wavelength of imaging beam. However, the conventional index of the narrowness of a Gaussian type curve is its width at half the peak value, termed 'full width- half max' or FWHM. The FWHM of the depth integrated intensity profile corresponds to z_{HW}

$$z_{HW} \approx 1/2\pi\,(f / a)^2 nu,$$

where f = 17.05mm (focal length of the eye)
n = 1.336 (refractive index of vitreous)
a = radius of pupil

Dreher et al calculated that by increasing the beam width of the illumination and having a pupil diameter of 6mm, and having a confocal aperture size of 30 μm, the theoretically detectable half width of the integrated intensity corresponded to $z_{HW} \approx \pm 20\mu m$. This means that the theoretical width of optical section, or lateral resolution, that can be imaged with the cSLO is 40μm. However, the eye is not diffraction-limited, and so this theoretical depth is never achieved.
Dreher et al (Dreher, Bille et al. 1989) were able to partially compensate for the aberrations introduced by the eye by using electrode-active mirrors, and found that for a 6mm pupil, the FWHM using their Argon cSLO improved from 487 μm to 220μm.
The optical section width of the HRT is between 300- 400 microns (pers. comm. G.Zinser, Heidelberg Engineering). The purpose of this study was to determine

the width of the optical section as obtained by using different confocal apertures for the Zeiss cSLO.

Methods

A model eye, consisting of a 16mm lens, a 7mm diameter stop, and a micrometer-mounted reflector (National Physics Laboratory) was attached to the cSLO. A 7mm stop size was chosen over smaller diameters as when imaging human eyes, the subject would be dilated, and this best represents the average pupil size. The SLO image of the reflector was grabbed using the HeNe laser source for a range of axial displacements of the reflector. The average intensity of a central 30 x 30 pixel area of the image of the reflector was plotted against the axial displacement. A curve fitting algorithm was applied to the data Sigmaplot 2001 (vers. 7.0, SPSS Inc), and the 'full-width, half-maximum' of the curve was measured as the thickness of the optical section.
This was performed for confocal aperture sizes 1 through to 4 of the Zeiss cSLO.

Results

The results are shown in figure 2.1.The thinnest optical section was obtained using stop size 1. Interestingly, the difference in FWHM obtained with stop sizes 1-3 was not vastly different. Although theoretically the size of the confocal aperture is an important factor in determining the lateral resolution of cSLO, practically, with this set-up, it did not seem to be the case. This may be because with a dilated pupil, the degrading effects of monochromatic aberrations have the greatest influence upon the image quality.
The results indicated that there was not much of a difference in FHWM between stop sizes 1-3. However, manual inspection of images showed that the lateral resolution of images degraded as the stop size decreased. With smaller stop sizes, less light enters the imaging system, thus making the image quality poorer. In view of these findings, it was decided that *in vivo* lamina cribrosa images should be taken using stop size 3. This gave a reasonable lateral resolution of images with a fairly narrow optical section.

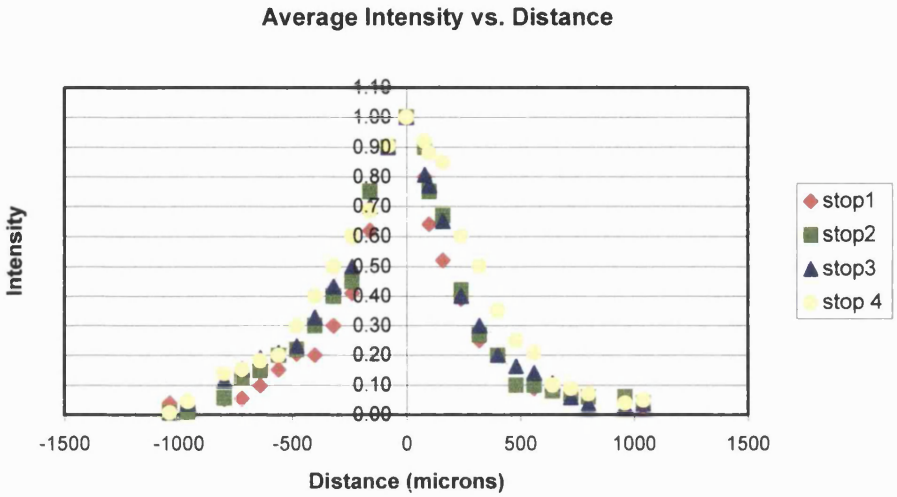

Figure 2.1b: Axial resolution of the Zeiss cSLO

From the graph, the full-width, half-maximum for each confocal aperture was measured as:

Stop 1: (0.02mm) 320 microns

Stop 2: (0.05mm) 350 microns

Stop 3: (0.075mm) 380 microns

Stop 4: (0.1mm) 600 microns

Table 2.1: Micrometer displacement and average intensity of reflector for different stop sizes.

	Average Intensity			
Micrometer distance	Stop 1	Stop 2	Stop 3	Stop 4
-1040	0.04	0.01	0.01	0.01
-960	0.02	0.01	0.04	0.04
-800	0.05	0.06	0.12	0.14
-720	0.06	0.12	0.15	0.15
-640	0.10	0.15	0.19	0.18
-560	0.15	0.20	0.21	0.20
-480	0.21	0.22	0.23	0.30
-400	0.20	0.30	0.33	0.40
-320	0.30	0.40	0.43	0.50
-240	0.41	0.45	0.50	0.60
-160	0.62	0.75	0.70	0.69
-80	0.90	0.90	0.90	0.91
0	1.00	1.00	1.00	1.00
80	0.80	0.90	0.81	0.92
100	0.64	0.75	0.77	0.88
160	0.52	0.67	0.65	0.85
240	0.39	0.42	0.40	0.60
320	0.25	0.27	0.30	0.50
400	0.20	0.20	0.20	0.35
480	0.10	0.10	0.16	0.25
560	0.09	0.10	0.14	0.21
640	0.08	0.08	0.11	0.10
720	0.07	0.07	0.06	0.09
800	0.05	0.06	0.04	0.07
960	0.04	0.06	0.03	0.04
1040	0.03	0.04	0.04	0.05

2.1.2.2 Image Distortions with the Zeiss and HRT cSLO

Introduction

The optics of the cSLO have been described in section I. The imaging technique is similar to that of standard confocal microscopy, and the optics of the eye serve as the objective lens. All refractive systems are subject to optical aberrations, be they inherent in the design of the system, or due to improper use (Keller 1989). These aberrations are usually well compensated for by the imaging systems, but do result in a reduction of resolution. In addition, with the SLO set-up, mirrors are used to relay light to and from the eye. A drawback of mirrors is that astigmatism can be induced if they are used off-axis. The purpose of this study was to investigate any image distortions produced with the two cSLO's.

Methods

A model eye based on the model described by Rudnicka (Rudnicka, Edgar et al. 1992) was constructed at the Institute of Ophthalmology. The model consists of a cornea and lens that were manufactured using a rigid gas permeable lens material (Boston RXD, Polymer Technology Corp., MA, USA). The fundus was a spherical surface of radius 11.5mm, and a circular insert of diameter 1.95 mm and depth 0.50 mm was fitted on the fundus surface, to represent the optic nerve head (figure 2.2). A micrometer screw attachment to the fundus allowed the precise variation of the vitreous chamber depth to produce axial ametropia from +11 to –15 D.

In order to establish whether any distortion of images was caused by the cSLO's, the eye target was imaged using a Nikon NF 505 fundus camera. The target was then imaged using the Zeiss cSLO at a 20 deg field of view, and the HRT at a 15 deg field of view, over a range of refractive errors between $\pm$ 8 dioptres.

The resultant images were stored in TIFF file format, and analysed using Matrox Inspector (version 2.1, Matrox Electronic Systems Ltd, Quebec). The height and width of the images generated were measured, and the ratio was plotted against refractive error.

Figure 2.2: The model eye

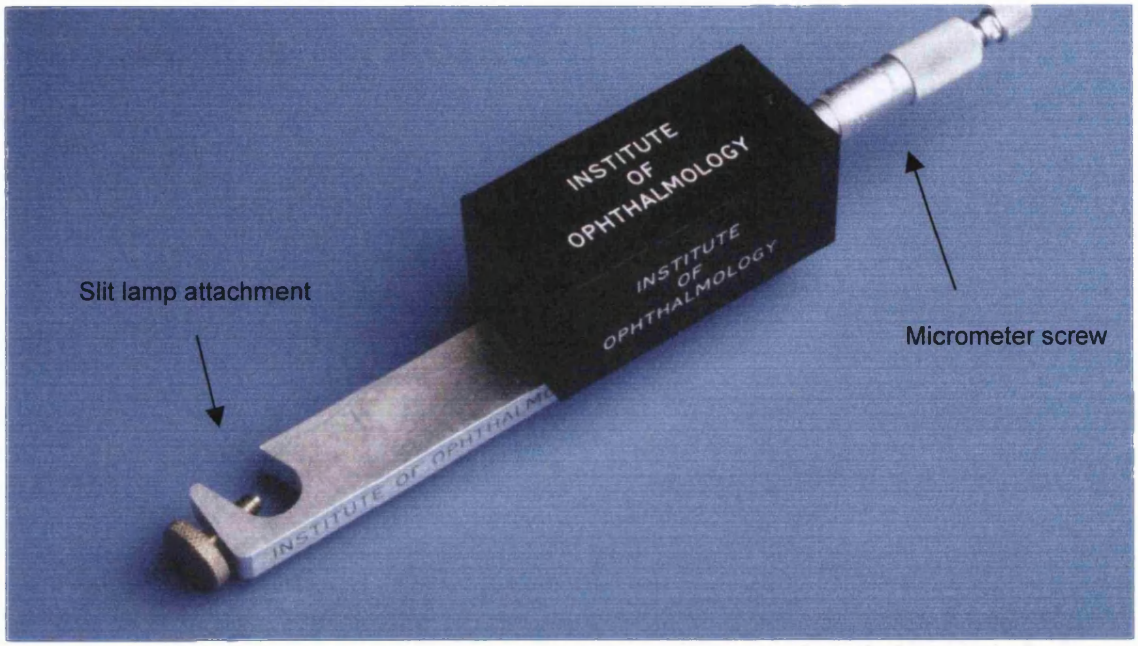

External view

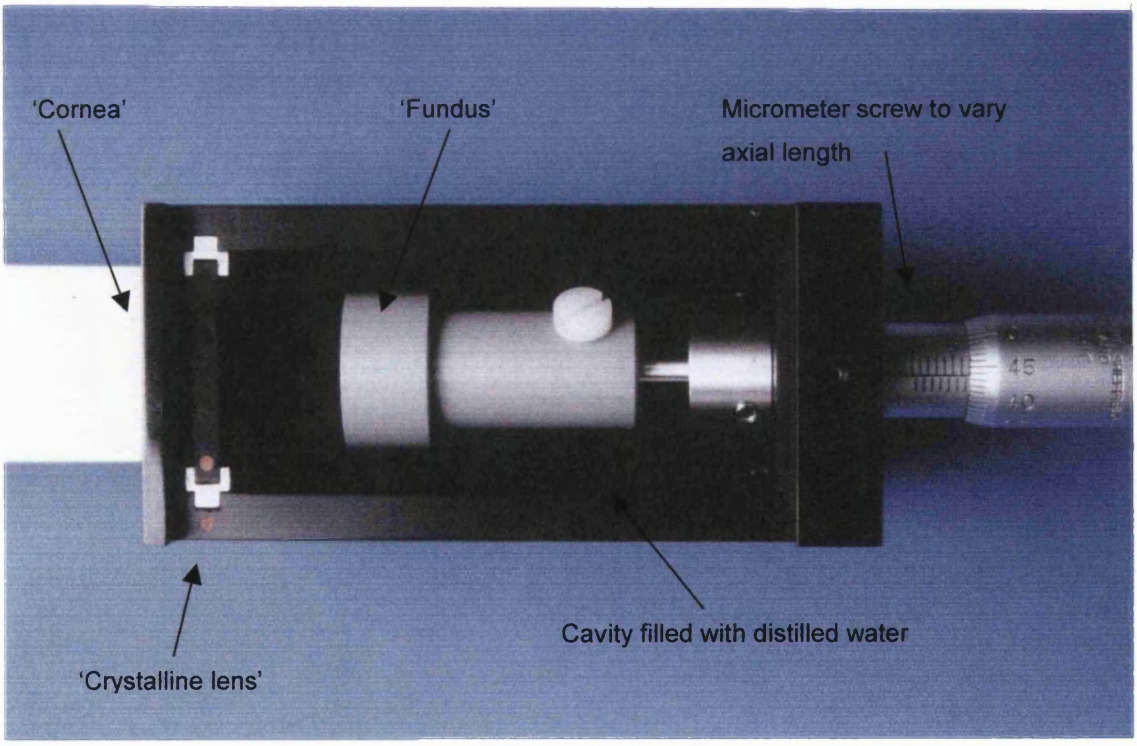

Internal view

Results

The results are shown in figure 2.3. From these results, it was shown that the Zeiss cSLO results in an elongated image, with the ratio of width: height being 1: 0.86. The HRT and Nikon NF 505 camera did not show any image elongation. All subsequent images taken with the Zeiss cSLO were scaled using this ratio.

The scanning laser ophthalmoscope laser beam encounters 2 scanning mirrors as it exits the system to scan the retina- a polygon 'horizontal scanning' mirror, and a mirror mounted on a galvanometer motor to scan the vertical dimension. There is a relay mirror between the two scanners to make them optically coincident, but this mirror is slightly tilted, and if the system is slightly misaligned, the laser beam is affected by astigmatic aberrations resulting in a slightly elongated image. The Zeiss cSLO is a prototype instrument, and is used considerably for research purposes. Therefore, slight errors in the optics are to be expected, and as long as these errors are known, it is possible to compensate for them.

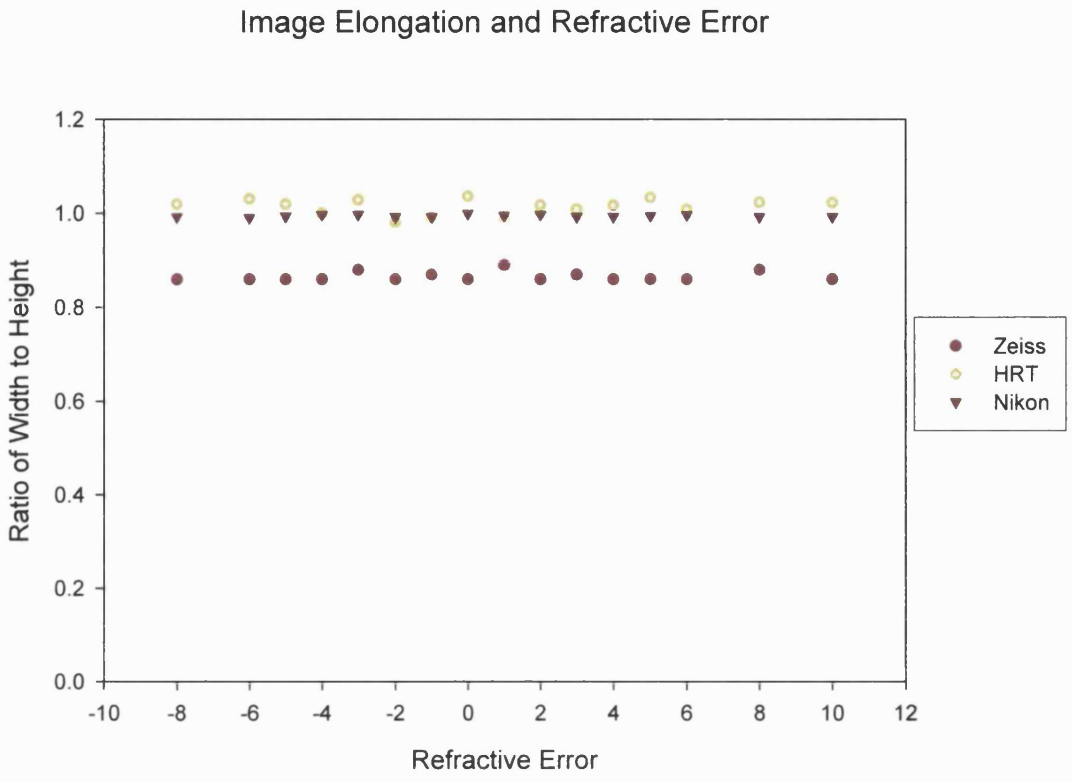

Figure 2.3: Elongation factor - Zeiss, HRT and Nikon camera

Graph showing ratio of width to height of images taken with the Zeiss cSLO, HRT and Nikon NF 505 camera, at different refractive settings. These were adjusted by changing the axial length of the model eye. The HRT and Nikon camera do not elongate the image. The elongation ratio for the Zeiss is 0.86 (average). All subsequent images taken with the Zeiss were scaled using this ratio.

2.1.3 Real Size of Fundus Features

2.1.3.1 Calculating the real size of fundus features

Introduction

The measurement of the true size of a retinal feature is dependent on the magnification due to the eye, and the magnification due to the camera. For paraxial features, the linear size of the photographic image **(s)** is related to the size of the retinal feature **(t)**, a factor related to the camera **(p)** and a factor related to the eye **(q)**, so that

$$t = p*q*s$$ (Bennett, Rudnicka et al. 1994)

The magnification factor of the camera depends on the model used, and so needs to be established (Bengtsson and Krakau 1992; Rudnicka, Edgar et al. 1992; Bennett, Rudnicka et al. 1994). A telecentric camera is one where the camera factor 'p' is independent of the refractive error of the eye. In non-telecentric designs, p normally varies with refractive error in a linear fashion. The HRT software algorithm has a magnification correction factor included, so that all retinal feature measurements are given in millimetres. It uses the Gullstrand model, but with a gradient index lens (G. Zinser *pers. comm.*). This model for retinal feature measurement gives good results when compared with *in vivo* measurements (Bartz-Schmidt, Weber et al. 1994). The calculations use the corneal curvature measurements, and these are input into the software program prior to image analysis.
It is also possible to store the aligned image series obtained by the HRT as a series of TIFF files, using a conversion program available with the HRT software, called HRTCONV. With these images, however, the HRT image analysis software can no longer be used, and so the p value of the HRT images under these conditions has to be calculated. The following describes the technique used to measure the p value for the Zeiss cSLO and the HRT.

Methods

In order to determine the value of 'p' for the cSLO, the formula for q:

$$q = 17.453\ n'/\ k' \qquad \text{(Rudnicka, Edgar et al. 1992)}$$

where k' is the axial length, and n' is the refractive index of the eye (normally taken as 1.336) based on Gullstrands schematic eye, was used.
From the earlier equation for t, p can be calculated thus:

$$p = t/\ (q*s)$$

The circular target of the model eye was imaged for refractive error settings between –10 and +8 dioptres. Images were acquired using the Zeiss and HRT, and the HRT image series were converted to individual TIFF files for analysis. Images were then loaded in Matrox Inspector Image Analysis software (version 2.1, Matrox Electronic Systems Ltd, Quebec). Zeiss images were rescaled to compensate for image aberrations caused by the optics of the cSLO (section 2.1.2.2).
HRT images were multiplied by a factor of 2, so that the image size increased from 256 x 256 pixels to 512 x 512 pixels.
The diameter of the circular target was measured for each image using the 'draw circle' tool available with the software, giving a value of 's' in pixels. As the value of 't' is already known, it was possible to calculate 'p' for the refractive errors imaged.

Results

Figure 2.4 graphically illustrates the relationship of 'p' and refractive error of the model eye. From this figure, it can be seen that the prototype Zeiss cSLO used in this study is of telecentric design, and has a value of 3.35 $\pm$ 0.07 (std) and the HRT is also of telecentric design, and has a p value of 3.38 $\pm$ 0.06 (std).
(These calculations of p do not incorporate a pixel-to-millimetre conversion).

Figure 2.4: p value for HRT and Zeiss

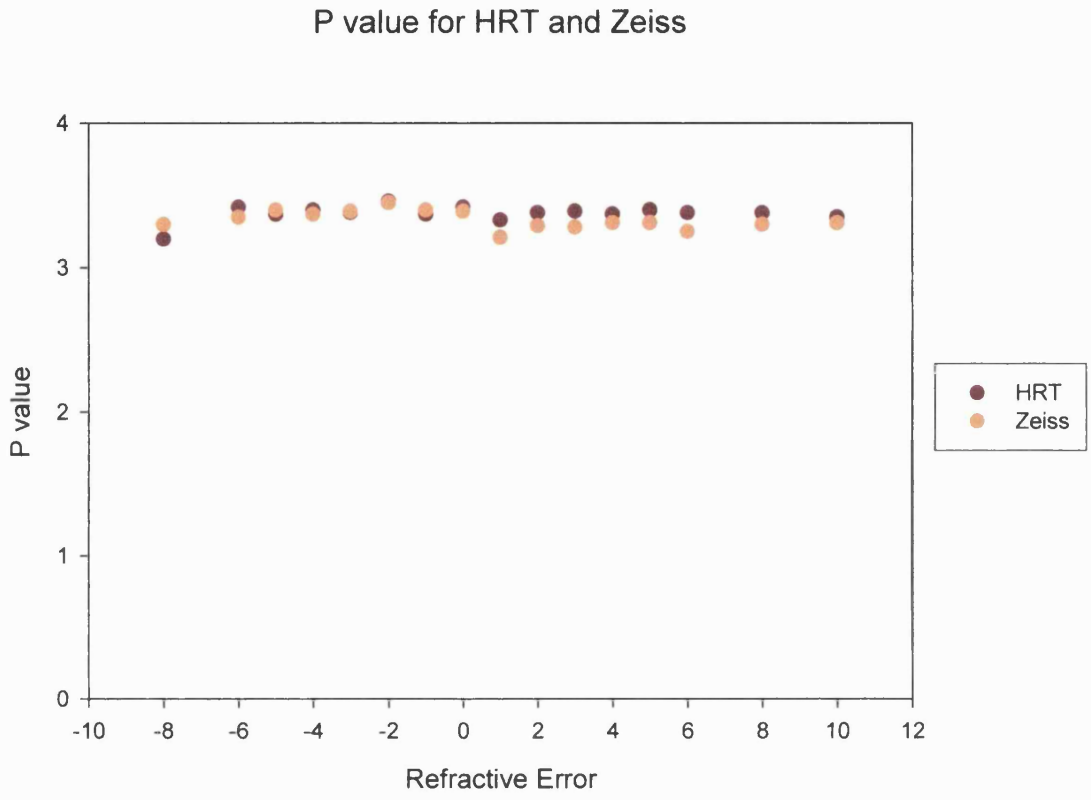

2.1.3.2 Ocular Factor

The ocular factor 'q' is dependent on the vergence of light within the eye- denoted by K' in dioptres. The most accurate way of determining K' is by ray tracing, and this is only possible if all the ocular dimensions are known (anterior and posterior radii of curvature of the cornea and crystalline lens, anterior chamber depth, axial length, and refractive index of all media within the eye, including the layers of the crystalline lens). It is possible, however, to estimate K' with knowledge of fewer parameters, and many methods are available based on knowledge of ametropia and keratometry (Bengtsson and Krakau 1992), axial length only (Bengtsson and Krakau 1992; Bennett, Rudnicka et al. 1994), axial length, anterior chamber depth, crystalline lens thickness, keratometry and ametropia (Bennett, Rudnicka et al. 1994). All of the methods make certain assumptions about the optics of the eye. Studies have shown that the methods using both axial length and keratometry measurements are more accurate at determining 'q' than using keratometry and refractive error alone (Garway Heath, Rudnicka et al. 1998). A new formula based on just the keratometry and ametropia measurements had been described by Garway-Heath (Garway Heath, Rudnicka et al. 1998), and this has been shown to give results closest to the axial length methods. For this study, 'q' was calculated using the new method

$$q = \{(17.21/r_1) + 1.247 + (A/ 17.455)\}^{-1}$$

where

r^1 = radius of curvature of the anterior cornea

A = ametropia

In all subsequent calculations of lamina pore area, the values of p and q as described above were used.

2.1.4 Image Processing

2.1.4.1 Introduction to Image Processing

Image processing is usually used to either improve the appearance of an image for aesthetic reasons, or to prepare images for measurement of features present. Image processing techniques can fall into two categories-

- Image restoration - methods with the aim of recovering original information about the object prior to the imaging process (for example by improving the signal to noise ratio {see section 2.1.1.2} or extending the effective resolution by deconvolution), or
- Image enhancement- methods that improve the appearance of the final image, without necessarily increasing the amount of information within the image.

The aim of the image processing techniques that are required for this thesis are to eliminate noise and improve the contrast of the *in vivo* lamina cribrosa images to gain information about the pore structure. The structure of the lamina cribrosa has been described in section 1. The beams of the lamina consist primarily of collagen, the pores being the spaces through which the nerve fibre bundles pass through. In order to enhance the edges of the pores both techniques of image restoration and enhancement were required. Image restoration was required to remove the effect of out-of-focus blur from the confocal images to improve resolution of the pore structure; image enhancement was required to prepare the images for measurement. Image enhancement can be performed in the spatial domain or in other domains.

2.1.4.2 Image Enhancement I- Processing in the Spatial Domain

Image processing in the spatial domain involves modification of the pixel values within an image directly. The following describes the steps employed when processing in the spatial domain.

Step 1: Eliminating the Luminance Gradient- Rank Levelling

The most basic form of image processing and analysis uses the brightness of regions within an image as a means of identification- it is assumed that similar features within an image will have similar brightness, thus forming a basis of discrimination for counting or measuring. When imaging an irregular surface, the amount of light reflected back to the observation unit depends upon the orientation of the surface with respect to the light source and the observation unit. Therefore, most images will have a luminance gradient- a change in illumination across the image that is not a function of the features within the image alone. The first step of image processing is to rid the image of the luminance gradient, as variations in the luminance may be mistaken for features within the image.

In ophthalmic imaging, the features of interest are often limited in size and smaller in scale than the background variations. An assumption can be made that everywhere within the image, the background is either lighter or darker than the features of interest. In operations to even out the illumination, the aim is to shrink the features of the image and extend the local brightness values into the area previously covered by the features. The resultant image has information only about the background brightness, and when this is subtracted from the original image, an image is produce that clearly distinguishes the features from the background.

Such operations that level out the brightness within an image are called **rank levelling** (Russ 1998). In these operations, each pixel within the image is compared to its neighbours within a small region (typically a 3x3 or 5x5 square). Depending on the type of operation intended, the value of the pixel 'under investigation' can be replaced by the darkest or brightest pixel value of its neighbours. The image processing algorithm often used for this purpose is called **grey scale erosion** or **dilation**, and is available on most image processing software packages.

The following figures are examples of how the rank levelling operation changes the appearance of the image.

Fig 2.5: Rank Leveling Operations.

In ophthalmic imaging, the features of interest are limited in size and smaller in scale than the background variations. To increase the visibility of the features it is important to eliminate the effects of the luminance gradient, as variation in the luminance may be mistaken for image features.

Raw Image: average of 32 frames, cropped to 512 x 512 square

Grey Scale Erosion: neighbourhood operation to replace pixel values with average of its neighbouring values. Results in an image with information about background brightness of original image.

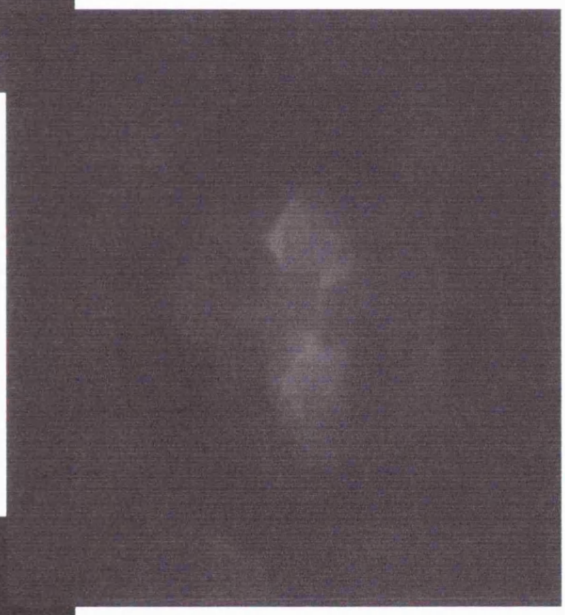

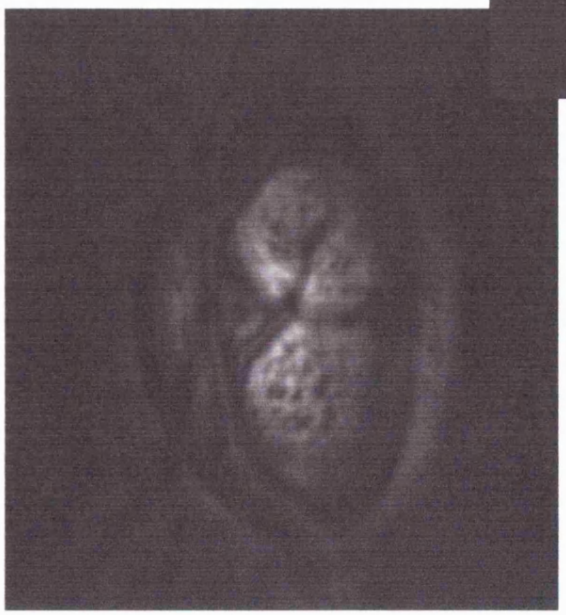

Leveled Image: Subtraction of eroded image from original image. Results in removal of luminance gradient.

Step 2: Highlighting Image Detail- Unsharp masking

Once the illumination gradient has been eliminated, the next step of the processing technique is to highlight the contrast of the small details within the image. The simplest method of doing this is by using a band pass filtering technique. The **unsharp masking** technique is the most common and effective method of enhancing edge values without enhancing noise (Frisen and Hoyt 1973; 1990; Barry, Cooper et al. 1990; Ogoda, Hishinuma et al. 1997; Sanchez-Martin 1999; Analoui 2001). The idea is to simulate a high pass filter by subtracting a smoother version of the image from the original. The following diagram illustrates how the method works for a 1 dimensional waveform.

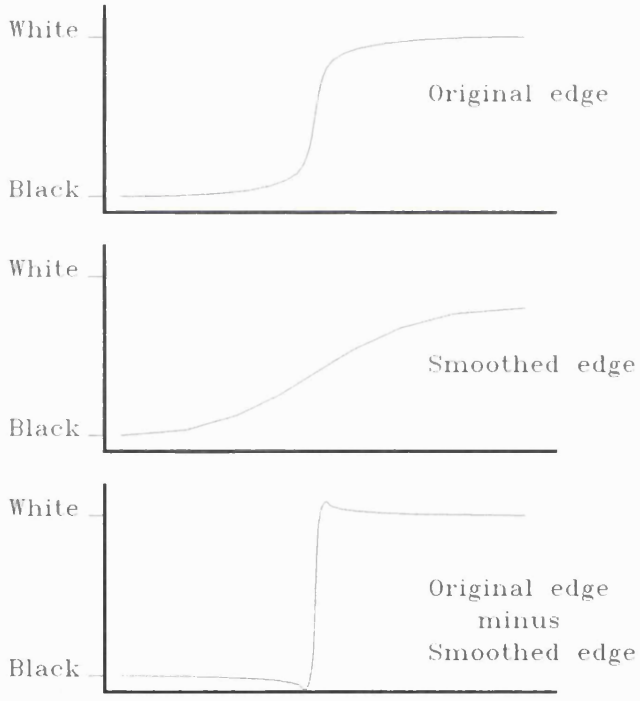

The unsharp masking technique illustrated

(Kind permission T.J. Fountain, Emeritus Professor, Image Processing Group, University College London)

In the case of the 2-dimensional lamina cribrosa images, a Gaussian smoothing filter was applied over the original image to smooth it and this was then subtracted from the original image. This resulted in an enhancement of edge detail. The following figures (figure 2.6) illustrate the technique.

Fig 2.6: Unsharp Masking.

Once the illumination gradient has been removed, the next step of the technique is to highlight detail. The unsharp masking technique is an effective method of enhancing edge values without enhancing noise.

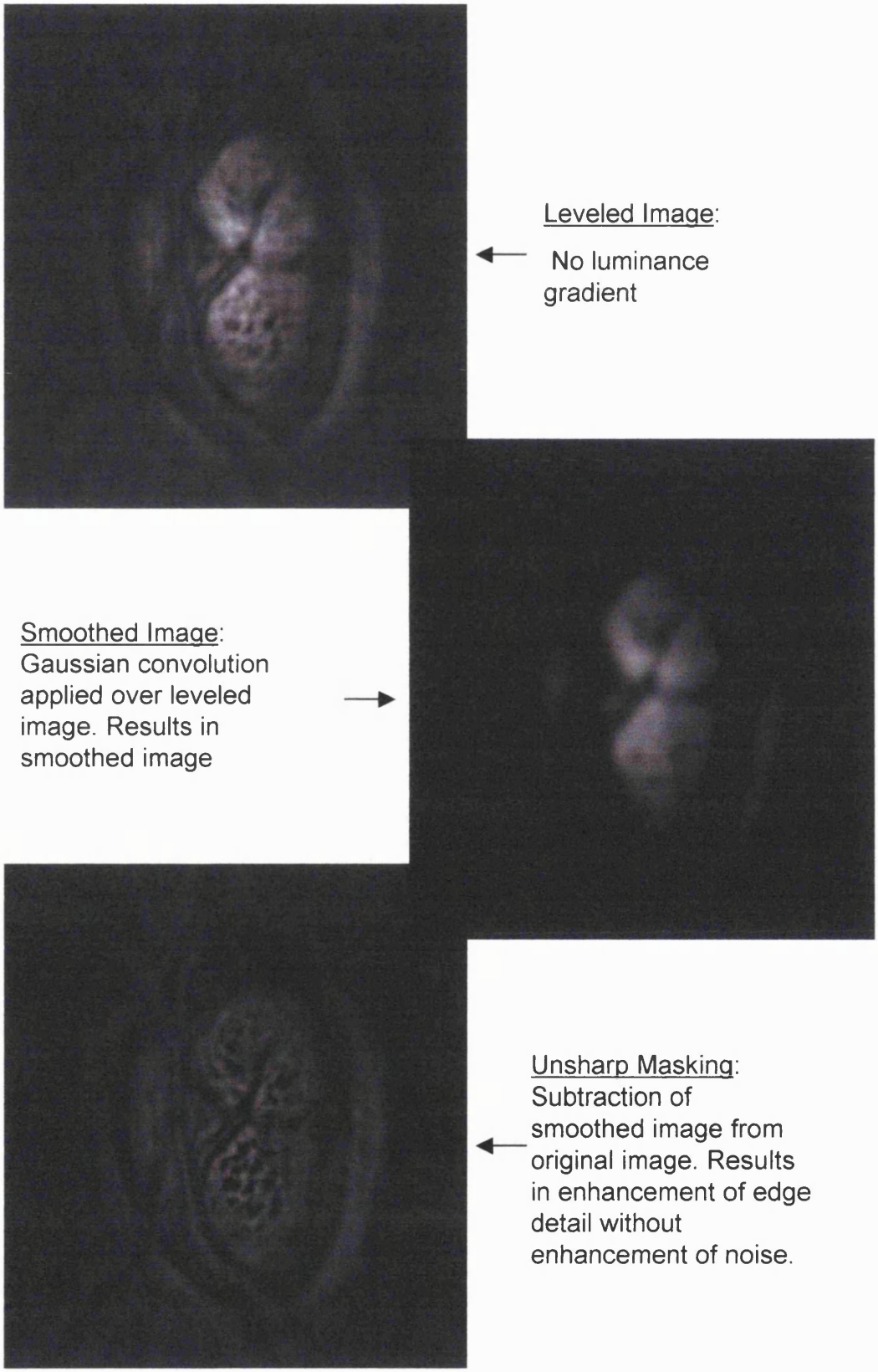

Step 3: Extending the range of pixel values- Contrast Stretching

The original averaged image has a range of brightness values as represented by the histogram **1** (Figure 2.7). For this particular image, pixel values range in brightness from between 0 and 33. Considering that there are 8 bits to an image (or 256 levels of brightness), the brightness range of this image is quite limited. In this case, there may not be enough contrast within the image to allow sufficient pore identification. It is possible to 'contrast stretch' the image, so that the values of the pixels are reassigned to cover as much of the available range as possible. There are a number of contrast stretching algorithms available, and for the purposes of this study, a simple 'window levelling' technique was employed. This is a linear operation, and the effects of applying it to the pre-processed image are shown on the following pages (figures 2.7 and 2.8). By extending the range of pixel values in our image, we are more likely to pick up subtle features within the image.

Fig 2.7: Contrast Stretching 1: Why contrast stretch?

In these monochromatic images there are 256 levels of brightness. However, it can be seen that the brightness range is quite limited. It is possible to 'contrast stretch' the image to increase the range of brightness.

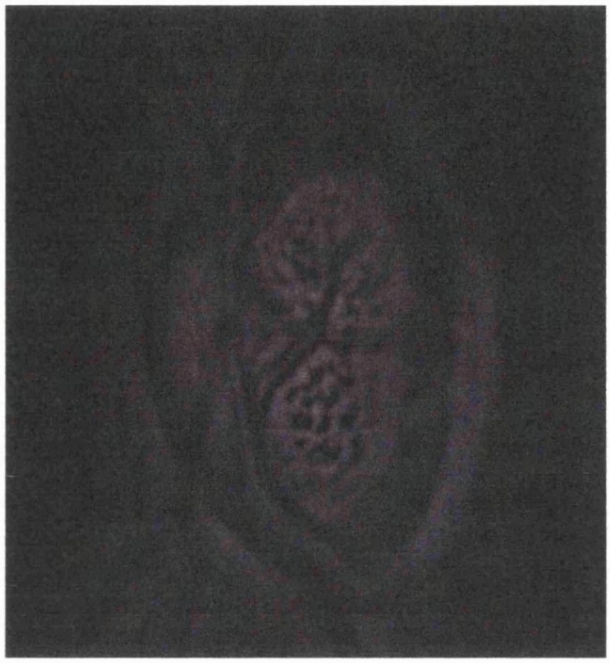

Pre-processed Image: Raw image that has had rank leveling followed by unsharp masking operations applied

Histogram 1: Range of pixel values of the image. X axis represents the grey scale value, Y axis the number of pixels with this value. The above image has pixel values ranging from 0 to 33. There are 256 grey values available, and so this represents a very limited range.

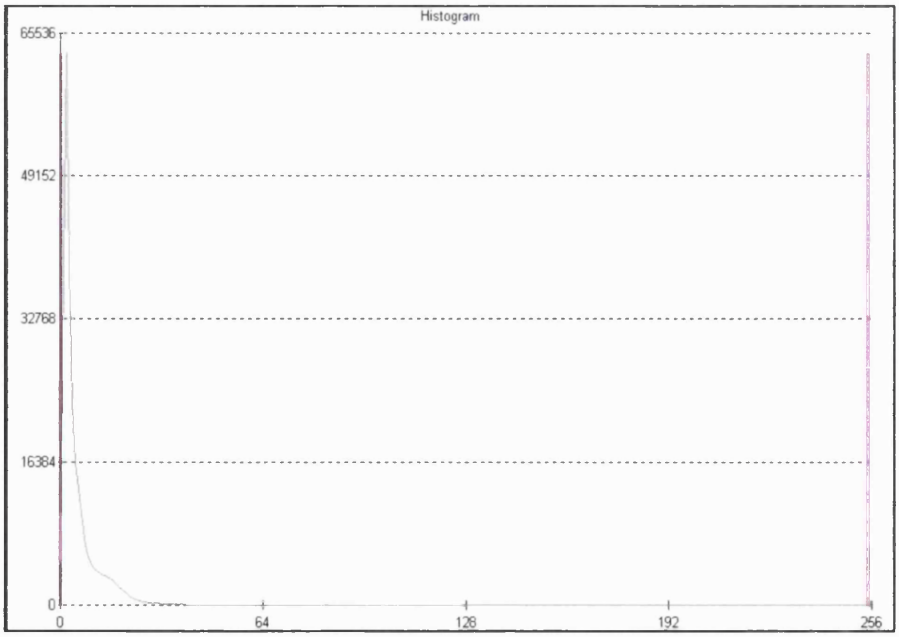

Fig 2.8: Contrast Stretching 2: Extending the range of pixel values.

Using one of the readily available contrast stretching algorithms- in this case the window levelling technique- the range of brightness values within the image is extended. This improves the ability to discern finer features in the image.

Matrox Inspector software version 2.1, Matrox Electronic Systems Ltd, Quebec

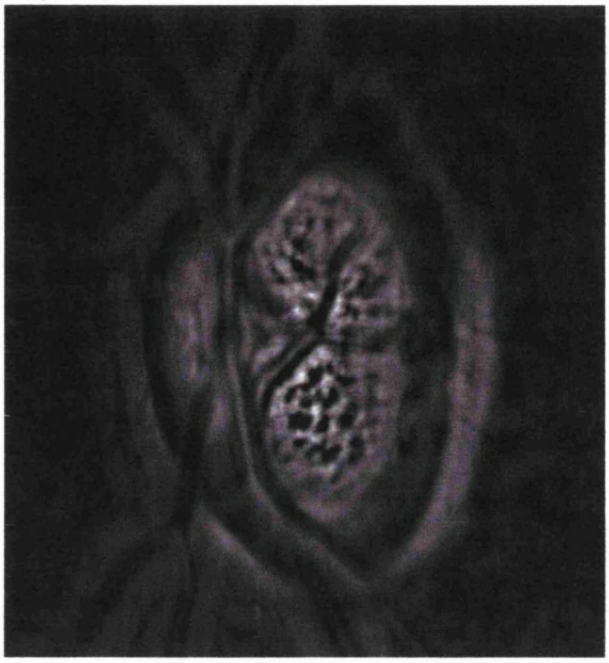

Stretched Image: Contrast stretching involves reassigning the original pixel values in the image to new values, so that they cover the entire range available

Histogram 2: Range of pixel values of the stretched image. X axis represents the grey scale value, Y axis the number of pixels with this value. The stretched image now has pixel values ranging from 0 to 109.

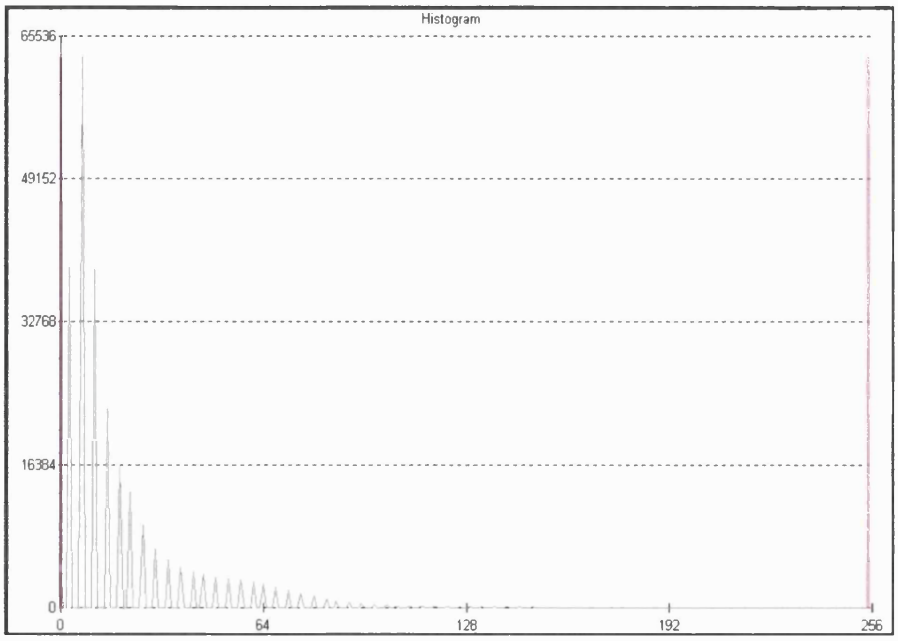

Fig 2.9: Image Processing in the Spatial Domain- Summary.

The steps of image processing in the spatial domain can be summarised in the following image sequence. Images are averaged, levelled, undergo unsharp masking and are finally contrast stretched.

Raw Image: average of 32 frames

Leveled Image →

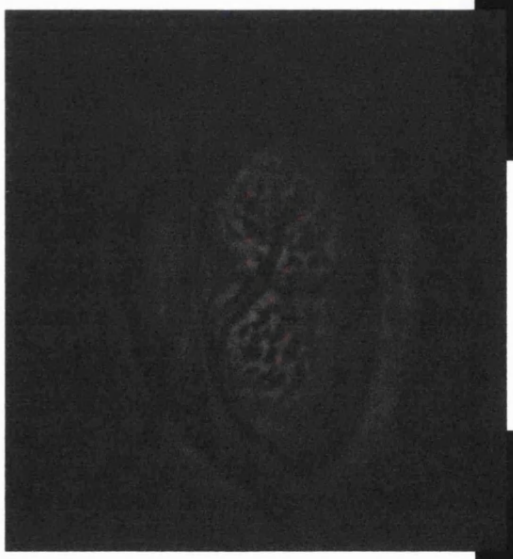

Application of Unsharp Mask Technique

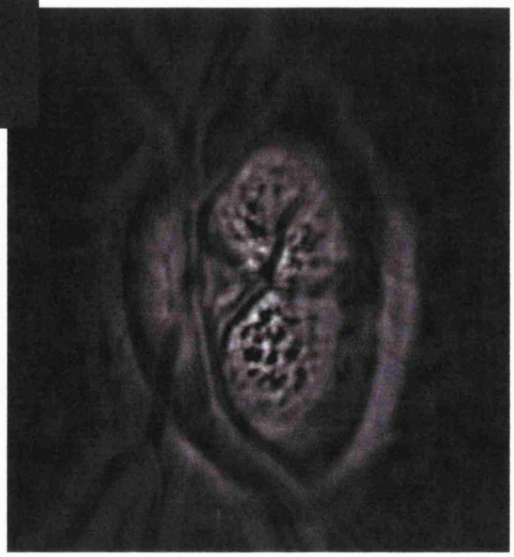

Contrast Stretched Image →

Step 4: Quantification of Image- Thresholding

The purpose of image enhancement is to prepare the image for quantification of features. Inspection of the image reveals that the lamina cribrosa pores range between a dark grey and black colour.

In order to extract information about the pore structure from the image, a **thresholding** technique can be used. This involves the measurement of the range of pixel brightness within the image, and selecting a 'cut-off' (or threshold) value, so that pixels below the value are assigned a new value of 0, and pixels above it are assigned a new value of 1. The result of applying the thresholding algorithm is a binary (black and white) image.

In the case of the lamina cribrosa images, the pores will be highlighted in black. Varying the threshold value results in a large variation of pore visualization, as can be seen from the following figures (figure 2.10).

Fig 2.10: Thresholding.

The processed image has its range of brightness values measured. A 'cut-off' value is selected. Pixels below this will be assigned a value of '0'; those above it a value of '1'. The result is a binary image.

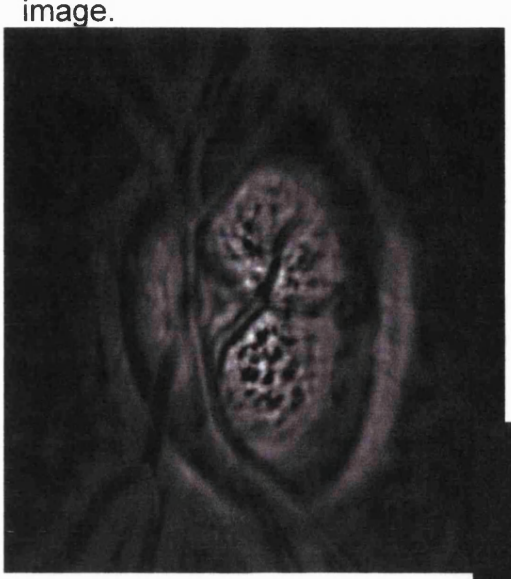

← Processed Image

Thresholded:

Mean pixel value chosen as threshold. →

← Thresholded2:

Lower threshold value.

Thresholded 3:

The amount of lamina pore information is affected by threshold ('cut-off') value chosen. →

Limitations of technique

The methods described above allow the visualisation of the lamina pore structure in the *in vivo* images using spatial domain processing.
Spatial domain processing manipulates the pixel brightness within an image to highlight regions of interest. It is a rather limited method of image enhancement, as it doesn't manipulate all the information available in the image- it simply makes the image 'look better'. We wished to find a technique of image processing that enhanced areas of interest within the image and attenuated undesirable information. For this, a technique more sophisticated that spatial domain processing is needed, and so we looked at Fourier transformations.

2.1.4.3 Image Enhancement II- Processing in the Frequency Domain

Fourier theory states that any signal (e.g. visual, acoustic) can be expressed as a sum of sinusoidal waves. Fourier transformations express the information of each sinusoidal as a single term. If an image is transformed from the spatial domain to the frequency domain using a Fourier transform, the result is a map of fine points. The position of each point represents the frequency, phase and amplitude of each component sinusoidal of the image.
The use of Fourier analysis in ophthalmology is not new and has been used in the analysis of corneal topography data (1990; Friedman, Zadnik et al. 1996; Keller, McGhee et al. 1998).
One of the advantages of using such frequency space transformations in the processing of images is that it is possible to control and limit the spatial frequency information within the image by applying various filters. For the purposes of this study, information about the lamina pore structure is required. The lamina pores have discreet edges, or boundaries, and have a distinct shape. This represents high spatial frequency information. By performing a Fourier transform on the lamina images, and then filtering out the low and medium spatial frequency information, it is possible to gain an image with only lamina pore features highlighted.

An FFT can only be performed on a square image. An image size of any multiple of 256 x 256 pixels is acceptable.
The Zeiss images were cropped to 512 x 512 pixels, and then scaled to compensate for induced astigmatism (section 2.1.2.2). As a result, the image size was reduced to 512 x 440. This image was magnified by 1.16 to increase the size to 596 x 512, and then cropped to 512 x 512 pixels for FFT analysis.
The HRT images were 256 x 256 pixels in size, and although this would be acceptable for the FFT process, for comparisons with the Zeiss images, and to keep the FFT filter the same for both the Zeiss and HRT, the HRT image was multiplied by 2.

Highlighting Lamina Pores

Scion Image software (National Institute of Health, Maryland, USA; shareware) was used to generate the FFT of the averaged lamina image, and a custom made filter was designed to filter out the unwanted spatial frequency information from the image (figure 2.11). The edges of the lamina pores need to be amplified in order to effectively measure them. Edge detail represents high spatial frequency information. In the FFT, low spatial frequency information is accumulated around the centre of the transform, with higher spatial frequencies increasing further from the centre. In view of this pattern, an annular filter was created to filter out the low spatial frequency information of the image and allow only the high spatial frequency information to pass (fig 2.12-2.13).

Fig 2.11: Image Processing in the Frequency Domain.

The Fourier transform is used to transform an image from the spatial domain into the frequency domain. Application of filters enables control of the spatial frequency information within the image.

Raw Image:

← Average of 32 frames.

Power Spectrum:

Map of the spatial frequency components of raw image. →

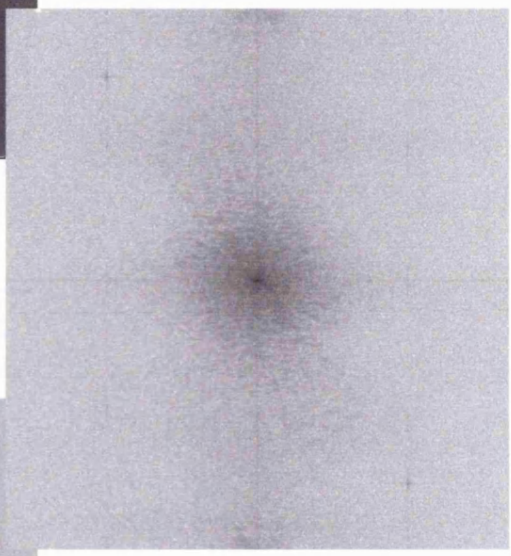

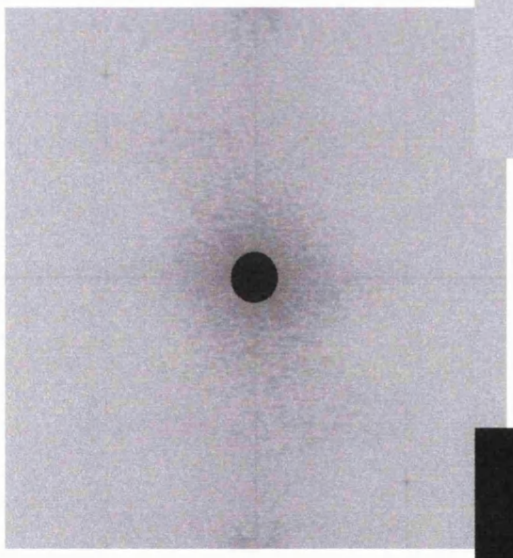

Application of Low Pass Filter;

Custom made filter applied to power spectrum. Blocks high spatial frequency information.

Inverse Transform:
New image with only low spatial frequency (shape/contour) information. Note lack of detail of lamina pores in cup area. →

Fig 2.12: Processing in the Frequency Domain II: Annular Filters.

Filters are used in transformed images to control the amount of spatial frequency information in the image. An annular filter was developed to highlight the lamina pore structure. The following illustrates the result of the application of such a filter.

Raw Image:

Average of 32 frames.

Annular Filter:Filter designed to pass high spatial frequency information and block low spatial frequency information (black=pass, white=mask).

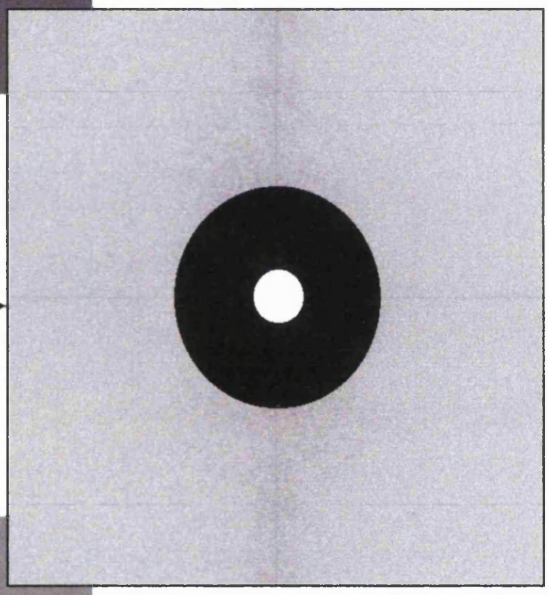

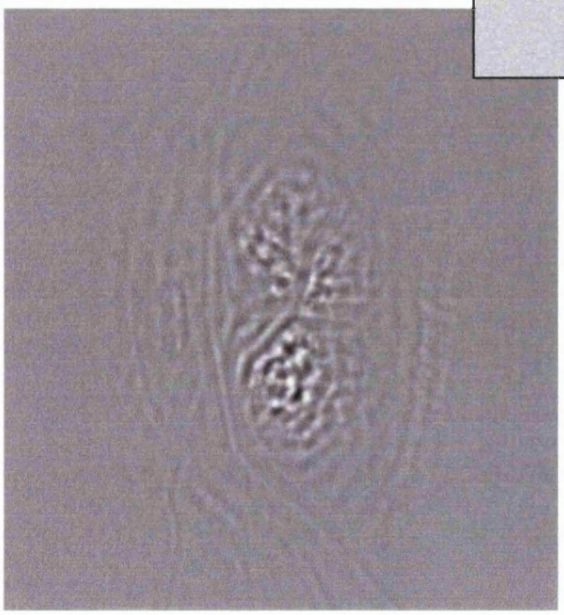

Inverse Transform: Results in image with mainly high spatial frequency information. Highlights lamina cribrosa pores and blood vessel edges.

Fig 2.13: Thresholding.

As seen from fig 2.10, the threshold value chosen has an effect on the pore information gained. However, it can be seen that there is more pore information in these examples compared with the spatially processed images in 2.10.

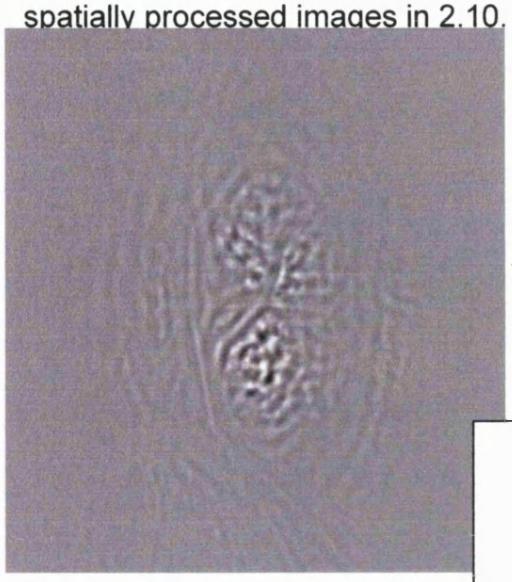

Processed Image

Thresholded:

Mean pixel value chosen as cut off.

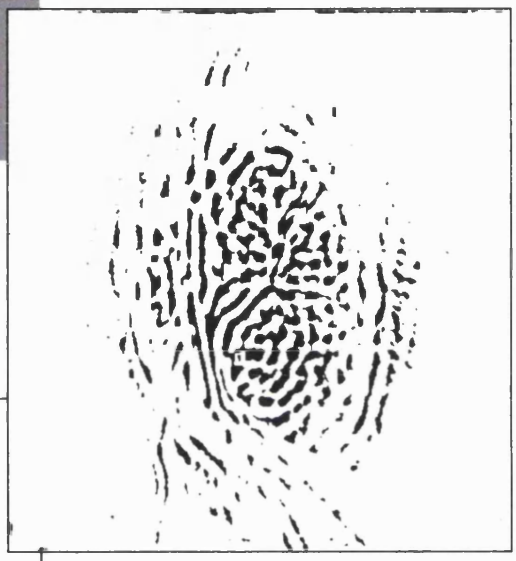

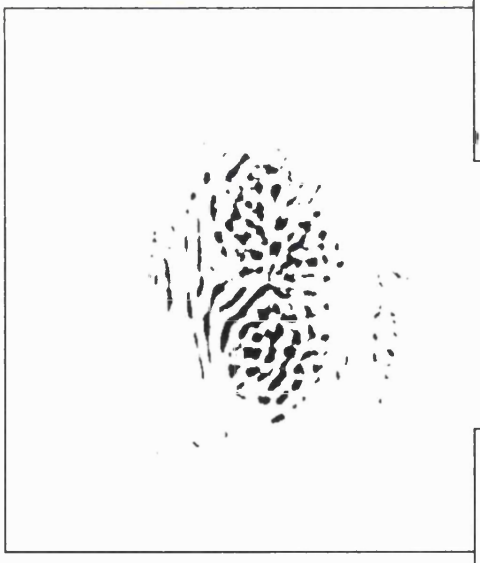

Thresholded 2:

Lower cut off value.

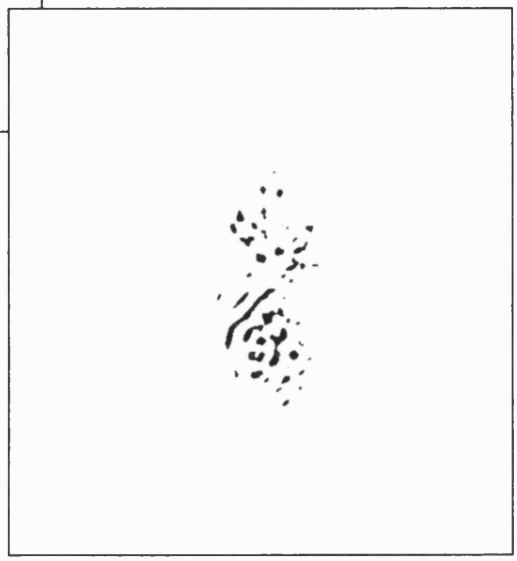

Thresholded 3:

Lower cut off value.

Noise

Section 2.1.1.2 discussed how image alignment and averaging was an effective method for attenuating random noise. Periodic noise, however, leaves distinct patterns in the Fourier domain representation of the image, and by filtering out these patterns periodic noise can be removed.

In order to see whether periodic noise may be present in the images grabbed using the cSLO, an image of a blank screen was taken (figure 2.14i). Thirty-two frames of the blank screen were aligned and averaged and the individual frames as well as the averaged image were saved as individual tagged image file format (TIFF) files. These images were taken into Scion Image, and FFT of the individual frames and the averaged image were produced. The results are shown on the following pages. All individual frames showed a distinct central cross-hair type pattern in their FFT and a number of other fine lines, which were present in the averaged image also. When a filter was applied to pass only this feature, a pattern of vertical and horizontal lines was produced (figures 2.14iii- ix).

Figs 2.14: The influence of noise- blank screen.

Alignment and averaging of image frames is an effective method for attenuating random noise. Periodic noise, however, leaves distinct patterns in the Fourier domain and, with appropriate filtering, can be eliminated. The following figures illustrate how the periodic noise elements in our cSLO images were isolated.

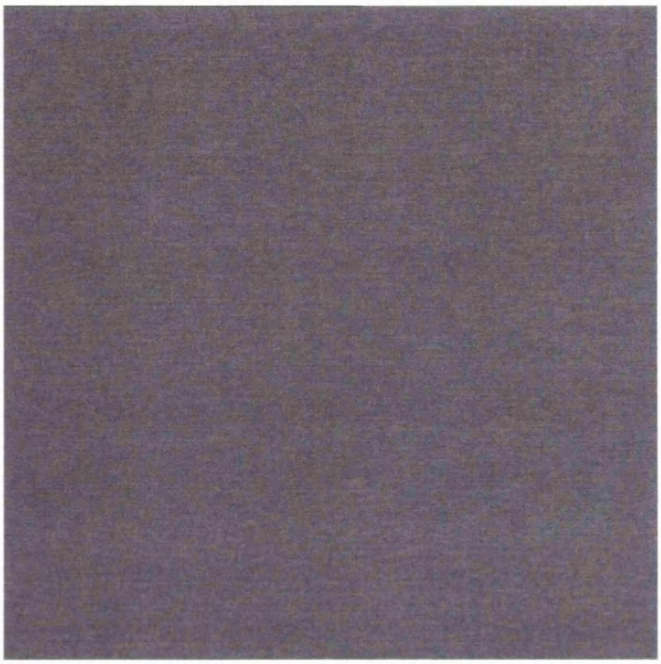

2.14 i

Single frame of image of a blank screen.

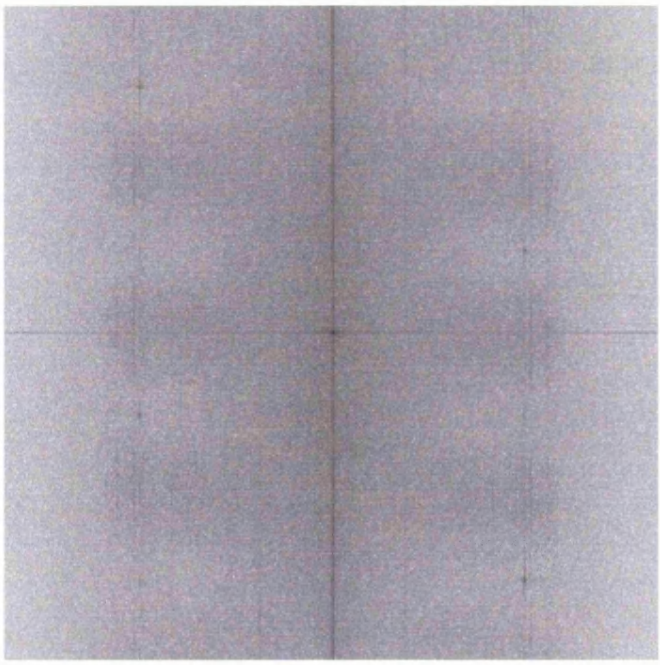

2.14 ii
Application of FFT (Scion Corporation) to above TIFF file. Note the fine horizontal and vertical lines in the transform. These represent a combination of periodic noise elements and changes in brightness across the image.

Figs 2.14 ctd: The influence of noise.

The figures illustrate the method of isolating and then removing the periodic noise elements in the Fourier transform overleaf.

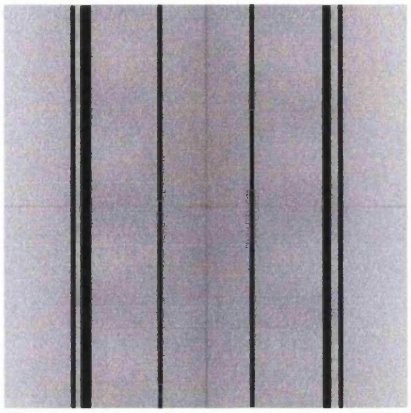

2.14 iii
'Pass-filter' applied to vertical lines of FFT.

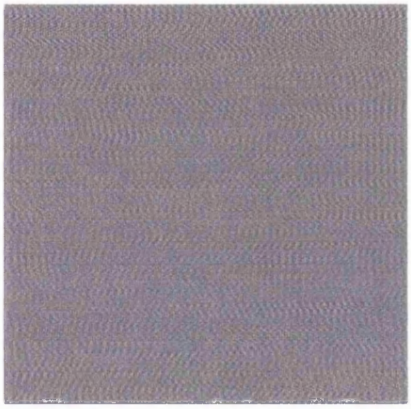

2.14 iv
Inverse transform of the above. The vertical lines of the FFT represent the noise element, shown here, of the original image.

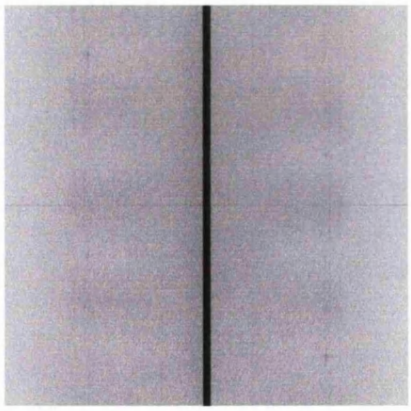

2.14 vii
Application of a 'pass-filter' to the central vertical line of FFT.

2.14 viii
Inverse transform of above. The vertical line of the FFT represents a fine horizontal line pattern of noise of the original blank TIFF image.

Figs 2.14 ctd: The influence of noise.

Further illustrations showing the effects of filtering of periodic noise elements within the Fourier transform.

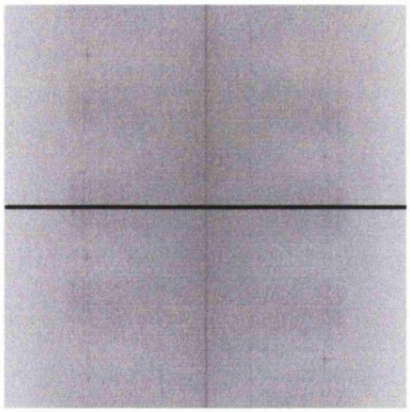

2.14 v
Application of a 'pass-filter' to main horizontal line of FFT.

2.14 vi
Inverse transform of above. The horizontal line of the FFT represents this pattern of vertical lines with a luminance gradient. This represents the luminance gradient within the original 'blank screen' image.

2.14 ix

Inverse transform representing 'pass-filter' of *all* vertical and horizontal line elements of original FFT.

These fine lines may originate from slight discrepancies in the x-y raster sweep of the laser.

Within all the transforms, there was the presence of a central crosshair and a number of discreet horizontal and vertical patterns. These fine horizontal and vertical lines might be a result of slight inconsistencies in the horizontal and vertical scanning of the cSLO.

In order to establish whether this noise was a factor of the cSLO and not the 'blank-screen' image, an image of an optic nerve head was also grabbed (figs 2.15). Single frames were analysed using Scion Image software, and it was noticed that, again, all the Fourier transforms had very fine horizontal and vertical lines within them. Performing an inverse transform passing these 'lines' in isolation produced an image shown in fig 2.15 iv. The patterns were present in all FFT's of the single frame images of the optic nerve head. It was thought that perhaps the noise might be reduced in the averaged image, due to the presence of involuntary saccadic eye movements that occur when imaging the living eye. The very nature of periodic noise means that it will be present in the same place within each image frame. Saccadic eye movements would result in the image of the optic disc being decentred in each frame, thus requiring image alignment prior to frame averaging. Aligning the images would result in the noise element of the image being in different places within the averaged image, thus reducing its influence in the averaged image (figure 2.16).

To test this hypothesis, we performed a Fourier transform on an optic disc image that was an average of 32 single frames (fig 2.17).

Figure 2.15: Periodic noise in optic disc images.

Figure 2.14 illustrated the periodic noise element in an image of a blank screen. The following illustrates the effect this noise has in an image of an optic disc.

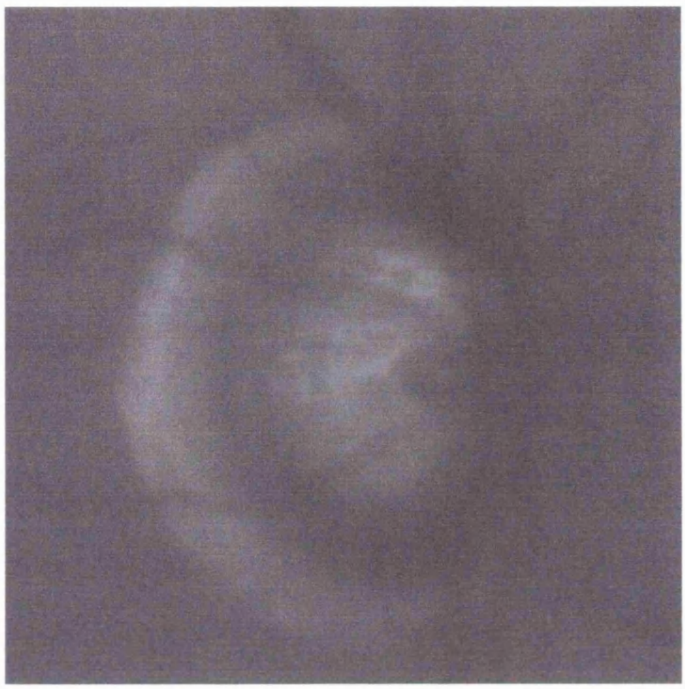

2.15 i
Single frame of optic disc.

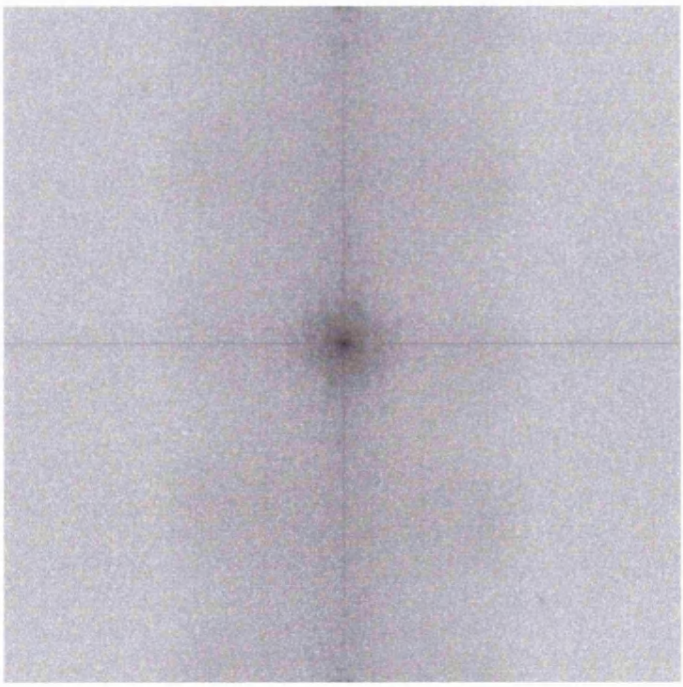

2.15 ii
FFT of above image. Note the presence of a fine crosshair pattern in the centre of the transform.

Figure 2.15 ctd: Periodic noise in optic disc images.

By creating a filter that only passes the information of interest within the transform, the noise element can be isolated.

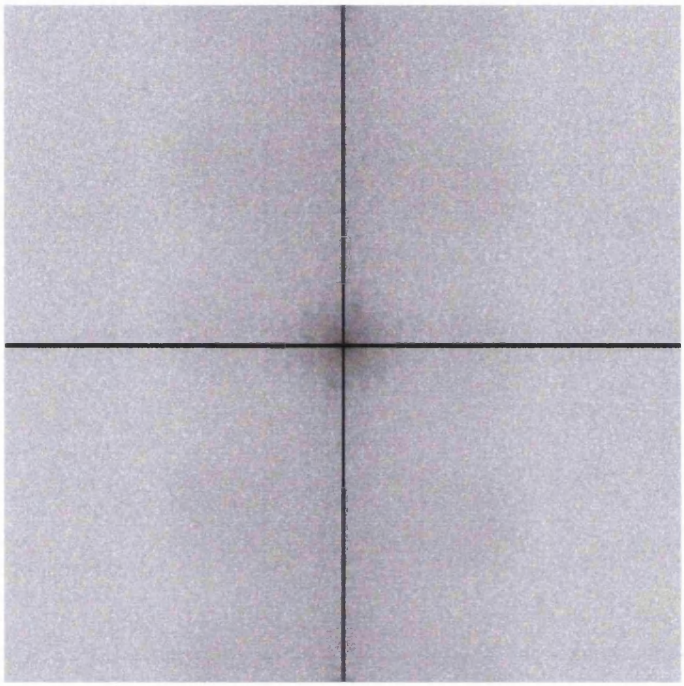

2.15 iii
Pass filter created to investigate the influence of the crosshair pattern on the optic disc image.

2.15 iv
Inv FFT of above transform. The crosshair represents the luminance change from background retina to bright foreground optic disc.
The fine lines are possible raster scan lines.There is also the presence of some low spatial frequency information (outline of disc). This is because the 'pass filter' encompassed an area in the central FFT that contains low spatial frequency information of the image.

Figure 2.16:Schematic diagram illustrating effect of saccadic eye movements on periodic noise.

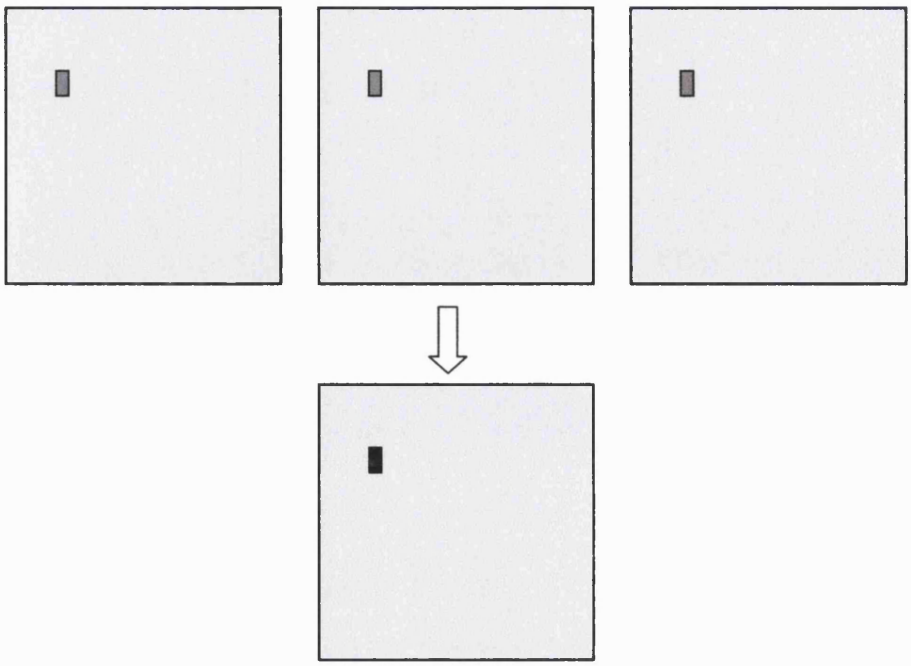

Above: When grabbing images of a stationary object, the periodic noise in individual frames is enhanced with averaging.

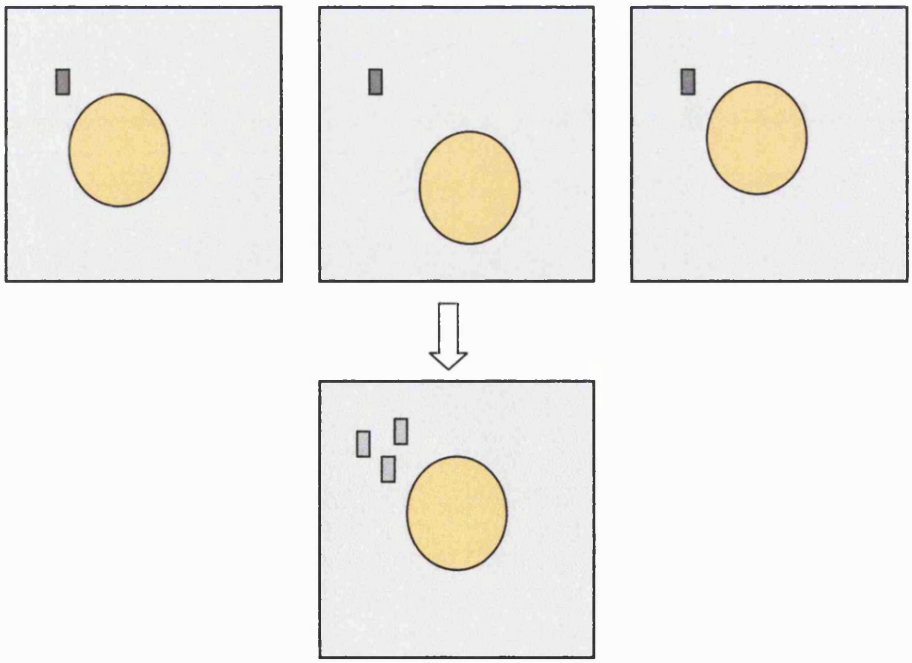

Above: When imaging the eye, saccadic eye movements are present, and these need to be corrected prior to image averaging. The alignment procedure results in the noise element being in different positions in the final averaged image. This results in their attenuation.

Figure 2.17: The influence of periodic noise- averaged optic disc image.

Figure 2.15 showed the periodic noise element of a single frame. It was thought that filtering this from all single optic disc frames *prior* to image averaging would eliminate such noise from the averaged image. However, the following illustrates that this was not the case.

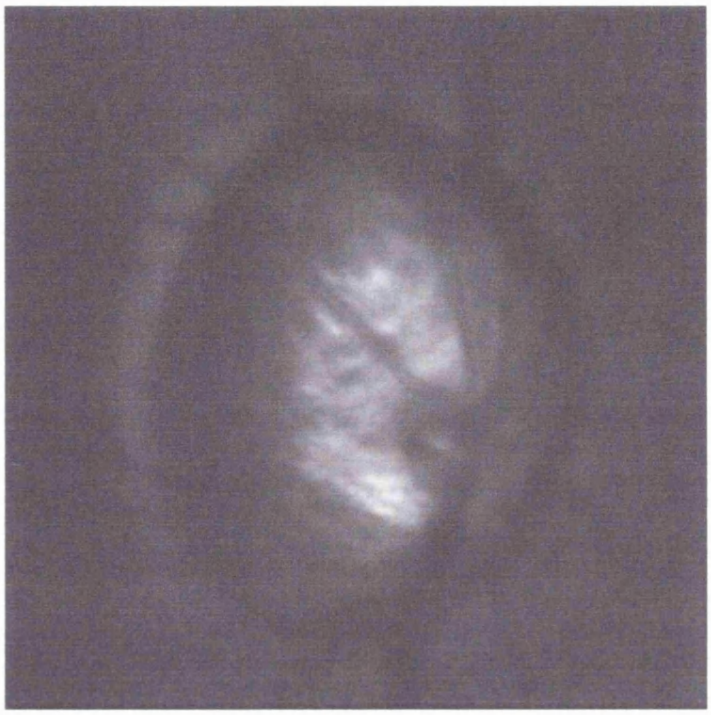

2.17 i
Average of 32 grabbed frames of an optic disc.

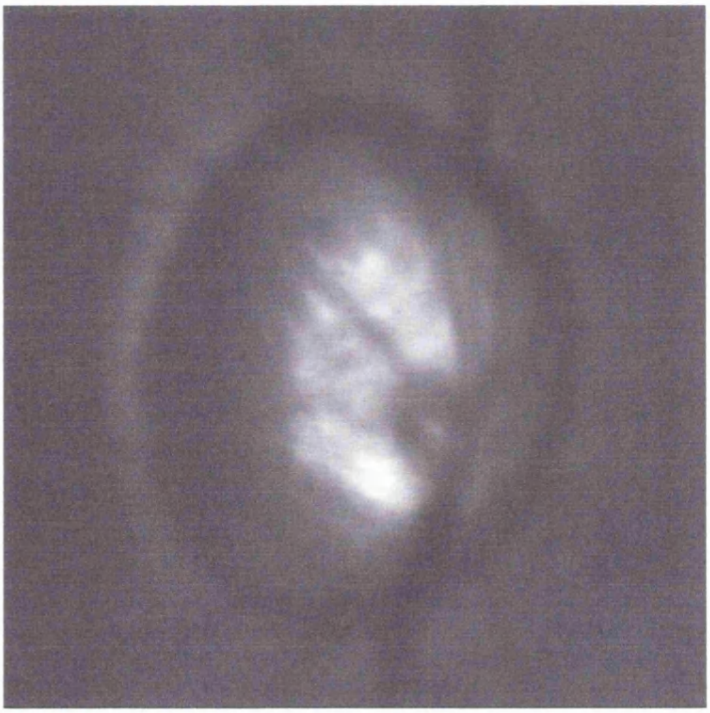

2.17 ii
Average of 32 frames of optic disc that have each had the fine periodic noise filtered prior to averaging.

Some features from the optic cup have been attenuated as a result of this pre-average filtering.

Figure 2.17 ctd: The influence of periodic noise.

Fourier transform of images on pp 91

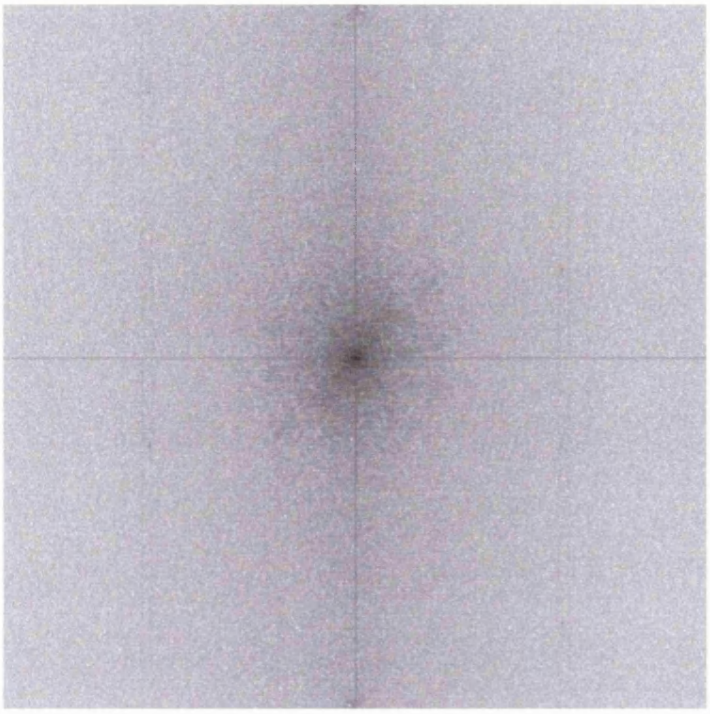

2.17 iii
FFT of image 'i' overleaf. Fine 'cross-hair' pattern of noise present in transform.

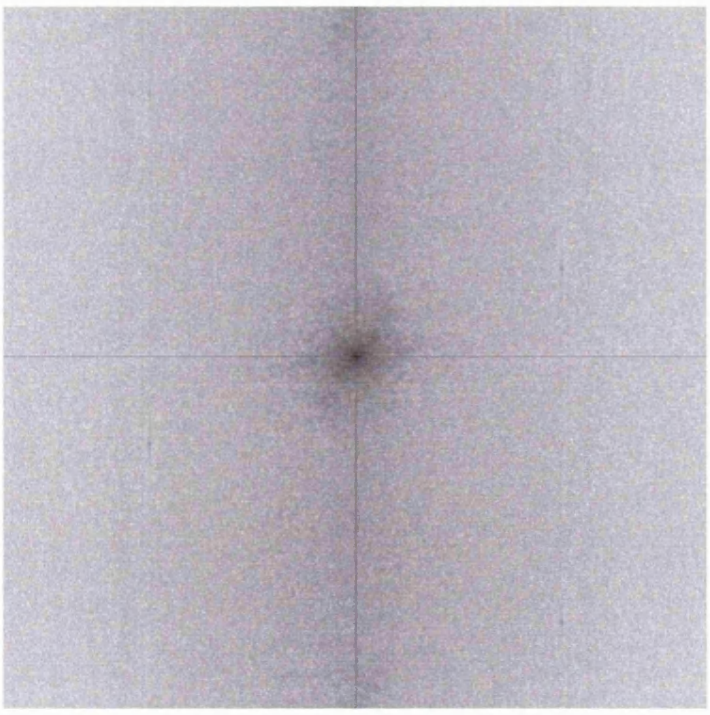

2.17 iv
FFT of image 'ii' overleaf. 'Noise' still present despite pre-average filtering. The central area of the FFT is reduced compared with the above transform, indicating a loss of spatial frequency information.

Figure 2.17 shows that, despite averaging, there was still the presence of the central crosshair in the transform. If one compares the FFT of the averaged image with pre-average filtering and the FFT of the averaged image without filtering (fig 2.17), there is little difference between them. If anything, there appeared to be reduced detail in the image that had noise filtering prior to averaging. Individual frames will have a low signal-to-noise ratio, as explained in section 2.1.12. It was also seen from the earlier example (fig 2.15) that by producing a pass filter of the fine crosshair pattern, an element of low spatial frequency information of the optic disc was passed also. Therefore, in attempting to remove what seemed to be noise from individual frames, an element of signal information of the image was also removed.

The presence of the central crosshair pattern can be explained by considering Fourier theory. Fourier theory expresses the image as though it is part of an infinitely repeating pattern - the image is treated as though it were closed up upon itself. To visualise this better, consider an image on a piece of paper. Join two edges of the paper to form a cylinder, and then join the two ends of the cylinder so that a 'doughnut' shape is formed. This is how Fourier theory expresses an image. Therefore, a feature of the transform of that image will be the spatial periodicity of the image itself (imagine traversing along the 'doughnut'- the image on the paper will be repeated periodically as the 'doughnut' is traversed). If the image has a luminance gradient, this will result in repeated pattern of 'light-dark-light'. This sinusoidal change in brightness will appear on the Fourier transformation as a distinct line. With the lamina images, the brightness change from the dark background of the retina to the bright foreground of the optic disc is large. This stark change in brightness will appear as a regular 'band' of 'light-dark-light' in the Fourier transformation, hence the large central crosshair. This would be impossible to eliminate, and explains why our attempts to do so failed. In light of all the above findings, this apparent noise element of the Fourier transform was deemed acceptable, and no further attempts were made to remove it.

Image artefacts

Inspection of the images will show that, when transformed, the edges of the blood vessels become 'ringed' in appearance (not to be confused with Fourier ringing as described in the previous section), and could be mistaken for lamina pores. Therefore, it is important to eliminate these image artefacts before quantifying the pore structure through automated techniques.

Most image processing packages offer tools for which to create a 'mask' to remove objects of no interest from the final image. For this study, we used Paint Shop Pro 6 (Jasc Software Inc) to create the mask. Using the 'freehand' tool, the outline of the blood vessels was traced from the original averaged image and a mask created. This mask was superimposed upon the thresholded image, and all pore quantification was made from this masked image.

Figure 2.18: Image artefacts.
By performing an FFT and attempting to isolate the high spatial frequencies of the image, it is possible to introduce image artefacts. Blood vessel edges become ringed in appearance and will be mistaken for lamina pores.

2.18 i
Average of 32 grabbed frames of an optic disc.

Note how the central retinal vessels obscure parts of the optic cup area.

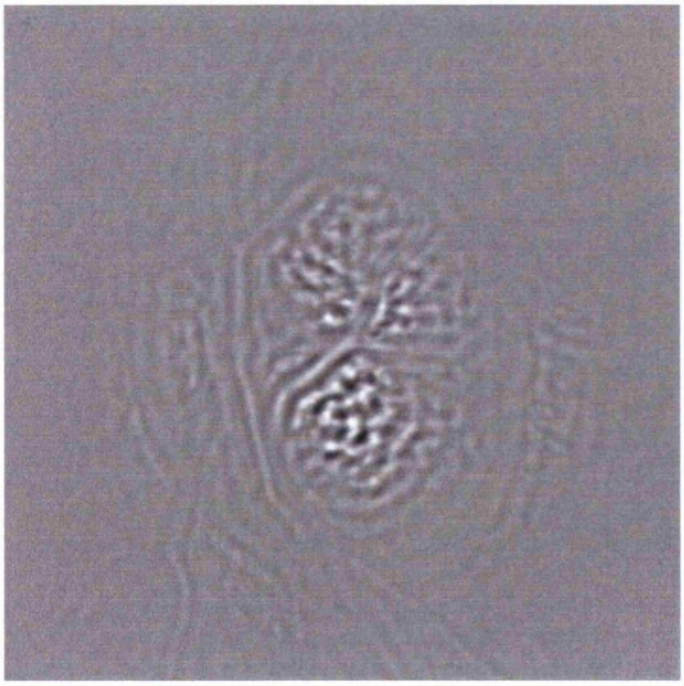

2.18 ii
Inverse transform following FFT filtering.

The edges of the blood vessels have become darkened and thickened in appearance.

Figure 2.18 ctd: Image artefacts
Thresholding the inverse transform overleaf results in the dark areas around the blood vessel edges are highlighted along with the lamina pores. This will result in an error when analysing lamina pore characteristics, as blood vessel features will be mistaken for pores.

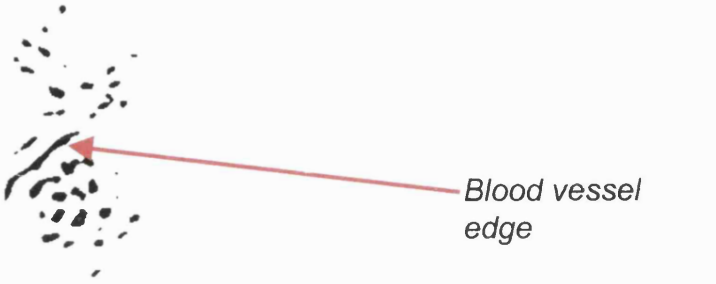

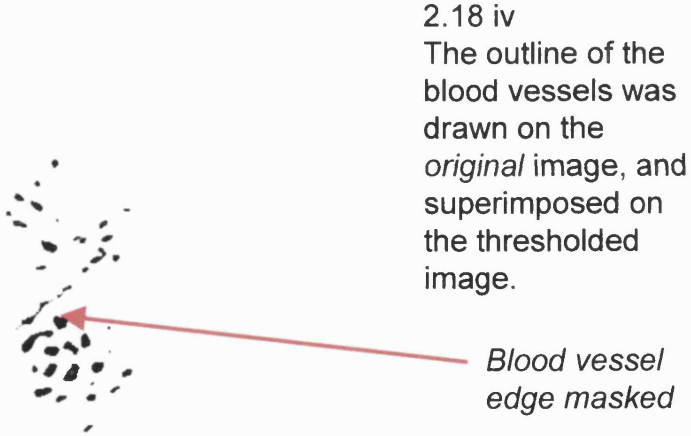

2.1.4.4 Image restoration- Deconvolution

From the above examples, it can be seen that processing the images in the frequency domain allows an improved method of pore visualisation. However, it is possible to improve the quality of the 'raw' images to try and increase the power of the processing technique.

Section 1.2.2.1 described the principle of confocal optics, whereby only light from the focal plane of the raster-scanning laser spot will be detected by the photodetector, and any light reflected from different planes or back-scattered will be ignored. By rejecting the defocused light far fewer photons are detected, increasing the quantum-photon noise component in the raw data. This 'image noise' is in addition to noise generated by the detection system itself - shot noise from random fluctuations in the photon intensity and thermal electronic noise from the detector itself. Since the properties of these noise sources are often known, it is possible to compensate for them to some degree in the final image. Additionally, any imaging system is far from perfect, and image quality is degraded by aberrations present in the imaging system, as well as those that are caused by the eyes optical system. Moreover, factors in the environment can prevent the optical system from optimum performance. Once the final image has been generated, it is theoretically possible to correct for optical aberrations present in the imaging path. This is termed as **deconvolving** the image. In order to deconvolve the image, we need to have accurate knowledge of the optical aberrations of the image acquiring system as well as the eyes optical system. The aberrations generated by an optical system can be measured by the **point-spread function (PSF)**(Fincham and Freeman 1980). It is possible to determine how the changing environment affects the performance of the optical system and apply methods to correct for them, a technique known as **adaptive optics**. Adaptive optics has been used in ophthalmic imaging to image the retinal cone mosaic (Miller, Williams et al. 1996; Liang and Williams 1997; Liang, Williams et al. 1997). However, for the purposes of this study, these systems are not used but are discussed in Appendix II. It is also possible to perform methods of

deconvolution onto images where the blurring function of the imaging system is not known- this is known as a **blind** deconvolution. Most blind deconvolution algorithms are adaptive- the first iteration makes a guess of the PSF of the imaging system, and after that 'moulds' the next PSF on the results obtained with each preceding iteration.

Deconvolution techniques are very useful in the restoration of images from both the HRT and the Zeiss cSLO. The two imaging systems differ fundamentally in their image acquisition techniques as described earlier in the chapter. With the HRT, the operator has to set an initial focus on the neuroretinal rim, but there is an ' image quality control' feature that will the guide the operator as to how to change the focus and depth setting to grab an optimal image series. In addition, rather than grabbing images at a single plane of focus, the HRT grabs 32 images that are and progressively deeper levels through the optic nerve head, giving a 3-dimensional reconstruction of the area. For the Zeiss cSLO, the operator manually focuses on the optic nerve head, and the images grabbed are all at a single plane of focus.

In view of these differences, the method of deconvolving the Zeiss and HRT images is quite different.

Deconvolving the HRT image

Each confocal section of the HRT image series is relatively deblurred already- the very point of confocal optics is to reject out-of-focus light. However, this system does not reject all of the out-of-focus light, and as a result the image retains substantial axial smearing. In addition to this, due to the rejection of non-confocal light, fewer photons are detected so a significant quantum-noise element may be present in the final image. A way of ridding this element is by using an averaging technique as discussed in section 2.1.1.2, but this technique cannot be applied to the HRT images, as each confocal image is at a different level within the optic nerve head. Therefore use of a 3-dimensional blind deconvolution to remove the effects of the above noise elements is warranted.

Deconvolving the Zeiss image

Deconvolution of the Zeiss averaged image is also possible, using a 2-D blind deconvolution. Although averaging images increases the signal to noise ratio (section 2.1.1.2), it is possible that deconvolving the image will enhance it further. The following figures illustrate the application of a 2 and 3-D blind deconvolution to the Zeiss and HRT images.

Figs 2.19: Image Restoration I: Blind Deconvolution of HRT images.

Deconvolving an image corrects for aberrations in the imaging path. It is possible to deconvolve an image without accurate knowledge of the optical aberrations of the imaging pathway. This is known as *blind deconvolution*.

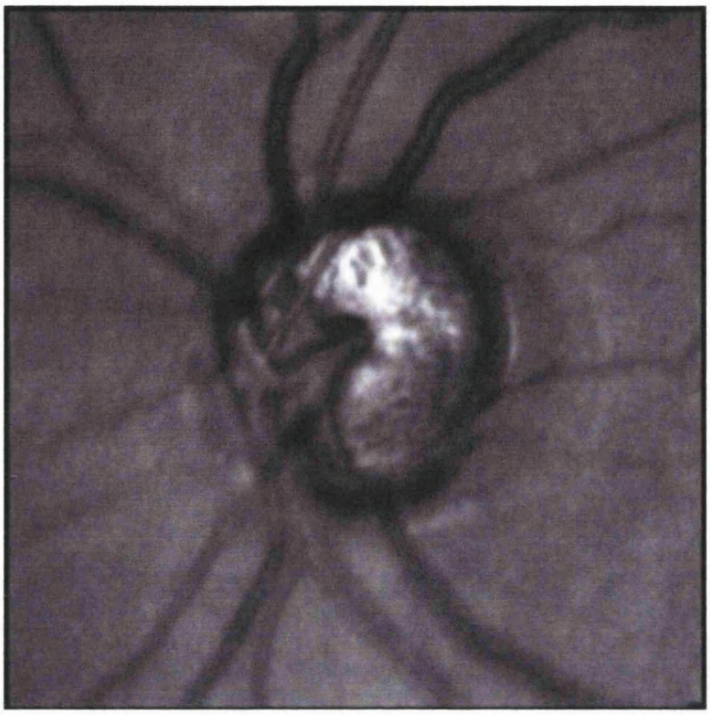

2.19 i

The HRT grabs a series of 32 images through the optic nerve head. This is a single image at the level of the optic cup surface.

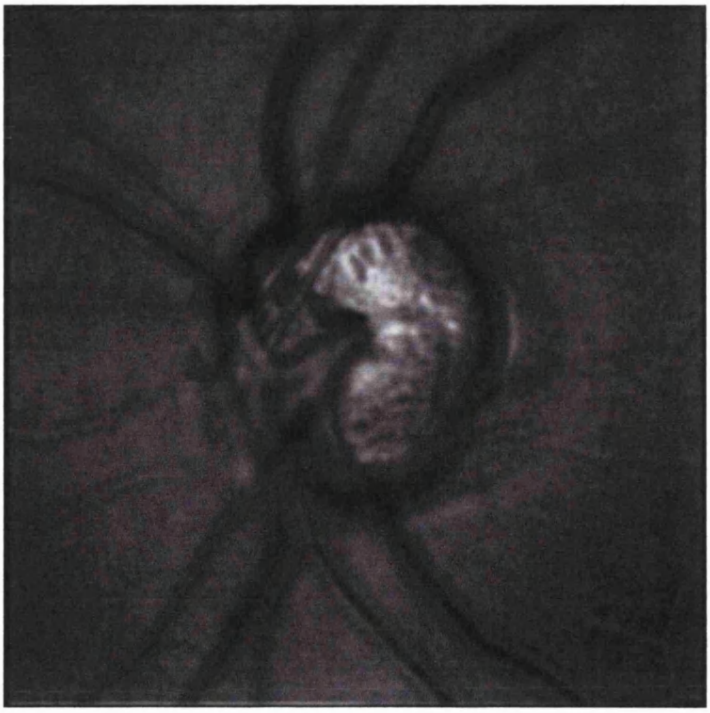

2.19 ii

Deconvolved image at the same level.

Autodeblur vers. 7.5 Gold

Figs 2.20: Image Restoration II- Processing the HRT images.

The images overleaf underwent a Fourier transformation, had an annular filter applied (fig 2.12) and an inverse transform. These are the results.

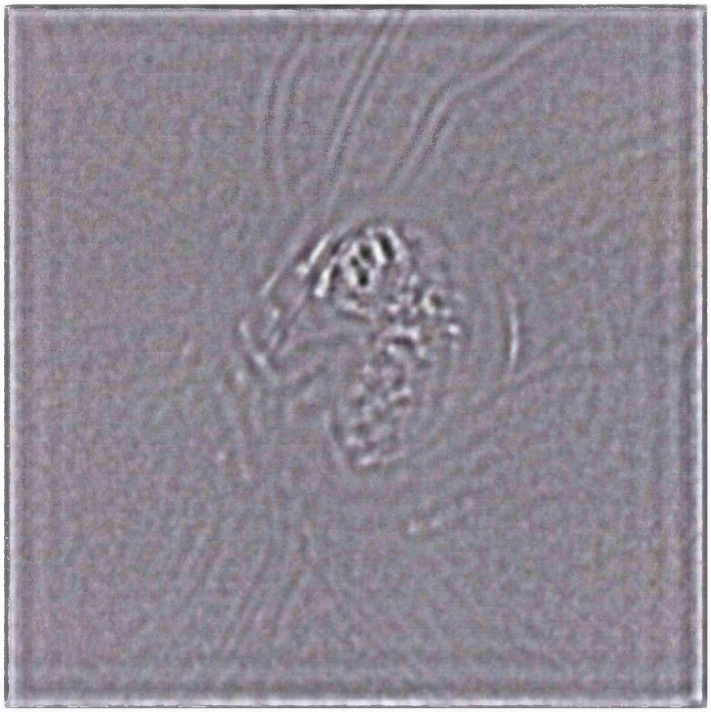

2.20 i

Inverse transform of 2.19 i following application of annular pass filter.

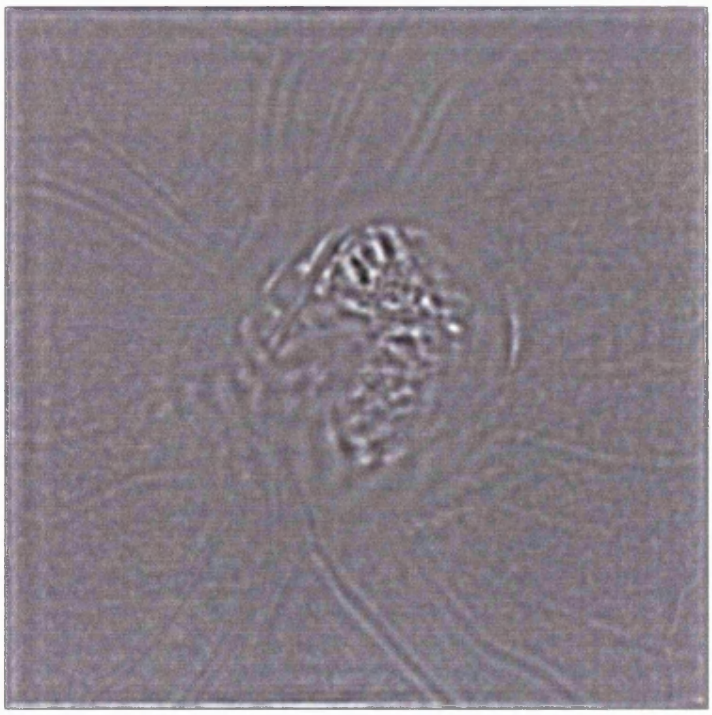

2.20 ii

Inverse transform of figure 2.19 ii following filtering.

Figs 2.21: Image Restoration III- Thresholding the HRT images.

Although the previous examples did not show a great difference in appearance, thresholding shows how more pore information is present in the image that was deconvolved prior to image processing.

2.21 i

Thresholding of image 2.20 i.

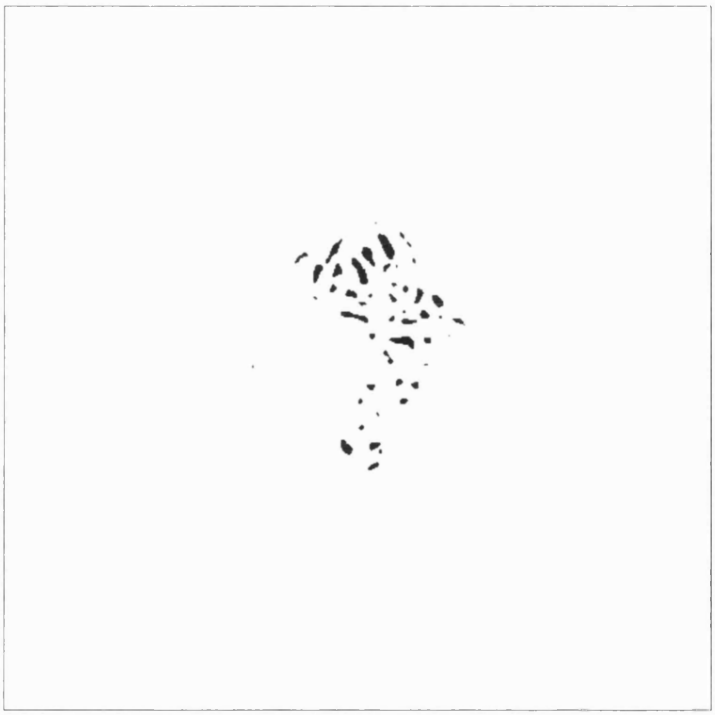

2.21 ii

Thresholding of image 2.20 ii.

The threshold value in both examples was the same.

Figs 2.22: Image Restoration IV- Blind deconvolution of Zeiss images.

Unlike the HRT, the Zeiss images are grabbed at one level. A 3-D blind deconvolution is not possible because there is no *axial* information. However, it is possible to perform a 2-D blind deconvolution, and the following examples illustrate the results.

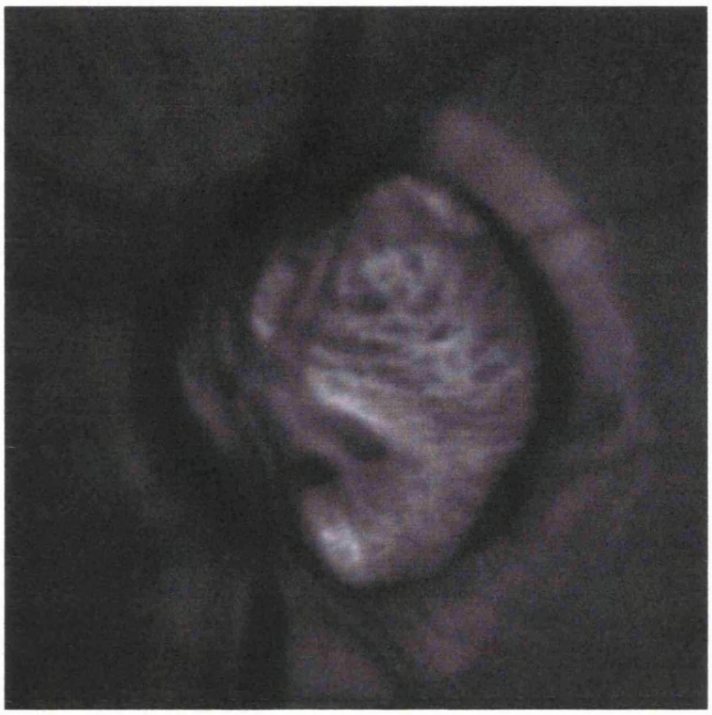

2.22 i

Averaged image of optic disc taken with Zeiss cSLO.

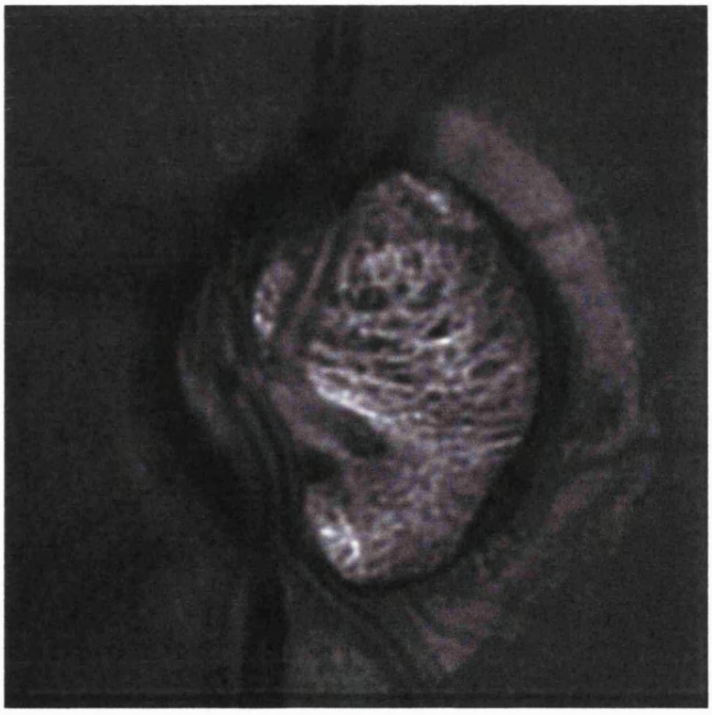

2.22 ii

Image after 2-D blind deconvolution.

The optic cup area appears less blurred and more lamina pores seem visible.

Figs 2.23: Image Restoration V- Processing the Zeiss images.

Images 2.22 post FFT filtering and inverse transform. More detail appears to be present on the lower image, which was deconvolved prior to FFT.

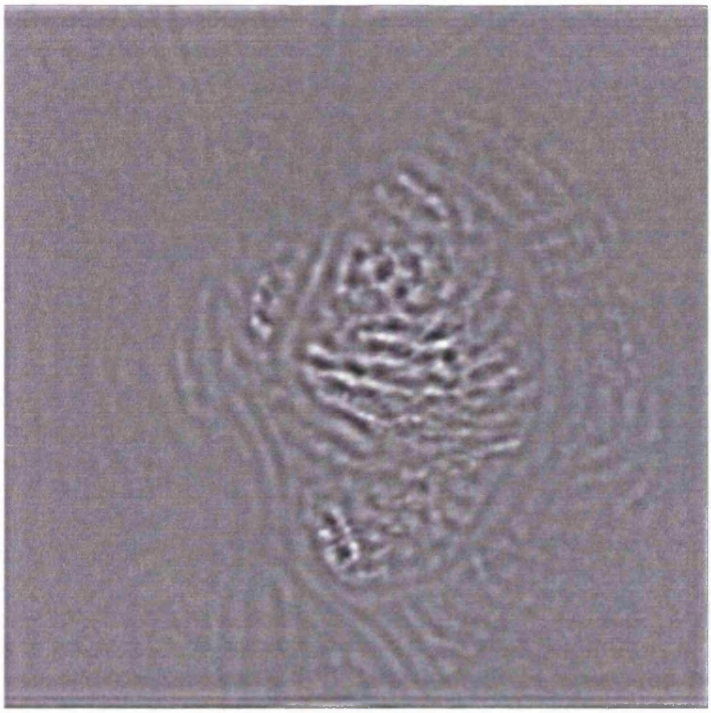

2.23 i

Inverse transform following FFT filtering of image 2.22 i overleaf.

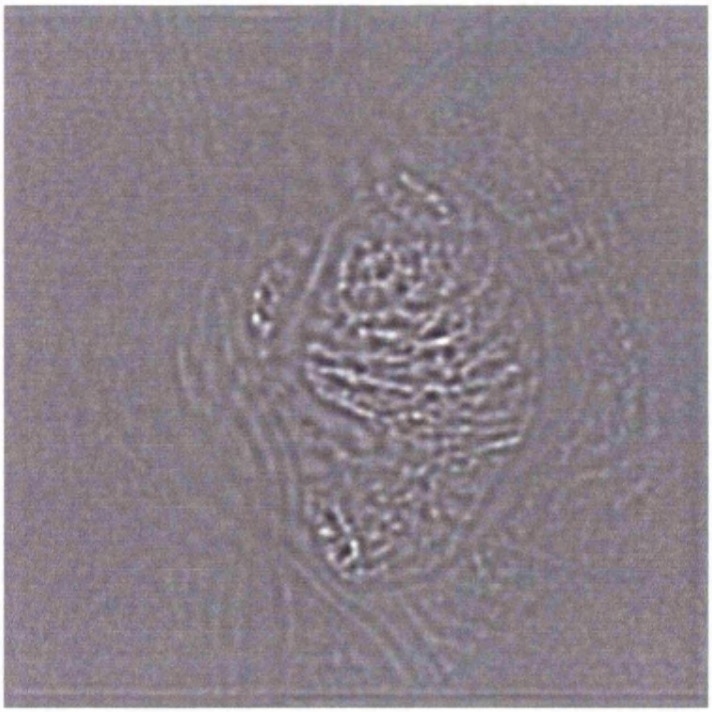

2.23 ii

Inverse transform following FFT filtering of image 2.22 ii.

Figs 2.24: Image Restoration VI-Thresholding the Zeiss images.

The same threshold value was applied to the images overleaf. Again, it appears that more information is present in the image that was deconvolved prior to image processing.

2.24 i

Thresholding of image 2.23 i.

2.24 ii

Thresholding of image 2.23 ii.

Pore sizes seem smaller and in greater number than in above image.

Figs 2.25: Image Restoration VII- Artefacts with Deconvolution.

Although performing a 2D blind deconvolution on the Zeiss image prior to FFT may improve image quality, it was found that in some images it produced an artefact. This was attributed to noise amplification in the deconvolution process.

2.25 i

Averaged Zeiss image.

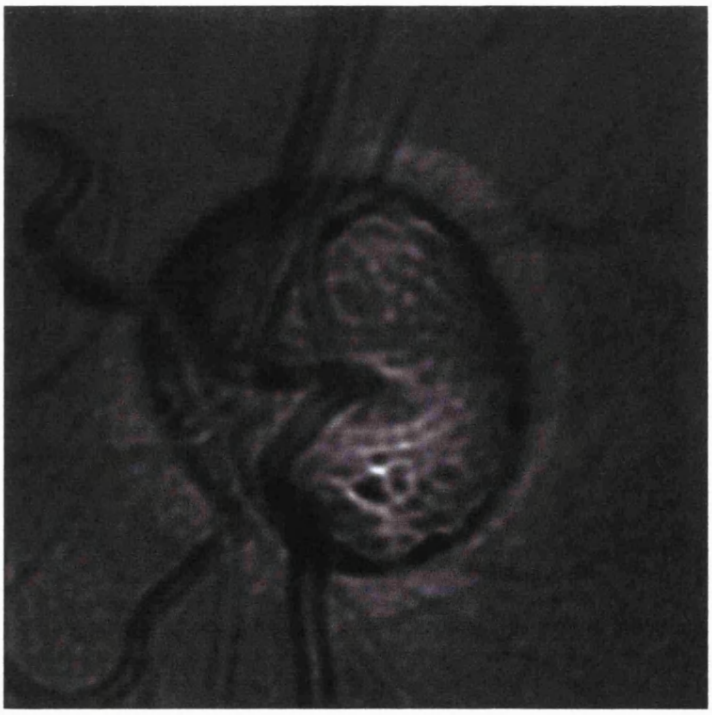

2.25 ii

Above image after blind deconvolution.

Note cup area 'ringing' appearance.

Figs 2.26: Image Restoration VIII-Artefacts with Deconvolution.

Image 2.25 post FFT filtering and inverse transform. The pore detailing on the lower image appears artefactual.

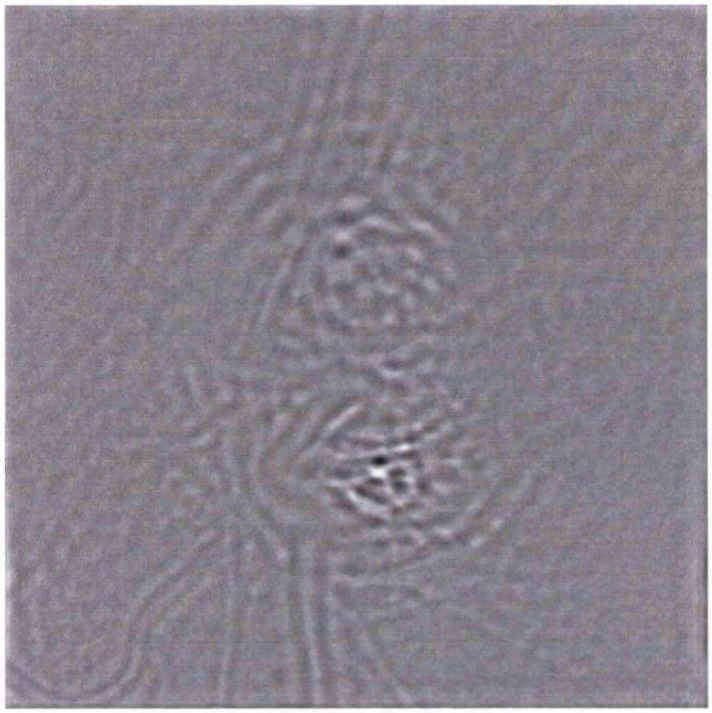

2.26 i

Inverse transform of 2.25 i after FFT filtering.

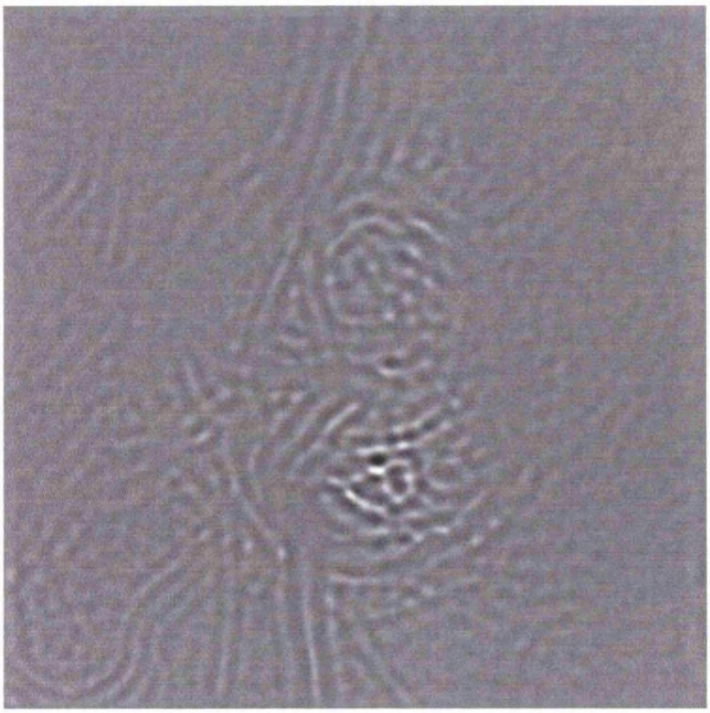

2.26 ii

Inverse transform of 2.25 ii after FFT filtering.

Pore detail appears artefactual, with ringed appearance.

Inspection of the images indicates that 3-D deconvolution of the HRT images does eliminate some out-of-focus blur, and increases the pore visibility following FFT.

For the 2-D deblur operation on the Zeiss images, 2 image examples have been shown. The first example (figs 2.22-2.24) illustrates how well the 2-D deconvolution improves the averaged Zeiss image. However, the second example (figs 2.25-2.26) reveals a slightly different result. Following deconvolution, the lamina pores appear 'ringed' in appearance. This may be as a result of noise amplification in the 2-D processing (D. Biggs, AutoQuant Inc, pers comm.). In view of this, it was decided that the 2-D deconvolution process would not be applied to the Zeiss images as a pre-processing step.

2.1.4.5 Mean luminance of images

Earlier in this section we discussed the procedure of thresholding. A cut off value is chosen to create a binary image which enables image quantification. In order to for comparisons to be made between images, the same threshold value needs to be used per image. A factor to take into account prior to imaging is the overall mean luminance of the image. If there is a slight difference in the mean luminance between images, thresholding at one value will give different amounts of information per image (figures 2.27-2.29).

In order to overcome this, each image (following FFT and filtering) was analysed to measure the histogram profile using Matrox Inspector. A constant was added or subtracted to the image in order to bring the peak of the profile to 128.

Fig 2.27: The effect of mean luminance on thresholding I

In order to make image comparisons, the same threshold value should be applied to each processed image. However, the mean luminance of the processed images is often not the same, and this will lead to differences in the number of pores detected, that is not a function of the eye, but of the image. The following shows how this may be limited.

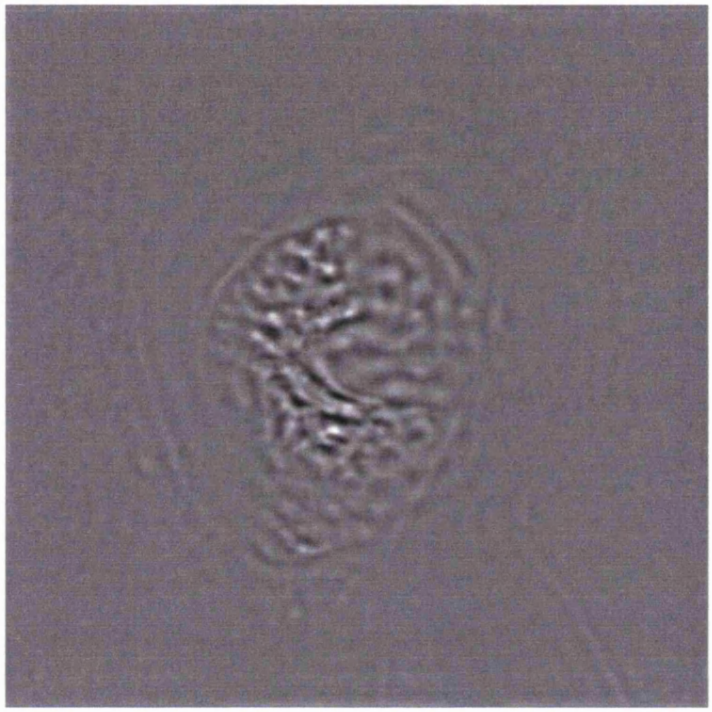

Inverse transform of optic nerve head following Fourier transformation and filtering. The histogram profile below shows the mean luminance of the above image being approx 107.

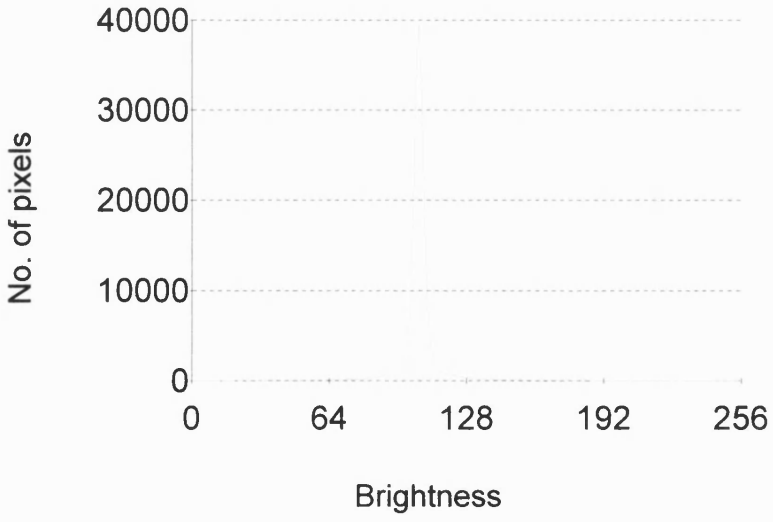

Fig 2.28: The effect of mean luminance on thresholding II

By adding a constant to the image, it is possible to shift the mean luminance. The mean luminance of all images, therefore, will be the same, and so the same threshold value can be used, enabling comparisons of pore information between subjects.

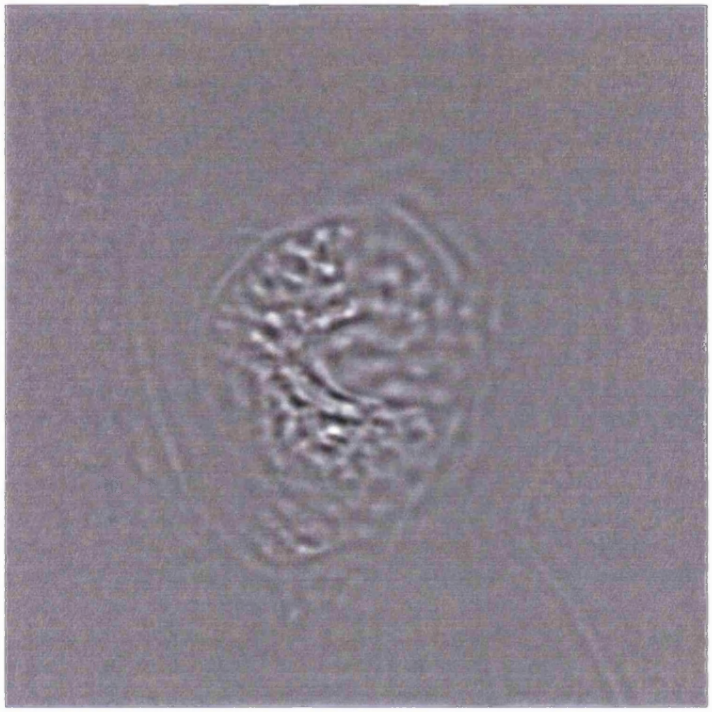

A constant has been added to image 'a' to shift the mean luminance of the image to 128.

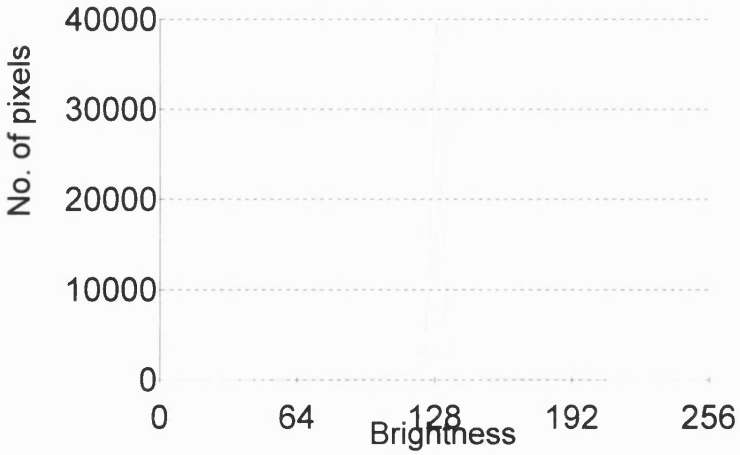

Fig 2.29: The effect of mean luminance on thresholding III

Both images 'a' and 'b' have been thresholded using the same value. The difference is striking. This illustrates the importance of equalising the mean luminance of all the images prior to thresholding.

Fig. 2.29 i

Thresholding of image 2.27. Mean Luminance of image was 107.

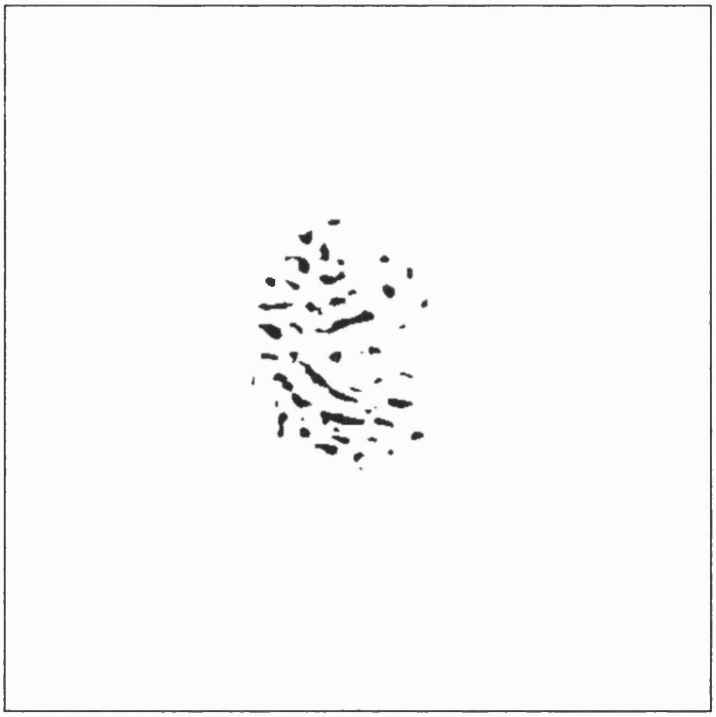

Fig. 2.29 ii

Thresholding of image 2.28. Mean luminance of image shifted to 128.

2.1.4.6 Final Image Processing Steps

The use of the FFT to process the lamina cribrosa images was chosen over the unsharp masking method. In addition, image deconvolution prior to FFT was found to be useful for the HRT images.

Therefore, images were grabbed by the two systems, and underwent the following image processing method:

HRT:

1. 32 images series grabbed by HRT
2. Images converted into individual TIFF files (HRTCONV program, HRT software)
3. TIFF files loaded into Autodeblur (version 7.5 gold, Autoquant Inc, New York, USA) and 3-D blind deconvolution of all 32 images
4. TIFF image of optic disc at the level of the neuroretinal rim chosen
5. Image magnified x2 to increase size to 512 x 512 pixels (for comparison with Zeiss)
6. FFT of said image (Scion Image, NIH shareware)
7. Application of custom-made* annular filter to remove appropriate spatial frequencies
8. Inverse FFT
9. Histogram arithmetic to shift mean intensity
10. Thresholding
11. Blood vessel mask placed over thresholded image
12. Image analysis

Zeiss:

1. Images recorded on videotape
2. 32 frames grabbed, inspected for distortive eye movements, aligned and averaged if clear (Grabber 3, Institute of Ophthalmology)
3. Image scaled to compensate for induced curvature and magnified (section 2.12)

4. Image cropped to 512 x 512 pixels (for FFT)
5. Average image loaded into Scion Image and FFT performed
6. Custom made filter* applied
7. Inverse FFT
8. Histogram arithmetic to shift mean intensity
9. Thresholding
10. Blood vessel mask over thresholded image
11. Image analysis

*The annular filter used to eliminate 'unwanted' spatial frequency information was determined thus: circular filters of progressively increasing size, with their origin at the centre of the transform, were examined to see what spatial frequency information was passed. From this, it was determined what size of circular pass filter contained the most low spatial frequency information, and what size of annulus was required to contain desirable high spatial frequency information- i.e lamina pore information- without inducing artefacts. The same size annulus was used for each subject (see figure 2.1).

Table 2.2: Comparison of image processing methods for HRT and Zeiss cSLO images.

HRT	Zeiss
32 image series through depth of optic nerve head digitally recorded.	Videotape recording of optic nerve head at a single image plane.
Individual images converted into TIFF file format.	32 images digitised, aligned, averaged and saved as TIFF file format.
Blind deconvolution of image series using Autodeblur (vers 7.5, Autoquant Inc.).	Averaged image scaled to compensate for image curvature.
Image at level of optic disc chosen and magnified x2 to increase image size to 512^2 pixels.	Averaged image cropped to 512^2 pixels.
FFT of image using Scion Image Software (NIH software).	As HRT.
Custom filter applied to eliminate low spatial frequency information.	As HRT.
Histogram arithmetic to shift mean intensity.	As HRT.
Thresholding.	As HRT.
Blood vessel mask applied over thresholded image.	As HRT.
Image analysis.	As HRT.

2.1.5 Scanning Laser Ophthalmoscopes II- Laser sources and penetration

2.1.5.1 Imaging the Lamina Cribrosa- Considerations

Anatomical details of fundus structures are more easily seen using monochromatic light, because of the different absorption and reflectance characteristics of the stratified layers of the fundus (Delori and Gragoudas 1976; Delori, Gragoudas et al. 1977; Delori and Pflibsen 1989). When imaging the lamina cribrosa, knowledge of the reflectance and absorption characteristics of the sclera is required, as this area closely resembles the lamina area. However, there are other ocular structures that might affect the amount of light transmitted to the lamina area and the scanning detector are the ocular media, blood vessel walls and stratified layers of the fundus, all of which have been discussed in section 1.2.3.

The aim of this initial study was to see which wavelength of laser light would be best to image the lamina cribrosa.

2.1.5.2 Wavelength of laser light and imaging the lamina cribrosa

The HRT cSLO used in this project has a single laser source of wavelength 670nm, which is capable of imaging retinal structures such as the macula and the optic nerve head. The prototype Zeiss cSLO has two inbuilt lasers, the argon (Ar; wavelength 512 nm) and helium-neon (HeNe; wavelength 632.8 nm) as described in section 2.12. An additional external near infrared (NIR; wavelength 830 nm) laser has been added, for the purpose of microperimetry testing. As it has been reported that longer wavelengths have greater penetration and scatter less (Manivannan, Sharp et al. 1993; Manivannan, Kirkpatrick et al. 1994; Elsner, Burns et al. 1996), we considered that using an 830 nm laser could give better images of the lamina cribrosa due to improved penetration. We wished to determine which of the laser sources best imaged the lamina cribrosa area, and this was investigated in the following.

Materials and Methods

The project was approved by the research ethics committee of Moorfields Eye Hospital, and performed in accordance with the 1964 Declaration of Helsinki. Two subjects were consented and had one eye dilated with guttae tropicamide 0.5%. Images of the optic nerve head were taken with the Zeiss cSLO at three wavelengths using the HeNe, Ar and NIR laser sources.

Images were recorded onto videotape and then digitised with custom-made digitisation software (Halfyard, Wade et al. 1999). The software enables individual inspection of digitised frames, for increased quality control. Frames were discarded if the optic disc appeared distorted (due to saccadic eye movements) or if the subject blinked.

To reduce noise in the images, 32 good quality consecutive frames were aligned and averaged. Digitisation, alignment and averaging of video frames were performed using purpose written software (Wade and Fitzke 1998, Wade, 1999 #619).

Scion Image software (National Institute of Health, Maryland, USA) was used to generate the FFT of the averaged image, and a custom made filter was designed to filter out the unwanted spatial frequency information from the image. The filtered FFT was then inversely transformed to recreate a new 2-dimensional image with only high spatial frequency information within it. Section 2.3 details the image processing technique. Details of pore structure were extracted from this final, filtered image.

Image quality-variance

When assessing images, it is desirable to find the 'best ' image of a series. This is often a qualitative measure of image quality. However, we wished to develop a method that would give a quantitative measure of image quality.

In statistical analyses, the variance of a set of data is a measure of the spread of data. It is given by the formula

$$\frac{\sum (x - \bar{x})^2}{N - 1}$$

Where x is the individual sample score, $\boldsymbol{x}$ is the mean score of all the samples, and N is the number of samples in the data set.

Digitised images are a series of pixels with varying grey values. It is therefore possible to measure the variance of an image by looking at the spread of these grey values.

Once the optic disc images have been processed, the lamina pores appear dark grey to black, and the lamina beams appear light grey to white. If an image has a large number of pores visible, the variance will be high as there will be pixels that fall within the pore area, thus having low intensity, and pixels falling within the cribrosal beam area, thus having a greater intensity. More pores means a greater spread of intensity values. In the above equation, x will be the individual intensity of each pixel, x will be the mean pixel value in the data set, and N the number of pixels in the data set.

A measure of image quality was required to determine which of the wavelengths of laser enabled the greatest lamina structure visualization. Therefore, the variance of the optic disc area of the processed lamina pore images was used as a measure of image quality, with the hypothesis that the greater the variance, the more lamina pores visible. The use of variance in digital image analysis has been used before in the estimation of signal to noise ratio (Wade 1998).

A purpose written program with use in Matlab (vers 6.0, MathWorks Inc., USA) was used to measure the variance of the optic disc area of each image (author A.S Halfyard: Appendix III).

Results

The results are shown in figures 2.30- 2.35. Images 2.30-2.32 are of a young subject, and 2.33-2.35 of an older subject. The variance levels of the images of the young subject were quite similar, whereas those of the older subject showed slightly greater differences between the wavelengths.

Figure 2.30: Imaging with different wavelengths I.

Near Infrared Wavelength 830 nm

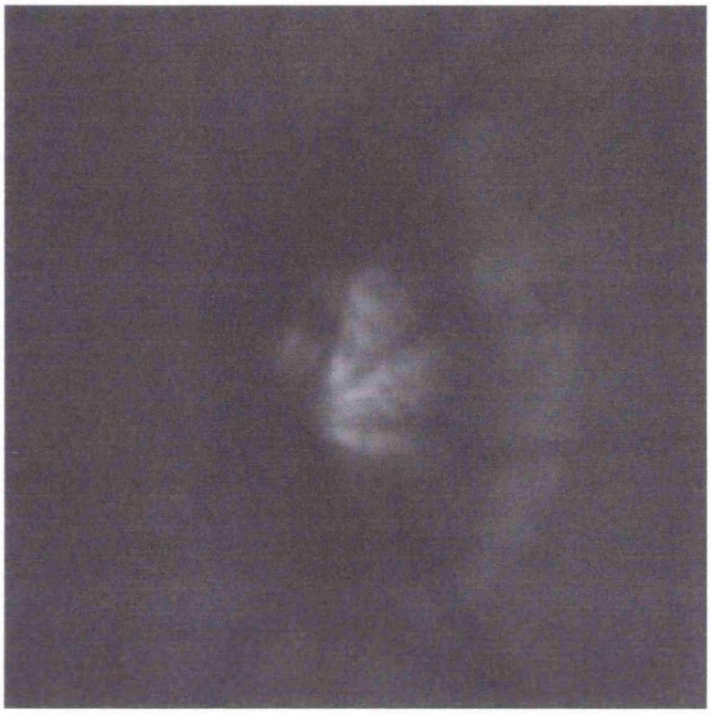

2.30 i

Averaged Image (young subject)

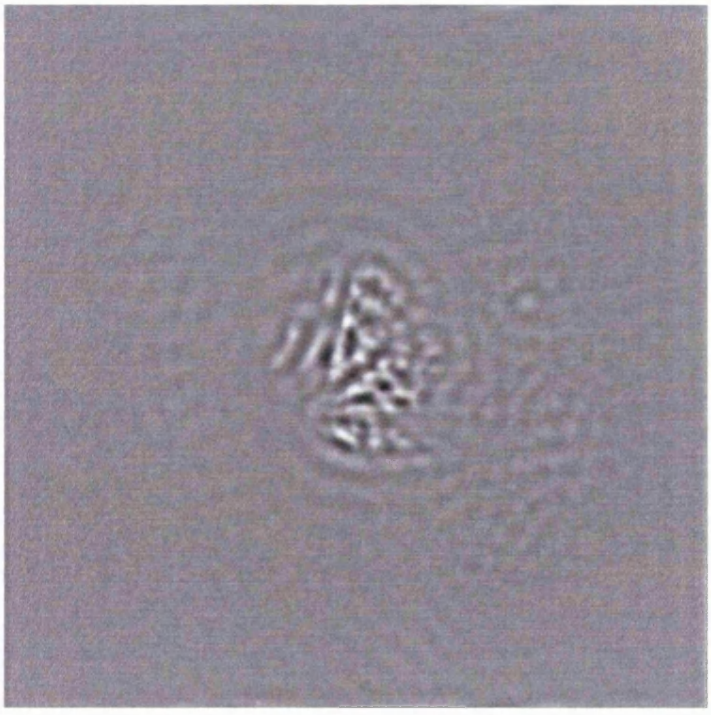

2.30 ii

Processed Image

(FFT and filtering)

Variance 285

Figure 2.31: Imaging with different wavelengths II.

Helium Neon Wavelength 632.8 nm

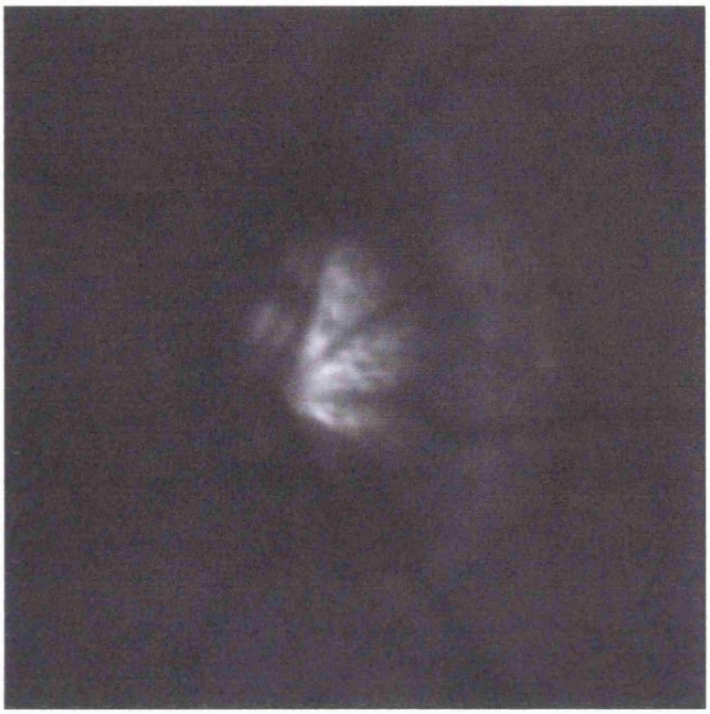

2.31 i

Averaged Image

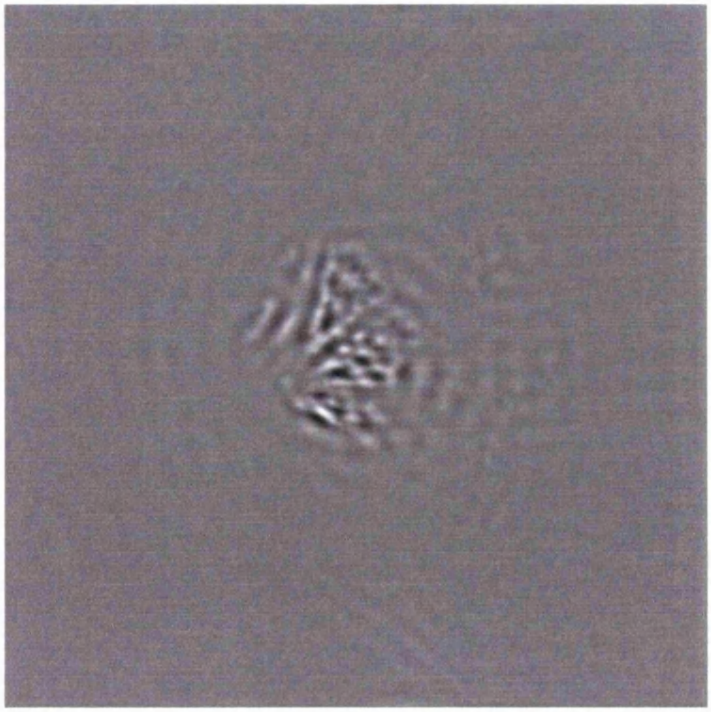

2.31 ii

Processed Image

(FFT and filtering)

Variance 280

Figure 2.32: Imaging with different wavelengths III.

Argon Wavelength 512 nm

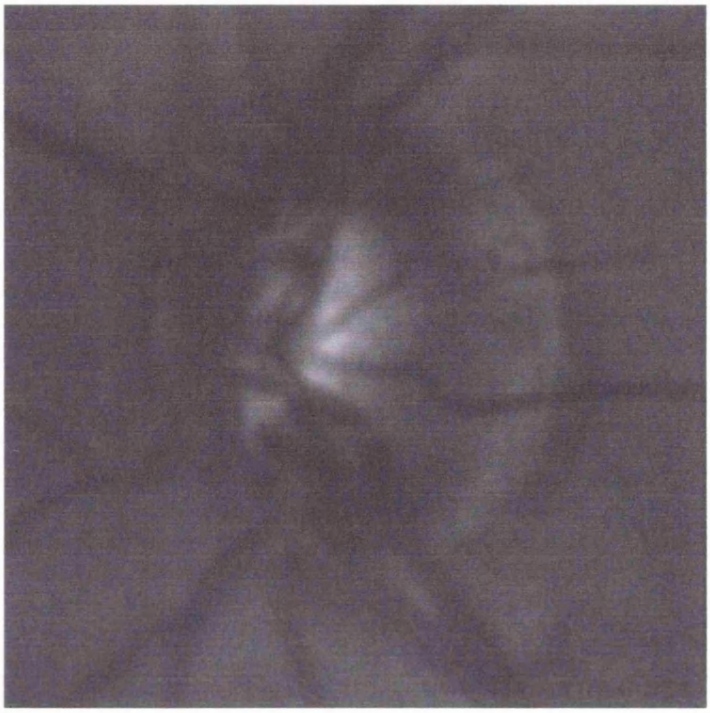

2.32 i

Averaged Image

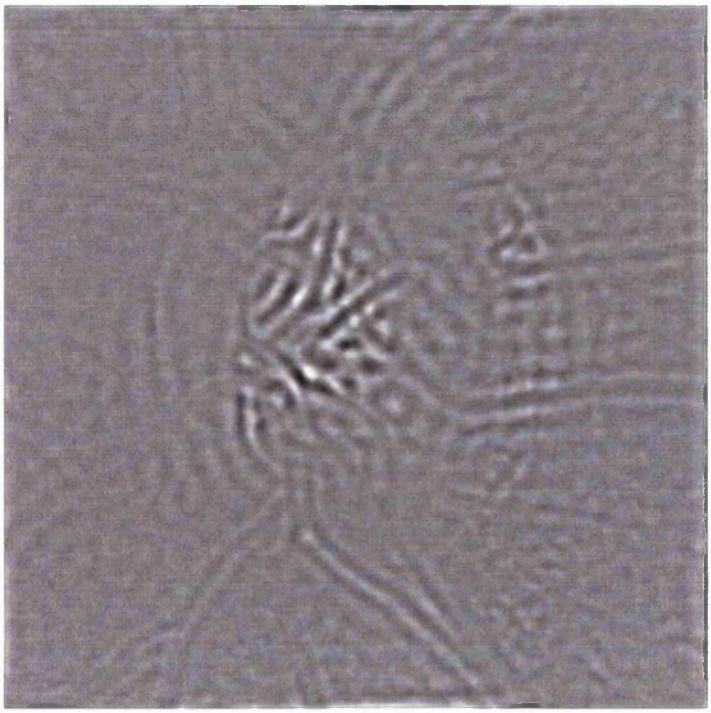

2.32 ii

Processed Image

(FFT and filtering)

Variance 300

Fig 2.33: Imaging with different wavelengths IV.

Near Infrared Wavelength 820 nm

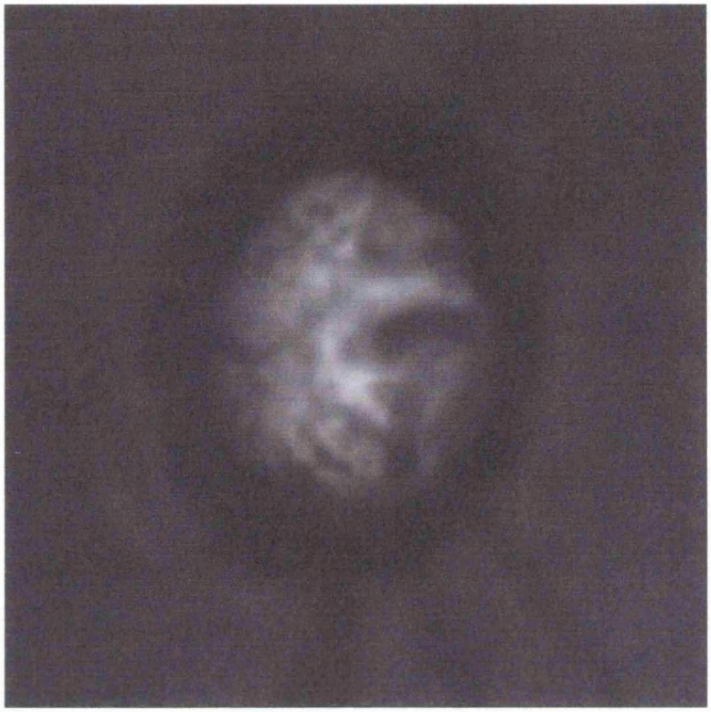

2.33 i

Averaged Image

(older subject)

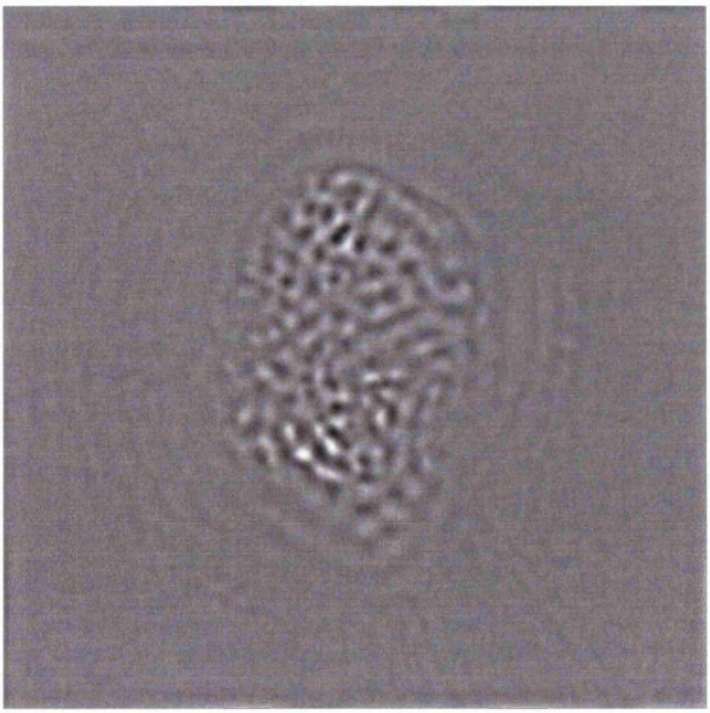

2.33 ii

Processed Image

(FFT and filtering)

Variance 250

Fig 2.34: Imaging with different wavelengths V.

Helium Neon Wavelength 632.8 nm

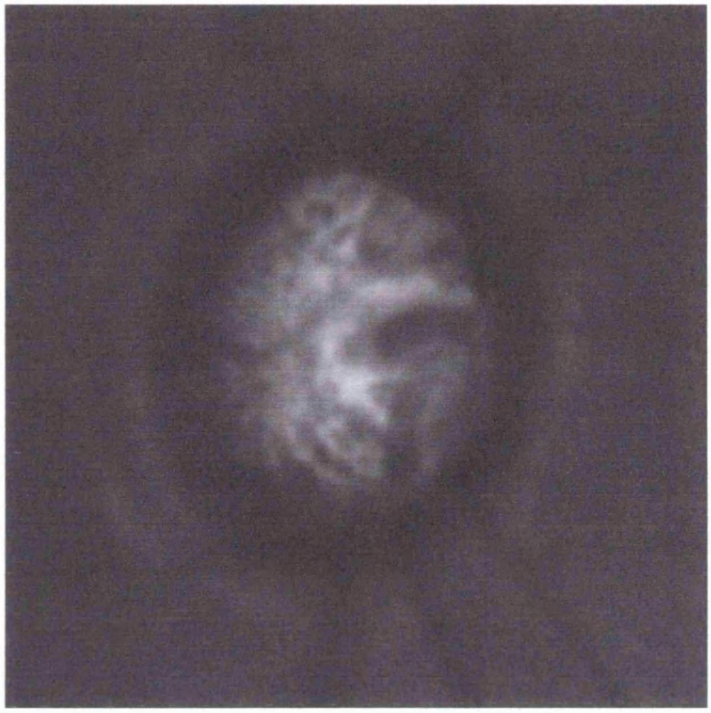

2.34 i

Averaged Image

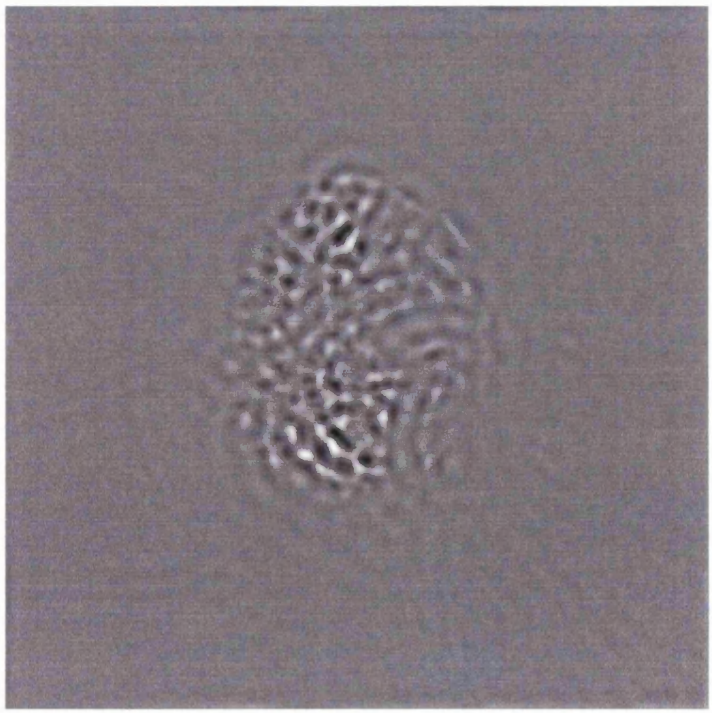

2.34 ii

Processed Image

(FFT and filtering)

Variance 335

Fig 2.35: Imaging with different wavelengths VI

Argon Wavelength 512 nm

2.35 i

Averaged Image

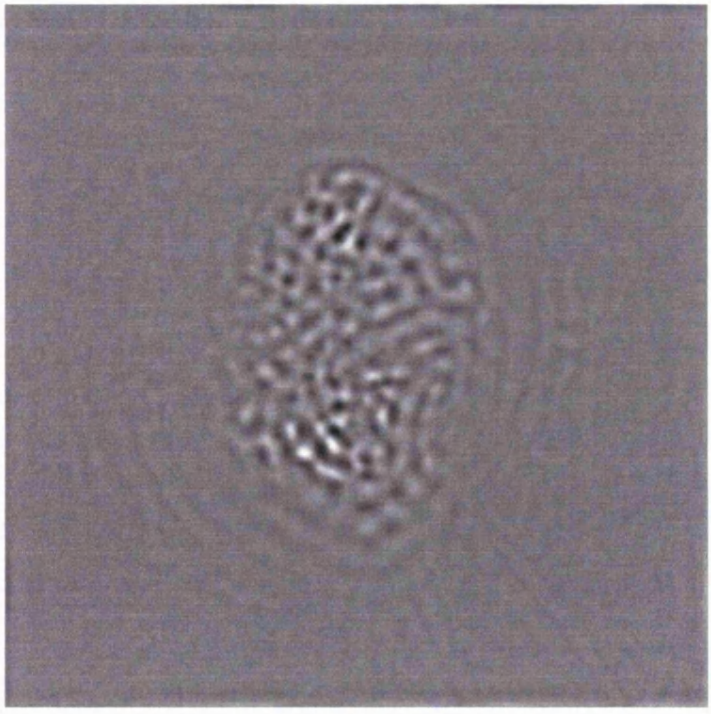

2.35 ii

Processed Image

(FFT and filtering)

Variance 290

Table 2.3: Variance measures of processed optic disc images for the different wavelengths of lasers used.

Wavelength of laser (nm)	Variance	
	Young subject	Older subject
830	285	250
632.8	280	335
512	300	290

Discussion

The images of the young subject did not show a large difference in variance measurements. This may be because the cup area was small and therefore many lamina pores were not visible. In addition, the blood vasculature prominence over the cup area may affect the pore visualisation. In the Ar image, which had the greatest variance, the blood vessels were most obvious, and following FFT processing, the blood vessel walls appear 'pore-like'. These would be masked during image analysis (section 2.1.4.6), but this was not done in this evaluation study, as the images were not required for pore quantification.
The images of the older subject showed that the HeNe source gave the most pore detail (HeNe variance 335, Ar 290). A potential problem using the Ar would be absorption of the light by lens opacities. Ar light is of short wavelength, and yellowing lens opacities such as those developed with nuclear sclerosis cataract would absorb a certain amount of light on entering and leaving the eye. (Lerman and Borkman 1976). This would be of great significance when imaging older eyes. In addition to the absorption by the ocular media, it has been shown that the oxyhaemoglobin component of the blood absorbs short to mid wavelengths. As the central retinal vein and artery exit and enter the eye at the optic nerve head, this absorption characteristic would make visibility of the optic cup – and therefore lamina- difficult with Ar light.

NIR light is reflected from the fundus to a greater extent than visible light and so allows lower illumination levels. Furthermore, because it is of a longer wavelength, its transmission through the eye would be relatively unaffected by the ocular media, and it should penetrate deeper into the fundus. (Manivannan, Sharp et al. 1993; Manivannan, Kirkpatrick et al. 1994; Elsner, Burns et al. 1996). Inspection of the original averaged images revealed the NIR image to appear slightly 'blurred' when compared with the HeNe and Ar images. Image processing did not show up any pore structure beneath the overlying neural tissue and the sides of the optic disc. Two reasons can explain this finding. The size of the output beam leaving the laser unit is known as the waist diameter. The waist diameter of the HeNe laser is 10 microns, the NIR 60 microns. The NIR waist diameter is somewhat larger than the HeNe as it is was added to the cSLO for microperimetry testing, not for imaging. The effect of a larger waist diameter is that the spot size on the retina will be larger. This will result in a slightly degraded lateral resolution, which would explain why the HeNe image seemed to show more detail than the NIR. Secondly, the irregular arrangement of the nerve fibres in the neuroretinal rim means that there will be a significant amount of scattering of light, both incident and reflected, and this would severely reduce the visibility of the lamina pores underlying the rim.

From this study it was concluded that imagining the lamina cribrosa with the HeNe laser source would give better information of the area when compared with the other imaging sources.

Chapter 3: In vivo imaging of the lamina cribrosa

3.1 Image acquisition with the HRT and the Zeiss

3.1.1 Introduction

Chapter 2 described the various image processing techniques that are available for lamina pore visualisation.

For this project, two cSLO instruments were available to acquire lamina cribrosa images- the Heidelberg Retina Tomograph (HRT) and the Zeiss cSLO. We have seen from chapter 2 that the two instruments differ fundamentally in their image grabbing techniques, and the methods of processing the images obtained with each are quite different initially (table 2.2). The purpose of this study was to compare and contrast the images obtained with each instrument with view to establishing the more appropriate method for measuring lamina pore morphology.

3.1.2 Materials and Methods

3.1.2.1 Image Acquisition

In vivo images of the lamina cribrosa were obtained using the Heidelberg Retina Tomograph (HRT, Heidelberg Engineering, Germany) and the prototype Zeiss cSLO (Carl Zeiss, Oberkochen, Germany).

HRT images were acquired using the 15 degree field of view setting. Images were acquired as set out in the HRT manual (Manual 1997) - refractive error and depth settings were set as instructed by the HRT software. The HRT software (version 2.01) has a quality control mechanism that informs the operator whether the images obtained meet the criteria set in the software. A good image set will display a gaussian-like curve of brightness values through the 32 images series, so that the topography of the optic nerve head under investigation is accurately plotted. The HRT displays a comment if the image series is deemed to be of good quality, but the series still has to be inspected for eye movements. Image series with eye movements that caused a distortion in the appearance of the optic disc were discarded.

Image acquisition with the Zeiss cSLO used the HeNe laser light source, with confocal stop size 3 and a 20 degree field of view. The focus setting was placed at the level of sharpest focus of the centre of the optic cup. Images were recorded onto videotape and then digitised with custom-made digitisation software (Halfyard, Wade et al. 1999) as detailed in section 2.1.1.2.
Images obtained with both instruments were scaled to compensate for image distortions (Zeiss) and magnified to achieve correct image size for Fast Fourier Transformation (Zeiss and HRT) as detailed in section 2.1.

3.1.2.2 Image Processing – HRT images

Image series obtained with the HRT were aligned using HRT version 2.01 software, and then converted to individual TIFF format images using the HRTCONV program that is available with the HRT software. The thirty-two individual tiff files underwent a blind deconvolution using AutoDeblur software (version beta 7.5, AutoQuant Imaging Inc., NY, USA). The blind deconvolution served to eliminate the out of focus blur as detailed in section 2.1.4.4.
The result of applying the blind deconvolution is a series of 32 images that have a greater degree of resolution at each section depth. The sections that are of interest in this project are those that are at the depth of the lamina pores. Settings for depth of scan ranged between 2.5mm to 4mm in 0.5 mm steps. Thirty-two optical sections were obtained for each depth setting, giving spacing of between 78 and 125 microns per optical section. In order to make comparisons with the Zeiss images, the optical section that was focused at the level of the neuroretinal rim was used in the analysis. Deconvolved images were taken into Scion Image software (National Institute of Health, Maryland, USA). As with the Zeiss images, FFT's were generated for the HRT images and custom made filters were applied.

3.1.2.3 Image Processing – Zeiss cSLO

Scion Image software (National Institute of Health, Maryland, USA; shareware) was used to generate the FFT of the averaged lamina image, and a custom

made filter was designed to filter out the unwanted spatial frequency information from the image, as detailed in section 2.1.4.3.

3.1.2.4 Image Quality Measurement: Variance

In order to determine which of the instruments gave the most information about the lamina area, the variance of the intensity of each pixel within the optic disc area of the images was measured. The use of pixel variance in assessing image quality has been described in section 2.1.5. For these images, only the variance within the optic disc area was assessed. However, the brightness of the images varies from image to image, depending on the instrument used as well as the individual subject (e.g. due to lens opacities), and, in addition the optic disc occupies different areas in the HRT and Zeiss images. These differences would certainly affect the 'spread' of intensity values in both the HRT and Zeiss images, thus causing a difference in the variance measure that would not be due to pore detail detected alone.

The use of the 'histogram arithmetic' function in the image processing technique described earlier (section 2.1.4.6) would help counteract the effect of the difference in brightness, or luminance, of the images. All the processed images are shifted so that they have a mean luminance of 128, thus eliminating the influence of brightness difference on the spread of intensity values.

The variance formula uses the number of pixels in the data set in its calculation. As the optic disc occupies a smaller area in the HRT image compared with the Zeiss image, the number of pixels measured in these two images will be different for each subject (figure 3.1). This will therefore affect the variance measure. A method of overcoming this would be to count the number of pixels in each data set, and take a ratio of the variance/number of pixels. This ratio was termed 'variance per pixel' (VPP)- a misnomer, because in fact there would be no such thing as variance per pixel *per se*. However, for the purpose of this thesis, it was felt that the term was suitable.

Figure 3.1: Optic Disc area within Zeiss and HRT images

The optic disc occupies a smaller area in the HRT image compared with the Zeiss. When measuring the variance, only the area of the optic disc is assessed. Therefore, there will be fewer pixels in the HRT image than in the Zeiss image, and this will affect the variance measures.

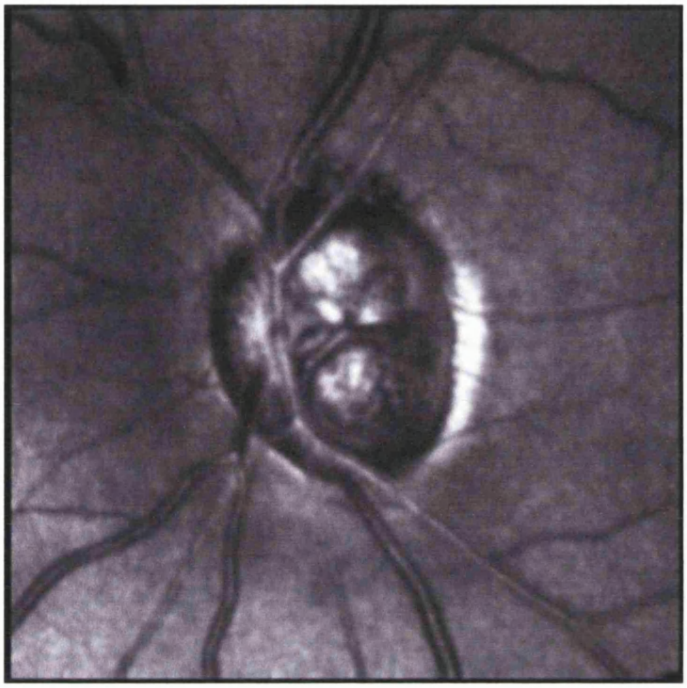

Image of optic disc taken with HRT.

Image of optic disc taken with Zeiss.

3.1.2.5 Lamina Pore Quantification

Matrox Inspector Software (version 2.1, Matrox Electronic Systems Ltd, Quebec) was used in the analysis of the final, filtered, lamina images. Images were thresholded, as described in section 2.1, and the same threshold value was used for all images. Matrox Inspector has a' blob analysis' function that quantifies the features within an image. Blob analysis allows the identification of connected regions of pixels (known as 'blobs') within a greyscale image. The value of the pixels to be classified as 'blobs' is set by the user, and in the binary images in this study the 'blobs' are be set as being black pixel regions, which represent the lamina pores. The 'blob analysis' feature gives information about the structure of the pore, and for this study the parameters 'blob area' (lamina pore area in microns^2) and the number of 'blobs' found were recorded.

3.1.2.6 Initial Study -Subjects

The project was approved by the research ethics committee of Moorfields Eye Hospital, and performed in accordance with the 1964 Declaration of Helsinki. Fifteen subjects were recruited from the ongoing Medical Research Council 5-Fluorouracil trial currently running at Moorfields Eye Hospital. All subjects were given informed consent and the only criteria for entry into the study was that they were at least 1 year post-trabeculectomy, so that post-op corneal curvature changes would have stabilised (Hugkulstone 1991; Cunliffe, Dapling et al. 1992; Claridge, Galbraith et al. 1995).
Subjects were refracted, had corneal curvature measurements using keratometry, and then imaged with the HRT and the Zeiss.

3.1.3 Results

Tables 3.1 and 3.2 detail the findings for each subject.
The pixel variance was used to quantify the image quality, and the VPP ratio was used as an attempt to counteract the effect that a difference in the number of pixels within the optic disc area of the HRT and Zeiss images would have. The VPP was significantly less in the HRT images compared with the Zeiss (student

t-test $p < 0.0001$). This implies that there was more variance of pixel values in the Zeiss images, which in turn suggests that more detail was present in the Zeiss images.

The average number of pores found with the HRT was 27, compared with 39 for the Zeiss, and this difference was statistically significant to the $p<0.01$ level. This would follow from the difference in the VPP measured- the Zeiss images have a greater pixel variance, indicating that possibly more pores were detectable. For 10 of the subjects imaged, a greater number of pores were detected using the Zeiss cSLO, compared with the HRT. Only in 1 subject were more pores detected by the HRT- for the other 4, the number of pores detected by both instruments were virtually equal.

Average pore area (the total pore area of the lamina cribrosa divided by the number of pores found) with the HRT was 1673.5 microns^2 and with the Zeiss 1949.2 microns^2, and this was statistically significant to the $p<0.05$ level. For 10 of the subjects, the average pore area was larger when using the Zeiss cSLO to image the lamina area.

Table 3.1: Comparison of pore details found with HRT and Zeiss cSLO's.

Subject	VPP HRT	VPP Zeiss	Pore Number HRT	Pore Number Zeiss	Ave Pore Area HRT (μ^2)	Ave Pore Area Zeiss (μ^2)
1	0.009	0.009	32	31	1098.8	1782.3
2	0.003	0.018	17	11	1681.3	1292.8
3	0.004	0.015	21	19	1141.9	1224.8
4	0.018	0.031	13	16	1963.1	3217.2
5	0.001	0.018	60	72	2355.8	2363.2
6	0.010	0.032	10	25	1766.7	1922.6
7	0.005	0.018	23	49	1363.9	1693.6
8	0.007	0.012	62	82	1889.7	2163.7
9	0.009	0.011	27	23	1283.0	2040.7
10	0.007	0.011	26	75	2530.2	2338.9
11	0.006	0.006	13	43	2741.9	2296.6
12	0.010	0.019	29	45	1132.0	1469.9
13	0.016	0.024	13	39	1601.0	1653.4
14	0.007	0.012	26	25	1093.1	1828.7
15	0.008	0.015	26	32	1459.1	1949.8
Ave	0.008	0.017	27	39	1673.5	1949.2

Student T-Test	P value	Student T-Test	P value	Student T-Test	P value
Variance	0.0001	Pore number	0.007	Pore area	0.036

Key: VPP = Variance per pixel, Ave = Average

The Zeiss results were greater than the HRT for all 3 parameters, and this was significant at the $p<0.05$ level.

3.1.4 Discussion

As discussed in section 2.1.5.4, the reason for using variance as a measure of image quality was because an image with a large variance indicated a large spread in the pixel values. Processed lamina cribrosa images will show the lamina pores to be dark grey/black and the collagen beams around them light grey/ white. The more pores in the image would result in a large spread of pixel values, thereby giving a large variance measure. As described earlier, the use of the ratio of 'variance per pixel' (VPP) was designed to counteract the effect of the differing number of pixels per optic disc area between the two imaging systems. The Zeiss images had an average VPP of 0.017, which was double that of the HRT, which had a VPP of 0.008. Therefore, it appears that the Zeiss cSLO gives a more detailed image of the lamina cribrosa, and therefore the pore structure, compared with the HRT. An explanation for this finding could be in the resolution. Although the axial resolution of the two instruments is quite similar (HRT 300 microns, Zeiss 340 microns), the lateral resolution is quite different. The HRT has a resolution of 256 x 256 pixels, whilst the Zeiss has 768 x 576 pixels. It would be fair to assume that greater pixel resolution in the initial image capture would lead to an improved quality of images- more pixels assigned per image area will lead to greater definition in that area. Another possible explanation for the difference in lamina cribrosa visibility is the difference in the level of focus. The Zeiss has a manual control, so that only optic disc images that appeared in focus at the level of the centre of the cup were grabbed. The HRT system grabs thirty-two images through the depth of the optic nerve head. As mentioned in the section 3.1.2.2, the spacing between the 32 image sections varies between 78 and 125 microns. The HRT images that were chosen for analysis were those sections that were focused *closest* to those grabbed with the Zeiss. It is likely that the HRT images chosen for comparison with the Zeiss were not focussed at exactly the same level. When dealing with images of an area as small as the lamina cribrosa, slight differences in focusing levels will have great effects on lamina resolution.
One would expect that if the Zeiss images were of a superior quality compared with the HRT, the number of pores detected would be greater in the Zeiss

images, and this appeared to be the case. Another interesting result was the difference in average pore area. The average pore area was greater in the Zeiss than in the HRT images. This may be because there were more pores detected in the Zeiss images, some of which may be larger, thereby shifting the overall average. But there is also a possibility that the pore sizes measured were not accurate due to the final stage in the image processing method. As described in section 2.1.4.2, thresholding classifies pixels within the image as either part of the foreground or background. The pixel range within the inverse transform images is quite limited, and this means that many pixels within a pore boundary line may be set as being part of the background during the thresholding operation. Therefore, pores that are adjacent to each other with fine boundaries may be counted as one single, large pore (Figure 3.2). This would result in pore areas being measured somewhat larger. To test this hypothesis, a second study was performed, and this is described in the following chapter.

Figure 3.2: Sources of error with automated thresholding

The figure below illustrates how the use of automated thresholding may miss subtle boundaries between pores, resulting in fewer and larger pores detected.

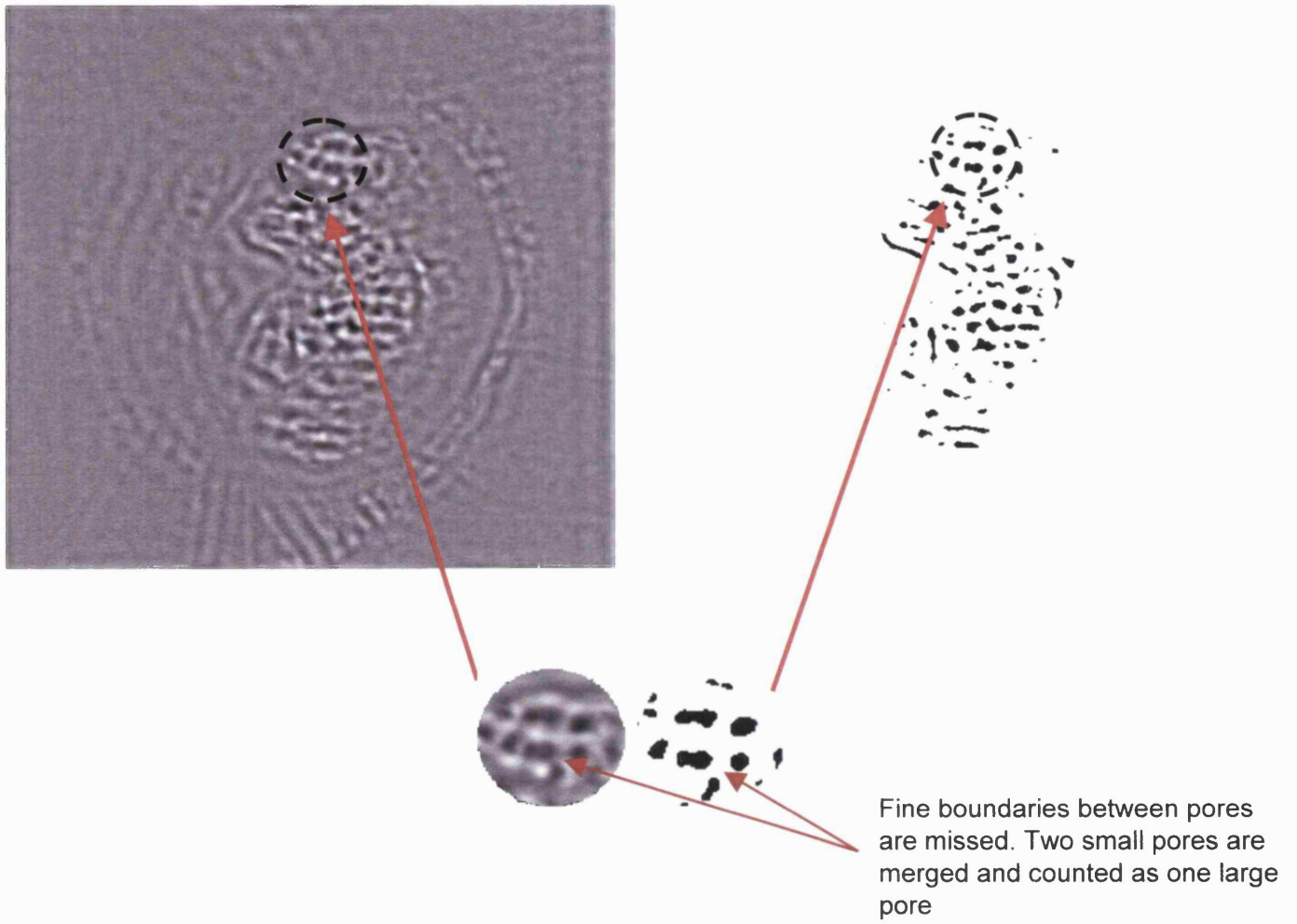

Chapter 4: In vivo imaging II- Pore Quantification techniques

4.1 Automated versus manual thresholding

4.1.1 Introduction

Section 2.1.4.2 detailed the final step in the image processing techniques to prepare an image for quantification. Thresholding an image has the precondition that similar features within an image will have similar grey values, and therefore by setting a threshold value, the features will be identifiable.

Difficulties arise in imaging three-dimensional structures such as the optic nerve head. With a bowed lamina cribrosa, only the surface pores in the focal plane of the imaging unit will be in focus, and those lying posterior to it will be out-of-focus. Pores that are out of focus will have different grey values to those in focus, even though they may all be on the anterior surface of the optic cup. In addition, as seen in figure 3.2, very fine boundaries between pores will have different grey values compared to the more distinct pore boundaries. Therefore, when a threshold value is set, some pores may be 'missed' and become part of the background in the thresholding process.

A 'gold standard' method to pick up all pore information within an image would be to manually draw around each pore in each image.

The previous study attempted to find which cSLO gave the most lamina pore information. In this second study, the images obtained underwent the normal automated thresholding technique and blob analysis function, but also had a manual outlining of pores from the processed images.

4.1.2 Materials and Methods

The processed images obtained from the previous study (chapter 3) were analysed in PaintShop Pro version 6.0 (Jasc Software, Inc, USA). Images were magnified 5 times their original size, and using the freehand tool, each pore was manually outlined using a drawing tablet and pen (Wacom graphire USB). These were saved as 'image masks' and taken into Matrox Inspector for blob analysis.

The number of pores found, pore area and elongation were recorded for the Zeiss and HRT images found with the automated thresholding technique and the manual drawing technique.

4.1.3 Results

4.1.3.1 Automated thresholding versus manual-draw methods for quantifying pores

The number of pores counted using the manual technique compared with the automated thresholding technique found with the HRT and the Zeiss is detailed in tables 4.1 and 4.2.

More pores were detected using the manual drawing method (HRT average count 59, Zeiss 83) compared with the automated method (HRT average 27, Zeiss 39). This was found to be significant at the $p<0.001$ level. The average pore area was found to be smaller using the manual draw method (HRT average 982.8 microns^2, Zeiss 1600.2 microns^2) compared with the automated method (HRT average 1673.4 microns^2, Zeiss 1949.2 microns^2).

Bland-Altman charts were plotted to illustrate the difference in the two techniques (figures 4.1- 4.3). These charts are useful when assessing the agreement between two methods of measurement (Bland and Altman 1986). The difference between the measurements found by the 2 methods is plotted against the average reading of the two methods. If the methods are in agreement, the difference between them will be close to zero for all the averaged readings. From the Bland-Altman plots shown, it can be seen that pore quantification using the manual technique was in poor agreement with the automated technique. As the average number of pores increased, the difference between the 2 instruments became more pronounced. Similar relationships were found with average pore area and elongation measurements. The larger the mean of the two methods of measuring these parameters, the greater the difference between the methods. The slope of the line-of-best-fit for the data is shown below the plots. For all pore parameters (number, average area and elongation) the value of the slope is

close to ± 1. This indicates that there is a direct relationship between the two methods of measuring pore parameters, rather than just a random difference between them. The larger the value of the pore parameter, the larger the difference between the two measurement techniques.

Table 4.1: Comparison of pore details found by automated thresholding (AT) method and by manual drawing (MD) for HRT cSLO.

Subject	No. of Pores-AT	No. of Pores-MD	Ave Pore Area μ^2- AT	Ave Pore Area μ^2- MD	Pore Elongation AT	Pore Elongation MD
1	32	52	1098.8	921.2	3.9	2.1
2	17	46	1681.3	1237.7	3.6	2.5
3	21	57	1141.9	1008.7	2.9	2.1
4	13	32	1963.1	1205.8	2.5	2.3
5	60	97	2355.8	1124.3	4.5	2.4
6	10	32	1766.7	817.6	4.5	1.8
7	23	61	1363.9	1001.3	3.0	2.0
8	62	90	1889.7	1162.4	3.2	2.3
9	27	45	1283.0	1062.7	3.5	2.0
10	26	71	2530.2	999.8	3.9	2.2
11	13	45	2741.9	973.3	4.4	1.9
12	29	92	1131.9	861.5	3.3	2.3
13	13	20	1601.0	806.7	4.7	2.9
14	26	70	1093.0	767.3	4.0	1.9
15	26	77	1459.1	790.9	3.4	1.9
Ave	27	59	1673.4	982.8	3.7	2.2

Student T-Test	P value	Student T-Test	P value	Student T-Test	P value
Pore number	0.0001	Pore area	0.0001	Elongation	0.0001

Significantly more pores, larger pores and pores with greater elongation were found with the manual draw method of pore quantification compared with the automated method.

Table 4.2: Comparison of pore details found by automated thresholding (AT) method and by manual drawing (MD) for Zeiss cSLO

Subject	No. of Pores-AT	No. of Pores-MD	Ave Pore Area μ^2-AT	Ave Pore Area μ^2-MD	Pore elongation-AT	Pore elongation-MD
1	31	72	1782.4	1560.6	3.1	2.5
2	11	59	1292.8	1225.6	3.0	2.4
3	19	33	1224.8	1720.0	4.1	2.6
4	16	15	3217.2	2961.0	3.6	2.6
5	72	121	2363.2	1578.4	4.0	2
6	25	38	1922.6	1825.5	2.6	1.7
7	49	153	1693.6	1311.8	5.6	2.2
8	82	117	2163.7	1597.7	2.9	2.2
9	23	41	2040.7	1591.2	3.5	2.7
10	75	120	2338.9	1932.5	4.5	2.4
11	43	119	2296.6	1614.7	3.5	2.4
12	45	122	1469.9	1220.4	3.0	2.3
13	39	41	1653.4	1298.6	10.2	4.4
14	25	77	1828.7	1490.4	2.9	2.4
15	32	110	1949.8	1074.9	3.5	2.1
Ave	39	83	1949.2	1600.2	4.0	2.5

Student T-Test	P value	Student T-Test	P value	Student T-Test	P value
Pore number	0.0001	Pore area	0.001	Elongation	0.001

As with the HRT results on the previous page, the pore parameter measurements were significantly greater when using the manual draw method of pore quantification in the Zeiss images.

Figure 4.1: Bland- Altman plot for pore number measurements

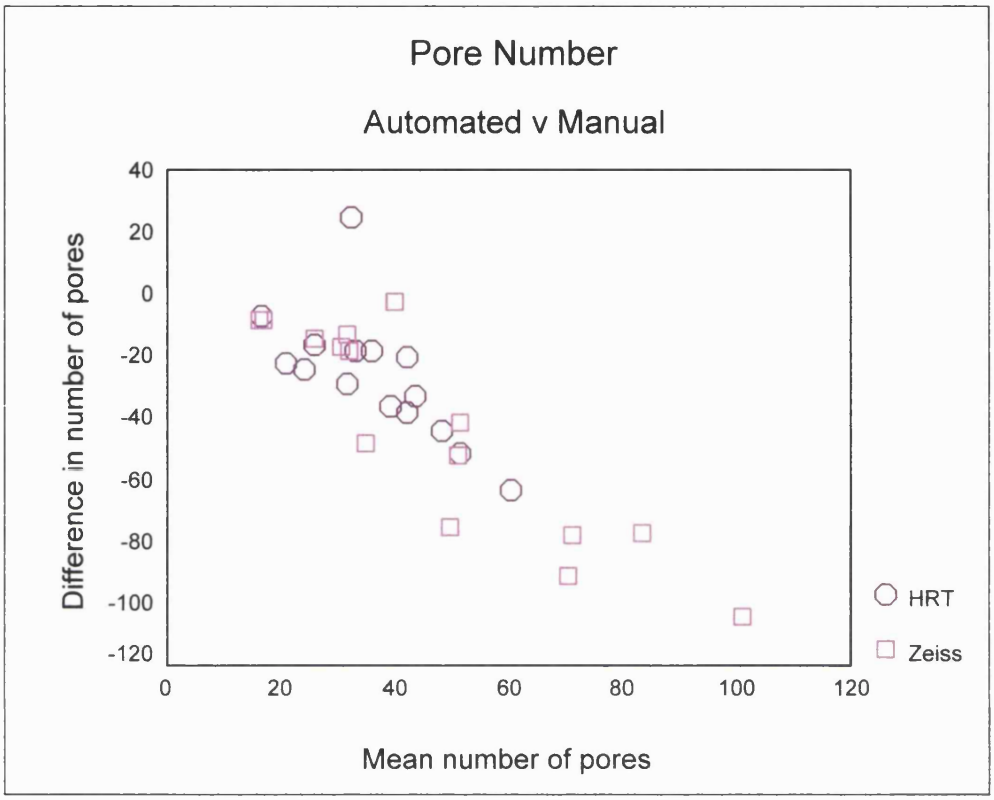

Slope values: *HRT: y= -1.2x* $R^2 = 0.48$ *p<0.01*

Zeiss: y= -1.3x $R^2 = 0.81$ *p<0.001*

Plot to assess the agreement between the automated-thresholding and manual-drawing (AT and MD) techniques of measuring the number of pores. Results for both the HRT and the Zeiss are shown. Plots indicate that there is poor agreement between the two methods for both cSLO's. As the mean number of pores measured by the 2 methods increases, the difference between the measures increase. For both instruments, the trend is statistically significant. As the overall number of pores increases, fewer pores are detected using the AT technique.

Figure 4.2: Bland- Altman plot for pore area measurements

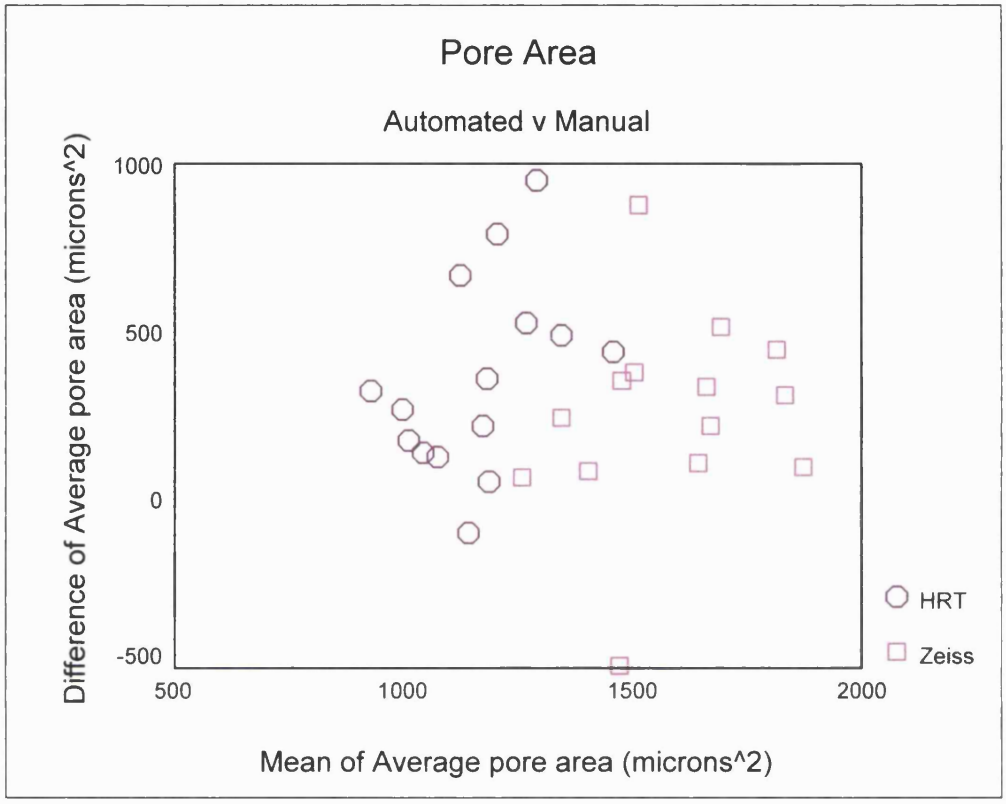

Slope values: *HRT: y= 0.9x* R^2*= 0.19* *p= NS*

Zeiss: y= 0.8x R^2*= 0.38* *p<0.05*

Plot assessing agreement between AT and MD techniques for measuring pore area. Results for both HRT and Zeiss are shown. Again, plots indicate that there is poor agreement between the two methods for both cSLO's. The trend indicates that larger the average pore area, the greater the difference between the 2 methods, although this is not statistically significant for the HRT data. However, for both instruments, the automated thresholding technique results in a larger average pore area compared with the manual-draw technique.

Figure 4.3: Bland- Altman plot for pore elongation measurements

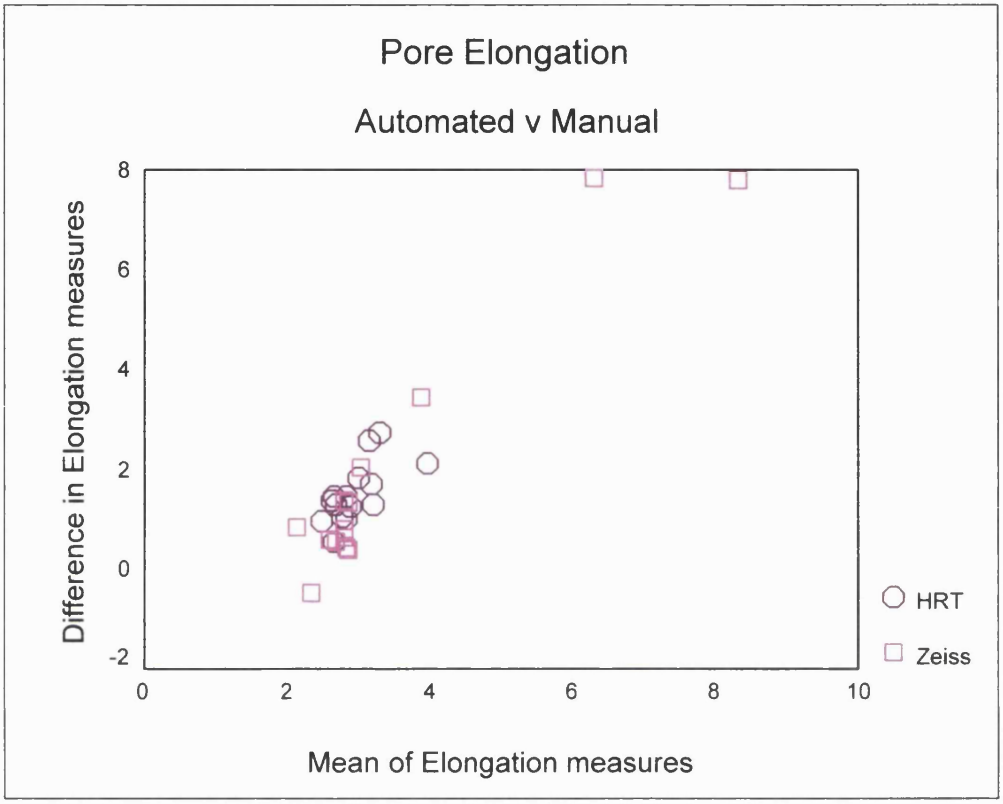

Slope values: *HRT: y= 1.1x* R^2*= 0.44* *p<0.01*

Zeiss: y= 1.5x R^2*= 0.91* *p<0.001*

Plot assessing agreement between AT and MD techniques for measuring pore elongation. There is poor agreement between the AT and MD methods, as has been found in the previous graphs (4.1 and 4.2). The larger the average elongation, the greater the difference in measurements. The automated thresholding technique results in larger pore-elongation measures than the manual-draw method.

The large R^2 value and the associated significance for the Zeiss elongation measures may be as a result of the two outlying data points (elongation value of 8). If these pores are omitted from the analysis, the R^2 value is 0.68, $p<0.01$.

Preliminary examination of the results (shown in figures 4.1-4.3) indicated that the greater the pore number, area or elongation, the greater the difference between the two measuring techniques. Following on from this, it was decided that it would be interesting to determine whether these differences were a function of cup-size, and so a sub-study was performed. The cup and disc areas of the fifteen subjects that were imaged for this study were recorded using the HRT (topography mode- HRT software version 2.1). On the following pages, a table showing the disc data and graphs plotting the difference in pore number, area and elongation between the automated and manual pore quantifying techniques against cup area and CD ratio are shown.

Table 4.5 Disc data and difference between AT and MD methods of pore quantification for HRT and Zeiss cSLO's.

Subject	Disc area mm^2	Cup area mm^2	CD ratio	PND HRT	PND Zeiss	PAD HRT (μ^2)	PAD Zeiss (μ^2)	PED HRT	PED Zeiss
1	2.4	1.3	0.6	-20	-41	177.6	221.8	1.8	0.7
2	2.2	1.0	0.5	-18	-17	-96.0	112.3	1.3	0.6
3	1.8	1.2	0.7	-29	-48	443.6	67.2	1.5	0.4
4	2.6	1.1	0.4	-33	-75	54.6	513.5	1.0	-0.5
5	1.7	1.2	0.7	-36	-14	133.3	-495.2	0.6	2.0
6	1.9	0.5	0.3	-22	-13	949.2	97.1	2.6	0.9
7	2.4	1.8	0.8	-38	-104	362.5	381.8	1.0	3.4
8	2.4	1.5	0.6	-18	-18	220.3	449.5	1.3	1.3
9	1.7	0.3	0.2	25	-8	489.4	316.8	1.3	0.4
10	1.4	0.7	0.5	-63	-77	270.5	249.5	1.1	0.5
11	1.7	0.7	0.4	-7	-2	794.3	354.8	2.8	7.8
12	1.9	1.6	0.8	-44	-52	325.7	338.3	1.7	0.6
13	2.2	0.5	0.2	-24	-8	529.6	1253.2	2.1	7.8
14	3.1	2.2	0.7	-16	-91	144.7	89.1	1.4	0.8
15	1.5	0.8	0.5	-51	-78	668.3	874.8	1.5	1.4

Key: PND pore number difference; PAD pore area difference; PED pore elongation difference

The 'difference' refers to the difference between the AT and MD methods of pore quantification within each imaging modality. The disc data was measured using the HRT in its normal topography mode (see appendix I). The following graphs illustrate the relationship between cup area and the difference between the techniques of measuring pore data.

Figure 4.4: Graph showing difference in pore number (AT/MD) vs. cup area

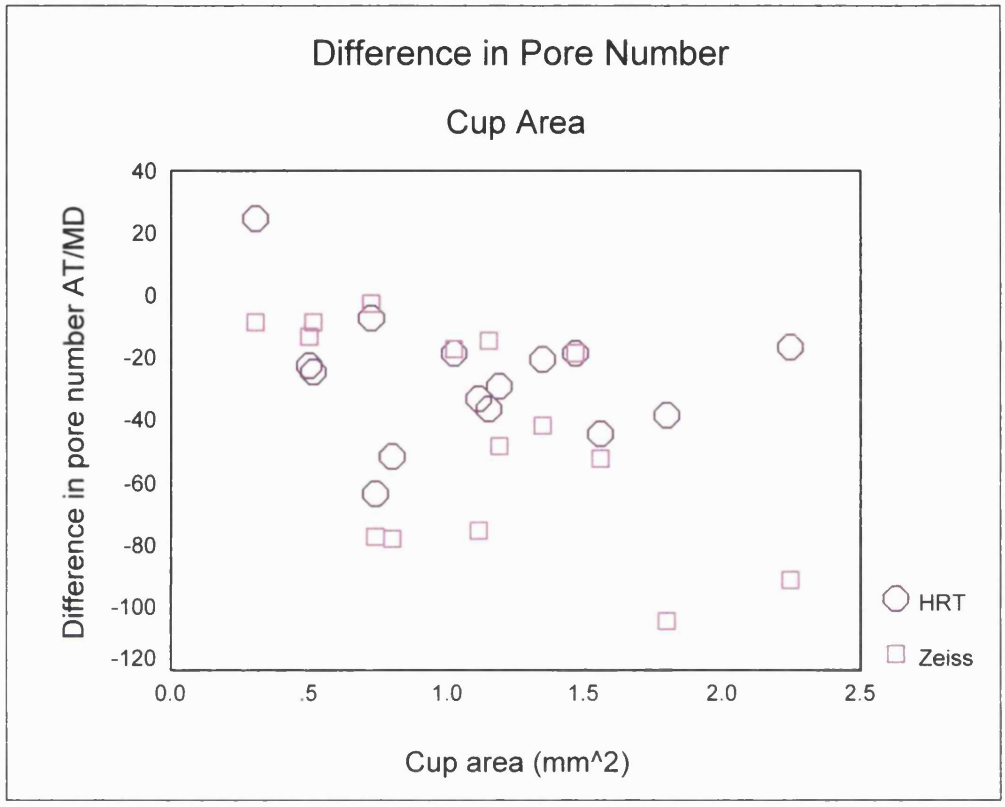

Linear regression *HRT:* $R^2 = 0.046$ $p < N.S$

Zeiss: $R^2 = 0.303$ $p < 0.05$

In large cups there is a greater difference between the number of pores found with the AT and MD techniques for the Zeiss cSLO. Although the graphs indicate a trend, the statistics show it not to be significant with the HRT. The trend indicates that more pores are detected using the MD method of pore quantification for both instruments in larger cups

Figure 4.5 Graph showing difference in pore number found with AT/MD techniques and CD ratio

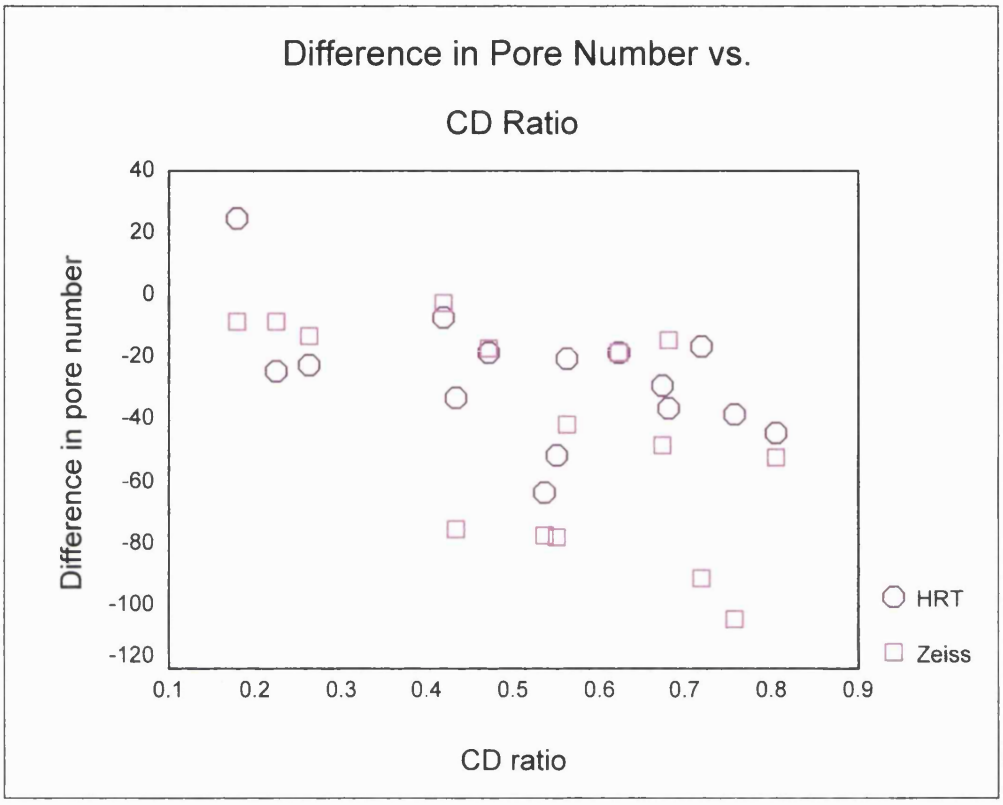

Linear regression *HRT:* $R^2 = 0.216$ $p < 0.05$

Zeiss: $R^2 = 0.283$ $p < 0.05$

The graphs and statistics show a relationship between the variables. The larger the CD ratio, the greater the difference between the pore number found with the AT and MD measuring techniques. The hypothesis was that with larger cups, more pores would be detected with the MD technique, and this seems to be the case.

Figure 4.6 Graph showing difference in pore area found with AT/MD techniques and cup area

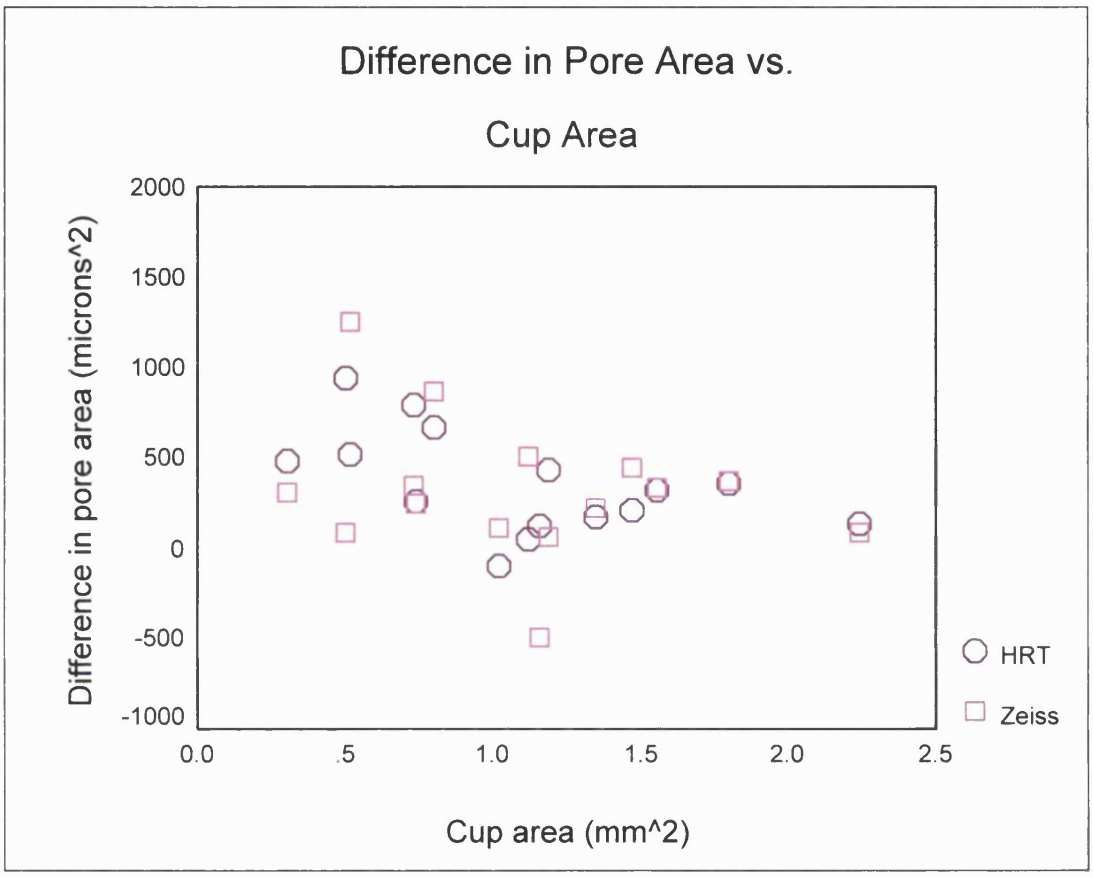

Linear regression *HRT:* $R^2 = 0.187$ $p <$ *N.S*

Zeiss: $R^2 = 0.077$ $p <$ *N.S*

The graphs indicate that there is no relationship between cup area and the difference found in pore area measurement techniques.

Figure 4.7 Graph showing difference in pore area found with AT/MD techniques and CD ratio

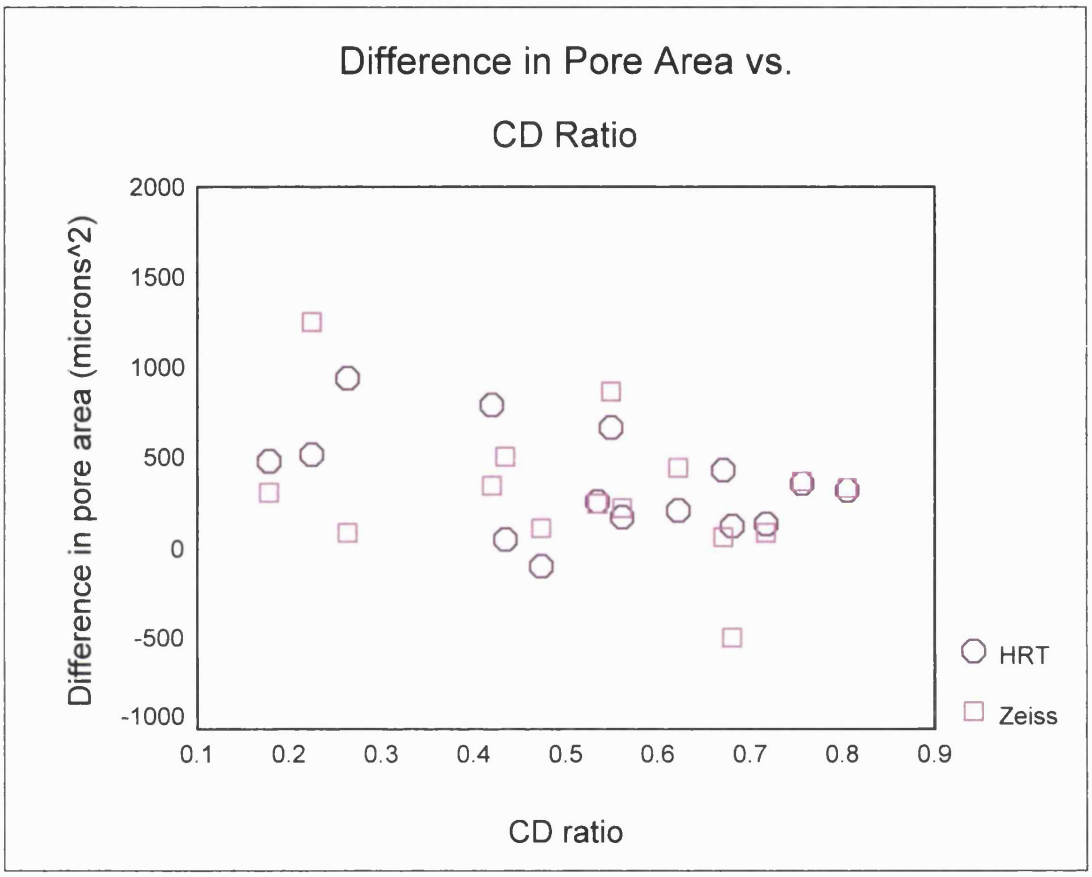

Linear regression *HRT:* $R^2 = 0.119$ $p = N.S$

Zeiss: $R^2 = 0.074$ $p = N.S$

The difference in pore area measurements with both AT and MD techniques is not dependant on the CDR.

No relationship was found between cup area and CDR and the difference in pore elongation measuring techniques [*Linear regression, HRT: pore elongation and cup area,* $R^2 = 0.071$, $p = N.S$, *CDR,* $R^2 = 0.130$, $p = N.S$; *Zeiss: pore elongation and cup area,* $R^2 = -0.015$, $p = N.S$, *CDR,* $R^2 = 0.001$, $p = N.S$]. No relationship was found between the difference in AT/MD for all pore parameters and disc area.

4.1.3.2 Manual Zeiss vs. Manual HRT

When comparing the two cSLO's, the average number of pores detected by manual drawing was greater in the Zeiss cSLO (83) than in the HRT (59) - this was significant at the $p<0.05$ level. Average pore area was greater in the Zeiss group (1600.2 microns$^{2)}$ than in the HRT group (982.8 microns$^{2)}$. This was significant at the $p< 0.001$ level. Pore elongation appeared fairly similar in both groups (HRT average 2.2, Zeiss 2.5) but the Zeiss did show consistently larger results and this was significant to the $p<0.05$ level (table 4.3).

The previous chapter results comparing the HRT and Zeiss cSLO pore quantification techniques using automated thresholding found that the pore number measures were consistently higher with the Zeiss images. This is also found with the manual-draw method of pore quantification. This would indicate that more pore information is present in the images captured with the Zeiss cSLO.

Table 4.3: Comparison of pore details found by manual drawing technique for Zeiss and HRT cSLO's.

Subject	No. of Pores-HRT	No. of Pores-Zeiss	Ave Pore Area μ^2-HRT	Ave Pore Area μ^2-Zeiss	Pore Elongation HRT	Pore elongation-Zeiss
1	52	72	921.2	1560.6	2.1	2.5
2	46	59	1237.7	1225.6	2.5	2.4
3	57	33	1008.7	1720.0	2.1	2.6
4	32	15	1205.8	2961.0	2.3	2.6
5	97	121	1124.3	1578.4	2.4	2
6	32	38	817.6	1825.5	1.8	1.7
7	61	153	1001.3	1311.8	2.0	2.2
8	90	117	1162.4	1597.7	2.3	2.2
9	45	41	1062.7	1591.2	2.0	2.7
10	71	120	999.8	1932.5	2.2	2.4
11	45	119	973.3	1614.7	1.9	2.4
12	92	122	861.5	1220.4	2.3	2.3
13	20	41	806.7	1298.6	2.9	4.4
14	70	77	767.3	1490.4	1.9	2.4
15	77	110	790.89	1075.0	1.9	2.1
Ave	59	83	982.8	1600.2	2.2	2.5

Student T-Test	P value	Student T-Test	P value	Student T-Test	P value
Pore number	< 0.05	Pore area	0.0001	Elongation	<0.05

There is a large difference in the average pore area between the HRT and Zeiss. This may be explained by the fact that more pores were detected using the Zeiss cSLO, and these may include larger pores, thus increasing the overall average pore area and possibly elongation.

4.1.3.3 Total Pore Area

The sum of the pore areas found for each subject with both cSLO's and both the automated and manual drawing methods were calculated to give a 'total pore area' for each subject- table 4.4. From this table it can be seen that the total pore area found within the HRT images was significantly less than that found in the Zeiss images. This was found when the pores were quantified with both the automated thresholding technique and the manual-draw method (HRT total pore area (TPA) with AT 659227.7 microns^2, Zeiss TPA with AT 1182690.9 microns^2 student t-test $P< 0.001$; HRT TPA with MD 874447.2 microns^2, Zeiss TPA with MD 1859321.1 microns^2 student t-test $p<0.001$).

In addition the total pore area was significantly greater when measured using the manual draw technique of pore quantification compared with the automated method for both cSLO's.

Table 4.4: Total pore area for each subject with both imaging techniques and lamina pore quantification methods.

Subject	AT- Zeiss mm^2	MD-Zeiss mm^2	AT-HRT mm^2	MD-HRT mm^2
1	0.055	0.112	0.035	0.048
2	0.014	0.072	0.029	0.057
3	0.023	0.057	0.023	0.057
4	0.051	0.044	0.026	0.039
5	0.170	0.191	0.125	0.109
6	0.048	0.069	0.018	0.026
7	0.083	0.201	0.031	0.061
8	0.177	0.187	0.117	0.105
9	0.047	0.065	0.035	0.048
10	0.175	0.232	0.066	0.071
11	0.099	0.192	0.036	0.044
12	0.066	0.149	0.033	0.079
13	0.064	0.053	0.021	0.016
14	0.046	0.115	0.028	0.054
15	0.062	0.119	0.038	0.061
Total	1.183	1.859	0.659	0.874

Student T-Test	p value	Student T-Test	p value
Zeiss AT/MD	0.0001	MD Zeiss/HRT	0.009
HRT AT/MD	0.0001	AT Zeiss/HRT	0.0001

Key: *AT= Automated Thresholding technique*

MD = Manual Drawing technique

The total pore area was significantly greater when using the manual draw method of pore quantification for both the HRT and Zeiss images. In addition, the TPA was consistently greater in the Zeiss images compared with the HRT images using either MD or AT techniques.

4.1.4 Discussion

The discussion of these results can be divided into two parts- the difference between the 2 modes of measuring the pore data and the difference between the two imaging techniques.

4.1.4.1 Automated vs. Manual

The manual method for identifying lamina cribrosa pores resulted in more pores being detected with both cSLO's when compared with the automated method. In the automated thresholding method, the inverse transform is converted into a binary image, setting pixels above a certain value as being the background, and those below the value as being the foreground. One of the difficulties with this simple binarisation technique is that subtle detail within the image may be missed as pores that are small or close together may merge into one. In addition, pores that had pixels values that fell below the threshold value would be classed as being part of the background. This would therefore result in a reduction in the number of pores detected by the automated method. It was thought that by manually drawing around the pores these errors would reduce, and different pore data would be gained.

The results comply with this hypothesis, and indeed many more pores with a smaller average pore area were found with the manual drawing method.

An interesting observation is how the differences between the automated and manual drawing methods become greater as the number of pores, average pore area and pore elongation increases (Bland-Altman plots figures 4.1- 4.3). For some subjects, the automated and manual drawing methods gave similar results for number of pores and average pore area. For others, more pores with smaller areas were detected with the manual method. This may be related to the amount of lamina area (cup area) visible for each subject. If more cup area was visible, a greater number lamina pores would be exposed. If the cup were large due to an acquired rim loss, there would also be some backward bowing of the lamina area (Chapter 1, sections 1.3 and 1.4). This in turn would mean that the pores at the edge of the cup may not be as clearly imaged as those at the centre of the cup,

and so may be 'lost' in the automated thresholding technique. This would not be the case with the manual drawing method, as the observer would pick these 'edge- pores' out. To test this hypothesis, a sub-study was performed.
The purpose of this sub-study was to try and explain the findings in figures 4.1-4.3, where the difference in the pore measuring techniques (AT versus MD) became larger as the pore number, area and elongation increased.
Figures 4.4- 4.7 indicate that in large cups where more lamina area is exposed, a greater number of pores are found using the manual draw (MD) method of pore quantification. The initial hypothesis was that this might be the case due to the limitations of the automated threshold technique, where a subtle difference in pixel value of adjacent pores may result in a loss of pore data in the binarisation step, particularly in large cups.
However, no relationship was found between cup size and the differences found in pore area and elongation between the AT and MD techniques. The AT technique results in larger and more elongated pore measurements, simply because of a lack of distinction between adjacent pores, regardless of how large the cup may be. A large cup is not necessarily a glaucomatous cup, and this sample of subjects was not chosen on whether they had glaucoma. The lack of a relationship between cup size and AT measures is almost a positive attribute. Larger and more elongated pores would be expected with acquired rim loss (Emery, Landis et al. 1974; Quigley and Addicks 1981; Quigley, Addicks et al. 1981; Quigley, Hohman et al. 1983; Miller and Quigley 1988), not just in a large cup. So although fewer, larger and slightly more elongated pores may be detected with this technique, it will not falsely identify acquired rim loss.
The MD method is more prone to observer error, as is any subjective method of image analysis. An objective method for any form of quantification is always desirable. In view of the above findings, it was decided that the automated thresholding technique of pore quantification should be used in subsequent studies.

4.1.4.2 HRT vs. Zeiss

The above study also highlights the differences between the two imaging techniques. In chapter 3 it was found that more pore information was present in the Zeiss images compared with the HRT images when using the automated thresholding technique. The study in this chapter confirms this finding with the manual draw method of pore quantification also. The reasons for this have been discussed in the previous chapter. The resolution of the Zeiss is superior to the HRT when imaging the lamina cribrosa area due to both the differences in lateral resolution and the method of image capture, between the two instruments.

From the previous two studies (chapters 3 and 4), it was decided that for subsequent investigations of the *in vivo* lamina cribrosa, images would be acquired using the Zeiss system and analysed using the objective automated thresholding technique.

Chapter 5: In vivo imaging III

5.1 Lamina pore morphology and optic disc topography

5.1.1 Introduction

Section 1.5 has discussed the previous attempts to quantify the lamina cribrosa structure. Most of the studies examined post mortem tissue, although recent studies by Bhandari, Fontana and Maeda (Bhandari, Fontana et al. 1997; Fontana, Bhandari et al. 1998; Maeda, Nakamura et al. 1999) have attempted to visualize the pores in vivo using scanning laser ophthalmoscopy.
These and other studies by Miller (Miller and Quigley 1988) have suggested that lamina pore characteristics differ in normals and glaucoma patients. The aim of the following study was two fold:

1. to quantify lamina pore structure as imaged in vivo with the Zeiss cSLO and compare these results with the previous studies, and
2. to determine whether there is a relationship between pore characteristics and optic nerve head topography, and whether this differs in glaucoma.

5.1.2 Materials and Methods

5.1.2.1 Image Acquisition

In vivo images of the lamina cribrosa were obtained using a prototype Zeiss confocal scanning laser ophthalmoscope (cSLO) (Carl Zeiss, Oberkochen, Germany), as described in section 2.1.1.2. Images were processed, thresholded and analysed also as detailed in section 2.1.4.6.

5.1.2.2 Initial Study -Subjects

The project was approved by the research ethics committee of Moorfields Eye Hospital, and performed in accordance with the 1964 Declaration of Helsinki. Eleven normal and twenty-four glaucomatous subjects were recruited and imaged. Normal subjects were recruited from staff at Moorfields Eye Hospital, London, and spouses of patients attending the glaucoma clinic, with no family history of glaucoma. Glaucomatous subjects were recruited from the ongoing Medical Research Council 5-Fluorouracil trial currently running at Moorfields Eye

Hospital. These subjects were chosen randomly and sequentially- i.e. the appearance of the optic nerve was not observed before imaging. This is an important difference from previous lamina imaging studies where the subjects were chosen on the basis of having a lamina cribrosa area that was well defined and visible with ophthalmoscopy (Bhandari, Fontana et al. 1997; Fontana, Bhandari et al. 1998; Maeda, Nakamura et al. 1999). After informed consent was obtained, one eye of each subject was randomly selected and dilated with guttae tropicamide 0.5 %.

The Heidelberg Retina Tomograph (HRT; Heidelberg Engineering, Germany) was used to quantify the optic nerve head topography. The instrument has been described in detail elsewhere (Rohrschneider, Burk et al. 1994). In this study, three good quality image series were recorded, and the mean topography generated. A contour line was drawn around the mean topography image, and information of the global optic nerve head topography was obtained (software version 2.01). The parameters disc area, rim area, rim volume, cup area, cup volume, maximum cup depth and 3rd moment in contour were recorded for each patient. In addition, a new parameter termed the 'rim index' was defined and recorded for
each subject.

Definition of Topography Data

Here follows a brief description of the parameters of the optic nerve head that were recorded.

Reference Plane

In order to describe the properties of the optic nerve head under evaluation, it is necessary to define a reference plane. All structures located posterior to the reference plane would be assigned to the optic nerve head cup, and all those anterior to the plane would be part of the neuroretinal rim.

The standard reference plane depth is set at 0.05mm posterior to the mean retinal surface between the optic nerve head margin and the papillo-macular bundle. The papillo-macular bundle is defined as being 4 to 10 degrees below the horizontal at the temporal region of the disc [Burk, 1995 #755].

Disc Area

Disc area was defined as the total area within the contour line.

Rim Area and Volume

Rim area was defined as the total area within the contour line minus the cup area. Rim volume was defined as the total volume of those parts within the contour line but above the reference plane.

Cup Area and Volume

Cup area was defined as the total area within the contour line below the reference plane. Cup volume was defined as the total volume below the reference plane.

Maximum Cup Depth

The HRT generates a surface other than the reference plane known as the 'curved surface'. The height of the centre of the curved surface is equal to the mean height of the optic disc margin (as defined by the drawn contour line). Mapping a straight line from this centre to a point on the contour line thus generates the surface itself. The maximum cup depth is therefore defined as the average depth of the 5% of pixels with the largest depth values within the disc measured from the curved surface.

Third Moment in Contour

The third moment in contour is a measurement of the frequency distribution of depth values within the contour line and below the 'curved surface.' The curved surface is a virtual plane generated by mapping a line from each point on the contour line to the centre of the optic nerve head. Thus its shape is dependant on the contour line profile.

Rim Index

The new HRT software incorporates a Moorfields Analysis Feature, that has been described in detail elsewhere (Wollstein, Garway-Heath et al. 1998; Uchida, Kitazawa et al. 2000). Briefly, it gives a predicted value of the global disc rim area based on the size of the optic disc and a range of normal values. For this study, the predicted global rim area was recorded, and the ratio of the actual rim area to the predicted rim area (for it to be classified as normal) for each of the 20

subjects was calculated. We have termed this ratio 'rim index' (Kotecha, Khaw et al. 2000; Kotecha, Siriwardena et al. 2001). If the rim index is a value of 1 or above, the rim area of the disc segment is within the predicted limits for the subjects disc size. If the rim index value is less than 1, it indicates that the rim area is less than that predicted. Thus, the lower the rim index value, the greater the likelihood that the segment has an acquired rim loss. The relationship between rim area and disc size is well established (Britton, Drance et al. 1987; Caprioli and Miller 1987), such that large discs have large cups and so it is possible that lamina pore characteristics may be more distinguishable in large discs. In order to see if there was a relationship between rim area and lamina pore characteristics without the influence of disc area, the rim index ratio was used.

5.1.2.3 Lamina pore characteristics

Optic disc images taken with the Zeiss cSLO were analysed according to the method described in section 2.1.4.6. The thresholded images were analysed using Matrox Inspector 2.1, and the 'blob analysis' feature was used. For this study, parameters recorded for each subject were: number of pores, average pore area, total pore area and pore elongation. In addition the range of pore areas was recorded for each subject.

Definition of pore characteristics

Here follows a definition of the parameters measured when investigating the lamina pore morphology.

Pore number

The total number of pores found within the optic nerve head for each subject.

Average pore area

The average pore for each subject.

Total pore area

The total area occupied by the lamina pores- the sum of the areas for all the pores for each subject.

Pore elongation

The ratio of length of pore over breadth.

Results were analysed using SPSS version 10.0.0 (SPSS Inc), and correlation measured using a Spearman's Rank coefficient.

5.1.3 Results

Of the thirty-five subjects that were recruited, adequate cSLO images were obtained for 33 of them. The presence of cataract in two glaucomatous subjects meant that imaging with either cSLO was not possible.

5.1.3.1 HRT summary

The average disc area of the glaucoma group (22 subjects) was 2.091 mm^2, and in the normal group (11 subjects) 1.955 mm^2 (Wilcoxon signed ranks test (WSR) p= NS). The average cup area and volume of the glaucoma group was 1.292 mm^2 and 0.505 mm^3 respectively, and for the normal group 0.572 mm^2 and 0.143 mm^3 (WSR $p<0.01$). Average rim area and volume in the glaucoma group was 0.799 mm^2 and 0.152 mm^3 and in the normal group 1.383 mm^2 and 0.346 mm^3 (WSR $p<0.01$). The average rim index in the glaucoma group was 0.517 and in the normal group 0.930 (WSR $p<0.01$). The results are detailed in table 5.1 and 5.2.

5.1.3.2 Zeiss Summary

The number of pores detected ranged from between 3 to 96. On average, more pores were detected in the glaucoma group than in the normal group (average number of pores in the glaucoma group =48, normal group = 20, WSR $p<0.01$). The average pore area in the subject group as a whole ranged from 750.1 to 2959.5 microns ^{2}. In the glaucoma group, the average pore area was greater (mean 1905.0 $microns^2$) when compared with the normal group (mean 1462.3 $microns^2$) (WSR $p=0.05$). The total pore area was greater in the glaucoma group (91267.5 $mcrons^2$) than in the normal group (32485.9 $microns^2$) (WSR $p<0.01$).

5.1.3.3 Pore characteristics and optic nerve head topography

The relationship between pore characteristics and optic nerve head topography for this group of subjects is summarised in table 5.4. There was an increase in the number of pores visible with increasing disc area (Spearman's rank coefficient $r = 0.555$ $p<0.01$), increasing cup area ($r= 0.729$, $p<0.001$), cup volume (0.695, $p<0.001$) and decreasing rim area (-0.375, $p<0.05$) and rim volume (-0.424, $p<0.05$). Pore number also increased with increase in third moment (0.616, $p<0.001$) and decreasing rim index (-0.581, $p<0.01$).

An increase in the average lamina pore area was associated with increasing cup area ($r = 0.372$, $p<0.05$) and with an increasing maximum cup depth (0.360, $p<0.05$) and decreasing rim index (-0.353, $p<0.05$).

No relationship between pore elongation and optic disc topography was found.

These results are illustrated graphically in figures 5.1 – 5.4 .

Table 5.1: Lamina pore morphology and optic disc topography- Glaucomas

Subject	Disc Area mm^2	Cup Area mm^2	Rim Area mm^2	Cup Volume mm^3	Rim Volume mm^3	Max Depth	3rd Moment	Rim Index	Pore Number	Total Pore Area $microns^2$	Average Pore Area $microns^2$	Elongation
1	1.748	1.507	0.241	0.667	0.018	0.765	0.097	0.17	27	57581.3	2132.6	3.7
2	2.100	1.607	0.493	0.576	0.111	0.819	0.041	0.32	62	101988.8	1645.0	3.1
3	1.925	1.455	0.470	0.575	0.058	0.809	0.035	0.33	49	72466.6	1478.9	3.4
4	3.192	2.397	0.795	2.237	0.081	1.395	0.097	0.35	55	123663.4	2248.4	3.4
5	1.573	1.129	0.444	0.503	0.061	0.736	0.070	0.38	96	184581.9	1922.7	3.3
6	2.372	1.744	0.628	0.569	0.074	0.605	0.069	0.38	62	116546.9	1879.8	3.1
7	2.016	1.449	0.567	0.523	0.089	0.825	0.021	0.39	62	127880.1	2062.6	2.8
8	1.803	1.246	0.557	0.289	0.093	0.576	-0.014	0.41	30	61313.0	2043.8	3.4
9	2.082	1.378	0.704	0.599	0.080	0.793	0.025	0.47	67	119624.4	1785.4	2.2
10	2.156	1.426	0.730	0.676	0.152	0.978	-0.018	0.47	90	126953.8	1410.6	3.4
11	2.360	1.582	0.778	0.482	0.135	0.659	0.058	0.49	56	80184.9	1431.9	2.4
12	1.841	1.170	0.671	0.421	0.085	0.825	-0.052	0.49	22	38059.1	1730.0	4.6
13	1.510	0.881	0.629	0.396	0.111	0.876	-0.024	0.50	29	85824.2	2959.5	4.0
14	1.970	1.186	0.784	0.595	0.096	0.929	-0.077	0.53	44	83890.0	1906.6	3.6
15	1.784	1.002	0.782	0.226	0.113	0.563	-0.103	0.56	30	69756.4	2325.2	3.1
16	2.380	1.428	0.952	0.536	0.301	0.928	0.022	0.57	48	99362.4	2070.1	3.0
17	2.632	1.512	1.120	0.329	0.279	0.800	-0.049	0.64	63	129040.2	2048.3	4.1
18	1.741	0.899	0.842	0.124	0.136	0.428	-0.017	0.64	5	7039.7	1407.9	2.4
19	1.807	0.915	0.892	0.219	0.163	0.589	-0.005	0.65	28	50944.8	1819.5	3.8
20	2.020	1.001	1.019	0.399	0.237	0.925	-0.123	0.70	31	55879.5	1802.6	3.3
21	2.476	1.181	1.295	0.180	0.239	0.614	-0.065	0.74	71	149032.4	2099.1	3.1
22	2.349	0.805	1.544	0.340	0.453	0.985	-0.151	0.91	39	66272.2	1699.3	3.3
Average	2.084	1.314	0.770	0.521	0.144	0.792	-0.007	0.50	48.5	91267.5	1905.0	3.3

Table 5.2: Lamina pore morphology and optic disc topography- Normals

Subject	Disc Area mm^2	Cup Area mm^2	Rim Area mm^2	Cup Volume mm^3	Rim Volume mm^3	Max Depth	3rd Moment	Rim Index	Pore Number	Total Pore Area $microns^2$	Average Pore Area $microns^2$	Elongation
1	1.784	0.632	1.152	0.265	0.300	0.935	-0.168	0.76	31	56499.3	1822.6	3.6
2	2.909	1.376	1.533	0.277	0.394	0.638	-0.004	0.79	36	77418.5	2150.5	4.4
3	2.256	0.814	1.442	0.155	0.329	0.535	-0.109	0.82	34	49838.5	1465.8	3.4
4	1.934	0.647	1.287	0.116	0.353	0.668	-0.114	0.86	9	10126.6	1125.2	3.0
5	2.210	0.716	1.494	0.216	0.415	0.881	-0.234	0.89	16	31048.4	1940.5	2.9
6	1.185	0.123	1.062	0.013	0.268	0.497	-0.341	0.90	5	3750.5	750.1	1.6
7	2.638	0.975	1.663	0.373	0.261	0.690	0.018	0.93	46	70455.1	1531.6	3.0
8	1.587	0.365	1.222	0.073	0.407	0.689	-0.170	0.95	7	15950.9	2278.7	5.9
9	1.577	0.237	1.340	0.027	0.288	0.418	-0.240	1.05	16	19987.0	1249.2	3.6
10	1.748	0.269	1.479	0.030	0.451	0.436	-0.219	1.06	21	19782.2	942.0	2.5
11	1.975	0.378	1.597	0.042	0.320	0.359	-0.148	1.12	3	2487.8	829.3	2.5
Average	1.982	0.594	1.388	0.144	0.344	0.613	-0.157	0.92	20.4	32485.9	1462.3	3.3

Table 5.3: Range of pore areas found for each subject group

Subject (Glaucoma)	Smallest pore area μ^2	Largest pore area μ^2
1	406.8	8542.9
2	387.1	9095.8
3	376.5	6023.2
4	441.8	8956.5
5	373.8	6354.6
6	372.5	5251.9
7	376.5	8244.3
8	377.8	4344.4
9	367.2	5507.6
10	387.1	5573.6
11	368.5	3906.1
12	376.5	7717.2
13	380.4	3855.6
14	388.4	6913.2
15	405.3	5674.9
16	379.1	7430.4
17	401.0	5686.5
18	1042.9	2048.6
19	432.7	4939.5
20	355.2	6252.3
21	377.8	10691.1
22	369.8	8653.8

Subject (Normal)	Smallest pore area μ^2	Largest pore area μ^2
1	381.8	5802.6
2	456.4	7882.9
3	400.3	6605.1
4	588.3	1680.8
5	644.5	6217.3
6	399.0	1835.3
7	377.8	7026.6
8	914.6	5121.8
9	491.8	2915.5
10	371.1	1707.3
11	512.2	1170.7

This shows the largest and smallest pore area found for each subject. The overall range for the group is between 355.2 microns^2 and 10691.1 microns^2. In the 'normal' subject group alone, the pore area range is between 371.1 microns^2 and 914.6 microns^2.

Table 5.4: Relationship between pore characteristics and optic nerve head topography.

Parameter	Pore Number	Average Pore Area	Total Pore Area	Pore Elongation
Disc Area	0.555 p<0.01	0.141 p=NS	0.475 p<0.01	-0.070 p=NS
Cup Area	0.729 p<0.001	0.372 p<0.05	0.755 p<0.001	0.070 p= NS
Cup Volume	0.695 p<0.001	0.324 p=NS	0.715 p<0.001	0.129 p=NS
Rim Area	-0.375 p<0.05	-0.259 p=NS	-0.452 p<0.01	-0.090 p= NS
Rim Volume	-0.424 p<0.05	-0.234 p=NS	-0.492 p<0.01	-0.053 p=NS
Max Cup Depth	0.436 p< 0.05	0.360 p<0.05	0.473 p<0.01	0.267 p=NS
3rd Moment	0.616 p<0.001	0.306 p=NS	0.650 p<0.001	0.005 p=NS
Rim Index	-0.581 p<0.01	-0.353 p<0.05	-0.643 p<0.001	-0.103 p=NS

The figures show Spearman's rank coefficients and significance values.
There was an increase in the number of pores visible with increasing disc area, increasing cup area, cup volume and decreasing rim area and rim volume. Pore number also increased with increase in third moment and decreasing rim index. An increase in the average lamina pore area was associated with increasing cup area and with an increasing maximum cup depth and decreasing rim index.

Figure 5.1: Relationship between pore morphology and disc area

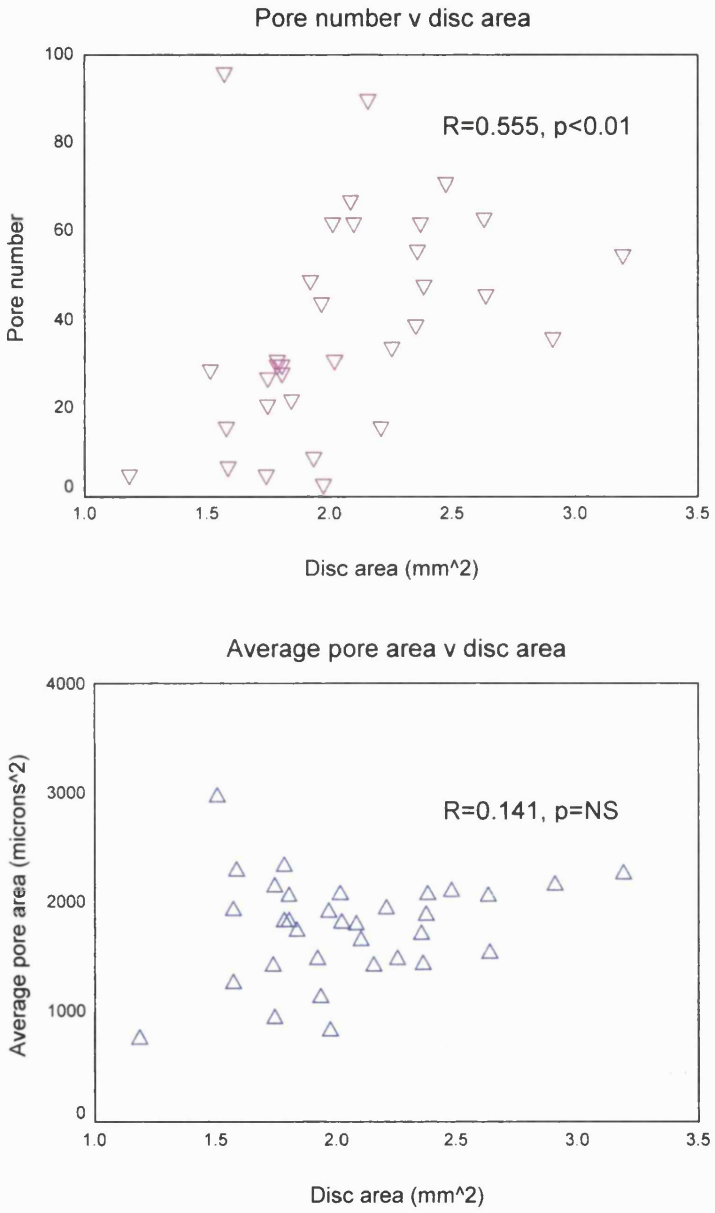

The upper graph shows that there is an increase in the number of pores visible with increasing disc area. The lower graph illustrates the lack of a relationship between the average pore area and disc area.

Figure 5.2: Relationship between pore morphology and cup parameters

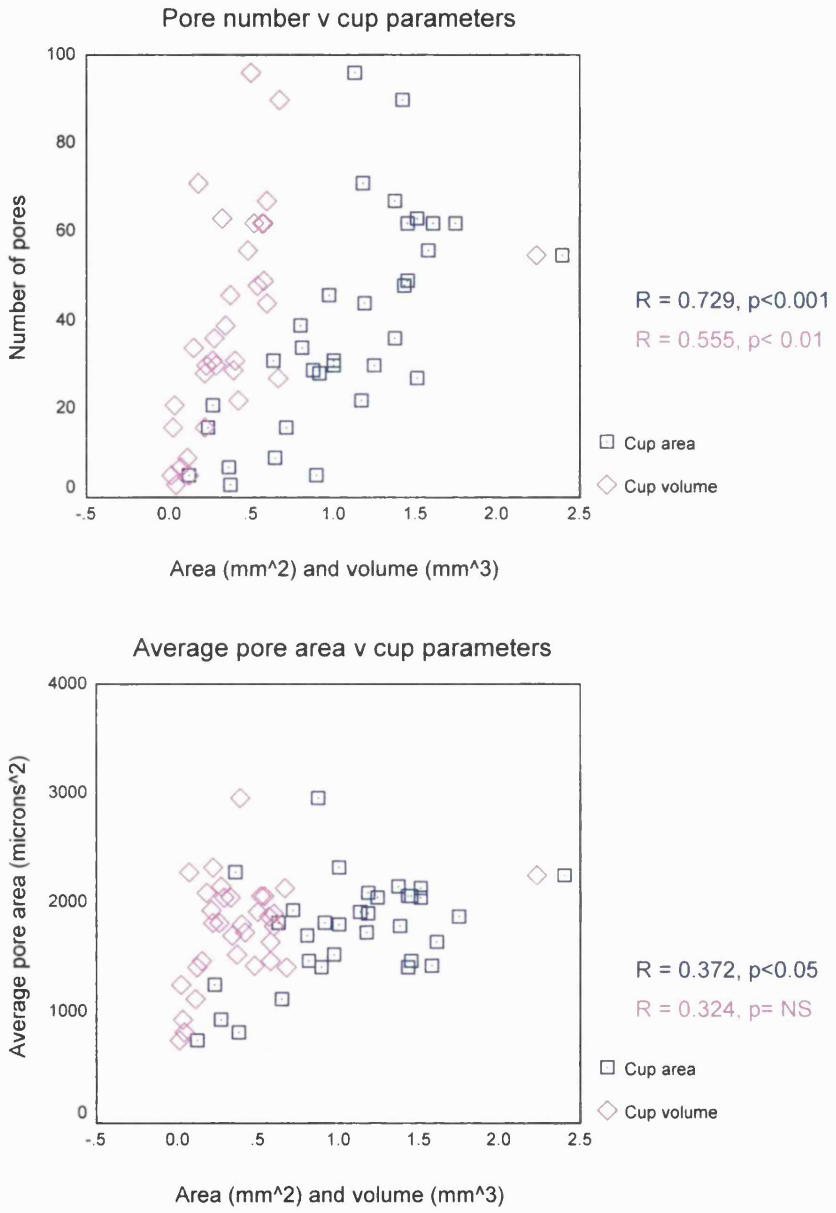

See legend on following page (172).

Figure 5.2: Relationship between pore morphology and cup parameters (ctd.)

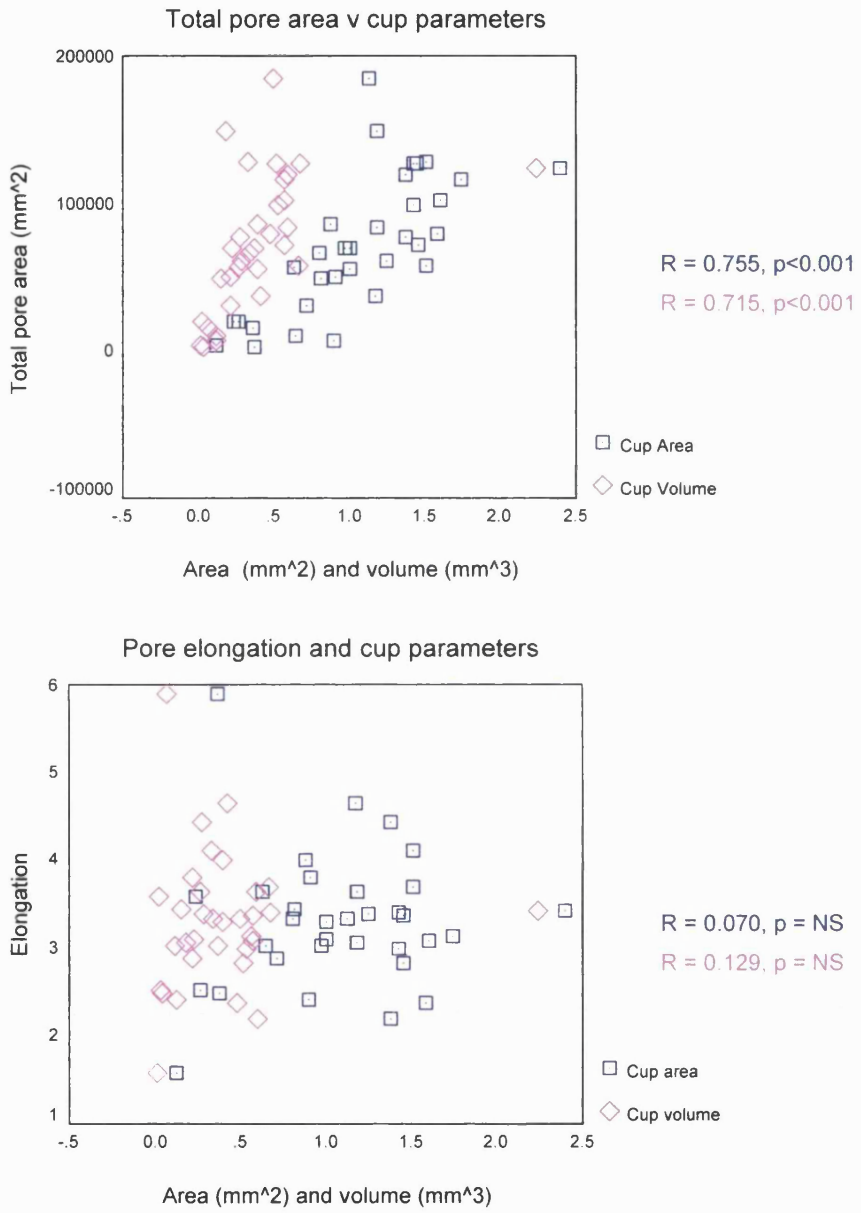

The number of pores increases with increasing cup size. There is a weak relationship between average pore area and cup area, but a strong relationship between the total pore area and both cup parameters, which may be related to pore number- more pores detected will give a greater total pore area. There is no relationship between pore elongation and cup parameters.

Figure 5.3: Relationship between pore morphology 3rd moment

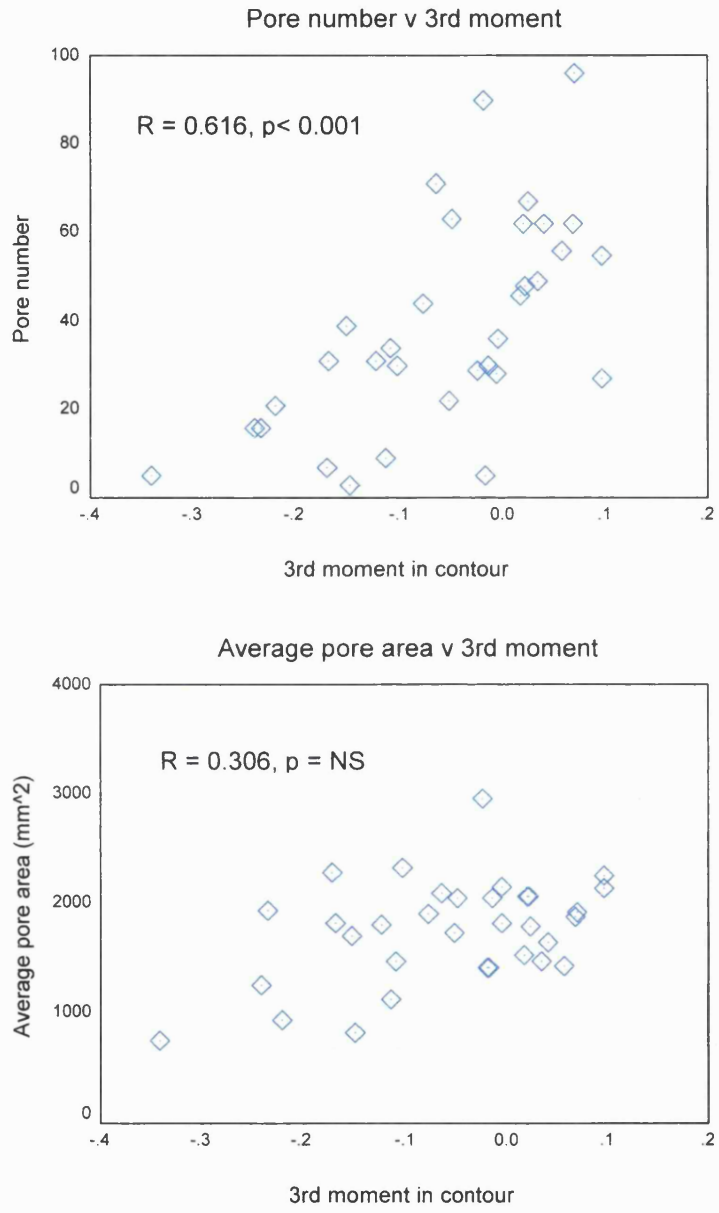

See legend on following page (p 174).

Figure 5.3: Relationship between pore morphology 3rd moment (ctd)

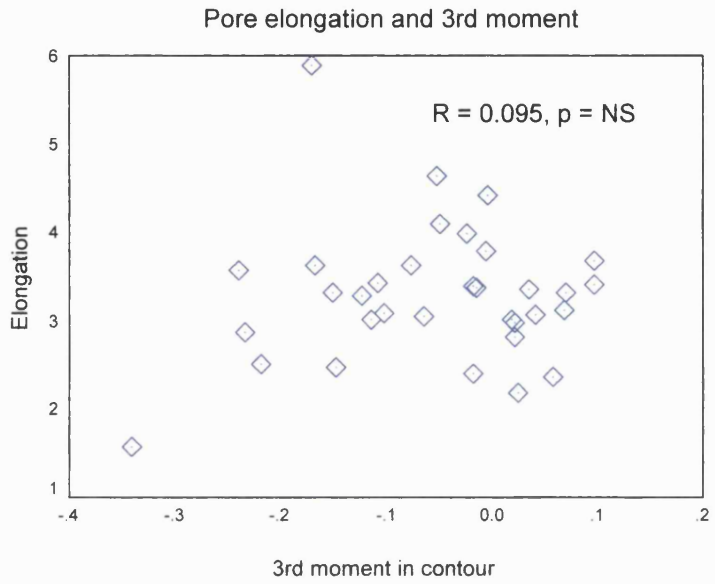

The 3rd moment in contour represents the skewness of depth values in the optic cup. The more positive the third moment, the deeper the cup is, indicating that the cup is glaucomatous. The first graph shows that the number of pores visible increases as the cup becomes deeper. There appears to be no relationship between average pore area or pore elongation and 3rd moment.

Figure 5.4: Relationship between pore morphology and rim index.

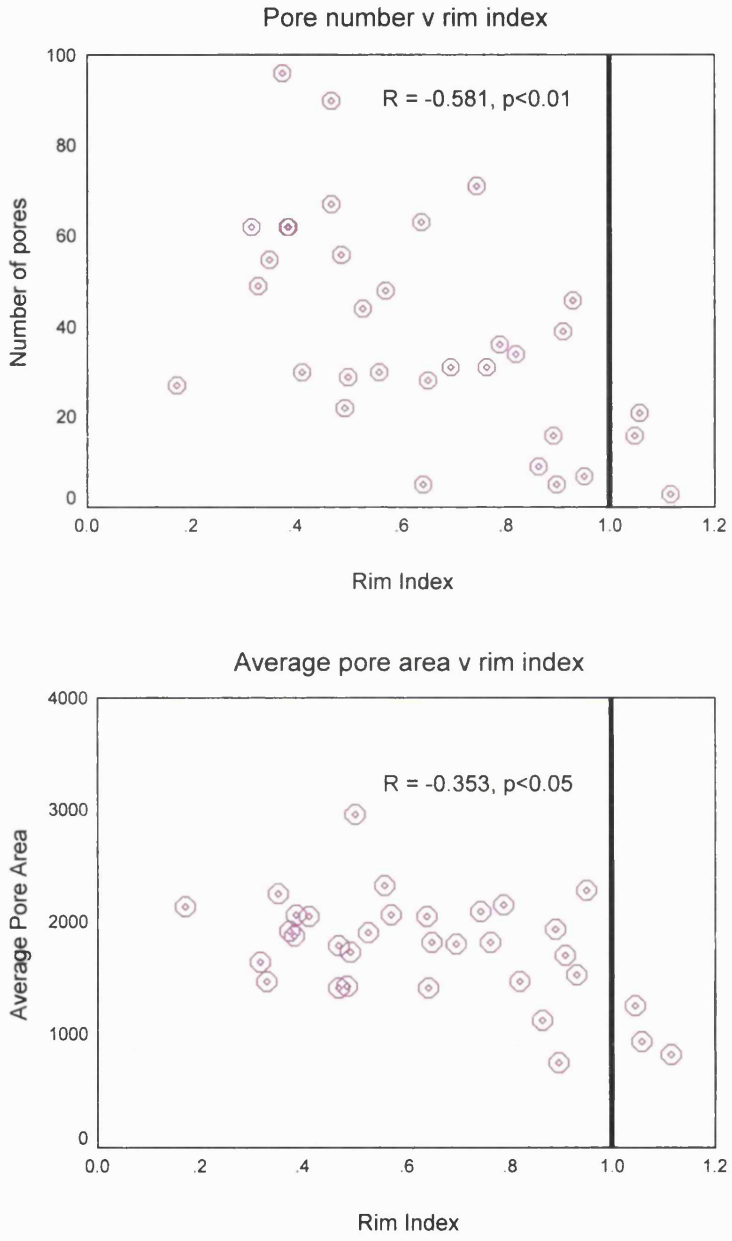

See legend on following page (176).

Figure 5.4 Relationship between pore morphology and rim index (ctd)

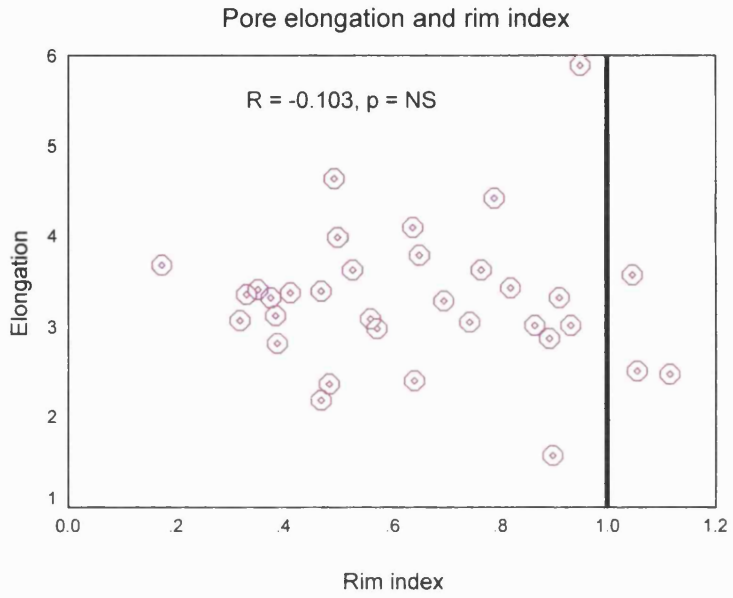

A low rim index gives an indication of acquired rim loss, so the graphs suggests that more pores are visible with an acquired rim loss. There is a weaker relationship between average pore area and rim index, indicating that the average pore area is larger in subjects with acquired rim loss.
The final graph shows that there is no relationship between pore elongation and acquired rim loss.

5.1.4 Discussion

In vivo imaging of the lamina cribrosa has been described previously (Bhandari, Fontana et al. 1997; Fontana, Bhandari et al. 1998; Maeda, Nakamura et al. 1999) but in previous work subjects were selected if they had lamina pore visibility with conventional ophthalmoscopy. The subjects in this study were not recruited on the basis of optic disc appearance.

The two main features that affect the quality of measurements from digital images are image acquisition and image processing. Since the initial work by Bhandari and Fontana (Bhandari, Fontana et al. 1997; Fontana, Bhandari et al. 1998), the resolution of the Zeiss image grabbing system has been increased from 256 x 256 pixels to 572 x 768 pixels.

The image processing method described by Bhandari and Fontana was based on the unsharp masking technique detailed in section 2.1.4.2, and no data for absolute size was available. In this study, the ocular refraction of all subjects was measured, and therefore the images could be corrected to obtain pore size measurements.

5.1.4.1 Pore morphology

Anatomical studies on pore morphology to date have been on dehydrated post mortem tissue. Quigley et al (Quigley and Addicks 1981) examined thirty-two normal eyes after either detergent or trypsin digestion. He established that there were between 200 to 400 pores on the surface, and that these sub-divided as they traversed through the cribrosal plates.

The results of this in vivo study find significantly fewer pores compared with the Quigley study. The number of pores detected in our group ranged from 3 to 96, which is rather less than the minimum of 200 that Quigley found. A reduction would be expected as many of the pores would be masked by the overlying neuroretinal rim tissue, but it may also be that the detected pore number was reduced through using the automated thresholding technique rather than manually counting the pores (chapter 4). It is also possible that the resolution of the cSLO is not enough to pick up smaller pores.

In Quigley's' study, the diameter range of the pores was between 10 to more than 100 microns. This would result in pore areas ranging from around 80 to 8000 microns^2. The individual subject pore area ranged between 355.2 to 10691.1 microns^2 (table 5.3) and the average pore area range was between 750.1 to 2959.6 (tables 5.1 and 5.2). From these tables, it can be seen that the largest pore size was not as large as that found in the Quigley study. This may be due to the cSLO being unable to image underneath the neuroretinal rim, thereby not detecting all of the pores in the optic nerve head region. The Quigley study also found that the largest pores were at the superior and inferior poles of the optic disc, and that the lamina cribrosa connective tissue beams were thinner in these areas. In our group, the average pore size was larger in the glaucoma group (1905 microns^2) compared with the normal group (1462.3 microns^2). In the glaucoma group, it is likely that the larger pores were exposed through acquired rim tissue loss (section 1.3.3), which explains this difference. However, the sizes are not as large as the levels that the Quigley study found, and this is likely to be due to range of severity of the disease in our subject group- not all the subjects had 'severe' disease, therefore a large proportion of the lamina cribrosa area would still be covered by neural tissue, thus masking the larger pores.

5.1.4.2 Relationship to optic nerve head topography

There was a relationship between the number of pores detected and disc area, with more pores being found in larger discs. Larger discs do tend to have larger optic cups (Caprioli and Miller 1987), and so one would expect that with a larger cup, more of the lamina area would be visible, thus increasing the visibility of the lamina pores. This idea is reinforced by the positive and significant correlation between pore number and increasing cup area and volume, and with decreasing rim area and volume (figs 5.1-5.2).

However, we wished to see if lamina pore visibility may be related to degree of glaucomatous damage, and the two indicators of this were third moment in contour and the rim index.

The third moment of contour essentially describes the skewness of depth measurements within the optic nerve head, and is a measure of overall cup shape. Normal eyes will typically show a negative value and glaucomatous eyes have a positive value (indicating excavation of the cup). There have been conflicting reports about the reliability of the third moment in contour as an indicator of glaucoma. It has been shown to be both a good (Uchida, Brigatti et al. 1996; Iester, Mikelberg et al. 1997; Iester, Swindale et al. 1997) and poor (Mardin and Horn 1998) indicator of glaucomatous damage, although the latter study by Mardin et al has suggested that there is an influence of disc size on the parameter, such that large discs will have a more positive third moment in contour, regardless of whether there is glaucomatous damage there. In this study, there is a positive correlation between increasing third moment and pore visibility, indicating that glaucomatous discs have an increase in the visibility of pores (fig 5.3). However, if optic disc size really is an influencing factor in this parameter, then this relationship would be expected in view of the positive relationship between disc size and pore number (fig 5.1).

The new parameter rim index may give a better measure of optic disc rim area and acquired rim loss, as it takes into account the effect of disc size. As discussed earlier in the chapter, the rim index is based on the Moorfields Regression Analysis feature. The rim index is the ratio of the actual rim area and the predicted rim area. Low rim index values indicate reduced rim area measurements and suggest acquired rim loss. More pores were visible in subjects with a low rim index (fig 5.4). The number of pores visible increased with decreasing rim index. This suggests that with acquired rim loss, the number of pores visible increase.

It was also found that the average pore area increased with decreasing rim index, increasing cup area and with increasing maximum cup depth. Anatomical studies on post mortem tissue have shown that there is a regional difference in pore size, such that pores are larger (and connective tissue beams thinner) in the inferior and superior poles of the optic nerve head (Quigley and Addicks 1981; Radius 1981). The rim index measure is an indicator of acquired rim loss, and so

it is possible that the larger pores in the vertical poles of the optic disc will be uncovered as the neuroretinal rim area decreases in acquired disease, which would help to explain our finding.

Other studies on post mortem tissue (Emery, Landis et al. 1974), and on observation of optic disc photographs (Miller and Quigley 1988) have found that lamina pores become more elongated with glaucomatous progression. In vivo studies of lamina pore morphology by Fontana et al (Fontana, Bhandari et al. 1998) also found that pores became more elongated with increasing severity of glaucomatous disease. In this study, no relationship was found between pore elongation and optic nerve head topography. Millers' study divided subjects into three groups, and found pore elongation in the 'severe' group. Fontana's study used 60 primary open angle glaucoma patients – all selected on the basis of lamina cribrosa visibility using slit-lamp biomicroscopy. This study had 22 glaucomatous eyes, and perhaps with a greater subject population a relationship between pore shape and other topography parameters may be found.

Chapter 6: Anatomical Studies

6.1 Architecture of lamina cribrosa

6.1.1 Introduction

Obtaining adequate *in vivo* lamina cribrosa images for pore morphology quantification depends upon the optical limitations of the cSLO and the physical limitations of the eye and the optic nerve head. The first few chapters discussed a method of grabbing, processing and analysing images of the *in vivo* lamina cribrosa. Extensive research has already been done on the post mortem lamina cribrosa area, but we wished to look at the structural architecture ourselves to see if it offered us any further clues as to how to improve upon the current imaging set-up to increase image resolution.

As described in chapter 1, the lamina cribrosa consists of a series of perforated collagenous plates through which the retinal blood vessels and ganglion cell axons exit the eye. The area can be divided into two parts- the posterior lamina cribrosa, which is derived from the adjacent sclera, and the anterior lamina cribrosa, which, although has collagenous septae, is richer in glial cells (Anderson 1969; Bron, Tripathi et al. 1997). The lamina cribrosa has been implicated in glaucoma as one of the main sites of damage to the ganglion cell axons (Quigley, Addicks et al. 1981; Radius and Gonzales 1981; Quigley, Hohman et al. 1983), particularly in cases of high tension glaucoma, where it is thought that the raised intraocular pressure results in a backward bowing of the lamina, resulting in a deformation of the ganglion cell axons. The areas' architecture has been investigated in great detail, using techniques that involve the dehydration and digestion of it and the surrounding tissue. The lamina area has regional differences in its thickness and pore size, with it being thicker in the horizontal (nasal to temporal) meridian, and having larger pores in the vertical (superior to inferior) poles (Quigley and Addicks 1981; Quigley, Addicks et al. 1981; Radius 1981; Radius and Gonzales 1981). These studies have led to hypotheses about the mode of damage in high tension glaucoma, giving explanation for the finding that nerve axons in the vertical meridian of the optic disc are the first to be damaged in the disease. The development of methods of

imaging the optic nerve head *in vivo* have led to experimental studies looking at the mechanical response of the area under different pressure loads (Yan, Coloma et al. 1994; Yan, Flanagan et al. 1998), and investigations of variations in lamina pore size and shape in normals and glaucoma subjects (Bhandari, Fontana et al. 1997; Fontana, Bhandari et al. 1998; Maeda, Nakamura et al. 1999). It is therefore of interest to know how the *in vivo* measurements are related to post-mortem tissue. A difference in both the size of the structure and its appearance between *ex* and *in vivo* studies would be expected due to these dehydration and digestion procedures during tissue preparation. The purpose of this study was to determine the longitudinal thickness of the lamina cribrosa in fresh/wet samples, and to investigate whether any changes in thickness occurred with age. In addition, we investigated whether there was any regional difference in the cribriform plate thickness.

6.1.2 Materials and Methods

Twenty-six human cadaver eyes were received from the corneal transplant service eye bank at Moorfields and Bristol Eye hospitals after corneas had been removed for transplantation. In cases where pairs of eyes had been received, only one eye from the pair was used in the study.
No history of ocular abnormality was given with these samples, but optic nerves and retinas appeared normal by gross examination during dissection.

6.1.2.1 Tissue Preparation

Optic nerve heads were dissected from the globe and stored in a solution of 20% sucrose in phosphate buffered saline (PBS) overnight. This method offers the cryo-protection of the tissue prior to the freezing and sectioning procedure (1996), so that minimal distortion of tissue occurs. Nerves were then fixed in gel-albumin/ 2.5% glutaraldehyde fixative and frozen before sectioning. Longitudinal sections of 50 microns thick were cut using a microtome. Sections were mounted on slides using PBS and standard cover glass, and examined under light microscopy at 20X magnification.

6.1.2.2 Measurement I: Thickness of Lamina

Previous studies have shown that regional variations exist in the lamina anatomy (Quigley and Addicks 1981; Radius 1981; Radius and Gonzales 1981). For this reason it was decided that lamina thickness measurements would be taken from sections close to the widest point of the optic nerve head, 100 microns either side of the exit of the central retinal artery. The change in collagen architecture around the central retinal artery and vein exit levels makes the demarcation of the lamina level difficult, so sections involving this area were avoided. Lamina cribrosa thickness was measured from the first collagenous plate to the myelinated nerve in 50 micron steps across the section (Figure 6.1). The age of the specimens was masked to the observer. Between 5 and 7 sections were measured for each specimen. The average of these measurements and the 95% confidence intervals were plotted against age.

6.1.2.3 Measurement II: Thickness of Laminar Plates

On observing the longitudinal sections of the optic nerve overall, it is easy to distinguish the discrete plates that form the lamina cribrosa. We wished to measure the individual thickness of each plate that comprised the cribrosa. Twelve of the 26 eyes were used for these measurements. One tissue sample from each eye that had been sectioned between 100 and 150 microns away from the central retinal artery section was mounted on a wet slide and examined under a light microscope connected to a computer via a CCD attachment at X40 magnification. The lamina cribrosa area was divided into 4 areas- posterior, mid-posterior, mid-anterior and anterior- all approximating 100 micron thickness (Figure 6.2). Measurements of cribriform plate thickness were made using Matrox Inspector Imaging Software (version 2.1, Matrox Electronic Systems Ltd., Quebec) (Figure 6.3).

Statistical analyses were performed using SPSS version 8.0. Linear regression analysis was used to determine the relationship between lamina cribrosa

thickness and age, and a Wilcoxon signed ranks test was used for analysis of regional measurements of cribriform plate thickness.

Figure 6.1 Schematic diagram illustrating method of sectioning optic nerve head. Lamina cribrosa thickness was measured from the first cribrosal plate [C] to the start of myelination of nerve fibres [D].

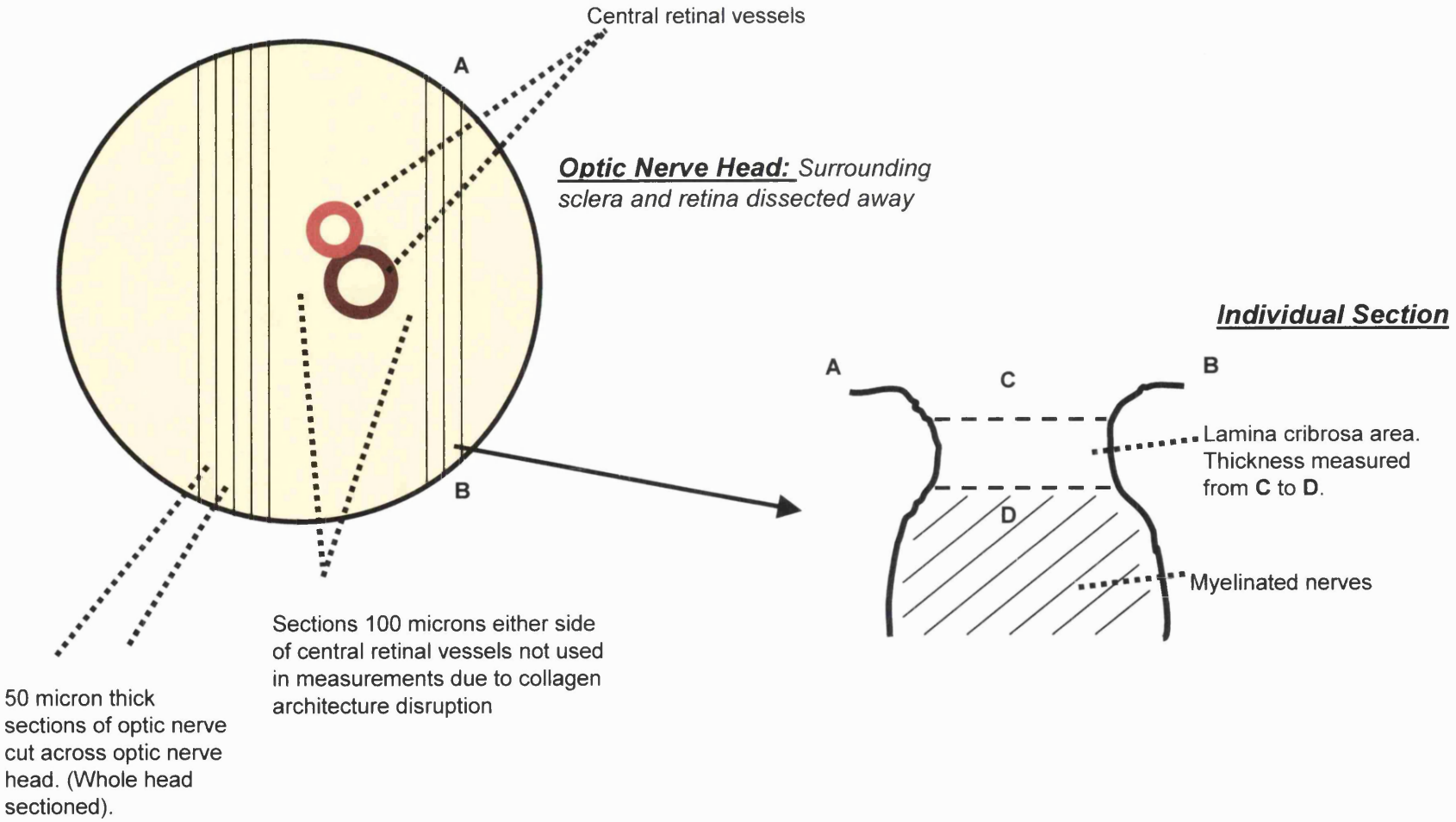

Figure 6.2: Section of lamina cribrosa to illustrate areas of cribrosal plate thickness measurements.

Plate thickness was measured in each of the 4 areas shown to investigate regional differences. *X 10 magnification*

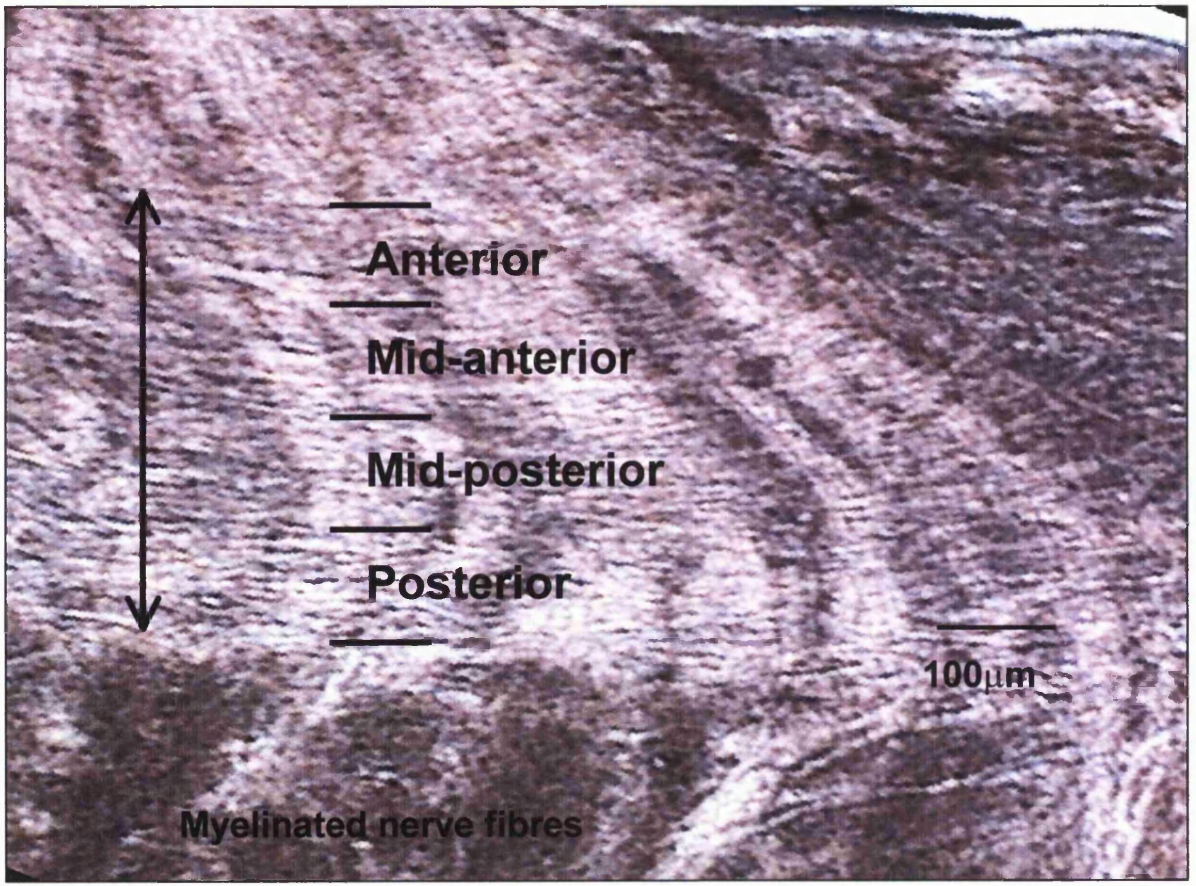

Figure 6.3
Measurement of cribrosa plate width. *X40 magnification*

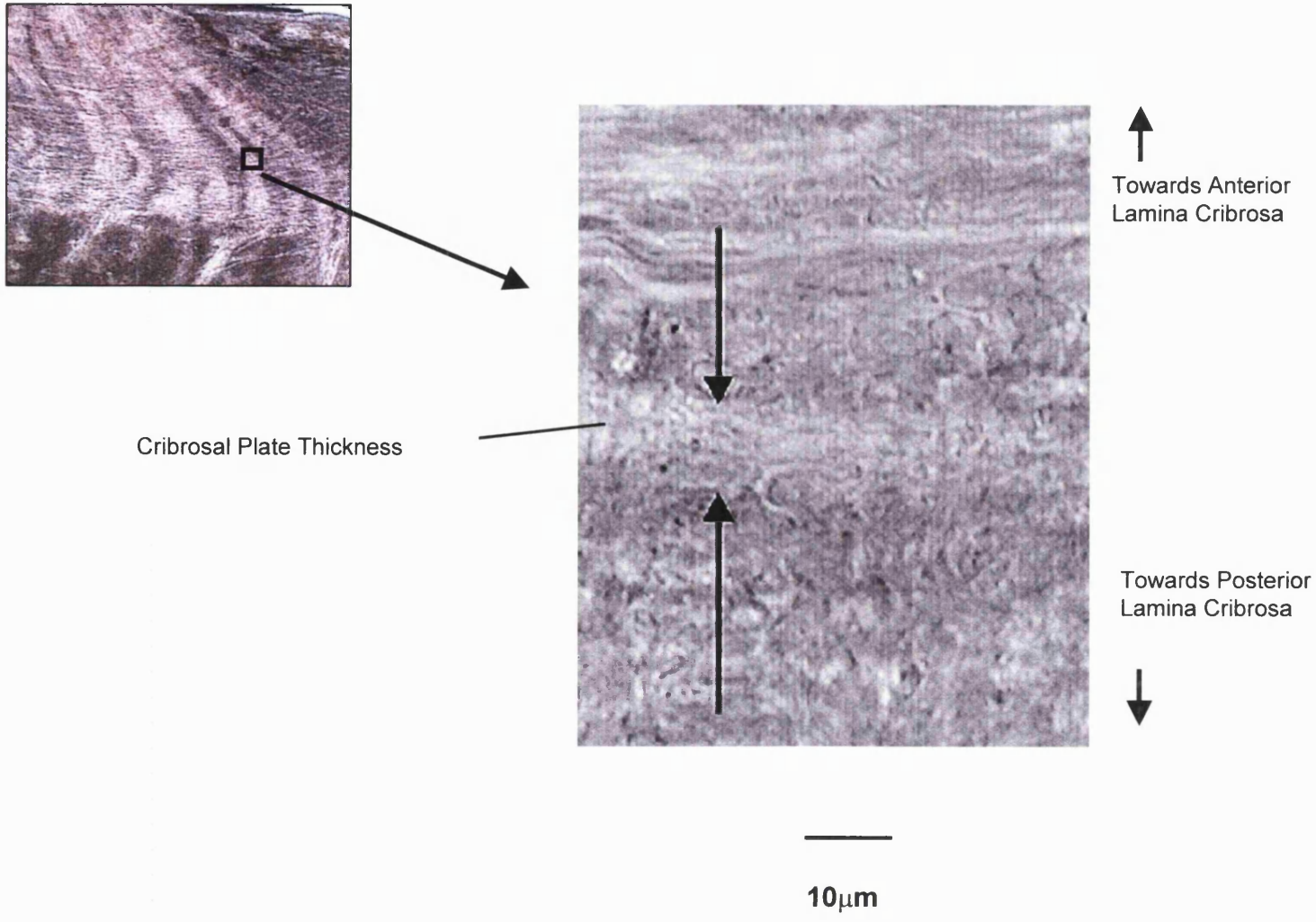

6.1.3 Results

Lamina cribrosa thickness ranged from 0.397 to 0.555 mm (average 0.487mm). There was a positive relationship between lamina cribrosa thickness and age, with increasing thickness as age increased (r^2 = 0.49, $p<0.0001$). This is represented graphically in figure 6.4.

There was a regional difference in cribriform plate thickness, with plates being thickest at the posterior cribrosa section (range posterior 6.12 – 9.69 microns, average 7.45 microns), and thinnest at the anterior cribrosa section (range 3.23 – 6.41 microns, average 4.80 microns) (Figure 6.5). The difference between the plate thickness in the posterior and mid-anterior and posterior and anterior sections of the lamina was statistically significant (Wicoxon $p<0.01$). There was a trend showing an increase in cribriform plate thickness with age (r^2=0.42, $p<0.05$)(Figure 6.6 and table 6.1).

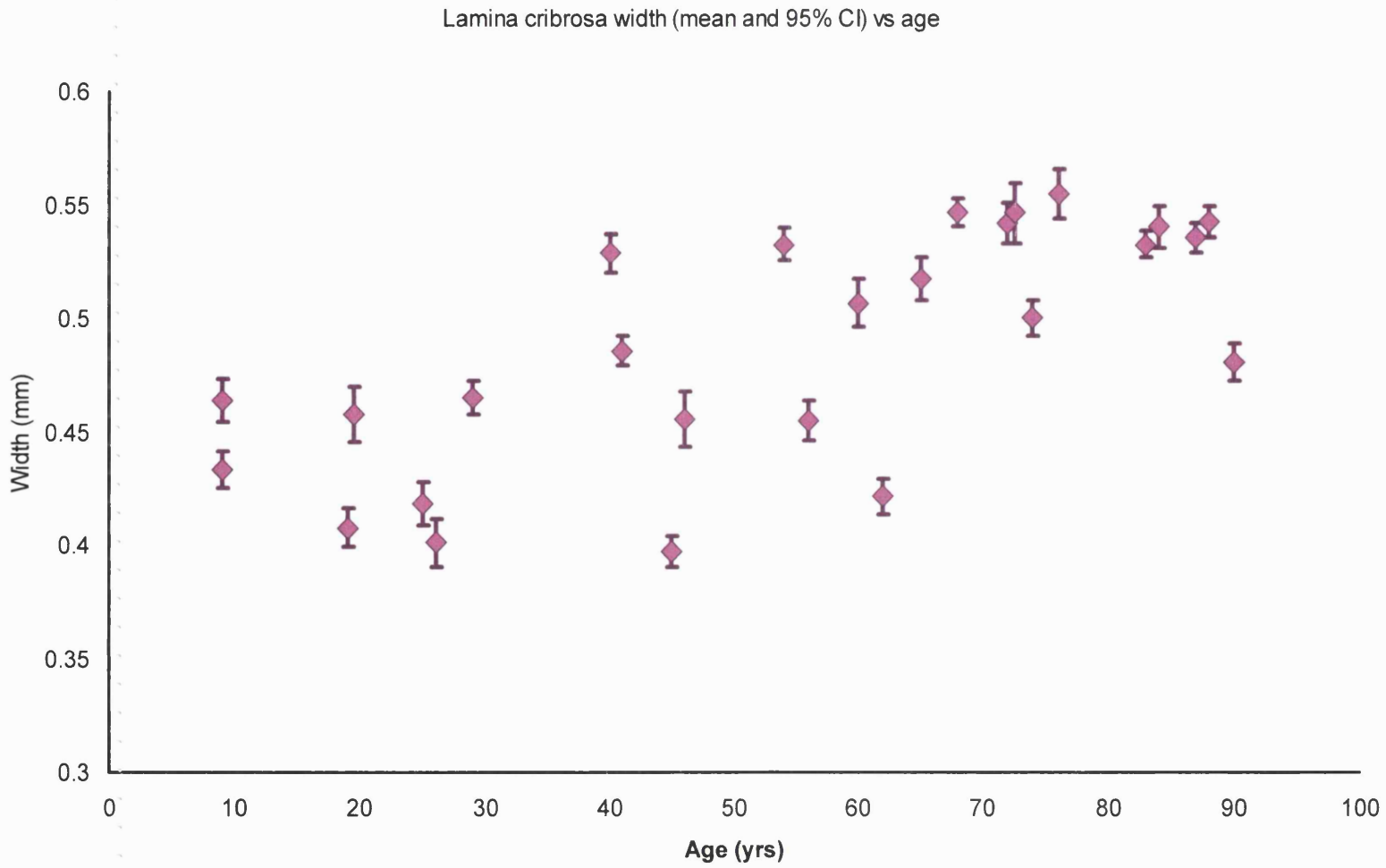

Figure 6.4 : Change in lamina cribrosa width with age: Data points are mean thickness with 95% confidence intervals.

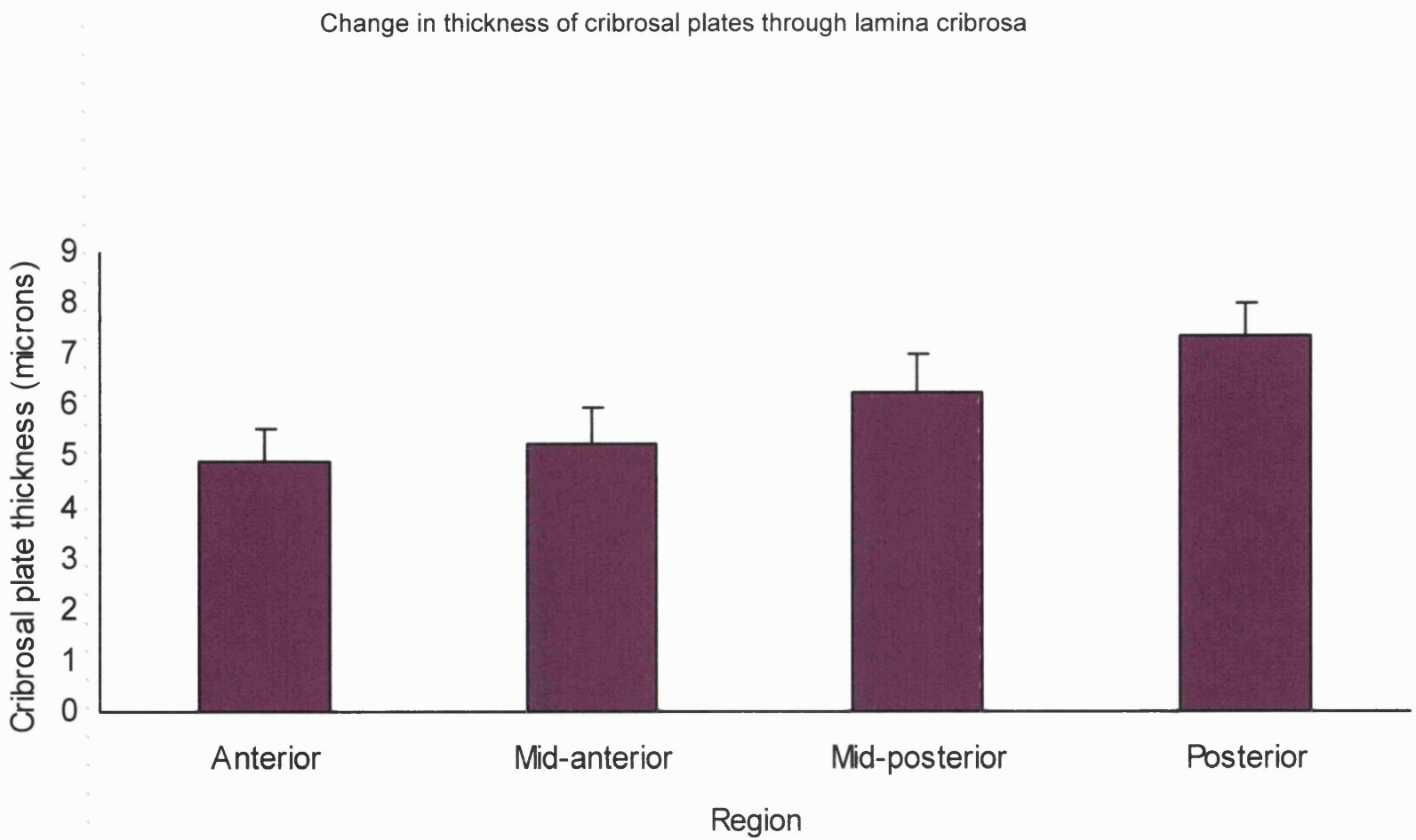

Figure 6.5: Thickness of cribrosal plates through lamina cribrosa. Average thickness of cribrosal plates in the 4 regions as defined in figure 6.2 (n=12). Note how the cribrosal plate thickness is greatest in the posterior region. Plate width in the posterior region is significantly greater than the anterior and mid-anterior regions (Wilcoxon Ranks test, $p<0.01$).

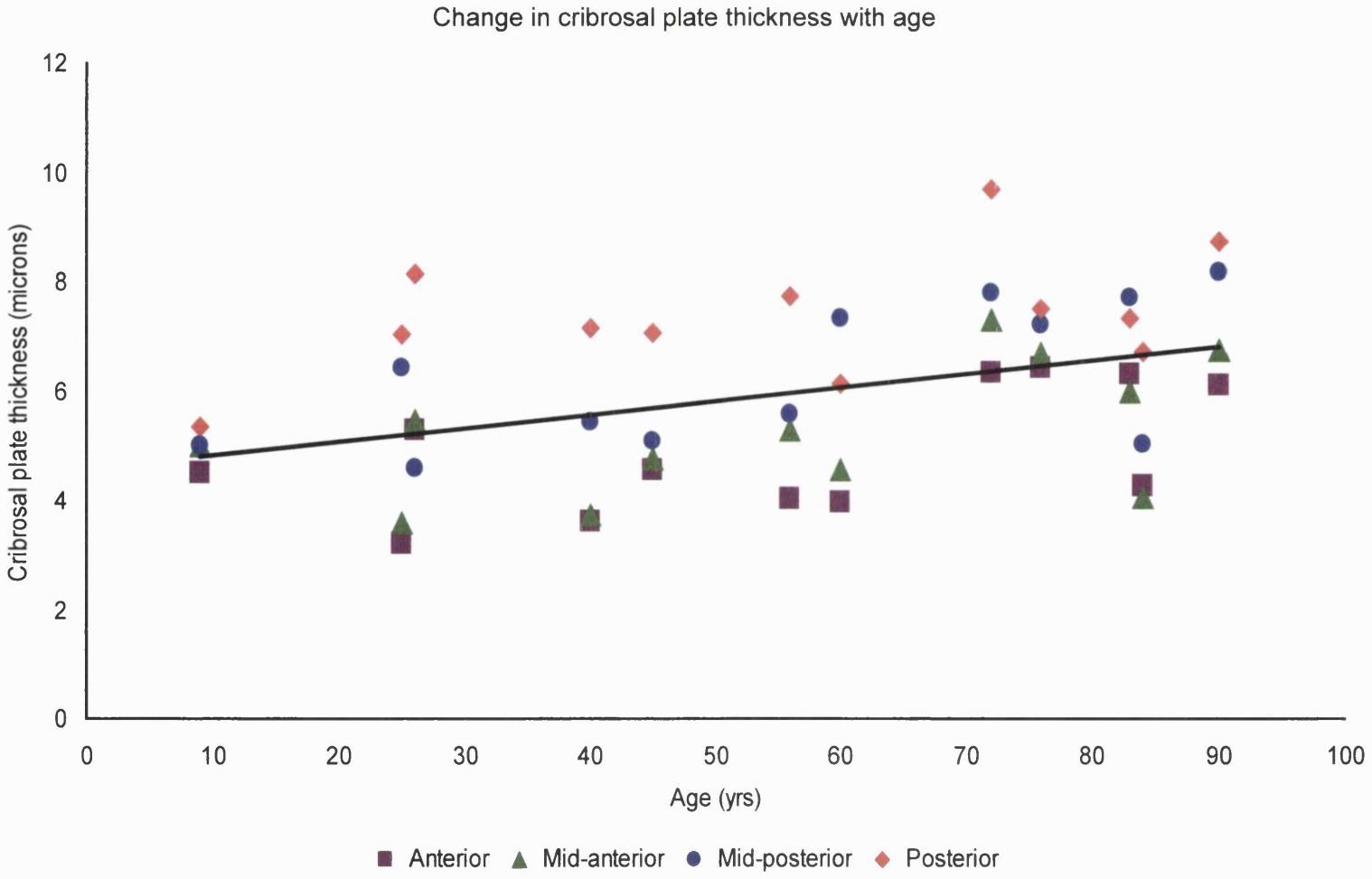

Figure 6.6: Change in cribrosal plate thickness with age- 12 samples. There is an increase in plate thickness with age ($r^2 = 0.42$, $p<0.05$).

Table 6.1: Cribrosal plate thickness change with age.

	Region of lamina (measurements in μ)			
Age (years)	Posterior	Mid-posterior	Mid-anterior	Anterior
9	5.33	4.98	4.98	4.51
25	7.03	6.41	3.59	3.23
26	8.15	4.59	5.46	5.29
40	7.16	5.42	3.74	3.62
45	7.06	5.08	4.75	4.57
56	7.73	5.59	5.29	4.03
60	6.12	7.31	4.57	3.97
72	9.69	7.81	7.31	6.34
76	7.5	7.2	6.69	6.41
83	7.33	7.7	6	6.31
84	6.72	5.01	4.07	4.27
90	8.72	8.18	6.74	6.09

Average thickness in microns of cribrosal plates in each of the areas as defined in figure 6.2. The cribrosal plates are thickest at the posterior lamina cribrosa region, and increase in thickness with age (linear regression, $r^2 = 0.42$, $p<0.05$).

6.1.4 Discussion

The purpose of this study was to investigate the longitudinal architecture of the lamina cribrosa to see if it offered any clues as to the limitations of our *in vivo* imaging technique.

Previous measurements of the thickness of the lamina area in fixed tissue have shown it to be of the order of 0.237mm (Quigley, Hohman et al. 1983). Experimental studies by Yan et al have shown it to range in thickness from 0.1-0.140mm under different pressure loads (Yan, Coloma et al. 1994). Our results using fresh, unfixed specimens indicate that, in conditions that more closely resemble the *in vivo* situation, the region is somewhat thicker. In the earlier study of lamina thickness (Quigley, Hohman et al. 1983), the tissue was investigated using scanning electron microscopy techniques. This involves the digestion and dehydration of tissue during its preparation. It has been shown that removal of axons from lamina cribrosa samples can induce shrinkage and distortion of the extracellular matrix of the region, and that up to 30% shrinkage in tissue occurs during preparation procedures for scanning electron microscopic techniques (Birch, Brotchie et al. 1997). Our findings of thickness approximately 50% greater (fig 6.4) would be expected due to the use of fresh material. The lamina area can be divided into two distinct parts, the prominent posterior lamina area, and the less densely packed anterior area (Radius and Gonzales 1981; Bron, Tripathi et al. 1997). It is possible that under *ex vivo* experimental conditions, as in those in Yan et al's study, the anterior area becomes less prominent, leading to an underestimation of the total lamina thickness.

We also found that the thickness of the lamina cribrosa increased with age, which agrees with most other studies looking at the change in collagen content. Albon et al reported a finding of an increase in the total collagen content of the lamina cribrosa to change from 20% in the young to over 50% in the elderly (Albon, Karwatowski et al. 1995). Morrison et al (Morrison, Jerdan et al. 1989) showed that collagen accumulates after birth and increases throughout life. Hernandez et al found similar changes in the macromolecular content of the optic nerve head with age (Hernandez, Luo et al. 1989), finding that in the ageing

lamina cribrosa there was an increase in the fibrillar forms of collagen in the core of the cribriform plates. Ogden et al (Ogden, Duggan et al. 1988) also found an increased area of connective tissue within the area with progressive age.
It has been observed that the appearance of the lamina cribrosa differs across its thickness, and that the trabeculae, or beams of the lamina cribrosa are less dense in the 'choroidal' (or anterior) lamina than the 'scleral' (or posterior) lamina (Radius and Gonzales 1981). We also observed a change in the degree of compactness of the cribriform plates across the lamina cribrosa, with a more regular arrangement of plates in the posterior regions compared to that found in the anterior region. Figure 6.6 shows that the thickness of the individual cribrosal plates increase with age, and that this rate of increase does not differ regionally i.e. increase is uniform in the posterior and anterior regions. No previous measures of cribrosal plate thickness are available to compare our findings, and this is the first time that measurements of the longitudinal lamina cribrosa area have been performed on hydrated tissue.
This study shows that the thickness of the lamina cribrosa in conditions that closely mimic *in vivo* conditions is greater than previously estimated in dehydrated tissue. It is essential to know the three-dimensional structure of the lamina cribrosa area in order to help us with our understanding of the mechanism of glaucomatous damage. Bellezza et al have published preliminary work modelling the optic nerve head as a biomechanical structure, using finite element modelling to estimate the stress caused by intraocular pressure(Bellezza, Hart et al. 2000). It may be important to not only know the diameter of the scleral opening, but the longitudinal thickness of the lamina cribrosa in further modelling techniques. In addition, in these conditions we have found that cribrosal plates are thicker in the posterior portion of the lamina cribrosa. This is of importance in *in vivo* studies of the lamina cribrosa area, and may also be of importance in development of models to study the effects of mechanical forces on the area to help with our understanding of the mode of glaucomatous damage.

For the purposes of this project, knowing that the longitudinal lamina thickness is of the order of 450 microns upwards helps with our understanding of the quality of images obtained. The FWHM of the Zeiss cSLO system is of the order of 360 microns (section 2.1.2). This means that the 'confocal' slices of the lamina area actually encompass the whole of the lamina cribrosa, possibly including some retrobulbar material as well. The images will, therefore, only be of the surface pore structure, and will be unable to go any deeper without optical modifications to the cSLO. These modifications have been used previously to image the retinal cone mosaic (Fitzke, Woon et al. 1991; Wade 1998). A micro-scanning adapter (MSA) can be attached to the cSLO to reduce the scanning angle of the laser and increase its magnification. This can reduce the FWHM to approximately 30 microns (through a 7mm pupil) (Wade 1998).

Attempts were made in this project to use such an adaptor to image the optic disc in a human subject. However, it was virtually impossible to gain any image data. It was found that using the MSA, only a small proportion of the optic disc would be imaged at any one time (2 degrees visual angle at the retina). For imaging the retinal cone mosaic, the subject was able to fixate directly on the laser imaging light source, (as that was the area that was being imaged). However, for optic disc imaging, off-axis fixation is required. The influence of microsaccadic eye movements is magnified when using the MSA, so only a fleeting glimpse of the optic disc was achieved at any one time. Also, in the images that were gained, it was impossible to establish which area of the disc was actually being imaged. Although a vast improvement in the confocal width of the cSLO is possible with the MSA, it is not feasible to use for imaging the optic disc.

As mentioned in section 1.5.2.4, OCT is becoming an increasingly popular mode of imaging due to the substantial improvement in resolution (both lateral and longitudinal) of the instrumentation compared with the cSLO. Commercially available instrumentation is able to give 'B scan' like images of the retina (figure 6.7). However, although research is being conducted into producing *en face* images of the retina using the OCT, current work suggests that the theoretical

increase in resolution of the instrument does not appear in the *en face* images due to difficulties in imaging the tilted/ spherical retina (Rogers J.A., Podoleanu A. Gh. et al. 2001). Adequate lamina cribrosa images have not been obtained yet using the current *en face* set up (figure 6.8). The results shown in this project show far superior *in vivo* lamina cribrosa images using the cSLO.

Figure 6.7: OCT image of optic disc obtained using the standard OCT

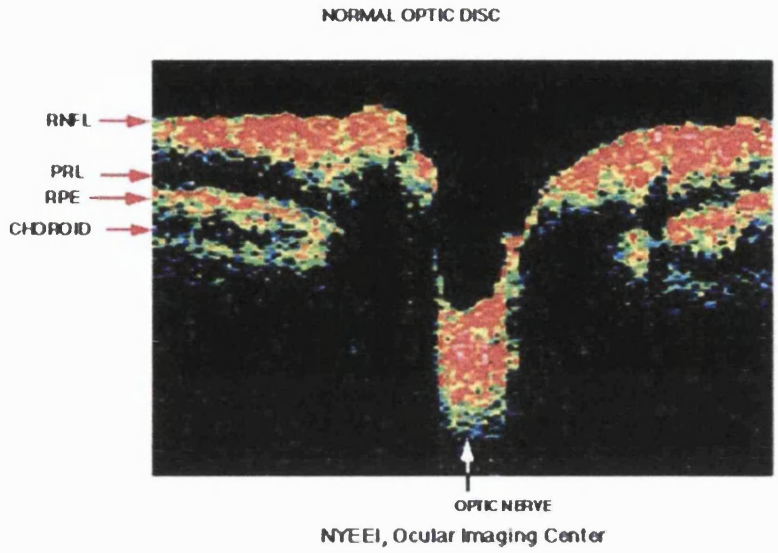

Image taken with a Humphrey OCT, Carl Zeiss Inc.

Taken from webpage http://www.nyee.edu/ with kind permission from Dr. R. Ritch, New York Eye and Ear Infirmary.

The image shows the individual layers of the surrounding retina around the optic nerve head. However, it only gives a longitudinal 'slice' through the retina.

Figure 6.8: *En face* image of optic nerve head taken with a modified OCT

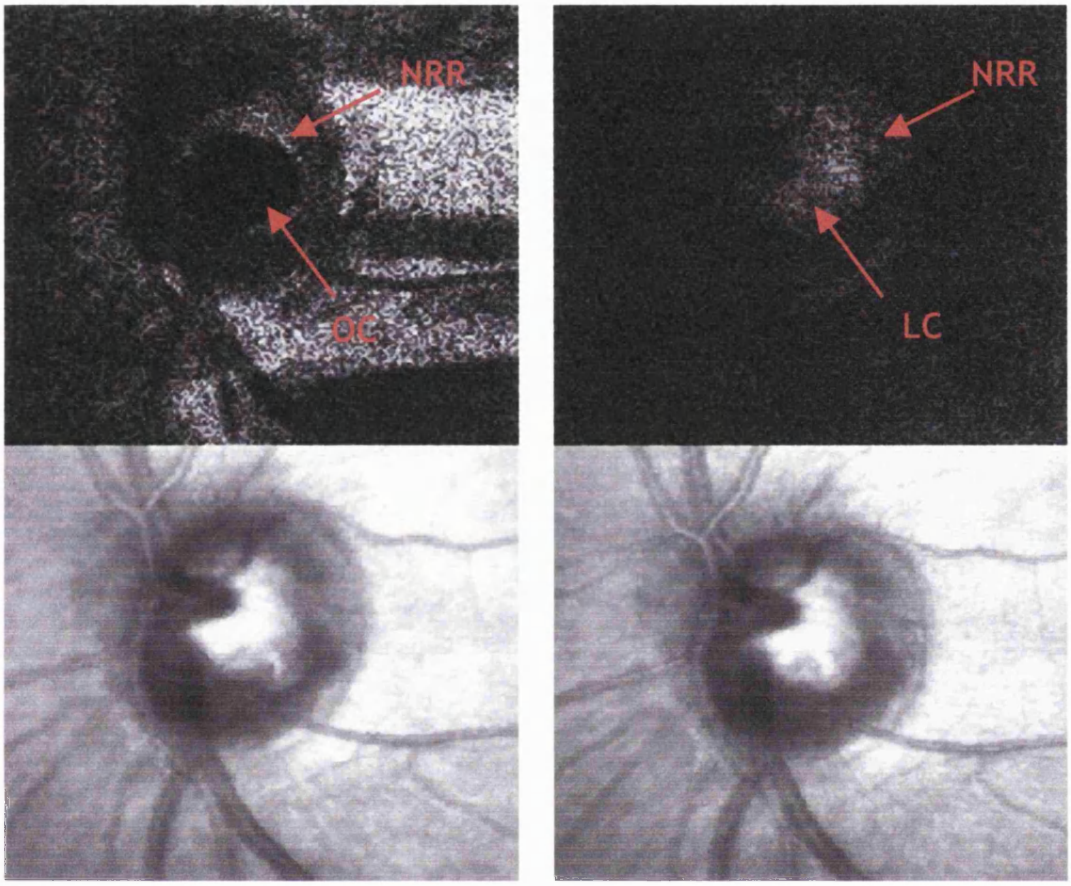

Two depths shown in these split images: *the upper image is an en-face OCT image, the lower a confocal SLO image of the same optic disc.* The image on the left is at the level of the neuroretinal rim, the one on the right is deeper.

KEY: NRR neuroretinal rim LC lamina cribrosa
OC optic cup

Even though the longitudinal resolution of the instrumentation is better than the cSLO, image artefacts due to the tilt and orientation of the eye mean that adequate images of the lamina cribrosa area are not currently possible.
(With thanks to A. Podoleanu and F.W. Fitzke for use of images. A movie file can be viewed at http://www.opticsexpress.org/abstract.cfm?URI=OPEX-9-10-533).

Chapter 7: Conclusions

7.1 Conclusions

In this thesis it has been demonstrated that the superficial surface of the lamina cribrosa in the living eye can be imaged using confocal scanning laser ophthalmoscopy (cSLO). An image processing method was developed that used a Fast Fourier Transform algorithm, and this enabled the analysis of images to measure pore morphology. Unlike previous *in vivo* studies, it was possible to extract pore information from images of eyes that were not pre-selected for their lamina visibility.

The advantage of using confocal optics is that there is a rejection of out of focus light, thus increasing the image contrast. The project found that the wavelength of light at which the lamina cribrosa area was most visible was with a helium-neon laser at 632.8nm. It was not possible to image below the overlying neuroretinal rim using the cSLO set-up, even using longer wavelength infrared light, despite the expected better penetration at this wavelength. This was attributed to the complex tissue structure of the neuroretinal rim causing a scattering of the incident light.

A Fast Fourier Transform algorithm for image processing was developed to analyse the lamina images. This method of image processing offers greater control over the spatial frequency information within the image, and therefore frequencies that were deemed to reduce the image quality were eliminated. This left an image with only structures of interest detailed.

The use of image deconvolution algorithms found that 3 dimensional images of the optic nerve head as taken with a commercially available cSLO, the Heidelberg Retina Tomograph, were suitably enhanced, and had out-of-focus image noise removed. However, this technique was not suitable for the images taken with another cSLO, the Zeiss, because series of depth images were not taken. However, the lateral resolution of the Zeiss was higher and its ability to resolve the lamina cribrosa was better.

For image analysis, it was found that the technique of automated thresholding was a more objective method for detailing lamina pore information and avoided the need for operator intervention. Although manual outlining of the pores gave

information about small pores that were adjacent to each other, and also was able to define out-of focus pores better than the automated thresholding technique- which often merged smaller adjacent and out of focus pores in to one- this technique does have the drawback of operator bias, as well as being more time-consuming.

In order to validate the method of imaging the lamina area, a group of unselected patients with and without glaucoma were imaged. Information about the lamina cribrosa area was successfully obtained from 33 of the 35 patients- it was not possible to obtain adequate images in 2 subjects due to lens opacities. It was found that there was an increase in pore visibility with acquired rim loss. Average pore size increased with increasing rim loss, and this agrees with post mortem findings that find that pore sizes are larger on the edges of the optic disc.

Histological studies were performed to establish the longitudinal thickness of the lamina cribrosa. Previous histological studies have been subject to dehydration artefacts. Consequently, histological analysis of post mortem human lamina cribrosa tissue was conducted using a technique designed to preserve hydration. This found that the longitudinal thickness of the lamina cribrosa was 2/3 greater than that previously reported. This was expected due to the dehydration methods used in previous tissue preparation for electron micrograph imaging. In the over 40 age group, lamina cribrosa thickness was found to be over 400 microns. The resolution of the cSLO system is 360 microns, which closely approaches the total lamina thickness. Consequently the majority of the lamina cribrosa would be expected to contribute to the *in vivo* imaging. Knowing this it may be possible to modify the current cSLO set up to increase the axial resolution to facilitate fine-section imaging of the area.

In conclusion, this study has provided the first quantitative imaging of the lamina cribrosa in subjects unselected for lamina cribrosa visibility. This technique will allow the *in vivo* investigation in glaucoma patients of the structure of this crucial anatomical component that has been implicated as the primary site of damage to the axons of the ganglion cells.

Appendices

I The Heidelberg Retina Tomograph

II Principals of Adaptive Optics

III Matlab Script for Variance Measure

Appendix I: The Heidelberg Retina Tomograph

The most popular commercially available instrument is the Heidelberg Retina Tomograph (HRT, Heidelberg Engineering GmbH, Germany). Due to the confocal optics of the instrument, high resolution 'optical sections' of the area of fundus under investigation are obtained. In the grabbing sequence, the instrument changes focus in an axial manner, thus generating a series of optical sections through the depth of the fundus. There are two models available- the HRT I that was made first available in November 1991, and the more recent HRT II, which was introduced in April 1999. For both HRT models, the laser source is a Helium Neon diode laser of wavelength 670 nm. The laser raster scans the x-y plane to obtain confocal optical sections of the retina. Once one plane has been scanned, the laser changes focus to scan a slightly deeper plane of the retina. This continues until a series of confocal optical sections through the depth of the fundus are obtained. The HRT I alone was used in this project, and therefore details of this model alone will be discussed.

Image acquisition – HRT i

The HRT I makes 32 scans through the retina resulting in a stack of optical sections that represent both an area (x-y) and depth (z) image of the retinal structure under investigation. The field of view can be set to three levels, 10° x 10°, 15° x 15° or 20° x 20°. The depth to which the laser scans varies between 0.5 and 4mm in 0.5 mm steps. Thirty two optical sections are generated at all of these depth levels, so the spacing between sections is closer at the lower depth levels, and greater at the higher depth levels. The camera must be placed 15mm from the examined eye, and the operator centres the optic disc on the monitor. The HRT I software has a quality control mechanism that informs the operator whether the image series is of good quality. Changes in focus and depth setting are advised until the series acquired is optimum. However, the operator has to examine the image series to establish whether there are any image-distorting eye movements. In such cases, the series have to be rejected. Generally, 3 optimum image series are obtained for each eye under examination. The topography images are then generated.

Generation of the topography image

Each confocal section of the 32 image series consists of 256 x 256 pixels. Each pixel location (x, y) has a varying brightness through the series. The distribution of reflected light intensity of each pixel through the 32 series is called the z-profile. The z-profile is a symmetric distribution with a maximum at the location of the light reflecting surface. By determining the position of the profile maximum, the height of each pixel can be determined (figure A1). The topography map is a colour coded representation of each pixel position within the 32 series. Each of the 32 confocal sections has been designated an arbitrary red value. Section 1 is dark red, section 32 is saturated white, and the sections in between decrease in redness from 1 down to 32 in equal 'steps'.

Alongside the topography image is a reflectivity image, which gives the most 'visual' information about the optic disc under examination- similar to a fundus photo (figure A2).

Image analysis

For both instruments, an operator has to define the edge of the optic nerve head, and this is done using the mouse. Once the optic nerve head margin has been defined, area and volumetric information about the optic nerve head are obtained (figure A3).

The Moorfields Regression Analysis

The Moorfields regression analysis software is available with both the HRT I the HRT II. The Moorfields feature was developed from a study of 51 glaucomatous and 80 normal Caucasian subjects (Wollstein, Garway-Heath et al. 1998). The optic disc appearance was not evaluated when establishing the normality of these subjects. The optic discs of these subjects were analysed, and disc parameters for the disc as a whole and in 6 pre-defined sectors were analysed. Linear regression analysis was performed on the relationship between normal disc parameters and optic disc area, and the normal ranges were defined by the 99% prediction intervals. These were applied to the glaucomatous group, and it was found that the parameter that had the greatest sensitivity and specificity for detecting a glaucomatous abnormality was the (log) neuroretinal rim. The

regression analysis feature developed from the results of this study compares the rim area of the optic nerve head imaged to a normal database, and gives a prediction of normality of the disc and sectors of the disc (Wollstein, Garway-Heath et al. 1998). Figure A4 shows an optic nerve head that has been classified according to the feature. Figure A5 shows the details of this classification, and from this it is seen that this disc does not appear to have any glaucomatous damage or any suspicious sectors. Figures A6 and A7 show the results of analysing a glaucomatous disc. The Moorfields feature highlights the rim area of the inferior and superior disc as being outside the normal database range, and the nasal disc rim area as being suspicious.

Figure A1a: Optical sections:

The HRT I takes 32 image series through the depth of the optic nerve head. The software aligns the images (but only compensates for small eye movements) and stacks them. The topography and reflectivity images are then generated.

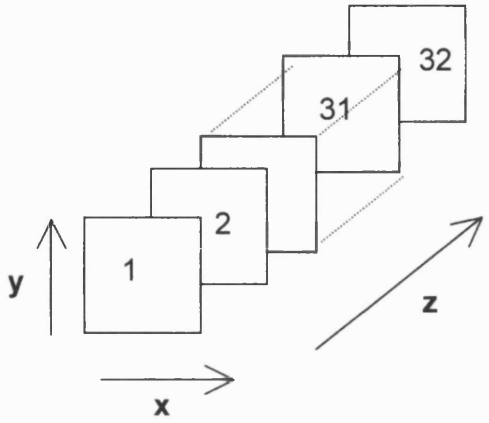

Figure A1b: Z-profile of pixel (x,y) in image series:

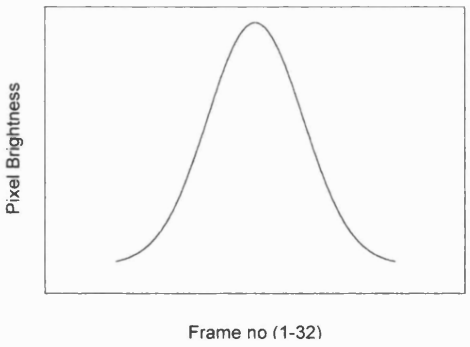

The frame in which the pixel has maximum brightness is at the depth of that pixel. By calculating the peak brightness of each of the 256 x 256 pixels, the topography of the optic nerve head can be determined.

Figure A2: Topography and reflectivity image

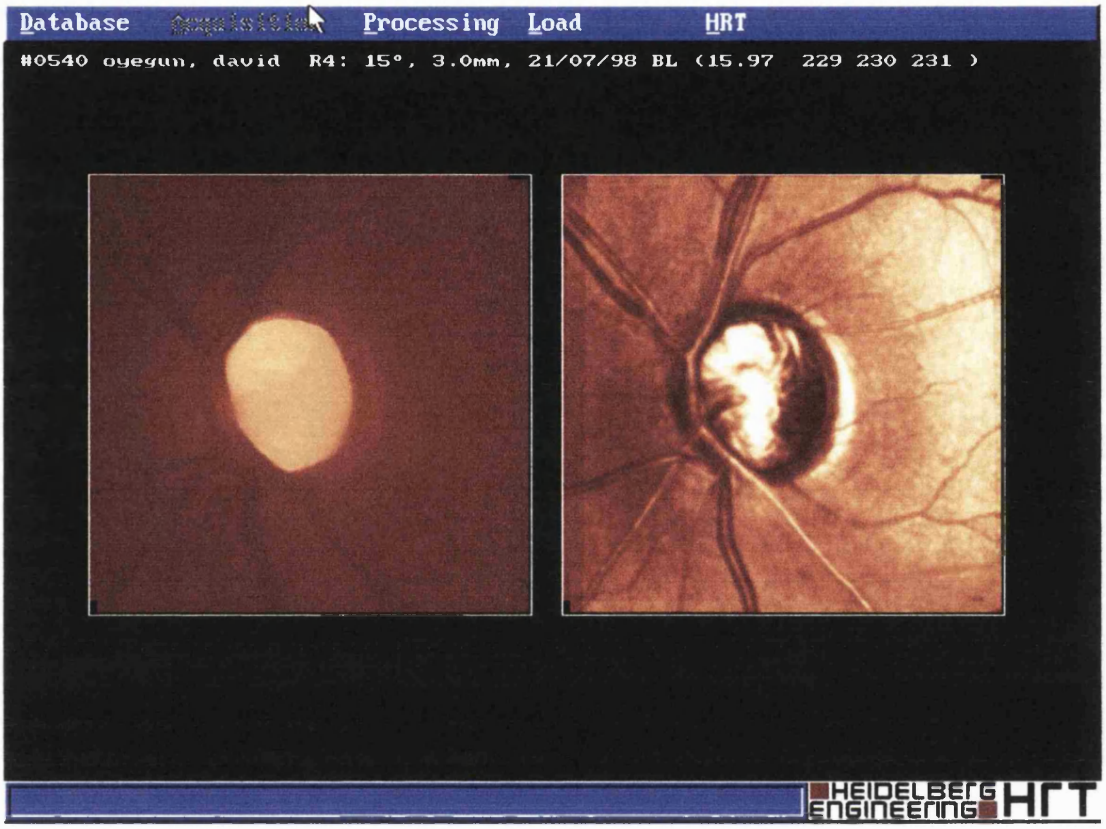

The topography (left) image is a colour-coded map. The redder areas are on the surface and the whiter areas are deeper in the scan. The reflectivity image (right) approximates a mean brightness of all the pixels.

Figure A3: Stereometric parameters – HRT I

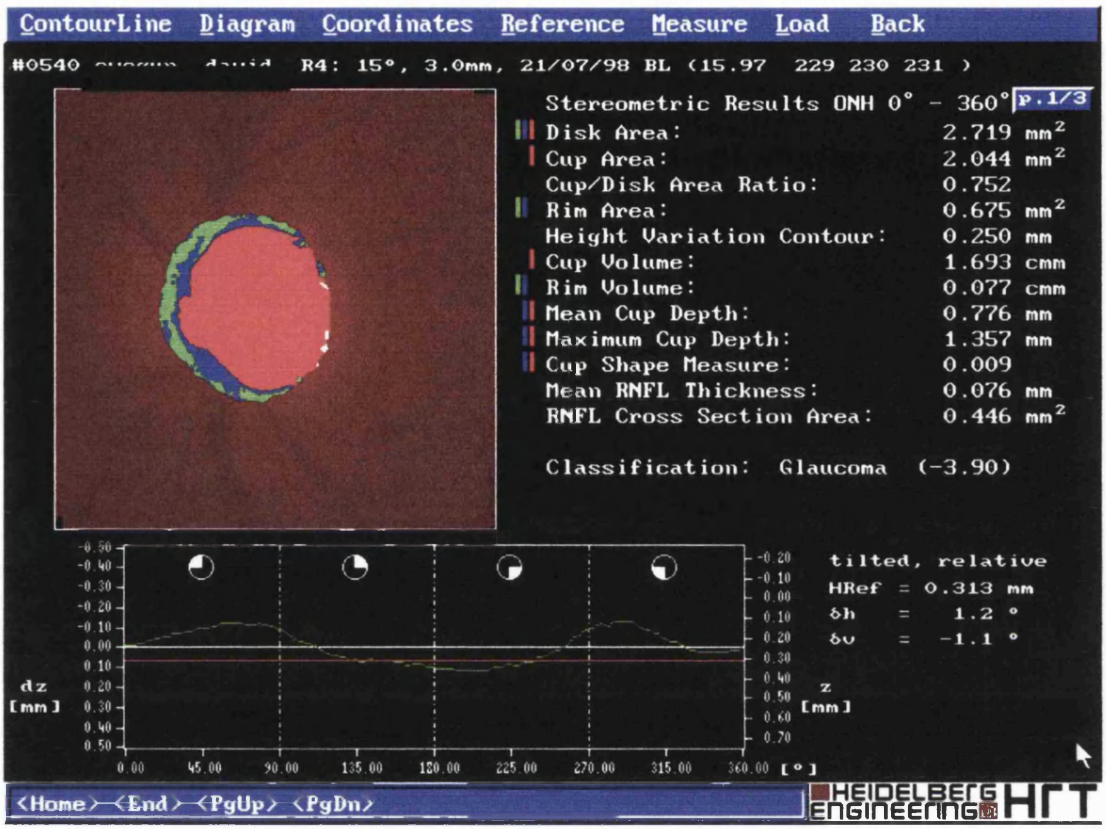

Once the contour line of the optic disc has been delineated, it is possible to extract information about the topography of the disc. The classification index of this disc is based on the Mikelberg ranked sector analysis.

Figure A4: Disc analysis with HRTII- Moorfields analysis feature

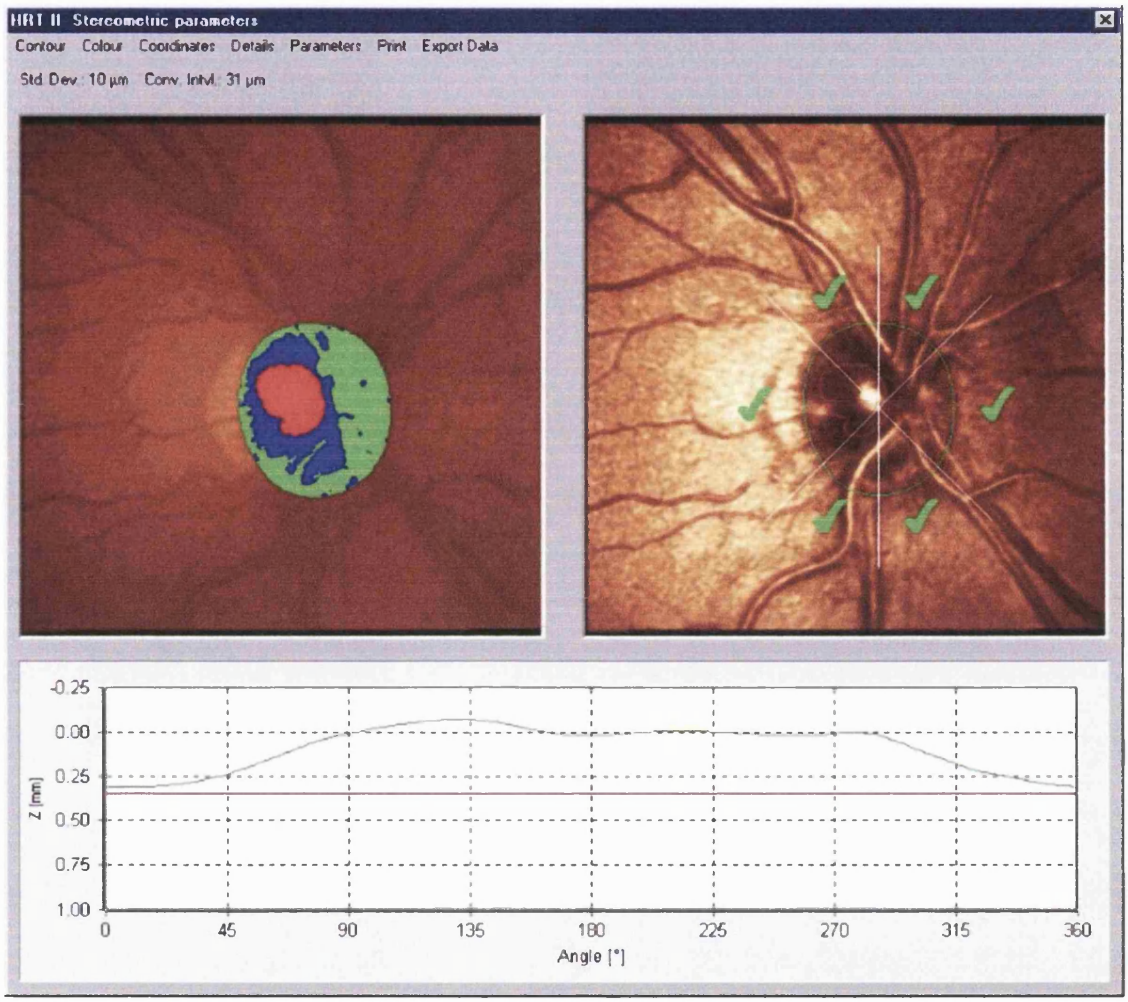

Once the contour line has been drawn, there is the option of using the Moorfields regression feature. This compares the optic disc imaged to a normal database and predicts the normality of the disc.

Figure A5: Moorfields analysis feature- details

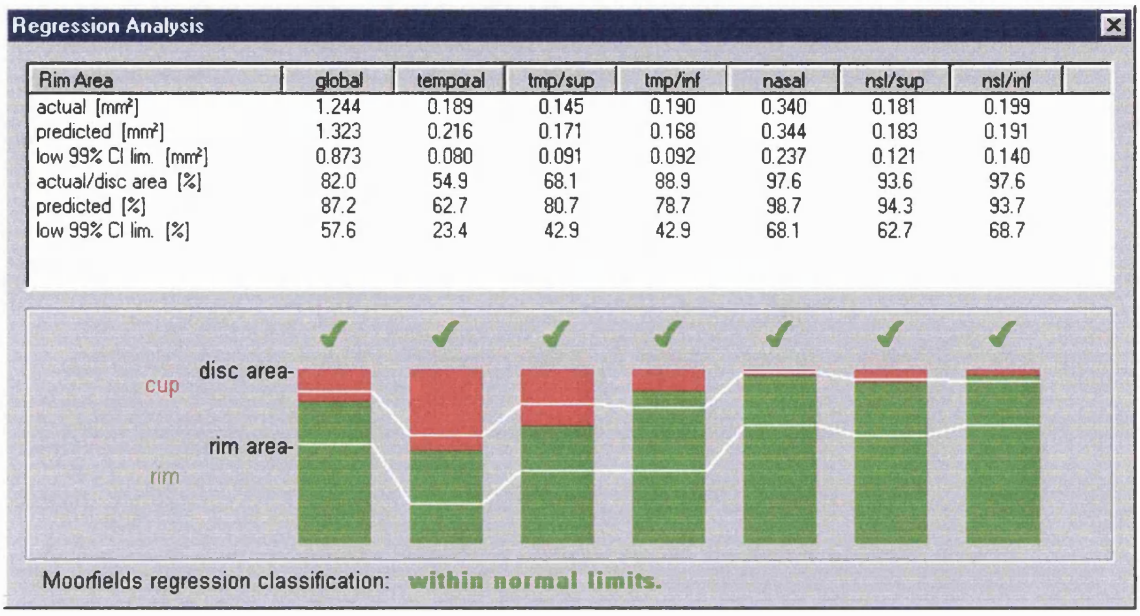

The regression classification looks at the disc overall and at 6 pre-defined sectors.

Figure A6: Disc analysis- glaucomatous disc

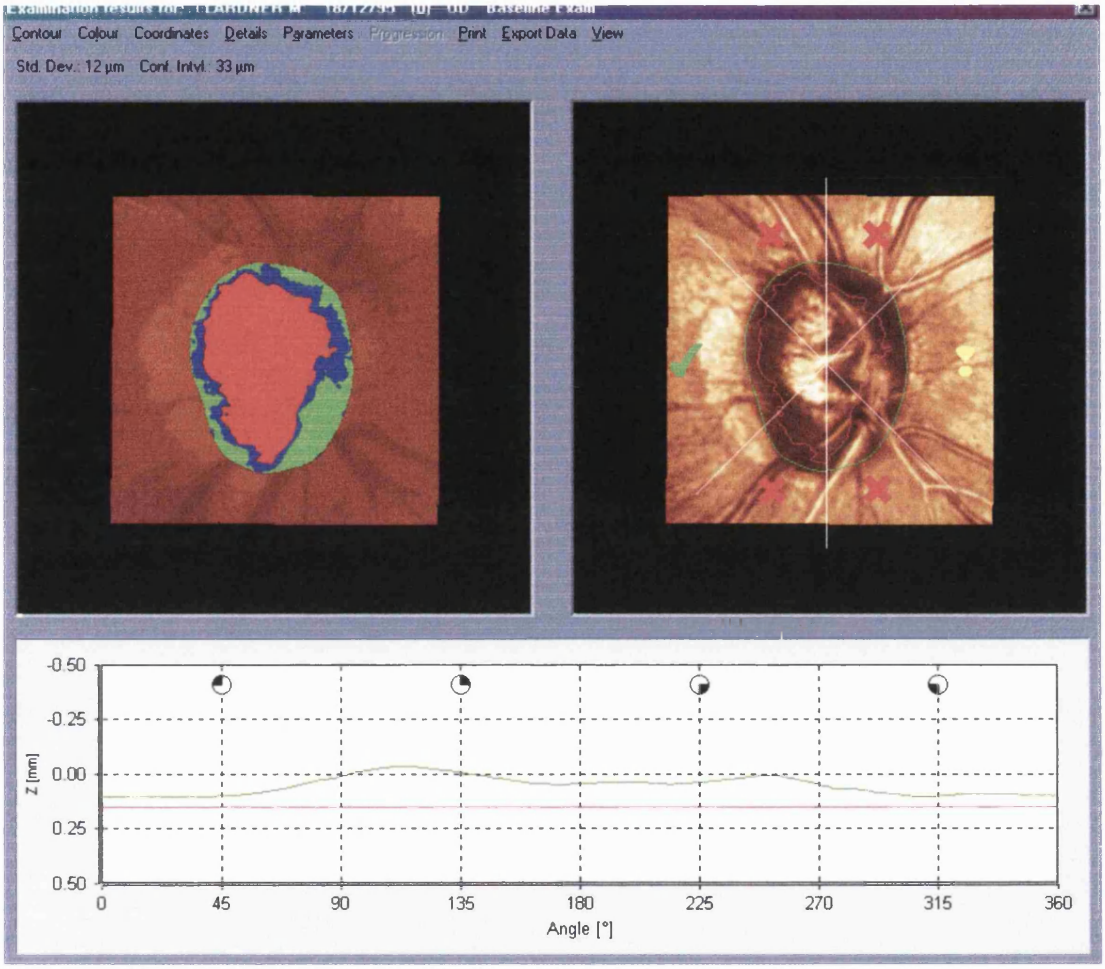

The inferior and superior sectors of the disc are deemed to be glaucomatous, the nasal sector suspicious, and the temporal sector is said to be normal.

Figure A7: Moorfields analysis feature- details

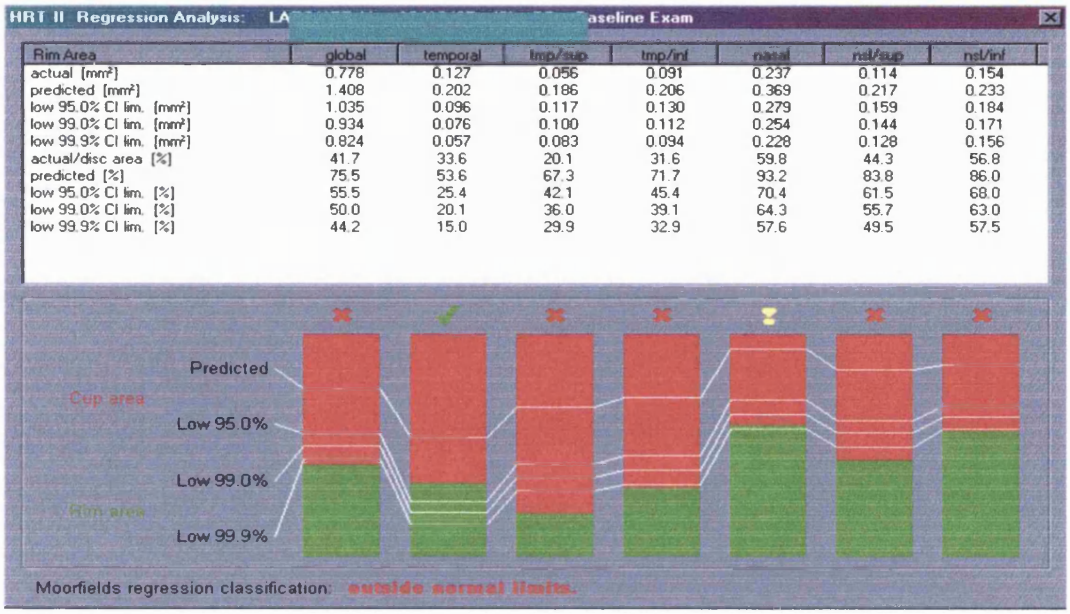

The details here show the 95%, 99% and 99.9% confidence intervals.

Appendix II: Principals of adaptive optics

Rayleighs criterion for the resolution of a telescope:

$$\alpha = 1.22\lambda / D$$

where α is the resolution in arc radians, and λ is the wavelength of light in nanometers (usually taken as 550nm), and D the diameter of the telescope in metres, assumes that the only limitation to the resolution of the system is diffraction. However, in reality this is not the case when viewing objects in space. Turbulence in the Earth's atmosphere produces inhomogeneities in the air refractive index that distorts astronomical images. So, large diameter telescopes deliver more light but no extra clarity. One of the ways to overcome this is to launch telescopes into space (such as the Hubble Space Telescope). However, this is a rather expensive option. In 1953, Horace Babcock, an astronomer at Mount Wilson Observatory in Pasedena, California, published his idea of *adaptive optics (AO)*. The process described by Babcock involved measuring the distortions of an incoming wavefront from a known source and correcting them very quickly so as to follow the rapidly changing patterns of atmospheric turbulence. The initial correction was done by using a tip-tilt mirror, which involved tilting the mirror several times a second to correct for the distortions.

Figure A8: Principle of deformable mirror

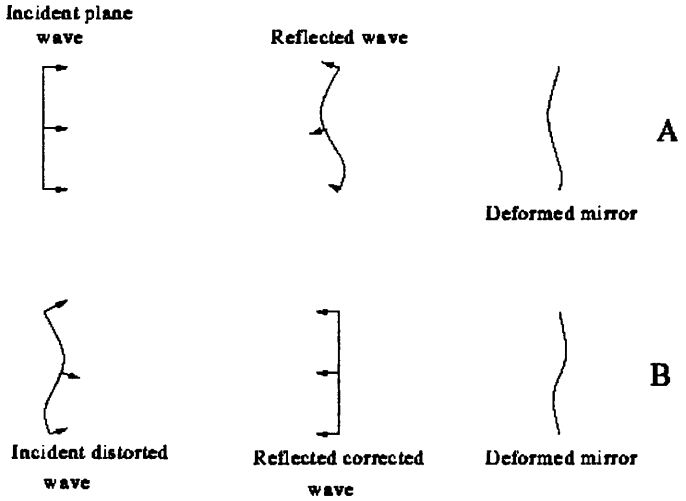

The mirror is deformed to compensate for irregularities in the incoming wavefront.

Nowadays, the system is more sophisticated due to the vast improvements in computer technology. The principle works thus: light from a distant bright object (known as a Guide Star or beacon) is passed through the telescope optics (figure A9). A beam splitter will send part of the light to a wavefront sensor. The wavefront sensor is often a collection of tiny lenslets that focuses the light onto a ccd camera (known as the Hartmann-Shack wavefront sensor).
Without any atmospheric distortion, the incoming light will be focussed by the lenslets into a regular array. The presence of atmospheric turbulence will result in an irregular image (Figure A10).
By rapidly measuring the mal-position of the spots, the electronics can send information to a computer that can adjust the deformable mirror to compensate for the atmospheric turbulence. This is then applied to the image of the unknown object under view. As changes in the atmosphere occur over the course of a few milliseconds, the speed of sensor detection, correction and application to the deformable mirror is extremely quick.

AO was first used in retinal imaging by Dreher and colleagues who used it to correct for aberration induced by the cornea and lens when imaging with a dilated pupil (Dreher, Bille et al. 1989). They used a Hartmann-Shack wavefront sensor, but many others are available [, 1988 #738]. The basic method is thus: collimated light from a laser source (most often HeNe) is passed into the eye and reflects off the retina. The reflected light, having passed through the cornea and lens, emerges from the pupil and is relayed to the Hartmann-Shack wavefront sensor, and the aberrations are detected and measured in the same way as that used for astronomical imaging (fig A10). By detecting the eyes aberrations, accurate corrections can be applied and this results in a vast improvement in the resolution of retinal images.
Using AO, Dreher and colleagues (Dreher, Bille et al. 1989) achieved a FWHM of 220 microns with a pupil diameter of 6.0mm. Since then, work has been done to image the retinal cone mosaic using AO, achieving a resolution of 1.4 microns laterally and 19 microns axially (Roorda 2000). Adaptive optics is also finding a

use in corneal refractive surgery (specifically laser in situ keratomilieusis, or LASIK). Laser refractive surgery corrects the sphero-cylinderical refractive errors of the eye, but in the process can often increase the effect of the higher order aberrations (such as coma and spherical aberration) . Wavefront-guided LASIK uses AO to try and compensate for these high order aberrations.

Figure A9: Principle of an adaptive optics system.

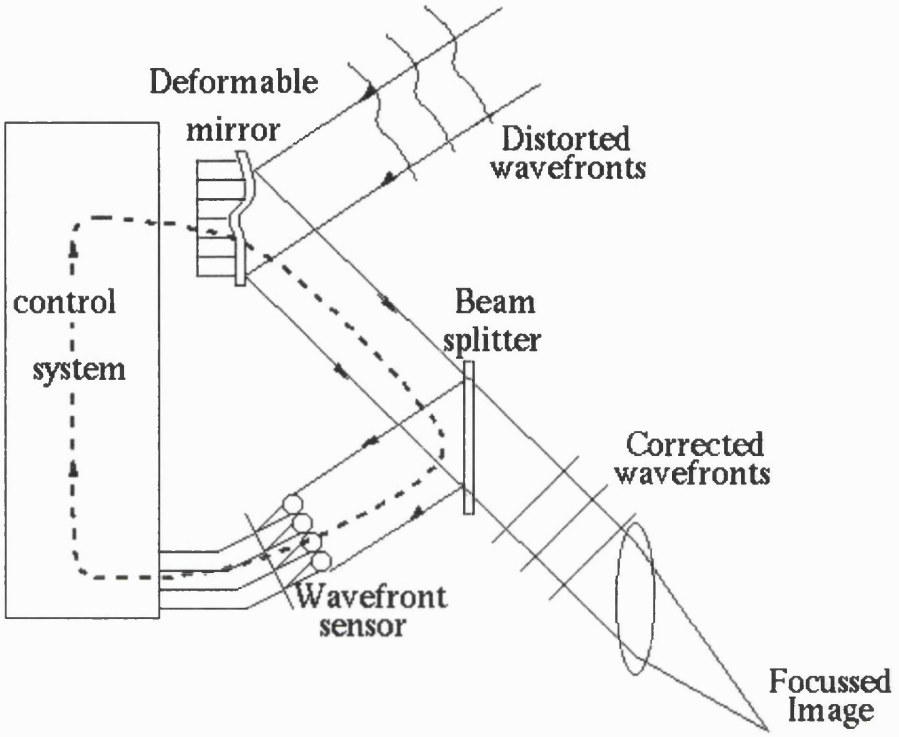

Light from a distant source is imaged through the telescope that has a deformable mirror. The light is split by a beam splitter that sends part of it to a wavefront sensor that identifies the distortions and sends corrections electronically to the deformable mirror so as to compensate for the distortions. This changes rapidly with changes in the atmospheric turbulence. Real-time focussed images of the object in question can therefore be produced.

Figure A10: Schematic diagram of wavefront detector.

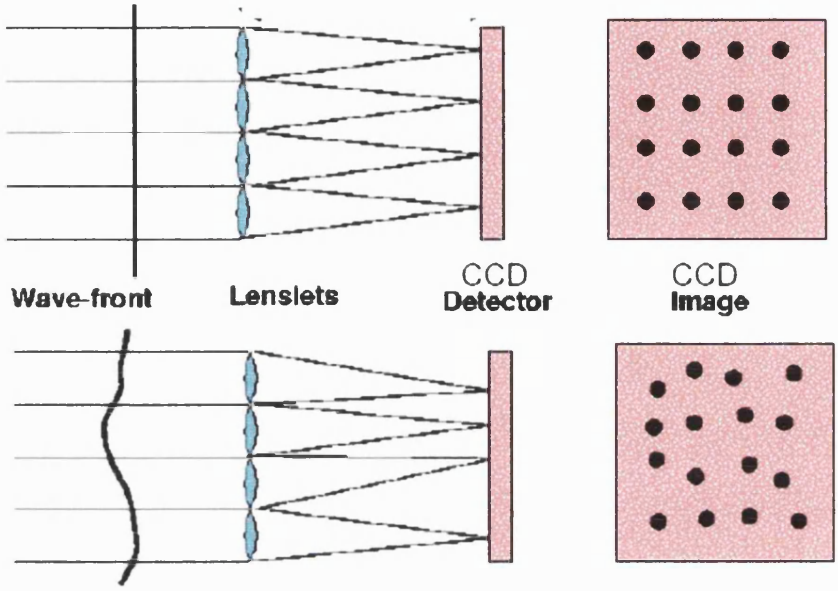

The above panel shows the ccd image produced by light unaffected by atmospheric turbulence. The panel below shows light affected by distortions. In this case, the irregularities in the array are corrected, and the compensatory factor is relayed to a computer controlling the deformable mirror. The mirror is deformed accordingly so that the image produced becomes virtually free from these distortions.

Figures A8 and A9 from
http://www.ctio.noao.edu/~atokovin/tutorial/part3/wfs.html
With kind permission from Andrei Tokovinin, Cerro Tololo Inter-American Observatory, La Serena, Chile.

Figure A10 from
http://www.met.ed.ac.uk/courses/projects/stuart_macrobbie/
With kind permission from S.G. McRobbie, Institute for Meteorology, University of Edinburgh, Scotland.

Appendix III: Matlab Script for variance measure

```
function af_analysis_script Dr A.S. Halfyard
%note: as this is a function all these vars are local and are not returned at the
end.
%af,analysis (simple version).
%PARAMS
LENGTH=750;
clim=[0 256];
BCK_SQ=10;
SAMPLE_WIDTH=5;
BRIGHTNESS=40; %WHITE BAND BRIGHTNESS

%read in the image
af=imread(filename);
colormap gray;
af=double(af);
af_image=af;cdcdcd
                        figure(1);imagesc(af_image,clim);
%locate the disc edges

TITLE ('Get Top Left');
[X1,Y1]=ginput(1);
X1=round(X1);
Y1=round(Y1);
TITLE ('Get Bottom Right');
[X2,Y2]=ginput(1);
X2=round(X2);
Y2=round(Y2);

af_sub=af(Y1:Y2,X1:X2);
[row_size,col_size]=size(af_sub)
imagesc(af_sub);
number_of_pixels=(X2-X1)*(Y2-Y1);
fprintf(1,'Number of pixels=%8f\n',number_of_pixels);
a=zeros(1,number_of_pixels);
for j=0:row_size-1,
for i=1:col_size,
        a(1+j*col_size:(j*col_size)+col_size)=af_sub(j+1,1:col_size);
end
end
variance_image=var(af_sub);
fprintf(1,'Variance=%6.2f\n',mean(variance_image));
```

References

References

(1990). Non-invasive Diagnostic Techniques in Ophthalmology. New York, Springer-Verlag.

(1996). Theory and Practice of Histology Techniques, Churchill Livingstone.

Airaksinen, P. J., A. Tuulonen, et al. (1992). "Rate and pattern of neuroretinal rim area decrease in ocular hypertension and glaucoma." Arch Ophthalmol **110**(2): 206-10.

Albon, J., W. S. Karwatowski, et al. (1995). "Changes in the collagenous matrix of the aging human lamina cribrosa." Br-J-Ophthalmol **79**(4): 368-75 issn: 0007-1161.

Albon, J., P. P. Purslow, et al. (2000). "Age related compliance of the lamina cribrosa in human eyes." Br J Ophthalmol **84**(3): 318-23.

Analoui, M. (2001). "Radiographic image enhancement. Part I: spatial domain techniques." Dentomaxillofac Radiol **30**(1): 1-9.

Anderson, D. R. (1969). "Ultrastructure of human and monkey lamina cribrosa and optic nerve head." Arch Ophthalmol **82**(6): 800-14.

Assad, A. and J. Caprioli (1992). "Digital image analysis of optic nerve head pallor as a diagnostic test for early glaucoma." Graefes Arch Clin Exp Ophthalmol **230**(5): 432-6.

Barry, C. J., R. L. Cooper, et al. (1990). "Simplification of unsharp masking in retinal nerve fibre layer photography." Aust N Z J Ophthalmol **18**(4): 411-20.

Bartz-Schmidt, K. U., M. Sundtgen, et al. (1995). "Limits of two-dimensional planimetry in the follow-up of glaucomatous optic discs [see comments]." Graefes Arch Clin Exp Ophthalmol **233**(5): 284-90.

Bartz-Schmidt, K. U., J. Weber, et al. (1994). "Validity of two-dimensional data obtained with the Heidelberg Retinal Tomograph as verified by direct measurements in normal optic nerve heads." Ger Journal of Ophthalmology **3**: 400-405.

Beems, E. M. and J. A. Van Best (1990). "Light transmission of the cornea in whole human eyes." Exp Eye Res **50**(4): 393-5.

Bellezza, A. J., R. T. Hart, et al. (2000). "The optic nerve head as a biomechanical structure: initial finite element modeling." Invest Ophthalmol Vis Sci **41**(10): 2991-3000.

Benedek, G. B. (1971). "Theory of transparency of eye." Appl. **10**: 459-473.

Bengtsson, B. and C. E. Krakau (1992). "Correction of optic disc measurements on fundus photographs." Graefes Arch Clin Exp Ophthalmol **230**(1): 24-8.

Bennett, A. G. and R. B. Rabbetts (1984). Clinical Visual Optics, Butterworths.

Bennett, A. G., A. R. Rudnicka, et al. (1994). "Improvements on Littmann's method of determining the size of retinal features by fundus photography." Graefes Arch Clin Exp Ophthalmol **232**(6): 361-7.

Bhandari, A., L. Fontana, et al. (1997). "Quantitative analysis of the lamina cribrosa in vivo using a scanning laser opthalmoscope." Curr-Eye-Res **16**(1): 1-8 issn: 0271-3683.

Birch, M., D. Brotchie, et al. (1997). "The three-dimensional structure of the connective tissue in the lamina cribrosa of the human optic nerve head." Ophthalmologica **211**(3): 183-91.

Bland, J. M. and D. G. Altman (1986). "Statistical methods for assessing agreement between two methods of clinical measurement." Lancet **1**(8476): 307-10.

Britton, R. J., S. M. Drance, et al. (1987). "The area of the neuroretinal rim of the optic nerve in normal eyes." Am J Ophthalmol **103**(4): 497-504.

Bron, A. J., R. C. Tripathi, et al. (1997). Wolff's Anatomy of the Eye and Orbit, Chapman and Hall.

Campbell, F. W. and R. W. Gubisch (1966). "Optical quality of the human eye." J Physiol (Lond) **186**(3): 558-78.

Caprioli, J., U. Klingbeil, et al. (1986). "Reproducibility of optic disc measurements with computerized analysis of stereoscopic video images." Arch Ophthalmol **104**(7): 1035-9.

Caprioli, J. and J. M. Miller (1987). "Optic disc rim area is related to disc size in normal subjects." Arch Ophthalmol **105**(12): 1683-5.

Chauhan, B. C., R. P. LeBlanc, et al. (1994). "Test-retest variability of topographic measurements with confocal scanning laser tomography in patients with glaucoma and control subjects." Am J Ophthalmol **118**(1): 9-15.

Chauhan, D. S. and J. Marshall (1999). "The interpretation of optical coherence tomography images of the retina." Invest Ophthalmol Vis Sci **40**(10): 2332-42.

Cioffi, G. A., A. L. Robin, et al. (1993). "Confocal laser scanning ophthalmoscope. Reproducibility of optic nerve head topographic measurements with the confocal laser scanning ophthalmoscope." Ophthalmology **100**(1): 57-62.

Claridge, K. G., J. K. Galbraith, et al. (1995). "The effect of trabeculectomy on refraction, keratometry and corneal topography." Eye **9**(Pt 3): 292-8.

Cunliffe, I. A., R. B. Dapling, et al. (1992). "A prospective study examining the changes in factors that affect visual acuity following trabeculectomy." Eye **6**(Pt 6): 618-22.

Dandona, L., H. A. Quigley, et al. (1990). "Quantitative regional structure of the normal human lamina cribrosa. A racial comparison." Arch Ophthalmol **108**(3): 393-8.

Delaye, M. and A. Tardieu (1983). "Short-range order of crystalline proteins accounts for eye lens transperancy." Nature **302**(5907): 415-7.

Delori, F. C. and E. S. Gragoudas (1976). "Examination of the ocular fundus with monochromatic light." Ann Ophthalmol **8**(6): 703-9.

Delori, F. C., E. S. Gragoudas, et al. (1977). "Monochromatic ophthalmoscopy and fundus photography. The normal fundus." Arch Ophthalmol **95**(5): 861-8.

Delori, F. C. and K. P. Pflibsen (1989). "Spectral reflectance of the human ocular fundus." Appl Optics **28**(6): 1061-77.

Dreher, A. W., J. F. Bille, et al. (1989). "Active optical depth resolution improvement of the laser tomographic scanner." Appl Optics **28**(4): 804-8.

Dreher, A. W., P. C. Tso, et al. (1991). "Reproducibility of topographic measurements of the normal and glaucomatous optic nerve head with the laser tomographic scanner." Am J Ophthalmol **111**(2): 221-9.

Drexler, W., U. Morgner, et al. (2001). "Ultrahigh-resolution ophthalmic optical coherence tomography." Nat Med **7**(4): 502-7.

Elsner, A. E., S. A. Burns, et al. (1996). "Infrared imaging of sub-retinal structures in the human ocular fundus." Vision Res **36**(1): 191-205.

Emery, J. M., D. Landis, et al. (1974). "The lamina cribrosa in normal and glaucomatous human eyes." Trans Am Acad Ophthalmol Otolaryngol **78**(2): Op290-7.

Fercher, A. F., C. K. Hitzenberger, et al. (1993). "In vivo optical coherence tomography." Am J Ophthalmol **116**(1): 113-4.

Feuk, T. (1970). "On the transparency of the stroma in the mammalian cornea." IEEE Trans Biomed Eng **17**(3): 186-90.

Fincham, W. H. A. and M. H. Freeman (1980). Optics, Butterworths.

Fitzke, F. W. and B. R. Masters (1993). "Three-dimensional visualization of confocal sections of in vivo human fundus and optic nerve." Curr Eye Res **12**(11): 1015-8.

Fitzke, F. W., H. Woon, et al. (1991). "Optical modifications to a Scanning Laser Ophthalmoscope for high magnification, narrow optical sectioning." Lasers and Light in Ophthalmology **4**(1): 7-14.

Fontana, L., A. Bhandari, et al. (1998). "In vivo morphometry of the lamina cribrosa and its relation to visual field loss in glaucoma." Curr Eye Res **17**(4): 363-9.

Friedman, N. E., K. Zadnik, et al. (1996). "Quantifying corneal toricity from videokeratography with Fourier analysis." J Refract Surg **12**(1): 108-13.

Frisen, L. and W. F. Hoyt (1973). "Unsharp masking in fundus photography." Invest Ophthalmol **12**(6): 461-4.

Fujimoto, J. G., M. E. Brezinski, et al. (1995). "Optical biopsy and imaging using optical coherence tomography." Nat Med **1**(9): 970-2.

Garway Heath, D. F., A. R. Rudnicka, et al. (1998). "Measurement of optic disc size: equivalence of methods to correct for ocular magnification." Br J Ophthalmol **82**(6): 643-9.

Garway-Heath, D. F., D. Poinoosawmy, et al. (1999). "Inter- and intraobserver variation in the analysis of optic disc images: comparison of the Heidelberg retina tomograph and computer assisted planimetry." Br J Ophthalmol **83**(6): 664-9.

George, L. D., J. Lusty, et al. (1999). "Effect of software manipulation (Photoshop) of digitised retinal images on the grading of diabetic retinopathy." Br J Ophthalmol **83**(8): 911-3.

Halfyard, A. S., A. R. Wade, et al. (1999). Grabber 3.

Hernandez, M. R., W. M. Andrzejewska, et al. (1990). "Changes in the extracellular matrix of the human optic nerve head in primary open-angle glaucoma." Am J Ophthalmol **109**(2): 180-8.

Hernandez, M. R., X. X. Luo, et al. (1989). "Age-related changes in the extracellular matrix of the human optic nerve head." Am J Ophthalmol **107**(5): 476-84.

Hernandez, M. R., X. X. Luo, et al. (1987). "Extracellular matrix of the human lamina cribrosa." Am J Ophthalmol **104**(6): 567-76.

Hitchings, R. A. (2000). Glaucoma. London, BMJ Publishing Group.

Hollows, F. C. and P. A. Graham (1966). "Intra-ocular pressure, glaucoma, and glaucoma suspects in a defined population." Br J Ophthalmol **50**(10): 570-86.

Huang, D., E. A. Swanson, et al. (1991). "Optical coherence tomography." Science **254**(5035): 1178-81.

Hugkulstone, C. E. (1991). "Changes in keratometry following trabeculectomy." Br J Ophthalmol **75**(4): 217-8.

Iester, M., F. S. Mikelberg, et al. (1997). "Correlation between the visual field indices and Heidelberg retina tomograph parameters." J Glaucoma **6**(2): 78-82.

Iester, M., N. V. Swindale, et al. (1997). "Sector-based analysis of optic nerve head shape parameters and visual field indices in healthy and glaucomatous eyes." J-Glaucoma **6**(6): 370-6.

Izatt, J. A., M. R. Hee, et al. (1994). "Micrometer-scale resolution imaging of the anterior eye in vivo with optical coherence tomography." Arch Ophthalmol **112**(12): 1584-9.

Jonas, J. B., G. C. Gusek, et al. (1988). "Optic disc morphometry in chronic primary open-angle glaucoma. I. Morphometric intrapapillary characteristics." Graefes Arch Clin Exp Ophthalmol **226**(6): 522-30.

Jonas, J. B., C. Y. Mardin, et al. (1991). "Morphometry of the human lamina cribrosa surface." Invest Ophthalmol Vis Sci **32**(2): 401-5.

Kamal, D. S., A. C. Viswanathan, et al. (1999). "Detection of optic disc change with the Heidelberg retina tomograph before confirmed visual field change in ocular hypertensives converting to early glaucoma." Br J Ophthalmol **83**(3): 290-4.

Keller, H. E. (1989). Objective lenses for confocal microscopy. Handbook of Biological Confocal Microscopy. J. B. Pawley. New York, Plenum Press.

Keller, P. R., C. N. McGhee, et al. (1998). "Fourier analysis of corneal topography data after photorefractive keratectomy." J Cataract Refract Surg **24**(11): 1447-55.

Kotecha, A., P. T. Khaw, et al. (2000). "*In vivo* imaging of the lamina cribrosa and its relationship to optic nerve head topography." IOVS: Supplement **41**(4).

Kotecha, A., D. Siriwardena, et al. (2001). "Optic disc changes following trabeculectomy: longitudinal and localisation of change." Br J Ophthalmol **85**(8): 956-61.

Lerman, S. (1984). "Biophysical aspects of corneal and lenticular transparency." Curr Eye Res **3**(1): 3-14.

Lerman, S. and L. Borkman (1976). "Spectroscopic evaluation and classification of the normal, aging and cataractous lens." Ophthalmic Res **8**: 335-353.

Liang, J. and D. R. Williams (1997). "Aberrations and retinal image quality of the normal human eye." J Opt Soc Am A **14**(11): 2873-83.

Liang, J., D. R. Williams, et al. (1997). "Supernormal vision and high-resolution retinal imaging through adaptive optics." J Opt Soc Am A **14**(11): 2884-92.

Lichter, P. R. (1977). "Variability of expert observers in evaluating the optic disc." Trans Am Ophthalmol Soc **74**: 532-72.

Lingren, M. (1968). "Techniques for tumor localization." Cancer **22**(4): 735-44.

Maeda, H., M. Nakamura, et al. (1999). "Morphometric features of laminar pores in lamina cribrosa observed by scanning laser ophthalmoscopy." Jpn J Ophthalmol **43**(5): 415-21.

Mainster, M. A., G. T. Timberlake, et al. (1982). "Scanning laser ophthalmoscopy. Clinical applications." Ophthalmology **89**(7): 852-7.

Manivannan, A., J. N. Kirkpatrick, et al. (1994). "Clinical investigation of an infrared digital scanning laser ophthalmoscope." Br J Ophthalmol **78**(2): 84-90.

Manivannan, A., P. F. Sharp, et al. (1993). "Digital fundus imaging using a scanning laser ophthalmoscope." Physiol Meas **14**(1): 43-56.

Manual (1997). Operation Manual for the Heidelberg Retina Tomograph Software Version 2.01. H. Engineering: 67.

Mardin, C. Y. and F. K. Horn (1998). "Influence of optic disc size on the sensitivity of the Heidelberg Retina Tomograph." Graefes Arch Clin Exp Ophthalmol **236**(9): 641-5.

Maumenee, A. E. (1983). "Causes of optic nerve damage in glaucoma. Robert N. Shaffer lecture." Ophthalmology **90**(7): 741-52.

Miller, D. T., D. R. Williams, et al. (1996). "Images of cone photoreceptors in the living human eye." Vision Res **36**(8): 1067-79.

Miller, K. M. and H. A. Quigley (1988). "The clinical appearance of the lamina cribrosa as a function of the extent of glaucomatous optic nerve damage." Ophthalmology **95**(1): 135-8.

Morgan, J. E., G. Jeffery, et al. (1998). "Axon deviation in the human lamina cribrosa." Br J Ophthalmol **82**(6): 680-3.

Morrison, J. C., J. A. Jerdan, et al. (1989). "Structural proteins of the neonatal and adult lamina cribrosa." Arch Ophthalmol **107**(8): 1220-4.

Nishimoto, K. and K. Sasaki (1995). "In vivo light scattering intensity in the lens versus in vitro spectral transmission in the nuclear region." Ophthalmic Res **27**(1): 1-11.

O Connor, D., T. Zeyen, et al. (1993). "Comparisons of methods to detect glaucomatous optic nerve damage." Ophthalmology **100**(10): 1498-503.

Odberg, T. and D. Riise (1985). "Early diagnosis of glaucoma. The value of successive stereophotography of the optic disc." Acta Ophthalmol (Copenh) **63**(3): 257-63.

Ogden, T. E., J. Duggan, et al. (1988). "Morphometry of nerve fiber bundle pores in the optic nerve head of the human." Exp Eye Res **46**(4): 559-68.

Ogoda, M., K. Hishinuma, et al. (1997). "Unsharp masking technique using multiresolution analysis for computed radiography image enhancement." J Digit Imaging **10**(3 Suppl 1): 185-9.

Podoleanu A. Gh., Rogers J.A., et al. (2000). "Three dimensional OCT images from retina and skin." Optics Express **7**(9): 292-298.

Puliafito, C. A., M. R. Hee, et al. (1995). "Imaging of macular diseases with optical coherence tomography." Ophthalmology **102**(2): 217-29.

Quigley, H. A. and E. M. Addicks (1981). "Regional differences in the structure of the lamina cribrosa and their relation to glaucomatous optic nerve damage." Arch Ophthalmol **99**(1): 137-43.

Quigley, H. A., E. M. Addicks, et al. (1981). "Optic nerve damage in human glaucoma. II. The site of injury and susceptibility to damage." Arch Ophthalmol **99**(4): 635-49.

Quigley, H. A., R. M. Hohman, et al. (1983). "Morphologic changes in the lamina cribrosa correlated with neural loss in open-angle glaucoma." Am J Ophthalmol **95**(5): 673-91.

Radius, R. L. (1981). "Regional specificity in anatomy at the lamina cribrosa." Arch Ophthalmol **99**(3): 478-80.

Radius, R. L. and D. R. Anderson (1979). "The course of axons through the retina and optic nerve head." Arch Ophthalmol **97**(6): 1154-8.

Radius, R. L. and M. Gonzales (1981). "Anatomy of the lamina cribrosa in human eyes." Arch Ophthalmol **99**(12): 2159-62.

Ridley, H. (1950). "Television in ophthalmology." XVI Concilium Ophthalmologicum Brittania Acta **2**: 1397-1404.

Ritch, R., M. B. Shields, et al. (1989). The Glaucomas, Mosby.

Rogers J.A., Podoleanu A. Gh., et al. (2001). "Topography and volume measurements of the optic nerve using en-face optical coherence tomography." Optics Express **9**(10): 533-545.

Rohrschneider, K., R. O. Burk, et al. (1994). "Reproducibility of the optic nerve head topography with a new laser tomographic scanning device." Ophthalmology **101**(6): 1044-9.

Rohrschneider, K., R. O. Burk, et al. (1993). "Reproducibility of topometric data acquisition in normal and glaucomatous optic nerve heads with the laser tomographic scanner." Graefes Arch Clin Exp Ophthalmol **231**(8): 457-64.

Roorda, A. (2000). "Adaptive optics ophthalmoscopy." J Refract Surg **16**(5): S602-7.

Rudnicka, A. R., D. F. Edgar, et al. (1992). "Construction of a model eye and its applications." Ophthalmic Physiol Opt **12**(4): 485-90.

Russ, J. C. (1998). The Image Processing Handbook, CRC and IEEE Press.

Sanchez-Martin, F. J. (1999). "Automatic segmentation of contours of corneal cells." Comput Biol Med **29**(4): 243-58.

Schuman, J. S., M. R. Hee, et al. (1995). "Optical coherence tomography: a new tool for glaucoma diagnosis." Curr Opin Ophthalmol **6**(2): 89-95.

Shields, M. B. (1989). Textbook of Glaucoma. Baltimore, Williams and Wilkins.

Shiose, Y. (1984). "The aging effect on intraocular pressure in an apparently normal population." Arch Ophthalmol **102**(6): 883-7.

Spencer, T., J. A. Olson, et al. (1996). "An image-processing strategy for the segmentation and quantification of microaneurysms in fluorescein angiograms of the ocular fundus." Comput Biomed Res **29**(4): 284-302.

Spencer, T., R. P. Phillips, et al. (1992). "Automated detection and quantification of microaneurysms in fluorescein angiograms." Graefes Arch Clin Exp Ophthalmol **230**(1): 36-41.

Spileers, W. and M. Goethals (1992). "Structural changes of the lamina cribrosa and of the trabeculum in primary open angle glaucoma (POAG)." Bull Soc Belge Ophtalmol **244**: 27-35.

Sturmer, J., D. Poinoosawmy, et al. (1992). "Intra- and inter-observer variation of optic nerve head measurements in glaucoma suspects using disc-data." Int Ophthalmol **16**(4-5): 227-33.

Takamoto, T. and B. Schwartz (1985). "Reproducibility of photogrammetric optic disc cup measurements." Invest Ophthalmol Vis Sci **26**(6): 814-7.

Tielsch, J. M., J. Katz, et al. (1988). "Intraobserver and interobserver agreement in measurement of optic disc characteristics." Ophthalmology **95**(3): 350-6.

Uchida, H., L. Brigatti, et al. (1996). "Detection of structural damage from glaucoma with confocal laser image analysis." Invest Ophthalmol Vis Sci **37**(12): 2393-401.

Uchida, H., Y. Kitazawa, et al. (2000). "Diagnostic ability of a new glaucoma classification program of Heidelberg Retina Tomograph II for early glaucoma." IOVS : Supplement **41**(4).

Varma, R. and G. L. Spaeth (1993). The Optic Nerve in Glaucoma. Philadelphia, J.B Lippincott Company.

von Jaeger, E. (1869). Ophthaloskopischer Handatlas. Vienna, Druck und Verlag der KK Hof und Staatsdruckerei.

Wade, A. R. (1998). High-resolution, *in vivo* imaging of the human cone photoreceptor mosaic. Institute of Ophthalmology. London, University College London: 209.

Wade, A. R. and F. W. Fitzke (1998). "A fast, robust pattern recognition system for low light level image registration and its application to retinal imaging." Optics Express **3**(3): 190-197.

Webb, R. H. and G. W. Hughes (1981). "Scanning laser ophthalmoscope." IEEE Trans Biomed Eng **28**(7): 488-92.

Webb, R. H., G. W. Hughes, et al. (1980). "Flying Spot T.V. Ophthalmoscope." Appl Optics **19**: 2991-7.

Weinreb, R. N., A. W. Dreher, et al. (1989). "Quantitative assessment of the optic nerve head with the laser tomographic scanner." Int Ophthalmol **13**(1-2): 25-9.

Wilczek, M. (1947). "The lamina cribrosa and its nature." Br J Ophthalmol **31**: 551-565.

Wollstein, G., D. F. Garway-Heath, et al. (1998). "Identification of early glaucoma cases with the scanning laser ophthalmoscope." Ophthalmology **105**(8): 1557-63.

Woon, W. H., F. W. Fitzke, et al. (1992). "Confocal imaging of the fundus using a scanning laser ophthalmoscope." Br J Ophthalmol **76**(8): 470-4.

Woon, W. H., F. W. Fitzke, et al. (1990). "The Scanning Laser Ophthalmoscope Basic Principles and Applications." Journal of Ophthalmic Photography **12**: 17-23.

Yan, D. B., F. M. Coloma, et al. (1994). "Deformation of the lamina cribrosa by elevated intraocular pressure." Br J Ophthalmol **78**(8): 643-8.

Yan, D. B., J. G. Flanagan, et al. (1998). "Study of regional deformation of the optic nerve head using scanning laser tomography." Curr Eye Res **17**(9): 903-16.